7. SITES 790/791[1]

Shipboard Scientific Party[2]

HOLE 790A

Date occupied: 29 April 1989

Date departed: 29 April 1989

Time on hole: 14 hr, 30 min

Position: 30°54.95′N, 139°50.66′E

Bottom felt (rig floor; m, drill-pipe measurement): 2232.7

Distance between rig floor and sea level (m): 10.50

Water depth (drill-pipe measurement from sea level, m): 2222.2

Total depth (rig floor; m): 2270.10

Penetration (m): 37.40

Number of cores (including cores with no recovery): 4

Total length of cored section (m): 37.40

Total core recovered (m): 35.71

Core recovery (%): 95.5

Oldest sediment cored:
Depth (mbsf): 37.40
Nature: vitric sand
Age: Quaternary
Measured velocity (km/s): 1.59

HOLE 790B

Date occupied: 29 April 1989

Date departed: 1 May 1989

Time on hole: 1 day, 5 hr, 45 min

Position: 30°45.96′N, 139°50.66′E

Bottom felt (rig floor; m, drill-pipe measurement): 2234.0

Distance between rig floor and sea level (m): 10.50

Water depth (drill-pipe measurement from sea level, m): 2223.5

Total depth (rig floor; m): 2372.90

Penetration (m): 138.90

Number of cores (including cores with no recovery): 15

Total length of cored section (m): 138.90

Total core recovered (m): 88.71

Core recovery (%): 63.7

Oldest sediment cored:
Depth (mbsf): 138.90
Nature: vitric sand and silt
Age: Quaternary
Measured velocity (km/s): 1.57

HOLE 790C

Date occupied: 1 May 1989

Date departed: 3 May 1989

Time on hole: 2 days, 19 hr

Position: 30°54.95′N, 139°50.69′E

Bottom felt (rig floor; m, drill-pipe measurement): 2234.0

Distance between rig floor and sea level (m): 10.50

Water depth (drill-pipe measurement from sea level, m): 2223.5

Total depth (rig floor; m): 2621.10

Penetration (m): 387.10

Number of cores (including cores with no recovery): 33

Total length of cored section (m): 302.10

Total core recovered (m): 127.32

Core recovery (%): 42.1

Oldest sediment cored:
Depth (mbsf): 387.10
Nature: nannofossil-rich silty clay, nannofossil-rich sandy mud (Core 126-790C-20X) and sandy silt (Core 126-790C-33X)
Age: Quaternary
Measured velocity (km/s): 1.56 (Core 126-790C-20X)

HOLE 791A

Date occupied: 4 May 1989

Date departed: 6 May 1989

Time on hole: 2 days, 6 hr

Position: 30°54.96′N, 139°52.20′E

Bottom felt (rig floor; m, drill-pipe measurement): 2279.0

Distance between rig floor and sea level (m): 10.50

Water depth (drill-pipe measurement from sea level, m): 2268.5

Total depth (rig floor; m): 2736.00

Penetration (m): 457.00

Number of cores (including cores with no recovery): 49

Total length of cored section (m): 457.00

Total core recovered (m): 179.86

Core recovery (%): 39.4

Oldest sediment cored:
Depth (mbsf): 428.40
Nature: crystal-vitric silty sand and sandy siltstone
Age: Quaternary
Measured velocity (km/s): 1.56

HOLE 791B

Date occupied: 6 May 1989

Date departed: 13 May 1989

Time on hole: 7 days, 6 hr

[1] Taylor, B., Fujioka, K., et al., 1990. *Proc. ODP, Init. Repts.*, 126: College Station, TX (Ocean Drilling Program).

[2] Shipboard Scientific Party is as given in the list of participants preceding the contents.

Position: 30°54.98′N, 139°52.19′E

Bottom felt (rig floor; m, drill-pipe measurement): 2279.0

Distance between rig floor and sea level (m): 10.50

Water depth (drill-pipe measurement from sea level, m): 2268.5

Total depth (rig floor; m): 3424.00

Penetration (m): 1145.00

Number of cores (including cores with no recovery): 79

Total length of cored section (m): 915.00

Total core recovered (m): 114.39

Core recovery (%): 15.48

Oldest sediment cored:
Depth (mbsf): 983.70
Nature: nannofossil-foraminifer claystone (Core 126-791B-47R) and crystal-vitric silt and sandy mud (Core 126-791B-62R)
Age: Quaternary
Measured velocity (km/s): 1.56 (Core 126-791B-39X)

Hard rock:
Depth (mbsf): 829.60
Nature: basalt breccia, basalt mousse, diabase
Measured velocity (km/s): 4.26–4.48

Principal results: Sites 790 and 791 are located near the center of Sumisu Rift, a backarc graben west of the Izu-Bonin island-arc volcanoes Sumisu Jima and Tori Shima. The sites are 2.4 km apart and are situated on the western side of the eastern inner-rift half-graben. The syn-rift sediments dip to the east with regional basal dips of 15° and are cut by 45°–60°, dominantly west-dipping, normal faults.

The principal objectives of this site were to determine (1) the vertical-motion history of the rift basin, (2) the nature of volcanism and sedimentation in the rift, (3) the duration of rifting and the nature of the rift basement, and (4) the chemistry of fluids circulating in the sediments. Site selection was determined from multichannel seismic (MCS) records and a short shipboard seismic survey; the sites chosen lie on *Fred Moore* 35-07, Line 4, at 1933Z (Site 790) and at 1953Z (Site 791). Sites 790 and 791 were occupied from 0656 hr (all times UTC), 29 April, to 1345 hr, 13 May 1989.

Hole 790A was spudded with the advanced hydraulic piston corer (APC) at 1400 hr on 29 April 1989, coring 35.7 m with 96% recovery. Potential entanglement with fishing line required a pipe round trip. Hole 790B recored the mud line and continued with an APC to 100.3 m below seafloor (mbsf) with 88% recovery before switching to the extended core barrel (XCB) for a further 38.6 m with 2% recovery. A top-drive electrical short ended the hole. Hole 790C overlapped the poorly recovered basal section of 790B, recovering 98% of the interval from 85 to 155.2 mbsf with the APC and continued with the XCB to 271.1 mbsf with 50% recovery. Recovery with the XCB in the basal 116 m of Hole 790C to 387.1 m total depth (TD) was 0.5%. Operations in Hole 790C ended at 2210 hr on 3 May after the lockable flapper valve jammed open and short trips showed repeated hole filling that made logging unsafe.

Hole 791A was spudded with an APC at 0730 hr on 4 May, coring 207.9 m with 83% recovery. The hole was continued with an XCB to 457 mbsf with 3% recovery. Hole 791B was spot cored and washed down to 416.3 mbsf and was then cored with the rotary core barrel (RCB) to 1145 mbsf. Recovery between 457 and 834 mbsf was 23% and in the basement below was 9%. Extensive hole conditioning in preparation for logging was ended when the pipe stuck at 825 msbf. After geochemical logging through the pipe of the sedimentary section, the pipe was severed at 46 mbsf with the third explosive charge.

Three lithologic units were defined at Sites 790 and 791:

1. Unit I, deposited in the last 0.2 m.y., is vitric silt and sand, pumiceous gravel, and vitric silty clay at Site 790, 0–165 mbsf, and is pumiceous gravel and sand, vitric silt, pumiceous pebbly sand, and nannofossil-rich silty clay at Site 791, 0–428 mbsf.

2. Unit II, deposited between 0.2 and 1.1 Ma, is burrowed nannofossil clay, nannofossil-rich clay, silty clay, and clayey silt at Site 790, 165–271 mbsf, and is nannofossil claystone, sandy mudstone, and vitric silt at Site 791, 428–834 mbsf.

3. Unit III is scoriaceous basalt at Site 790, 269–387 mbsf, and, in order of first occurrence downsection, is composed of basalt breccia, basalt, diabase, basaltic "mousse," and mafic to felsic tuff and lapilli tuff at Site 791, 834–1145 mbsf. A vitric siltstone occurs at 329 mbsf in Site 790, and a coarse sandy silt occurs at 975 mbsf in Site 791. Both sedimentary layers are Pleistocene.

Units I and II are well dated using nannofossils, foraminifers, radiolarians, and paleomagnetics. Eight chronostratigraphic datums at each site show that sedimentation rates increased exponentially from 80 and 300 m/m.y. at 1 Ma to 1000 and 2250 m/m.y. in the last 100 k.y. at Sites 790 and 791, respectively. The rapid sedimentation provides high-resolution records of bioevolution and magnetic reversals. Applying the average sedimentation rates for the period 0.46–0.83 Ma to the Brunhes/Matuyama polarity transition indicates that the decrease of dipole intensity is limited to about 600 yr and that the reversal in inclination occurred in perhaps as little as 100 yr. However, it is possible that we recovered only one of several reversals in the polarity transition zone.

Bimodal mafic-felsic volcanism is recorded throughout the sedimentary history of the basin, although the relative proportions of each component change. Explosive arc volcanism, possibly from Sumisu and/or South Sumisu calderas, provided thick deposits of felsic pumiceous sand and gravel four times during the deposition of Unit I at approximately 60-k.y. intervals. One geochemical analysis indicates that the mafic scoria and ash probably derived from intrarift basaltic eruptions. Thin ash beds and scattered clasts of basaltic scoria and felsic pumice, with the mafic components dominant, are present throughout Unit II and increase in proportion downhole.

Carbonate contents are $<3\%$ in the coarse clastic rocks of Unit I, up to 20% in the finer interbeds, and 20%–40% in Unit II. Because of the high sedimentation rates in Unit II at Site 791, the burial of organic carbon led to reducing conditions in the sediment and precipitation of iron sulfides. Concentrations of sedimentary organic carbon vary from below detection in the coarse clastic rocks to as much as 1.2%. Fluid geochemistry studies indicate that fluids other than seawater are not circulating through the sediments.

The differential subsidence between the two sites is matched by the clastic and the biogenic sedimentation, with rates for Unit II at Site 791 almost four times those at Site 790. This, and the lack of coeval material on at least the eastern rift flank, requires that a large proportion of the pyroclastic and pelagic materials were (re)deposited by submarine mass flows. Benthic foraminifers are consistent with deposition in 2-km water depths during the Brunhes Chron and at somewhat greater depths during earlier time intervals.

Bedding at Site 790 is near horizontal, but at Site 791 the dip gradually increases to 15°–20° by 600 mbsf and then abruptly increases to 35°–45° by 760 mbsf down to basement. The MCS data indicate that the dips are easterly above 650 mbsf, and magnetic declinations, after tilt corrections, indicate that the dips remain easterly above basement. Near basement, Hole 791B may have crossed into the footwall of an intra-rift fault, thereby missing a few hundred meters (about 0.1 m.y.) of the early syn-rift sediments. The dips of the basement rocks vary from 40° at the top to 5°–40° in some of the basal fault slices.

The sparsely phyric basaltic volcanic rocks at Sites 790 and 791 are highly vesicular, despite their eruption in deep water, probably because of their high pre-eruption water contents. One more-differentiated lava contains clinopyroxene in addition to the olivine and plagioclase typical of the more mafic lavas that it overlies. The diabase intrusions range from relatively olivine rich and as mafic as any of the basalts, to Fe-Ti-rich and more differentiated than any of the basalts. The 135-m-thick basaltic "mousse" consists primarily of highly expanded basaltic glass, with vesicular "clasts" in an even more vesicular glassy matrix of the same composition. It is interpreted as the product of a large-volume, deep-submarine eruption of gas-rich basalt.

The rift basement basalts may be distinguished from Izu-Bonin Arc basalts by lower Ba (<30 ppm) and higher TiO_2 ($>0.95\%$) contents with respect to MgO, Zr, and V. They are inferred to be of syn-rift origin, but are more similar to rift-wall rocks dated at 1.0–1.4 Ma and to seamounts in the outer rift than to the 250-ka pillow ridges of the inner rift, which implies a temporal evolution of rift volcanism toward compositions more depleted in high-field-strength elements.

The basalts at Hole 791B have lower concentrations of Ba and Rb than do those at Hole 790C and the younger rocks of the inner rift. These concentrations are as low as those in Mid-Ocean Ridge basalts (MORB) and in the most mature backarc basins.

The tuff and lapilli tuffs at the base of Hole 791B show strong flattening of pumice shards and the development of a eutaxitic texture. They are interpreted as a sequence of hot pyroclastic flows from a proximal eruption site. They are dominantly andesitic, with one basal basaltic unit. Their most immobile elements have strong island-arc characteristics (Ti/Zr = 195 and Zr/Y = 1.5), implying that the tuffs cap an arc basement of unknown age. However, alteration effects make this conclusion preliminary. Alteration increases down the basement section from fresh to zeolite or lower greenschist facies in the basal 41 m, which penetrated a fault zone evidenced by slickensides, fault gouge, massive gypsum, and minor pyrite.

Physical properties measurements of the sediments indicate that (1) average bulk density values increase downhole from 1.55 to 1.8 g/cm^3 at Site 790 and to 1.9 g/cm^3 at Site 791; (2) average porosity values decrease from 70% to 60% at Site 790 and to 55% at Site 791; (3) sonic velocity data range from 1.53 to 1.61 km/s in Unit I, in Unit II to 1.52–1.55 km/s at Site 790 (a small velocity inversion), and to 1.61–1.84 km/s at Site 791; and (4) average thermal conductivity measurements increase downhole from 0.9 to 1.1 and 1.2 W/m · K at Sites 790 and 791, respectively.

The range of basement physical properties data at Site 791 includes (1) bulk density, 2.2–3.0 g/cm^3; (2) porosity, 8%–44%; (3) sonic velocity, 2.6–5.2 km/s, and (4) thermal conductivity, 1.0–1.2 W/m · K. The lower velocity and density and the higher porosity values are from the basaltic "mousse." The lowest porosity values are from the basal lapilli tuffs, and the highest velocity value is from a gypsum vein.

Geochemical logging at Site 791 identified isolated natural gamma-ray peaks with some of the silty clay beds. These high values are mostly caused by thorium. Long sections in Unit I with uniformly low gamma-ray values are associated with unrecovered pumiceous sand and gravel.

The principal results of this site are as follows:

1. Rifting began, and rift basement depths exceeded 2 km, prior to 1.1 Ma.
2. Basement was formed by early rift basaltic lavas and intrusives, as well as by arc pyroclastic rocks metamorphosed to zeolite or lower greenschist facies.
3. A large-volume, deep-submarine eruption of water-rich basalt produced basaltic "mousse," a highly expanded basaltic glass, with vesicular "clasts" in an even more vesicular glassy matrix of the same composition.
4. Extremely rapid, differential, and accelerating subsidence and sedimentation occurred in the inner-rift half-graben in the last 1.1 m.y.
5. Intra-rift basaltic eruptions and rhyolitic arc eruptions were common 1.1–0.2 Ma, but explosive arc volcanic activity dramatically increased about 0.2 Ma.
6. A large proportion of the pyroclastic and pelagic materials were (re)deposited by submarine mass flows.
7. Fluids other than seawater are not circulating locally through the sediments.
8. The decrease of dipole intensity and the reversal in inclination associated with the Brunhes/Matuyama polarity transition is limited to about 600 yr and occurred in perhaps as little as 100 yr, respectively.

BACKGROUND AND OBJECTIVES

Site 790 is located at 30°54.96′N, 139°50.66′E, at 2223 m below sea level (mbsl), and Site 791 is located at 30°54.97′N, 139°52.20′E, at 2268 mbsl. Each site is near the center of Sumisu Rift, a backarc graben west of the active Izu-Bonin Arc volcanoes Sumisu Jima and Tori Shima (Figs. 1 and 2). The sites are 2.4 km apart and are located on the western side of the eastern inner-rift half-graben (Figs. 2–5). The syn-rift sediments dip to the east with regional basal dips up to 15° and are cut by 45°–60°, dominantly west-dipping, normal faults (Fig. 5).

The pre-rift "basement" is not well imaged by the MCS profiles, probably because of the structural complexity. By drilling in the rift, we sought to determine the following: (1) the vertical-motion history of the rift basin, (2) the nature of volcanism and sedimentation in the rift, (3) the duration of rifting and the nature of the rift basement, and (4) the chemistry of fluids circulating in the sediments.

The first of these objectives was addressed through a combination of paleontological estimates of paleobathymetry, backstripping the sedimentation history using the physical properties and logging data, and seismic stratigraphic analyses of the interconnecting MCS profiles. To meet the second and third objectives required recovery, dating, and characterization of the syn-rift section. The surface sediments in the rift basin include hemipelagic muds and volcaniclastic turbidites, with ash and pumice layers (Nishimura and Murakami, 1988). However, the rates and styles of deposition of the up to 1.5-km-thick rift-basin sediment fill and the duration of rifting were unknown prior to drilling.

The frequency, chemistry, and eruptive style of the syn-rift arc margin and the rift basin volcanism was ascertained from studies of the volcaniclastic sediments. The basement petrology determined whether the rift is floored by stretched, subsided arc crust, recently intruded crust, or some combination of the two. Finally, the fourth objective, which is concerned with the chemistry of the fluids that heat-flow and mineralization studies indicate are circulating in the basin, was investigated by examining the chemistry of pore fluids squeezed from the cores and hydrothermal alteration products.

SEISMIC STRATIGRAPHY

Correlation of site-survey MCS data with recovered core material (Fig. 6) was accomplished by using physical properties velocity data, averaged over each lithologic unit (see "Physical Properties" section, this chapter), to convert depths (mbsf) into two-way traveltimes. Sites 790 and 791 were drilled in the eastern inner-rift graben of Sumisu Rift, bounded to the east by a west-dipping master fault zone. Normal faulting, synthetic to the master fault, has created a series of east-dipping tilted fault blocks within the rift basin. These fault blocks are also cut by minor antithetic faulting. Both fault sets extend to the seafloor, indicating that they are currently active.

The pattern of faulting is responsible for concentrating basin subsidence adjacent to the eastern margin of the rift and for thinning the sedimentary section toward the west. Synthetic faulting has created sedimentary reflectors that exhibit increasing dip with depth, indicating that subsidence is syn-depositional. Continuous tilting of the fault blocks has resulted in progressive onlap and, in some cases, erosional truncation by younger sedimentary strata.

Unit I (see "Lithostratigraphy and Accumulation Rates" section, this chapter) is characterized by a series of rather continuous, high-amplitude reflections that can be traced between the two sites. Several strong reflectors within Unit I, which are correlatable throughout the south Sumisu Rift basin, document that subsidence is greatest in the eastern inner-rift graben. The upper portion of Unit I at Site 791 (seafloor to 3.22 s, 0–167 mbsf) returns discontinuous low-amplitude reflections that possibly are a result of the greater amount of coarse debris-flow material accumulating in this topographic low. The base of these discontinuous low-amplitude reflections corresponds to the base of pumice bed II (see "Lithostratigraphy and Accumulation Rates" section, this chapter).

The Unit I/II boundary occurs at 3.17 s at Site 790 and 3.56 s at Site 791. At Site 791, this boundary is near high-amplitude reflection events; however, at Site 790, onlap has juxta-

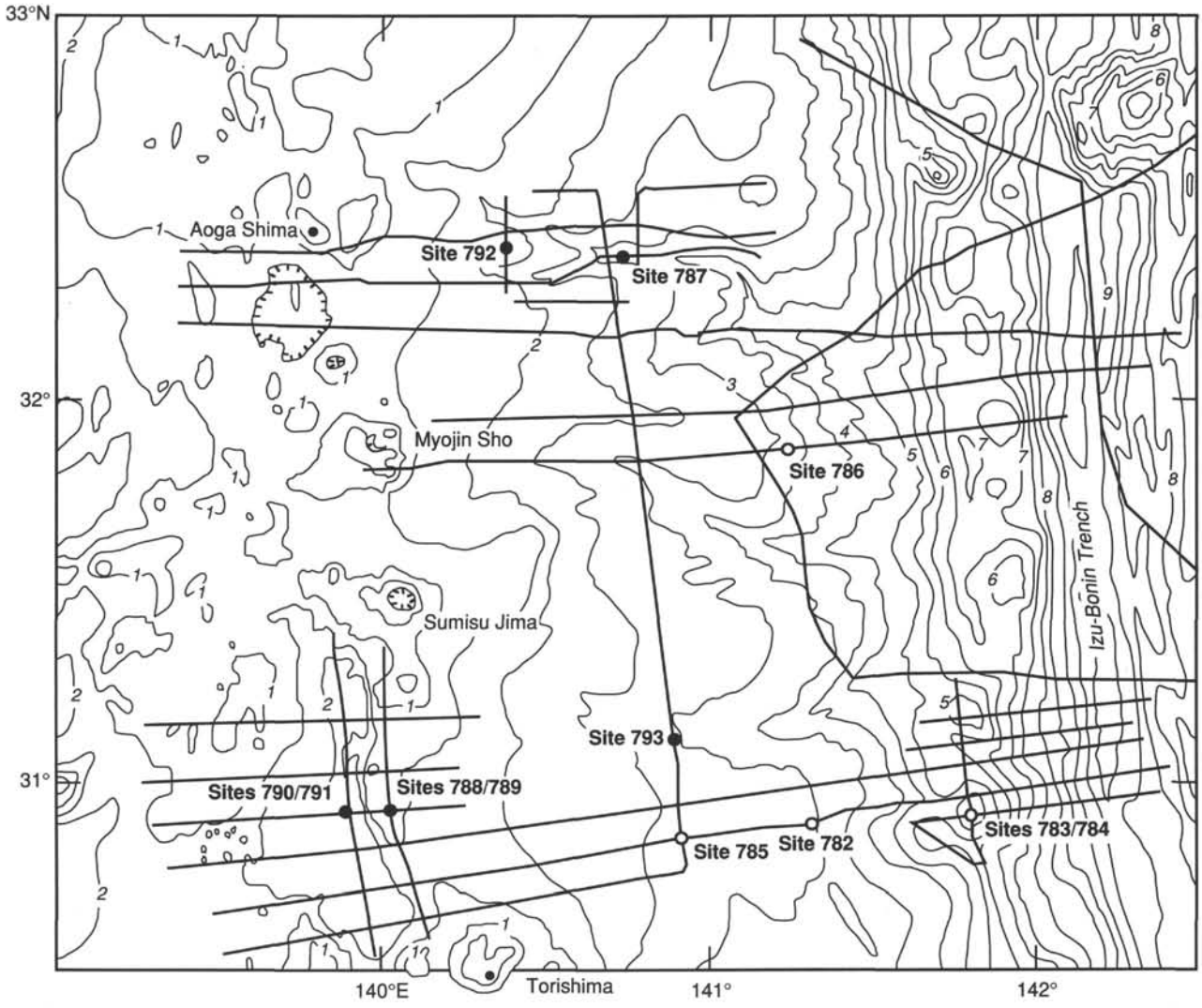

Figure 1. Bathymetric map at 0.5-km-contour interval of the Izu-Bonin arc-trench system between 30.5° and 33°N. The locations of sites drilled on Legs 125 (open circles) and 126 (filled circles) are shown on the map as are the locations of MCS site survey lines.

posed strata with less impedance contrast. Unit II is characterized at each site by an absence of any strong or continuous reflectors. This is probably a result of low-impedance contrasts within this unit (see "Physical Properties" section, this chapter) combined with structural disruption by pervasive rift faulting. Correlation of this unit throughout the rift basin is difficult because of the lack of strong continuous reflectors, complex faulting, and local deposition in small, fault-block-bounded depocenters. A strong reflection event between 3.25 and 3.30 s at Site 790 does not appear to correlate with a distinct lithologic or physical property change and may be an out-of-plane reflection.

Two-way traveltimes for lithostratigraphic, biostratigraphic, and paleomagnetic horizons observed at Sites 790 and 791 were calculated using physical properties velocity data (Table 1). These horizons include the base of the coarse pumice unit above Key Bed #7, Key Bed #7, lithologic unit boundaries I/II and II/III (see "Lithostratigraphy and Accumulation Rates" section, this chapter), the first occurrence (FO) of *Emiliania huxleyi* at 275 ka and the last occurrence (LO) of *Pseudoemiliania lacunosa* at 460 ka (see "Biostratigraphy" section, this chapter), and the Brunhes/Matuyama boundary (730 ka; see "Paleomagnetics" section, this chapter). These horizons and the correlation of major seismic reflectors are shown in Figure 7. This figure demonstrates the dramatic thickening of the sedimentary section from Site 790 east to Site 791 as a result of rift-basin faulting and differential subsidence. This structural evolution has created reflectors that onlap older tilted horizons and sometimes cause erosional truncation by younger horizons.

The pattern of recent sediment accumulation in this area of actively subsiding and rotating fault blocks is a modern analogue for the deposition of deeper seismic reflectors. The transparent, surficial layer observed in the high-resolution seismic record (3.5 kHz; Fig. 8) at Site 791 thins considerably, and may onlap, toward Site 790. Thicker and coarser recovered core material at Site 791 and seismically observed stratigraphic onlap supports this interpretation of structurally controlled sedimentation.

Correlation of these horizons to the east of Site 791 shows that sedimentation rates there are even higher than those observed at Site 791. Reflector correlation, although complicated by tilting, faulting, and onlap, is possible down to the horizon corresponding to the FO of *E. huxleyi* (Horizon H; Fig. 7). However, below this horizon, seismic correlation between Sites 790 and 791 is not possible. The difficulty in correlating the three lowermost horizons (L, B, and II, Fig. 7) probably results from a combination of (1) complex faulting that progressively

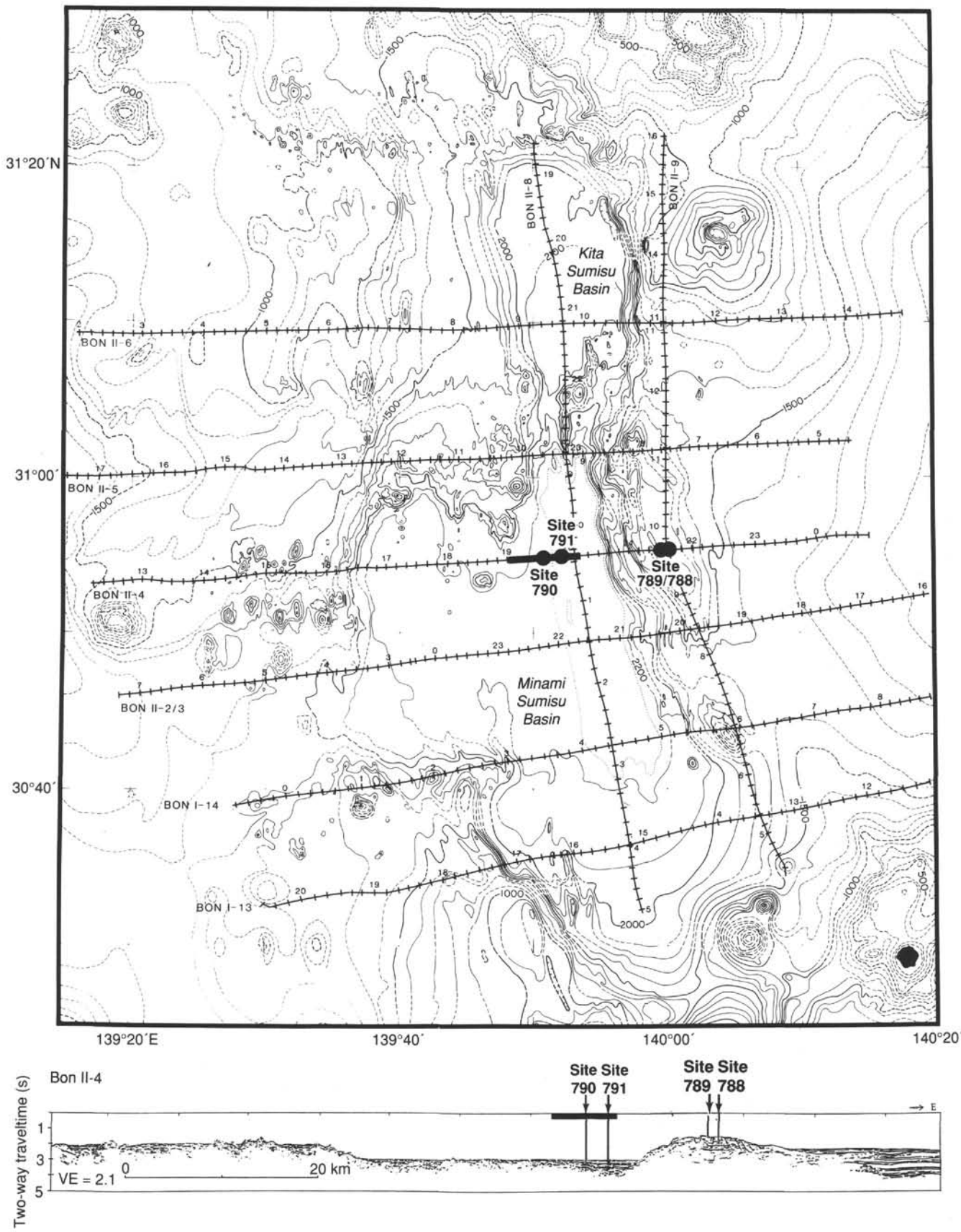

Figure 2. Bathymetric map (100-m-contour interval) of Sumisu Rift and surrounding area showing the location of MCS site survey tracks and of Sites 788–791. A line drawing of MCS line BON II-4 (*Fred Moore* 35-07) is shown at the bottom of the figure. The segment of this line shown in Figure 6 is indicated by the solid bars in the upper and lower parts of the figure.

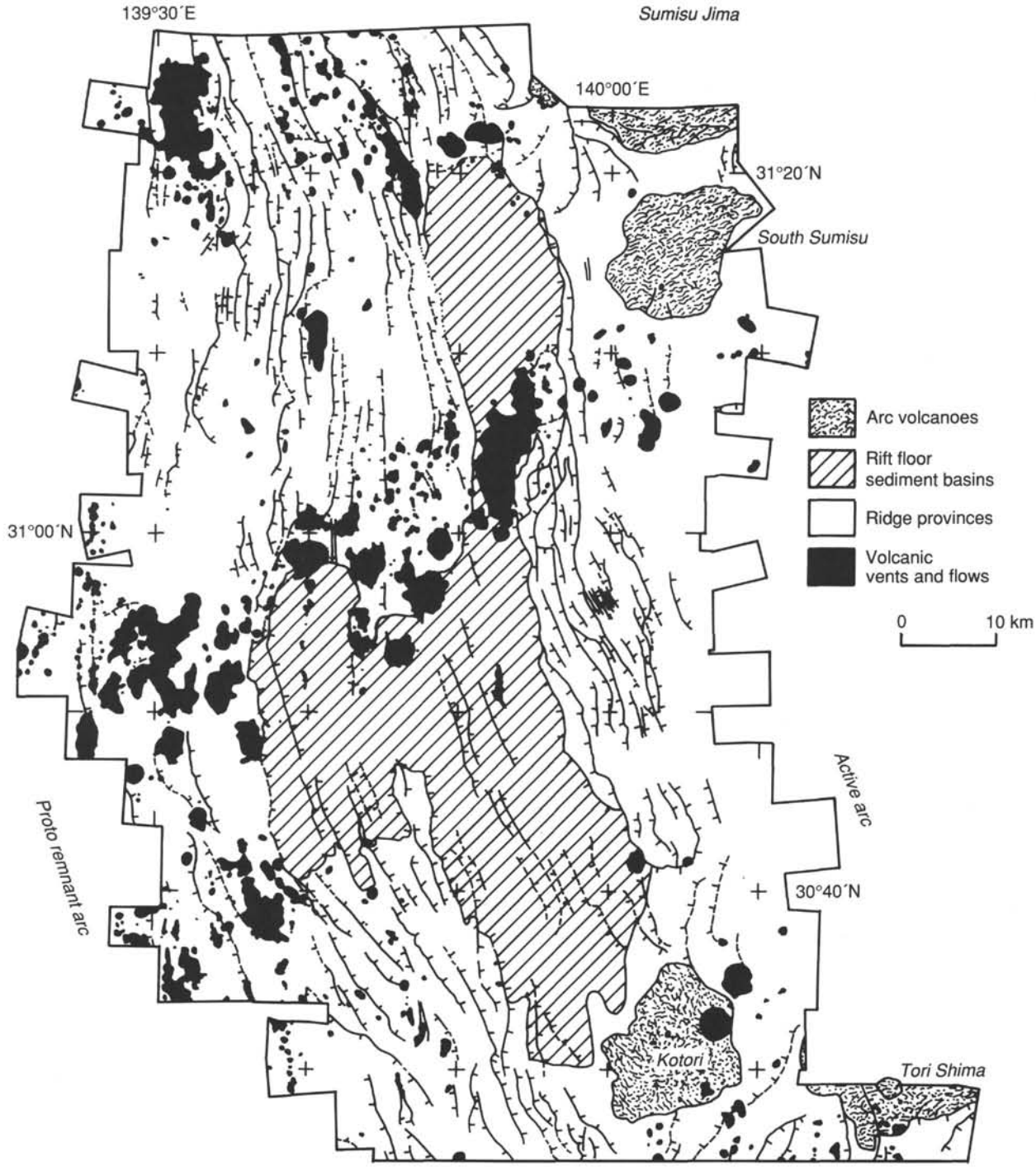

Figure 3. Simplified geological interpretation of the Sumisu Rift SeaMARC II sidescan data (Taylor et al., 1988a, 1988b) showing the main faults, volcanic fields, sedimentary basins, and adjacent arc volcanoes (from Taylor et al., in press).

offsets deeper horizons to a greater degree, (2) pre-rift and early syn-rift volcanism that overprints and obscures the sedimentary horizons, and (3) high-amplitude, possibly out-of-plane seismic reflections.

The Unit II/III boundary occurs at 3.32 s at Site 790 and 4.05 s at Site 791. At Site 791, this boundary correlates very well with a high-amplitude reflection that is a result of the large impedance contrast across this boundary (see "Physical Properties" section, this chapter). This high-amplitude reflection is interpreted to be a fault surface with Unit II claystones in fault contact with Unit III basaltic lavas. At Site 790, the Unit II/III boundary does not correspond to a similar high-amplitude reflection. Furthermore, correlations of seismic "basement" documented by drilling at Site 791 to any similar reflector at Site 790 indicates that acoustic basement at Site 790 may occur as deep as 3.5–3.6 s. This implies that acoustic basement may be more than 200 m below the basalt scoria at the bottom of Site 790. Furthermore, at Site 790, the basalt scoria is characterized by transparent to low-amplitude discontinuous reflections that are different from the acoustic basement observed at Site 791. Acoustic basement throughout the rift basin is characterized by discontinuous, chaotic reflections.

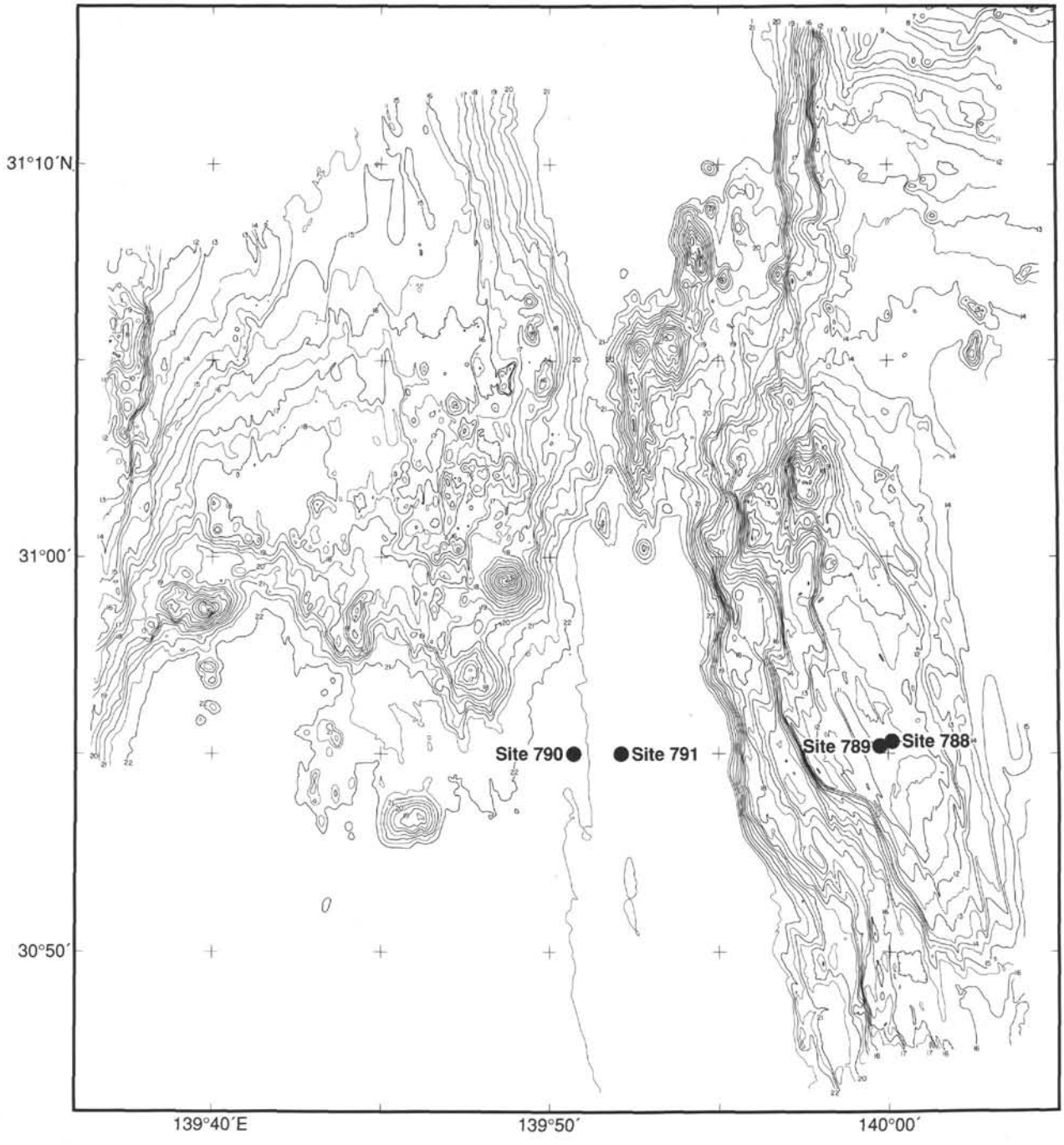

Figure 4. SeaBeam bathymetric map (50-m-contour interval) of the central Sumisu Rift showing the location of Sites 788–791 (after Taylor et al., in press a).

OPERATIONS

Site 790 (BON-1A)

The vessel made the transit from Site 789 to Site 790 in 3 hr and dropped a beacon at 0656 hr (all times UTC) on 29 April 1989.

Hole 790A

Because the seafloor sediments were assumed to be soft enough for piston coring, an APC/XCB bottom-hole assembly (BHA) was made up and run to the seafloor. It included a lockable float valve (to allow logging through the bit, if desired) and a nonmagnetic drill collar (to allow magnetic orientation of the piston cores). The mud-line APC core was taken at 1425 hr on 29 April 1989. Four APC cores were recovered (Table 2). While Core 126-790A-4H was being retrieved, a lighted buoy and several smaller floats from nearby fishing vessels were observed floating in the water on both sides of the ship. If the floats were attached to nets or long fishing lines, they were close enough to represent a hazard to the dynamic-positioning thrusters. As a precautionary measure, the thrusters were shut down and retracted. Because station-keeping ability could not be guaranteed, the drill string was pulled clear of the seafloor until the fishing-float problem could be solved. The bit cleared the seafloor at

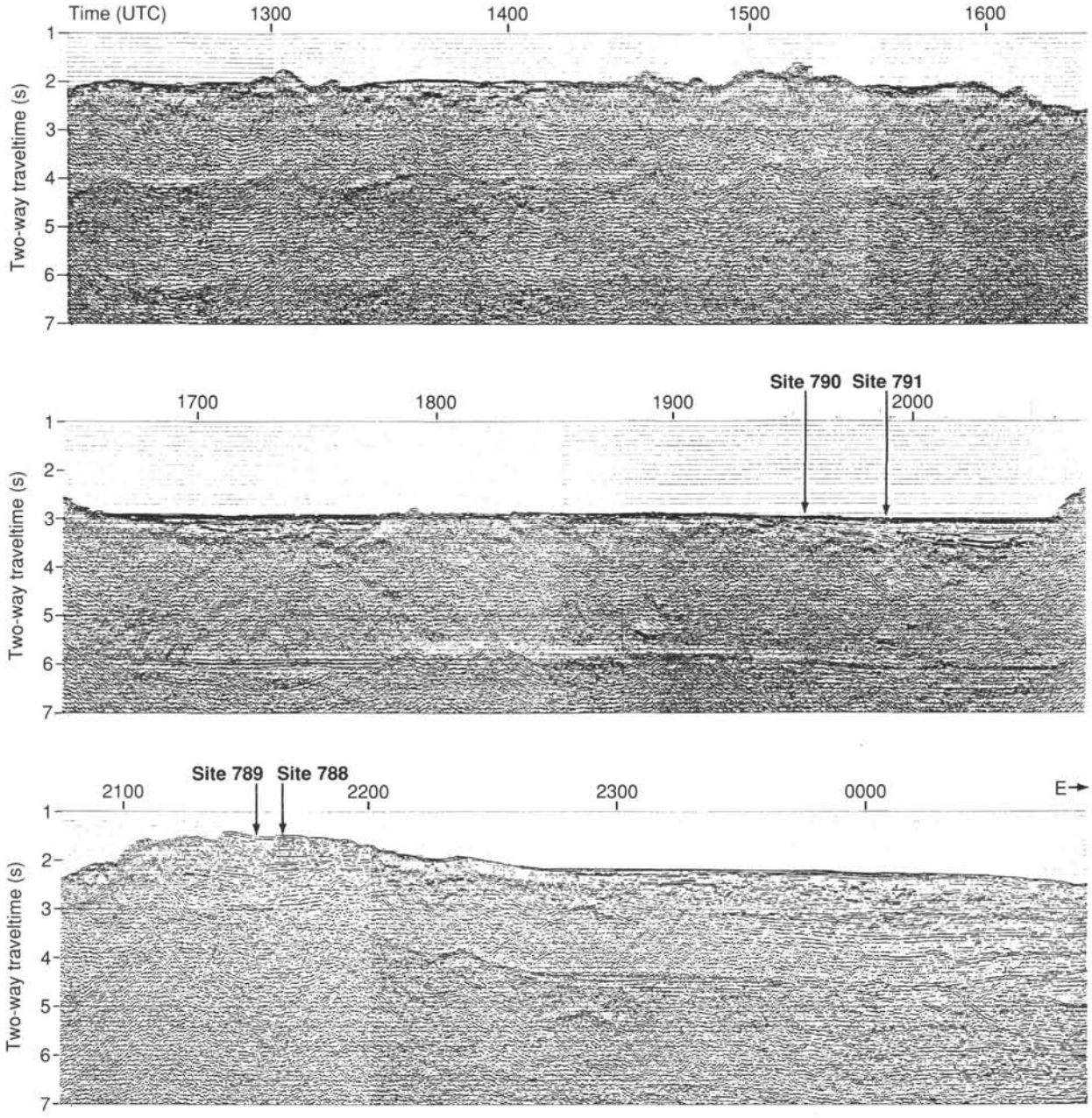

Figure 5. Latitudinal MCS profile BON II-4 (Taylor et al., this volume) across the eastern half graben of the Sumisu Rift at 30°55′N (see Fig. 2 for location). Sites 790 and 791 are located on the western side of the eastern half graben. Below 750 mbsf, Site 791 may cross one of the several 45°–60°, dominantly west-dipping, normal fault zones.

1655 hr and was on deck at 2130 hr on 29 April, ending Hole 790A.

Hole 790B

The fishing vessels responsible for the floats and long lines eventually came by to collect their wayward equipment and were seen pulling the lines aboard, close by the *JOIDES Resolution*. While pulling in their lines, they apparently snagged one under the drillship in the vicinity of the drill pipe. They seemed to cut that line, and then they departed, leaving the potential problem of lines fouled around the drill string. The thrusters could not be lowered safely because we could not see the lines in the water in the darkness. Without positive station-keeping ability, drilling could not proceed, so the drill bit was pulled to the deck and checked for fishing lines or nets. Nothing was found, so the ship was offset 20 m north, the BHA was run to the seafloor, and coring operations proceeded.

The short coring sequence completed in Hole 790A was repeated with a 3.3-m vertical overlap between the two holes. We recovered 11 APC cores with good success despite the sandy nature of the formation, which usually frustrates piston-coring attempts. An unsuccessful pore-water/heat-flow sample run was attempted after Core 126-790B-5H was cut.

Following Core 126-790B-11H, a 55,000-lb overpull in a sticky clay interval dictated a change to the XCB coring system. The switch was apparently too soon, however, because the next four XCB cores netted a total of only 0.8 m of loose, sandy material. Before more coring could be accomplished, a serious ground

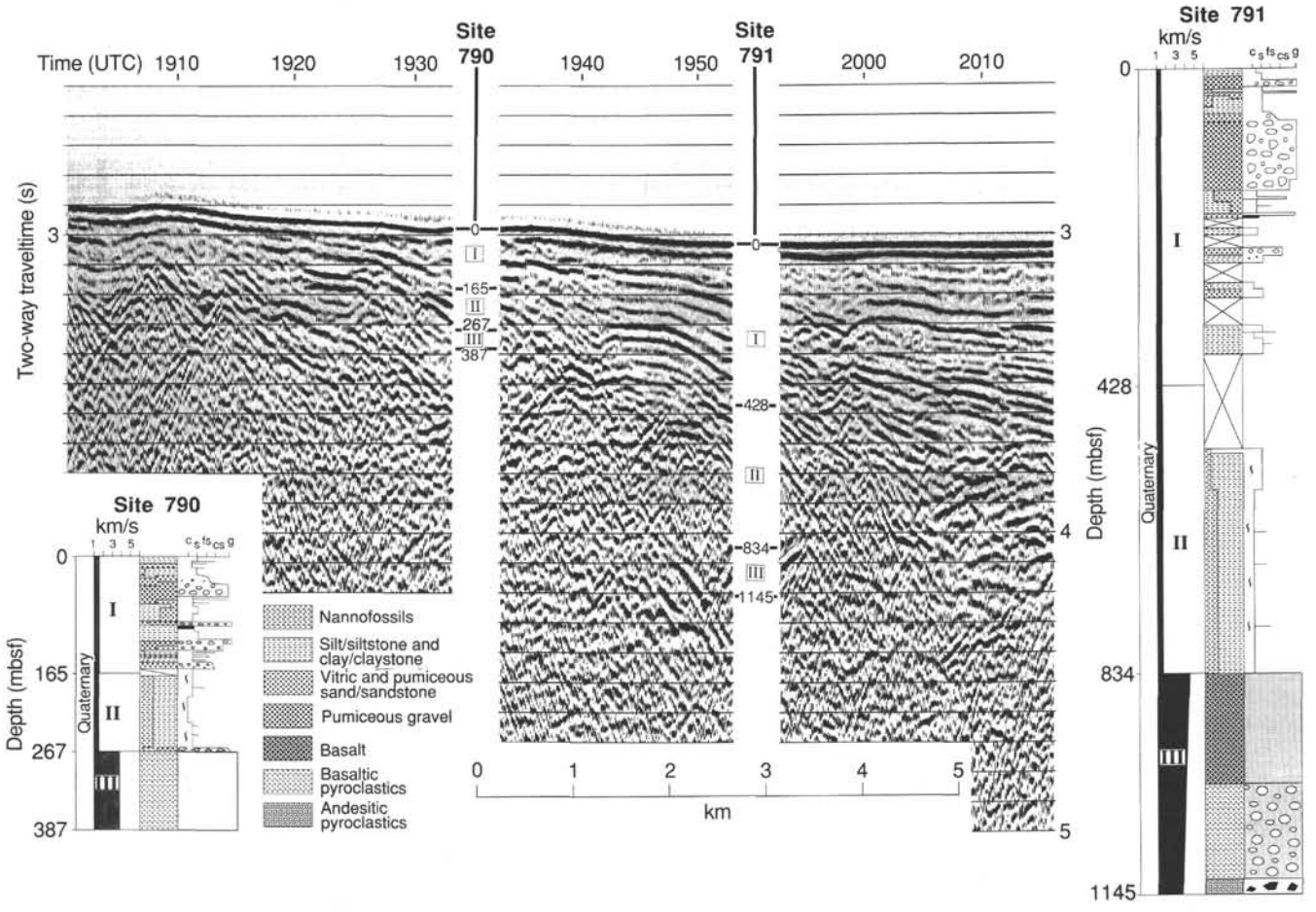

Figure 6. Correlation of Sites 790/791 lithostratigraphy with MCS seismic data. Lithologic units are identified on the seismic section, unit boundaries are given in meters below seafloor (mbsf), and lithologic columns (see "Lithostratigraphy and Accumulation Rates" section, this volume) are presented. The location of the *Fred Moore* seismic line is shown in Figure 2. The seismic profile has been stacked (48 fold), deconvolved, migrated, and filtered 10–60 Hz. The vertical exaggeration is ~4×; c = clay, s = silt, fs = fine sand, cs = coarse sand, and g = gravel/conglomerate.

fault in the top-drive power cables was discovered. Because the problem appeared to be one that would require many hours to fix, we ended drilling in Hole 790A and pulled the bit above the seafloor at 0315 hr on 1 May 1989.

Hole 790C

After 20.5 hr, the shorted-out umbilical lines to the top drive were repaired and coring operations were continued. Hole 790C was spudded at 1610 hr on 1 May, and the bit was washed without coring to 85 mbsf where piston coring resumed. This time the overpull through the sticky zone from 90 to 100 mbsf was tolerable (< 30 Kpsi), and we extended APC coring to Core 126-790C-8H at 155.2 mbsf. During most of this sequence, the APC did not achieve full stroke in the sand/silt-dominated sediment and the high recovery rate observed was probably because of flow-in.

We changed to XCB coring at Core 126-790C-9X and proceeded with fine results through Core 126-790C-20X at 271 mbsf. At that point, a new lithologic unit was encountered that resisted all recovery attempts with XCB-coring methods. The traces of material trapped in the recesses of the core catchers indicated that the missing sediment was very loose sand or gravel. The lack of recovery continued to frustrate all efforts until Core 126-790C-31X at 367 mbsf.

While running in with the sand line to retrieve Core 126-790C-31X, the bit plugged. The core barrel was also found to be stuck, undoubtedly by sand packed around the cutting shoe and bit throat. To remedy the stuck core barrel situation, the drill string was pulled until the bit was out of the gravel/sand zone at 261 mbsf. At that point, circulation was again achieved and an extensive mud treatment was pumped through the system to stabilize the hole and wash away the material jamming the core barrel.

The pipe was washed back to total depth through 44 m of fill that had collected when the hole partially caved in, and XCB coring resumed. Three more cores were cut, but with negligible recovery, in a formation consisting of pebbly gravels. At each connection and when attempting to insert the sinker-bar assembly, severe backflow was observed. The implication was that the hole annulus was heavily laden with sand and/or cuttings. Because backflow did not decrease when the core barrels were out of the string, it was assumed that the float valve was jammed open and therefore unable to prevent the ingress of sand. Temporary bit plugs were experienced after each backflow. We ended Hole 790C at 387.1 mbsf when the backflow was deemed to be too great a hazard to personnel and downhole equipment.

Before pulling the pipe completely out of the hole, the possibility of logging the lower unrecovered interval was evaluated by doing a short pipe trip up 100 m and back down. The short trip took less than 1 hr, but the hole was already filled with more than 30 m of sand. The possibility of getting a logging tool into the unstable zone was considered remote, and we abandoned

Table 1. Depth (mbsf) and two-way traveltimes for stratigraphic horizons observed at Sites 790 and 791.

Horizon	Site 790	Site 791
Base of pumice bed II (P)	54.65 mbsf 0.070 s	167 mbsf 0.214 s
Key Bed #7 (K)	87.85 mbsf 0.112 s	205 mbsf 0.262 s
I/II Boundary (I)	165 mbsf 0.210 s	428 mbsf 0.543 s
FO *Emiliania huxleyi* (H) (275 ka)	187 mbsf 0.239 s	518 mbsf 0.654 s
LO *Pseudoemiliania huxleyi* (L) (460 ka)	219 mbsf 0.280 s	659 mbsf 0.828 s
Brunhes/Matuyama (B) (730 ka)	244 mbsf 0.313 s	750 mbsf 0.933 s
II/III Boundary (II)	271 mbsf 0.350 s	834 mbsf 1.024 s
Total depth	387 mbsf 0.410 s	1145 mbsf 1.188 s

Notes: The stratigraphic boundaries include lithologic unit boundaries I/II and II/III (see "Lithostratigraphy and Accumulation Rates" section, this chapter), the Brunhes/Matuyama boundary, the first occurrence of *E. huxleyi* (see "Biostratigraphy" section, this chapter), Key Bed #7, and the base of pumice bed II (see "Lithostratigraphy and Accumulation Rates" section, this chapter). Letters and numbers in parentheses identify horizons shown in Figure 7. Two-way traveltimes are given in seconds below seafloor and are derived from physical properties velocities (see "Physical Properties" section, this chapter). FO = first occurrence and LO = last occurrence.

logging plans. The pipe was pulled out of the hole, and the bit reached the deck at 2215 hr, 3 May 1989.

Site 790 to 791

Although we had planned to run the drill string back to the bottom at Site 790 for coring Hole 790D with the RCB system, a change of heart occurred when geophysical interpretation determined that the site had been located too far from the sediment structure originally targeted. Thus, the site was abandoned and the vessel made a very short transit to a position 1.5'E of Site 790. The move was beyond beacon offset range, so a new beacon was dropped at 0138 hr on 4 May 1989 and Site 791 (proposed Site BON-1A) was begun.

Hole 791A

An APC/XCB BHA was put together and run to the seafloor. It included the nonmagnetic drill collar to enable oriented piston coring. A prototype set of Hydrolex mechanical jars were also included, and an extra stand of drill collars was added above the jars for hammer weight if needed. The mud-line coring attempt with the APC encountered unexpectedly firm material at the surface, and the core barrel was not able to extend to its full length. Since the roller cone bit and drill string were hanging some 5 m above the seafloor, the column-loaded piston corer barrel was unsupported and it subsequently buckled. The bent barrel could not at first be pulled back into the drill string. The stuck barrel was dislodged after a few minutes of hammering with the sand-line link jars. On deck, it was found that the lower 15-ft core-barrel section had broken off from the upper section. The upper barrel was bent beyond reuse, and the cutting shoe, core catchers, and the core itself were lost.

Rather than risk another buckled core barrel with a mud-line shot, the next core was taken at the normal location for the second core in the sequence with the BHA buried 4.5 m. The results were good, and piston coring continued for a total of 23 cores to a depth of 207.9 mbsf. The formation penetrated in the APC sequence was dominated by sand and pebbly gravel. The coring results were unusual for APC performance in sands, with recovery averaging 82% and over half of the shots registering full stroke of the core barrel. The recovery figures in the cases of partial stroke were clearly augmented by flow-in. Poor penetration finally dictated APC refusal and the change was made to the XCB.

Recovery in the XCB sequence (Cores 126-791A-24X through -49X) was poor, as the material continued to be dominated by vitric silts and sands that were virtually impossible to coax into the core barrel. No combination of drilling parameters or core-barrel mechanical adjustments could be found to improve the results. Of the 26 XCB cores recovered, 17 contained less than 1 cm of material. Penetration rates were naturally very quick, and an enforced cautious pace in advancing the drill string did not improve the core recovery. It probably helped, however, in keeping the unstable material from collapsing around the drill string. Liberal gel mud sweeps were used after each second core in an attempt to hold off erosion of the walls in the hole.

The hole was abruptly ended when the rope socket on top of the sinker-barrel assembly backed off, leaving the sinker bars and core barrel in the pipe. An attempt was made to wireline fish for the sinker bars using a jury-rigged taper tap, but the tap broke off after engaging the fish. The drill string was pulled, and the core-barrel wash was removed on deck. Hole 791A ended when the bit reached the deck at 0745 hr on 6 May 1989.

Hole 791B

With the basement objective and firmer lithology expected to appear only a little deeper than the total depth of Hole 791A, the RCB was chosen for Hole 791B. A 12-drill-collar BHA was assembled, including the Hydrolex jars. The hole was spudded at 1640 hr on 6 May and drilled with a center bit to 173 mbsf. Some tight-hole conditions were experienced at that point that required 45 min of remedial hole conditioning. Center-bit drilling continued to 230 mbsf where the first spot core was attempted but with no recovery. The pipe was washed down to 250 mbsf where it became stuck while making a connection. The new jars were used to hammer the BHA free. The wash interval ended at 416 mbsf, where routine RCB coring commenced.

Cores 126-791B-4R to -8R were overlaps of the base of the XCB coring interval at Hole 791A. Recovery was virtually zero over this zone, but it picked up slightly as the hole deepened and some clay layers were encountered. While attempting to retrieve Core 126-791B-19R, the sinker-bar assembly came apart at the 3-lug quick release (Q/R). The Q/R was successfully fished with another wireline run, and coring continued without further difficulties.

Fairly normal RCB coring conditions and results prevailed through Core 126-791B-46R as a series of interbedded units of claystones and silts were recovered. At 834 mbsf, a hard interval was detected by the driller, and basalt breccia was recovered in the core barrel (Core 126-791B-47R). Core recovery dropped off dramatically as a zone of gravel and pumice material was penetrated. Hole stability in this zone was significantly poorer than in the clays above, but it was not enough to prohibit advancing the drill string. As at Hole 791A, liberal usage of gel mud was applied throughout the coring of the hole.

At about 1100 mbsf, the formation turned to hard rock, and the rapid penetration rates fell off to a range of 2–5 m/hr. The

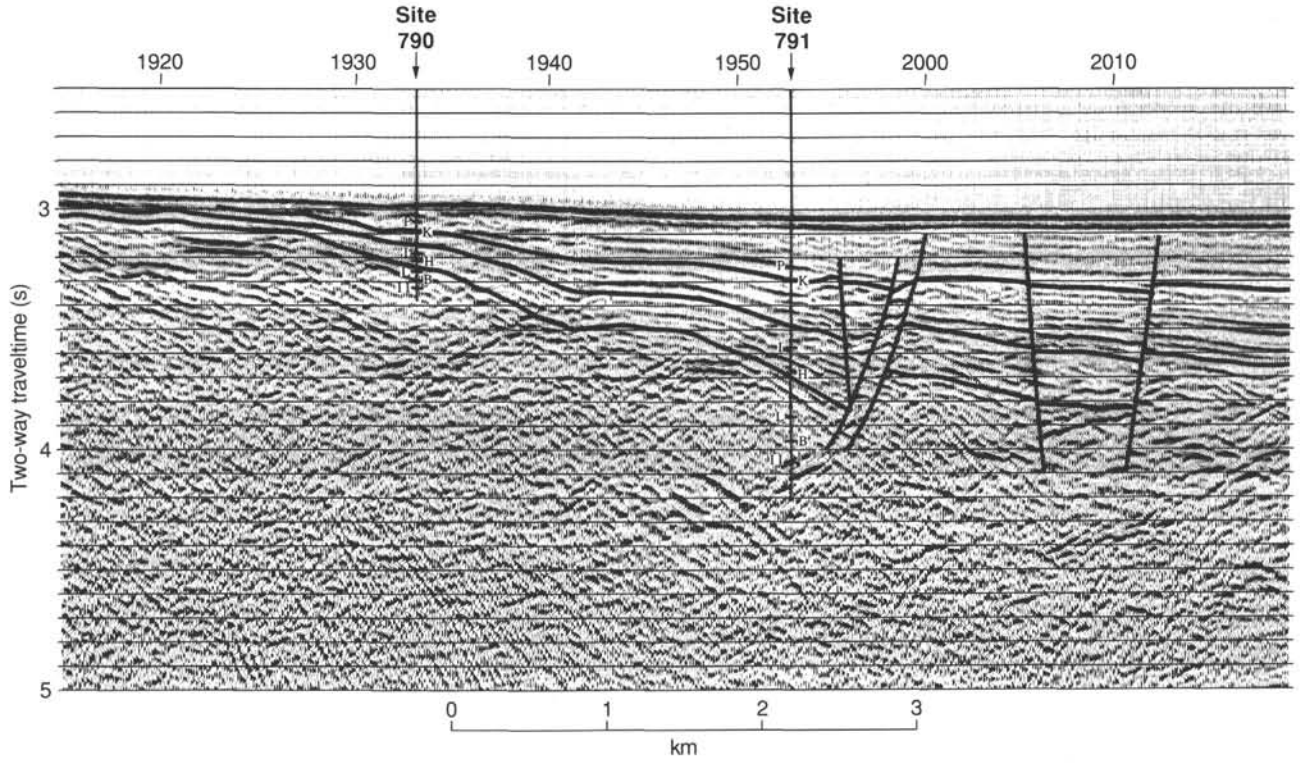

Figure 7. Detailed seismic correlation of specific stratigraphic horizons identified at Sites 790 and 791. Horizons identified on the seismic section are (P) the base of the coarse pumice unit above Key Bed #7, (K) Key Bed #7, (I) Unit I/II boundary, (H) the FO of *Emiliania huxleyi* (275 ka), (L) the LO of *Pseudoemiliania lacunosa* (460 ka), (B) Brunhes/Matuyama boundary (730 ka), and (II) Unit II/III boundary. Solid lines represent general seismic stratigraphic correlation and principal faults. Note the distinct difference in seismic character at and below the Unit II/III boundary between the two drill sites. The difficulty in correlating the three lowermost horizons (L, B, and II) results from a combination of (1) complex faulting that progressively offsets deeper horizons to a greater degree, (2) pre-rift and early syn-rift volcanism that overprints and obscures the sedimentary horizons, and (3) possible out-of-plane seismic reflections. The location of this seismic line is shown in Figure 2. The vertical exaggeration is ~2×.

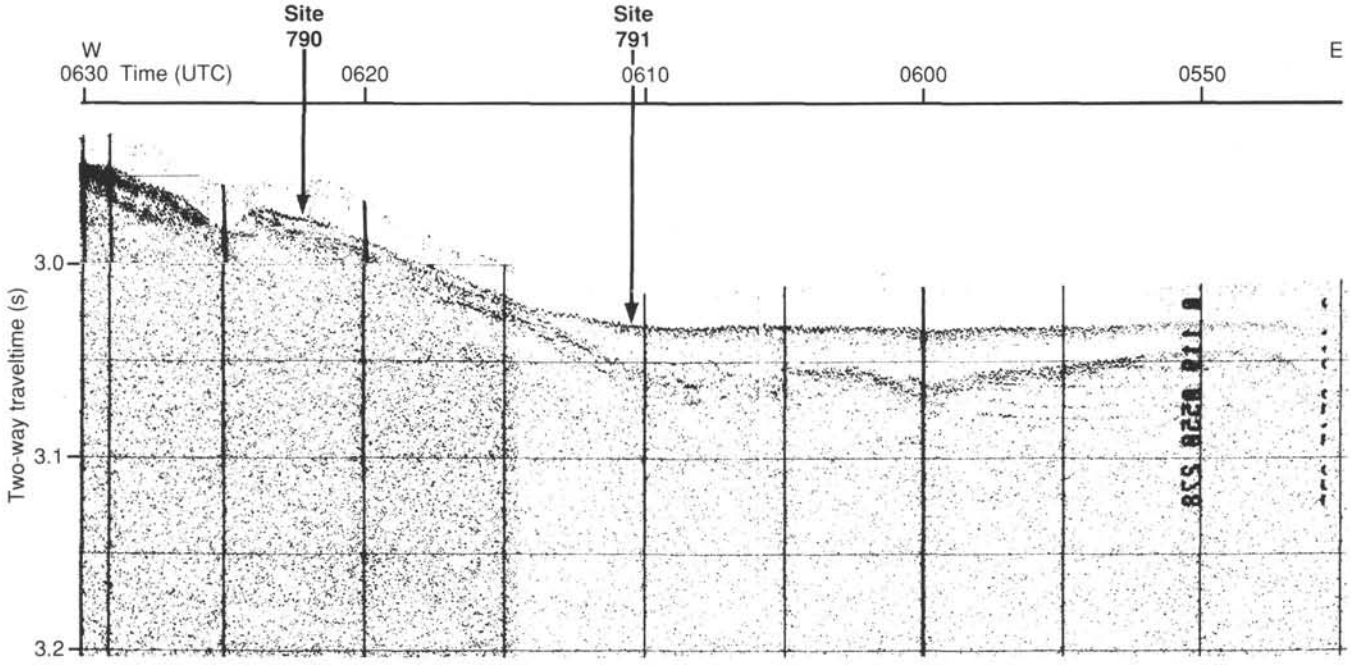

Figure 8. High-resolution seismic record (3.5 kHz) illustrating the pattern of recent sediment accumulation in this area of actively subsiding and rotating fault blocks. Note the thicker transparent ash layer observed at Site 791 that thins considerably toward Site 790.

Table 2. Coring summary for Sites 790 and 791.

Core no.	Date (1989)	Time (UTC)	Depth (mbsf)	Cored (m)	Recovered (m)	Recovery (%)
126-790A-						
1H	Apr 29	1425	0–8.8	8.8	8.81	100.0
2H	Apr 29	1510	8.8–18.3	9.5	9.65	101.0
3H	Apr 29	1600	18.3–27.8	9.5	9.60	101.0
4H	Apr 29	1645	27.8–37.4	9.6	7.65	79.7
Coring totals				37.4	35.71	95.5
126-790B-						
1H	Apr 30	0230	0–4.5	4.5	4.44	98.2
2H	Apr 30	0325	4.5–14.0	9.5	8.82	92.8
3H	Apr 30	0405	14.0–23.5	9.5	9.40	98.9
4H	Apr 30	0510	23.5–33.0	9.5	9.35	98.4
5H	Apr 30	0600	33.0–42.5	9.5	8.58	90.3
6H	Apr 30	1000	42.5–52.0	9.5	5.84	61.5
7H	Apr 30	1050	52.0–61.6	9.6	9.23	96.1
8H	Apr 30	1140	61.6–71.3	9.7	9.66	99.6
9H	Apr 30	1225	71.3–81.0	9.7	4.18	43.1
10H	Apr 30	1340	81.0–90.7	9.7	9.25	95.3
11H	Apr 30	1445	90.7–100.3	9.6	9.16	91.6
12X	Apr 30	1550	100.3–110.0	9.7	0	0
13X	Apr 30	1640	110.0–119.6	9.6	0	0
14X	Apr 30	1730	119.6–129.3	9.7	0	0
15X	Apr 30	1845	129.3–138.9	9.6	0.80	8.3
Coring totals				138.9	88.71	63.9
126-790C-						
1H	May 1	1910	85.0–94.5	9.5	9.53	100.0
2H	May 1	1955	94.5–104.2	9.7	10.01	103.2
3H	May 1	2040	104.2–113.9	9.7	9.84	101.0
4H	May 1	2120	113.9–123.5	9.6	8.79	91.5
5H	May 1	2215	123.5–133.2	9.7	9.00	92.8
6H	May 1	2300	133.2–142.7	9.5	9.68	102.0
7H	May 1	2345	142.7–145.7	3.0	2.54	84.6
8H	May 2	0035	145.7–155.2	9.5	9.39	98.8
9X	May 2	0140	155.2–164.9	9.7	0	0
10X	May 2	0230	164.9–174.6	9.7	1.71	17.6
11X	May 2	0310	174.6–184.2	9.6	7.05	73.4
12X	May 2	0400	184.2–193.9	9.7	1.77	18.2
13X	May 2	0445	193.9–203.6	9.7	4.89	50.4
14X	May 2	0530	203.6–213.2	9.6	3.74	38.9
15X	May 2	0615	213.2–222.8	9.6	0.38	4.0
16X	May 2	0700	222.8–232.4	9.6	8.12	84.6
17X	May 2	0800	232.4–242.1	9.7	9.79	101.0
18X	May 2	0845	242.1–251.7	9.6	6.44	67.1
19X	May 2	0940	251.7–261.4	9.7	8.47	87.3
20X	May 2	1040	261.4–271.1	9.7	5.32	54.8
21X	May 2	1130	271.1–280.6	9.5	0.09	1.0
22X	May 2	1245	280.6–290.2	9.6	0	0
23X	May 2	1425	290.2–299.9	9.7	0.06	0.6
24X	May 2	1630	299.9–309.5	9.6	0.26	2.7
25X	May 2	1800	309.5–319.2	9.7	0	0
26X	May 2	1920	319.2–328.8	9.6	0	0
27X	May 2	2100	328.8–338.5	9.7	0.26	2.7
28X	May 2	2240	338.5–348.1	9.6	0	0
29X	May 3	0035	348.1–353.0	4.9	0.01	0.2
30X	May 3	0355	353.0–358.1	5.1	0	0
31X	May 3	0820	358.1–367.7	9.6	0	0
32X	May 3	1215	367.7–377.4	9.7	0.03	0.3
33X	May 3	1440	377.4–387.1	9.7	0.15	1.5
Coring totals				302.1	127.32	42.1
126-791A-						
1H	May 4	0820	0–4.5	4.5	0	0
2H	May 4	0910	4.5–14.0	9.5	9.76	103.0
3H	May 4	1000	14.0–23.5	9.5	4.63	48.7
4H	May 4	1040	23.5–33.0	9.5	7.27	76.5
5H	May 4	1145	33.0–42.5	9.5	9.15	96.3
6H	May 4	1225	42.5–52.0	9.5	2.83	29.8
7H	May 4	1300	52.0–61.6	9.6	6.84	71.2
8H	May 4	1350	61.6–71.3	9.7	9.76	100.0
9H	May 4	1440	71.3–81.0	9.7	9.36	96.5
10H	May 4	1520	81.0–90.7	9.7	8.88	91.5
11H	May 4	1600	90.7–100.4	9.7	8.84	91.1
12H	May 4	1640	100.4–110.1	9.7	9.16	94.4
13H	May 4	1715	110.1–119.8	9.7	9.01	92.9
14H	May 4	1805	119.8–129.5	9.7	8.80	90.7
15H	May 4	1845	129.5–139.2	9.7	8.88	91.5

Table 2 (continued).

Core no.	Date (1989)	Time (UTC)	Depth (mbsf)	Cored (m)	Recovered (m)	Recovery (%)
126-791A- (Cont.)						
16H	May 4	1925	139.2–148.8	9.6	9.35	97.4
17H	May 4	2010	148.8–158.5	9.7	8.65	89.2
18H	May 4	2055	158.5–168.1	9.6	9.38	97.7
19H	May 4	2330	168.1–177.7	9.6	9.69	101.0
20H	May 5	0000	177.7–187.4	9.7	8.87	91.4
21H	May 5	0035	187.4–196.9	9.5	1.65	17.3
22H	May 5	0110	196.9–206.4	9.5	9.46	99.6
23H	May 5	0145	206.4–207.9	1.5	2.02	134.0
24X	May 5	0240	207.9–217.1	9.2	0	0
25X	May 5	0345	217.1–226.7	9.6	0.92	9.6
26X	May 5	0430	226.7–236.4	9.7	0	0
27X	May 5	0525	236.4–246.0	9.6	0	0
28X	May 5	0615	246.0–255.6	9.6	1.29	13.4
29X	May 5	0745	255.6–265.3	9.7	0	0
30X	May 5	0840	265.3–274.9	9.6	0.33	3.4
31X	May 5	0915	274.9–284.6	9.7	0.03	0.3
32X	May 5	1000	284.6–294.3	9.7	0.02	0.2
33X	May 5	1052	294.3–304.0	9.7	1.24	12.8
34X	May 5	1140	304.0–313.6	9.6	0.98	10.2
35X	May 5	1230	313.6–323.3	9.7	0.03	0.3
36X	May 5	1310	323.3–332.9	9.6	0.01	0.1
37X	May 5	1350	332.9–342.6	9.7	0	0
38X	May 5	1425	342.6–352.3	9.7	0.01	0.1
39X	May 5	1525	352.3–362.0	9.7	1.18	12.1
40X	May 5	1620	362.0–371.7	9.7	0.54	5.6
41X	May 5	1705	371.7–381.4	9.7	0.07	0.7
42X	May 5	1750	381.4–391.0	9.6	0.67	7.0
43X	May 5	1830	391.0–399.8	8.8	0	0
44X	May 5	1910	399.8–409.1	9.3	0	0
45X	May 5	1955	409.1–418.8	9.7	0	0
46X	May 5	2050	418.8–428.4	9.6	0.30	3.1
47X	May 5	2130	428.4–437.7	9.3	0	0
48X	May 5	2215	437.7–447.3	9.6	0	0
49X	May 6	0745	447.3–457.0	9.7	0	0
Coring totals				457.0	179.86	39.4
126-791B-						
1R	May 7	0100	230.0–239.5	9.5	0	0
2W	May 7	0450	239.5–339.7	100.2	0.01	Wash core
3W	May 7	0802	339.7–416.3	76.6	0.10	Wash core
4R	May 7	0900	416.3–425.7	9.4	0	0
5R	May 7	1015	425.7–435.0	9.3	0.01	0.1
6R	May 7	1100	435.0–444.7	9.7	0	0
7R	May 7	1200	444.7–454.3	9.6	0	0
8R	May 7	0835	454.3–463.6	9.3	0	0
9R	May 7	1325	463.6–473.3	9.7	0.24	2.5
10R	May 7	1405	473.3–482.9	9.6	1.02	10.6
11R	May 7	1500	482.9–492.6	9.7	0.18	1.9
12R	May 7	1550	492.6–502.1	9.5	0	0
13R	May 7	1635	502.1–511.8	9.7	2.76	28.4
14R	May 7	1715	511.8–521.5	9.7	0	0
15R	May 7	1800	521.5–531.2	9.7	0.24	2.5
16R	May 7	1850	531.2–540.9	9.7	0.49	5.1
17R	May 7	2000	540.9–550.6	9.7	0.14	1.4
18R	May 7	2045	550.6–560.3	9.7	0.61	6.3
19R	May 7	2245	560.3–569.7	9.4	0	0
20R	May 7	2340	569.7–579.3	9.6	0.38	4.0
21R	May 8	0015	579.3–589.0	9.7	0.15	1.5
22R	May 8	0100	589.0–598.7	9.7	0.91	9.4
23R	May 8	0140	598.7–608.4	9.7	5.38	55.4
24R	May 8	0220	608.4–618.1	9.7	1.23	12.7
25R	May 8	0300	618.1–627.7	9.6	3.02	31.4
26R	May 8	0345	627.7–637.0	9.3	0.99	10.6
27R	May 8	0430	637.0–646.6	9.6	0.89	9.3
28R	May 8	0515	646.6–656.3	9.7	5.85	60.3
29R	May 8	0600	656.3–666.0	9.7	0.24	2.5
30R	May 8	0645	666.0–675.6	9.6	5.94	61.9
31R	May 8	0730	675.6–685.3	9.7	4.93	50.8
32R	May 8	0810	685.3–695.0	9.7	1.51	15.5
33R	May 8	0850	695.0–704.6	9.6	0.32	3.3
34R	May 8	0945	704.6–714.3	9.7	6.51	67.1
35R	May 8	1025	714.3–723.6	9.3	1.25	13.4
36R	May 8	1110	723.6–733.2	9.6	6.40	66.6
37R	May 8	1155	733.2–742.8	9.6	2.62	27.3
38R	May 8	1235	742.8–752.4	9.6	5.25	54.7
39R	May 8	1320	752.4–762.1	9.7	3.09	31.8
40R	May 8	1400	762.1–771.7	9.6	3.74	38.9
41R	May 8	1445	771.7–781.3	9.6	4.40	45.8
42R	May 8	1530	781.3–791.0	9.7	4.49	46.3

Table 2 (continued).

Core no.	Date (1989)	Time (UTC)	Depth (mbsf)	Cored (m)	Recovered (m)	Recovery (%)
126-791B- (Cont.)						
43R	May 8	1605	791.0-800.7	9.7	1.60	16.5
44R	May 8	1655	800.7-810.3	9.6	2.76	28.7
45R	May 8	1745	810.3-820.0	9.7	3.35	34.5
46R	May 8	1835	820.0-829.6	9.6	2.84	29.6
47R	May 8	1945	829.6-839.2	9.6	1.21	12.6
48R	May 8	2120	839.2-848.9	9.7	0.25	2.6
49R	May 8	2240	848.9-858.6	9.7	0.22	2.
50R	May 9	0005	858.6-868.3	9.7	0.17	18
51R	May 9	0125	868.3-878.0	9.7	0.17	.8
52R	May 9	0315	878.0-887.6	9.6	0.30	3.1
53R	May 9	0440	887.6-897.3	9.7	0.27	2.8
54R	May 9	0605	897.3-906.6	9.3	0.02	0.2
55R	May 9	0730	906.6-916.3	9.7	0.04	0.4
56R	May 9	0920	916.3-925.9	9.6	0.34	3.5
57R	May 9	1100	925.9-935.5	9.6	1.02	10.6
58R	May 9	1225	935.5-945.2	9.7	0.06	0.6
59R	May 9	1335	945.2-954.8	9.6	0.64	6.7
60R	May 9	1525	954.8-964.5	9.7	0.25	2.6
61R	May 9	1740	964.5-974.1	9.6	0.17	1.8
62R	May 9	1920	974.1-983.7	9.6	1.07	11.1
63R	May 9	2115	983.7-993.0	9.3	0.98	10.5
64R	May 9	2245	993.0-1002.7	9.7	1.48	15.2
65R	May 10	0015	1002.7-1012.4	9.7	0.89	9.2
66R	May 10	0150	1012.4-1022.1	9.7	1.52	15.7
67R	May 10	0335	1022.1-1031.8	9.7	3.05	31.4
68R	May 10	0615	1031.8-1041.5	9.7	0.43	4.4
69R	May 10	0805	1041.5-1051.1	9.6	0.30	3.1
70R	May 10	1000	1051.1-1060.8	9.7	0.58	6.0
71R	May 10	1215	1060.8-1070.4	9.6	0.34	3.5
72R	May 10	1425	1070.4-1080.0	9.6	2.93	30.5
73R	May 10	1640	1080.0-1089.7	9.7	2.70	27.8
74R	May 10	1805	1089.7-1099.3	9.6	0.16	1.7
75R	May 10	2000	1099.3-1109.0	9.7	0.56	5.8
76R	May 11	0000	1109.0-1118.6	9.6	2.06	21.4
77R	May 11	0445	1118.6-1128.3	9.7	2.60	26.8
78R	May 11	0800	1128.3-1137.6	9.3	0.77	8.3
79R	May 11	1235	1137.6-1145.0	7.4	1.00	13.5
Coring totals				738.2	114.28	15.5
Washing totals				176.8	0.11	
Drilled interval = 230.0						
Combined totals				1145.0	114.39	

coring operation was continued to 1145.0 mbsf, at which point the scientific objectives were deemed satisfied. The final core was cut short by 2 m when a sudden increase in torque with the bit on the bottom indicated possible bit failure.

The hole was displaced several times with both sweep mud and seawater before beginning a wiper trip to the logging depth (121 mbsf) and back to total depth. Greater-than-normal care was taken during the wiper trip in an attempt to prepare a potentially unstable formation for open-hole logging runs. The top drive was engaged to ream a tight hole from 165 to 336 mbsf. The bit was lowered without rotation through a 548-m interval of open hole without encountering any bridges or detectable obstructions. At 261 m above the former total depth (884 mbsf), a solid bridge was found and just above a probable gauge-sized pinch spot immediately overlying the basal zone. After the top drive was picked up, the pipe was found to be stuck and the annulus packed off, apparently around the lower drill collars. The Hydrolex jars again were used to free the pipe by applying up to 60,000-lb jars. With the pipe again free to move, the bit was pulled up to 826 mbsf to regain circulation. The hole was swept with high-viscosity mud, and the process of drilling out the fill/bridge began.

Before the redrilling process could proceed, the annulus was again apparently packed off as stand-pipe pressure increased dramatically. Neither rotation nor circulation was lost, but the pipe was only free to move vertically about 4 m before becoming stuck in either the up or down direction. With free rotation of the bit, it was not possible to apply left-hand torque to cock the Hydrolex jars. It could not even be determined if the upper stuck point was above or below the jars. Within the hour, rotation and the limited amount of vertical movement were both lost as the hole apparently began to slough ever faster. After 3 hr of pulling and attempting to rotate the pipe without any success, it became evident that the pipe would not come free.

The geochemical log was run through the stuck drill pipe before severing the pipe. The geochemical tools (NGT/ACT/GST/TEMP) were rigged and run into the pipe until they encountered an "obstruction" in the pipe apparently 203 m above the bit. (Later log analysis and inventory of the pipe in the rackers revealed that a 203-m pipe tally error had occurred during the downgoing portion of the wiper trip [one layer of the 5½-in. pipe racker had been missed]. The "obstruction" in the pipe was actually the bit itself.) As the logging tools would not go any deeper, the logging run commenced. Data were acquired solely on the uphole run of the combination tool, at a speed of 450 ft/hr (137 m/hr), starting at a depth of 811.67 mbsf.

After logging, one more attempt was made to free the stuck pipe by picking up the top drive and circulating while attempting to rotate, pull free, and activate the drilling jars. All our efforts were fruitless and the severing charges were rigged. In the hope of saving the experimental, and much needed, Hydrolex jars, the first severing shot was intended to be fired in the drill collars just below the jars. The severing charges, of course, were stopped by the mysterious "obstruction" since the pipe tally error still had not been discovered. The 84-pellet high energy engineering (HEE) severing charge was triggered at the "obstruction" point, but it did not fire because of a flooded firing assembly.

A second severing charge was rigged, run to the "obstruction" point, and fired. The pipe was still found to be stuck after the severing charge was removed. It was assumed that the shot had been fired near the top of the BHA (rather than near the bit as it actually was), so the depth for the next severing attempt was chosen to be near the seafloor to guarantee that the pipe would be freed on the next attempt. The charge was run in the pipe and detonated at a point 46 mbsf and the pipe was freed. The remains of the drill string were recovered with the severed stub arriving on deck at 1345 hr on 13 May.

LITHOSTRATIGRAPHY AND ACCUMULATION RATES

Sites 790 and 791 are located west of the Izu-Bonin Arc in the eastern half-graben of the Sumisu Rift. The sites are 2.4 km apart (Figs. 6–7). Site 791 was drilled on the western edge of the flat basin floor of the eastern half-graben, whereas Site 790 is situated on a slight rise and structural high to the west of the flat basin floor. The sedimentary section at Site 791 is about three times thicker than the time-equivalent section at Site 790. Nevertheless, lithotypes and generalized stratigraphy at the two sites are similar. The successions at Sites 790 and 791 are first described separately and then are interpreted in a common section.

Site 790

Three APC/XCB holes were drilled at Site 790. Cores from these holes were correlated by means of sets of key beds, and a 377.6-m-thick composite section was constructed (Figs. 9 and 10). The stratigraphic succession (Table 3) consists of three lithologic units composed predominantly of volcanogenic materials; the upper two are sedimentary, whereas the basal unit is igneous. The sedimentary units also contain variable quantities of biogenic materials, mainly nannofossils. The contact between Units I and II was not recovered, but it is placed at 165 mbsf; the contact between Units II and III was recovered at 266.6

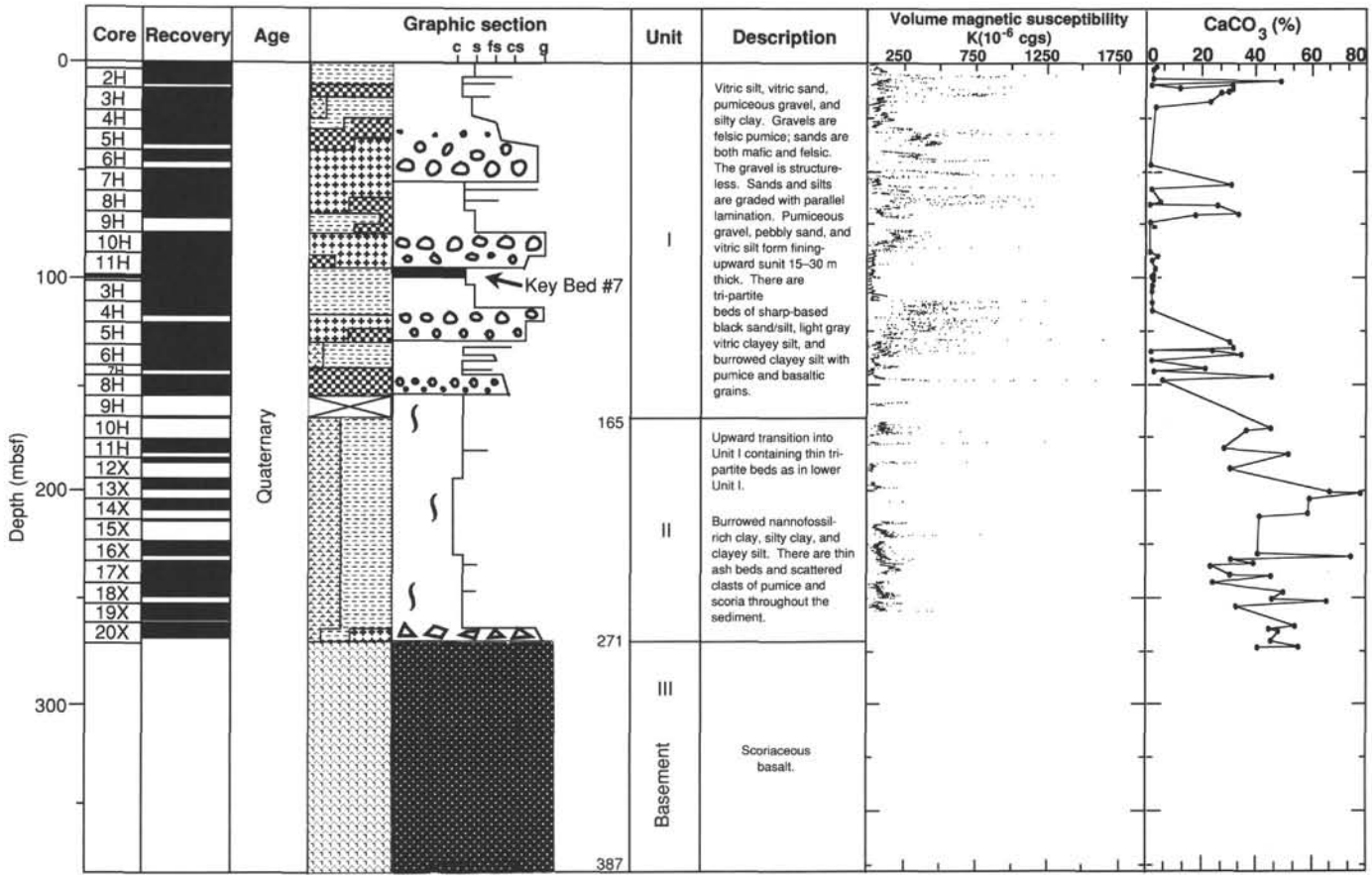

Figure 9. Composite stratigraphic section for Site 790 showing unit boundaries and downhole variations in magnetic susceptibility and total carbonate. The carbonate curve is primarily a function of the distribution of nannofossil tests throughout the section, whereas the magnetic susceptibility data reflect the distribution of coarse mafic volcanic lithics and crystals. The proportions of sediment types in Holes 790B and 790C have been combined and are shown in the Lithology column (see Fig. 6 for key); the format is more generalized than in core descriptions in that it reflects the percentages of groups of sediment types observed within any cored section (i.e., silt + clay, sand, gravel, carbonate), and does not show mixed biogenic/siliclastic lithotypes. The graphic column is a simplified sedimentologic log displaying relative grain size on the horizontal axis (c = clay/claystone, st = silt/siltstone, ss = sand/sandstone, and g = gravel/conglomerate); on this column, sedimentary structures (Fig. 6, "Explanatory Notes" chapter, this volume) and bedding within the cored units are schematically displayed.

mbsf. Although the lithology for Unit III is shown in Figure 9, this material is described in a later section (see "Igneous Petrology" section, this chapter). The recovery for Unit I varied in the three holes, ranging from as low as 64% to as high as 95% between the top and bottom parts of the unit (Table 4). Some of the "apparent" high recoveries in Unit I are artificial, caused by cave-in or flow-in (see "Description" sections that follow). Recovery was 54% for Unit II but extremely low (1%) in Unit III (Table 4).

Sediment types and sedimentary structures (Units I and II) are summarized in Table 3. Also shown in Figure 9 are plots of the downhole distribution of carbonate content and magnetic susceptibility. Peaks in magnetic susceptibility correlate with relative concentrations of ferromagnetic or paramagnetic minerals (e.g., magnetite, ilmenite, pyrrhotite, and hematite), either as solitary phases or as minute inclusions in basaltic glass. Units I and II contain numerous ash layers (a total of 135 were catalogued in Hole 790C) that vary in thickness from millimeters to meters (Table 5). Sediments of Unit II tend to have carbonate contents of 20%–40%, whereas sediments of Unit I generally contain less than 20% carbonate. High values of magnetic susceptibility are generally restricted to Unit I.

Bedding is horizontal in all cores, and there is no evidence for either syn-sedimentary or tectonic deformation.

Unit I

Intervals: Cores 126-790A-1H through -4H, Cores 126-790B-1H through -15X, and Cores 126-790C-1H through -9X
Age: Quaternary
Depth: 0–165 mbsf

Sediments assigned to Unit I were recovered from all three holes at this site, but the unit was completely penetrated only in Hole 790C. Sets of key beds showing identical composition, sedimentary structures, thickness, and mutual stratigraphic separation are recognizable in each hole. Six key beds allow detailed correlation of sections and intervals in Hole 790A with Hole 790B (Fig. 11), which demonstrates that a continuous section was recovered at Site 790 down to a depth of 41.58 mbsf. A similar correlation can be made between Holes 790B and 790C (Figs. 12 and 13); the main key bed for this correlation is "Key Bed #7." The percentages of sediment types indicated below are determined for a composite section on the basis of the above correlations.

There are large-scale alternations in Unit I of (1) pumiceous gravel, pebbly sand, and vitric silt in intervals 15–30 m thick; and (2) 10- to 15-m-thick intervals of clayey silts interbedded with thin- to thick-bedded (3–100 cm) sand and silty sand. The basal contact of Unit I is placed just below the lowest interval of

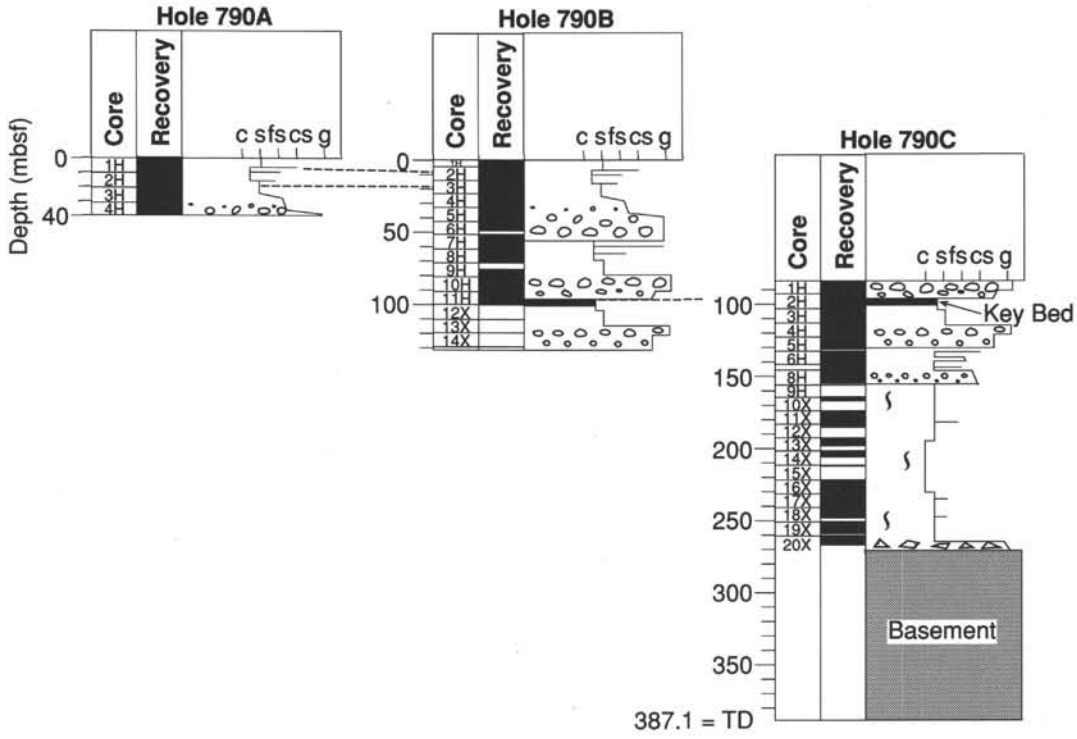

Figure 10. Detailed correlation between stratigraphic sections recovered at Holes 790A, 790B, and 790C. Stratigraphic columns constructed as in Figure 9.

Table 3. Summary of lithology and sedimentary structures of units at Site 790.

Unit	Lithology	Sedimentary structures	Interval (mbsf)	Age	Occurrence
I	Vitric silt, vitric sand, pumiceous gravel, clayey silt, and silty clay. Gravels are felsic; sands are mafic and felsic. Triplet beds of black sand/silt, light gray vitric clayey silt, and burrowed clayey silt with pumice and basaltic grains.	Structureless gravel, graded sands and silts with parallel lamination. Pumiceous gravel, pebbly sand, and vitric silt units are 15–30 m thick and fine upward. Sharp-based black silts/sands and burrows in hemipelagic intervals.	0–165	Quaternary	126-790A-1H to -4H 126-790B-1H to -15X 126-790C-1H to -9X
II	Nannofossil clay, nannofossil-rich clay, silty clay, and clayey silt. Thin ash beds. Scattered pumice and scoria clasts. Triplet beds from 165 to 184 mbsf as in Unit I.	Burrow mottling.	165–266.6	Quaternary	126-790C-10X to 20X-CC, 34 cm
III	Scoriaceous basalt.		266.6–387	Quaternary	126-790C-20X-CC, 34 cm, to -33X

Table 4. Calculated recovery for units at Site 790.

Unit	Hole	Interval (core-core)	Depth (mbsf)	Cored (m)	Recovery (m)	Recovery (%)
I	790A	1H–4H*	0–37.4	37.4	35.7	95
	790B	1H–15H*	0–138.9	138.9	88.71	64
	790C	1H–9X	0–165.0	80.0	68.38	86
II	790C	10X–20X	165.0–266.6	106.1	57.68	54
III	790C	20X–33X	266.6–387.1	120.5	1.00	1

Note: Asterisk (*) indicates that the lower contact of Unit I was not penetrated.

pumiceous gravel and pebbly sand. Gravel- to silt-size sediments throughout Unit I are composed almost exclusively of volcanogenic glass, pumice, minor crystals, and rare microcrystalline lithic fragments. For brevity, therefore, the modifier "vitric" will generally be omitted from lithologic names in this site chapter, except where emphasis is desired. Glass is predominantly transparent and colorless in the pumiceous units and brown to colorless in the thinner interbedded sandy and silty beds.

Unit I consists of 40% silt, 35% sand, 15% gravel, and 10% silty clay. The gravel, and much of the sand and silt, is present in thick to very thick beds (maximum apparent bed thickness about 15 m) that are commonly structureless or, less commonly, normally graded. Gravel-size clasts are angular to subrounded. The gravel is poorly sorted, with abundant sand- to silt-size matrix (Fig. 14). The coarsest gravels tend to occur at the tops or

Table 5. Volcanic ash layers at Site 790.

Core, section, interval (cm)	Thickness (cm)	Description and remarks
126-790B-		
1H-1, 14 (top)–2H-2-140 (base)	726	Thick pumice layer I
2H-2, 145–150	5/3/2	Very dark gray (5Y3/1)/brownish black (5YR2/1)/grayish black (N2); silt/silt/very fine sand
2H-3, 0–5		
2H-3, 7–11	4	Brownish black (5YR2/1); silt
2H-3, 17–20	3	Brownish black (5YR2/1); silt
2H-3, 39–46	7	Grayish black (N2)/brownish black (5YR2/1); silt
2H-3, 148–150	20	Grayish black (N2); silt (laminated at lowest 5 cm)
2H-4, 0–18		
2H-4, 61–74	13	Light olive gray (5Y6/1); silt
2H-4, 127–150	76/85	Light olive gray (5Y4/1); silt/very fine sand–medium sand (grading)
2H-5, 0–138		
2H-6, 42–77	35	Brownish black (5YR2/1); silt
3H-1, 27–56	29	Grayish black (N2); silt
3H-1, 70–150	44/65	Grayish black (N2); silt/fine–medium sand (laminated)
3H-2, 0–29		
3H-2, 58–150	152/77	Olive gray (5Y5/2)/olive gray (5Y4/2)/dark olive gray (5Y3/2); silt/silt-medium sand (graded)
3H-3, 0–137		
3H-4, 29 (top)–7H-3-7 (base)	3628	Thick pumice layer II
7H-3, 27–31	4	Brownish black (5YR2/1); silt
7H-3, 63–66	3	Olive black (5Y2/1); silt
7H-3, 85–93	3/3/2	Olive gray (5Y4/1)/olive gray (5Y4/2)/olive gray (5Y4/1); silt/silt/silt
7H-3, 115–150	50/55/230/	Gray (5Y5/1)/olive gray (5Y4/1)/(5Y4/1)/olive gray
7H-4, 0–150	45/35/50	(5Y4/2)/(5Y4/2)/(5Y4/2); silt/silt/very fine sand/very
7H-5, 0–150		fine sand/fine sand/medium sand with dark olive gray
7H-6, 0–130		(5Y3/2) laminations
7H-6, 143–147	4	Reddish gray (10R6/1); silt
8H-1, 0–150	+90/25/11/	Light gray (5Y7/1)/gray (5Y5/1)/(5Y5/1)/olive gray
8H-2, 0–90	1/23/70/17/3	(5Y4/1)/(5Y5/1)/(5Y4/1)/dark olive gray (5Y3/2)/olive black (5Y2/1); pumice granule (maximum diameter = 3.5 cm)/mixture of pumice pebble and silt/silt/silt/silt/ silt/very fine sand/fine sand
8H-2, 106–150	39/1/40/9/	Brownish black (5YR2/1)/grayish black (N2)/olive black
8H-3, 0–85	32/8	(5Y2/1)/(N2)/(N2)/dark olive gray (5Y3/2); silt/very fine sand/silt with grayish black, very fine sand thin layers/very fine sand/fine sand/very fine sand
8H-3, 143–148	5	Dark olive gray (5Y3/2); very fine sand
8H-4, 0–38	35/3	Olive black (5Y2/1); silt/fine sand (laminated)
8H-4, 48–62	10/2/2	Olive black (5Y2/1)/grayish black (N2)/olive black (5Y2/1); silt/very fine sand/silt
8H-4, 115–150	26/18	Olive black (5Y2/1)/grayish black (N2); silt with very fine
8H-5, 0–9		sand laminated/very fine–fine sand (graded)
8H-5, 38–131	11/41/41	Brownish black (5YR2/1)/olive black (5Y2/1)/grayish black (N2); fine sand with pumice medium sand laminated/silt with grayish black (N2) very fine sand thin layers/very fine–medium sand (graded)
8H-6, 14–17	3	Dark olive gray (5Y3/2); silt
8H-6, 33–35	2	Dark olive gray (5Y3/2); silt
8H-6, 54–63	9	Gray (5Y5/1); silt
8H-6, 74–92	3/2/7/2/2	Olive black (5Y2/1)/grayish black (N2)/olive black (5Y2/1)/grayish black (N2)/olive black (5Y2/1); silt/ very fine sand/silt/very fine sand/silt/
8H-7, 43 (top)–10H-5, -15 (base)	1622	Thick pumice layer III
10H-5, 22–24	2	Brownish black (5YR2/1); silt
10H-5, 32–150	5/5/83/2/	Olive gray (5Y4/1)/dark greenish gray (5GY4/1)/(5Y4/1)/
10H-6, 0–146	23//8/1/4/	very dark gray (5Y3/1)/(5Y4/1)/(5Y4/1)/olive gray
	5/6/44/34/	(5Y4/2)/(5Y4/1)/(5Y4/2)/(5Y4/1)/(5Y4/2)/dark olive
	14/2/8/20	gray (5Y3/2)/(5Y3/2)/gray (5Y5/1)/olive black (5Y2/1)/(5Y3/2); silty clay/silty clay/silt/silt/silt/very fine sand/silty very fine sand/silt/very fine sand/silt/ coarse silt/very fine sand/fine sand/fine sand/medium sand
126-790C-		
1H-4, 70–72	2	Olive gray (5Y4/1); very fine sand
1H-4, 115 (top)–5H-3, -43 (base)	3628	Thick pumice layer IV
5H-3, 55–59	4	Olive (5Y5/4); fine sand
5H-3, 67–70	3	Olive (5Y5/4); fine sand
5H-3, 87	<1	Dusky green (5G3/2); silt
5H-3, 91–111	20	Grayish black (N2); clayey silt–fine sand (graded)
5H-3, 111–150	39/60	Grayish black (N2)/dark gray (N3); silt/coarse sand (graded)

Table 5 (continued).

Core, section, interval (cm)	Thickness (cm)	Description and remarks
126-790C- (Cont.)		
5H-4, 0–60		
5H-4, 96–136	26/14	Dark gray (N3)/black (N1); clayey silt/medium sand
5H-5, 6–15	9	Dark gray (N3); silt
5H-5, 20–35	15	Dark gray (N3); clayey silt/very fine sand
5H-5, 43–95	49/3	Dark gray (N3)/grayish black (N2); clayey silt/medium sand
5H-6, 6–21	15	Medium dark gray (N4); silt–very fine sand (graded)
5H-6, 62–72	10	Medium dark gray (N4); silt–very fine sand (graded)
5H-6, 82	<1	Dusky green (5G3/2); silt
5H-6, 85	<	Dusky green (5G2/1); silt
5H-6, 120–150	2/28	Medium light gray (N6)/olive gray (5Y4/1); silt/silt
6H-1, 0–150	150/31	Olive gray (5Y4/1)/olive gray (5Y4/1); fine–medium sand/
6H-2, 0–31		Pumiceous medium–coarse sand (graded) (laminated)
6H-2, 47–65	18	Light olive gray (5Y6/1); fine sand (graded)
6H-2, 80–144	57/7	Light olive gray (5Y6/1)/dark gray (N3); silty clay/medium sand
6H-3, 34–135	29/73	Light olive gray (5Y6/1)/medium gray (N5); silt/medium sand (graded) (pumice maximum diameter = 1 mm)
6H-4, 5–51	5/25/16	Light olive gray (5Y6/1)/light olive gray (5Y6/1)/dark gray (N3); fine sand/silty clay/medium sand
6H-4, 60–81	11/10	Light olive gray (5Y6/1)/dark gray (N3); silty clay with scattered pumice/fine sand with an erosive base
6H-4, 99–140	2/23/16	Olive gray (5Y4/1)/olive gray (5Y4/1)/dark gray (N3); silty very fine sand/silty clay/medium sand
6H-5, 7–77	52/18	Light olive gray (5Y6/1)/dark gray (N3); clayey silt/fine sand (laminated)
6H-5, 96–118	14/8	Light olive gray (5Y6/1)/dark gray (N3); clayey silt/fine sand (laminated)
6H-5, 141–150	29/17	Light olive gray (5Y6/1)/dark gray (N3); clayey silt/silty
6H-6, 0–37		Very fine sand
6H-6, 41–47	6	Light olive gray (5Y6/1); very fine sand
6H-6, 73–142	11/53/5	Light olive gray (5Y6/1)/light olive gray (5Y6/1)/dark gray (N3); silty clay/silty fine sand/fine sand
7H-1, 0 (top)–8H-CC, –18 (base)	1250	Thick pumice layer V
11X-1, 25	<1	Silt
11X-2, 10–16	6	Very light gray (N8); clayey silt–very fine sand (graded)
11X-2, 45–50	5	(10Y6/2); silt (graded)
11X-3, 17–30	12/1	Olive gray (5Y5/2)/very light gray (N8); clayey silt–very fine sand (graded)/clayey silt
11X-3, 109–110	1	Very light gray (N8); silt
11X-4, 32–47	10/5	Olive gray (5Y5/2)/dark gray (N3); clayey silt/coarse sand
11X-4, 70–72	2	Medium light gray (N6); very fine sand
11X-4, 110–120	10	Dark gray (N3); silt (graded)
11X-4, 139–150	15/4/3/3	Olive gray (5Y5/2)/olive gray (5Y5/2)/light gray (N7)/
11X-5, 0–14		Medium dark gray (N4); silt/medium sand/silt/very fine sand with an erosive base
12X-1, 5–14	9	Olive gray (5Y4/1); silt
12X-1, 20–23	3	Olive gray (5Y4/1); silt
12X-1, 26–28	2	Olive gray (5Y4/1); silt
12X-1, 35–37	2	Olive gray (5Y4/1); silt
12X-1, 40–42	2	Olive gray (5Y4/1); silt
12X-1, 45–69	5/4/6/4/5	Olive gray (5Y4/2)/olive gray (5Y4/1)/olive gray (5Y4/2)/ olive black (5Y2/1)/olive black (5Y2/1); silt/silt/ medium sand with pumice coarse sand/fine sand/silt
12X-1, 71–76	5	Olive black (5Y2/1); fine sand
12X-1, 130–140	43	Light olive gray (5Y4/1); silt
12X-CC, 0–33		
13X-1, 18–44	7/5/4	Gray (5Y5/1)/olive gray (5Y4/1)/olive black (5Y2/1); clayey silt/silt/fine sand
13X-1, 50–52	2	Olive gray (5Y4/2); silt
13X-1, 66–68	2	Olive black (5Y2/1); silt
13X-1, 71–72	1	Olive black (5Y2/1); silt
13X-1, 79	<1	Olive black (5Y2/1); silt
13X-1, 81	<1	Olive black (5Y2/1); silt
13X-2, 15–55	31/9	Gray (5Y5/1)/gray (5Y5/1); clayey silt/silt
13X-3, 71–75	4	Gray (5Y5/1); silt
14X-1, 0–7	+7	Gray (5Y5/1); silt
14X-1, 87–88	1	Light brownish gray (5YR6/1); clayey silt
14X-2, 136–147	6/5	Very dark gray (N2)/olive gray (5Y4/1); fine sand/scoria granule (maximum diameter = 1 cm)
15X-1, 7–8	1	Olive black (5Y2/1); silty very fine sand
15X-1, 12–17	10	Olive black (5Y2/1); medium sand
15X-CC, 0–5		
15X-CC, 10–22	12	Olive black (5Y2/1); medium sand
16X-1, 0–28	7/3/16/2	Gray (5Y5/1)/very dark gray (5Y3/1)/gray (5Y5/1)/very dark gray (5Y3/1); silt/silt/silt/very fine sand

Table 5 (continued).

Core, section, interval (cm)	Thickness (cm)	Description and remarks
126-790C- (Cont.)		
16X-1, 99–104	5	Olive gray (5Y4/1); silt
16X-1, 106	<1	Olive gray (5Y4/1); silt (5 mm thick)
16X-2, 8–12	4	Olive gray (5Y5/2); silt
16X-2, 35–38	3	Gray (5Y5/1); silt
16X-4, 63–67	1/3	Dark olive gray (5Y3/2)/olive gray (5Y4/1); silt
16X-5, 52–66	14	Very dark gray (5Y3/1); medium sand
16X-5, 118–120	2	Light olive gray (5Y6/1); silt
16X-6, 17–20	3	Olive gray (5Y4/2); silt
16X-CC, 0–4	4	Dark olive gray (5Y3/2); silt
16X-CC, 18–20	1/1	Gray (5Y5/1)/dark olive gray (5Y3/2); silt
17X-1, 130–145	15	Olive gray (5Y4/1); silt–sandy silt (graded)
17X-7, 27–32	2/2/1	Very dark gray (5Y3/1)/olive gray (5Y4/2)/olive black (5Y2/1); silt/silt/medium sand
17X-CC, 34–35	1	Light olive gray (5Y6/1); silt
18X-1, 145	<1	Silt
18X-3, 135–136	1	Silt
18X-4, 58–60	2	Very light gray (N8); silt
18X-4, 100	<1	Very light gray (N8); silt
18X-4, 123–124	1	Very light gray (N8); silt
19X-1, 46–53	7	Olive gray (5Y4/2); silt
19X-1, 65–68	3	Olive gray (5Y4/2); silt
19X-1, 94–96	2	Gray (5Y5/1); silt
19X-2, 98–106	8	Gray (5Y5/1); silt
19X-3, 52–60	8	Olive gray (5Y4/2); clayey silt
19X-3, 81–85	4	Olive gray (5Y4/2); clayey silt
19X-4, 92–150	36/14/11	Dark gray (N3)/grayish black (N2)/olive black (5Y2/1);
19X-5, 0–3		Pebble-granule gravel with sandy silt matrix/very coarse sand–granule/granule with medium sand matrix
19X-5, 57–59	2	Olive gray (5Y4/2); silt
19X-6, 13–14	1	Medium light gray (N6); silt
19X-6, 20	1	Medium light gray (N6); silt pocket
19X-6, 39–45	4/2	Olive gray (5Y5/2)/light olive gray (5Y6/1); silt
20X-2, 63–150	217	Pumice gravel scattered in sandy mud (maximum diameter = 4 cm)
20X-3, 0–130		
20X-CC, 28–50	6/16	Light olive gray (5Y6/1)/grayish black (N2); sand/scoria (maximum diameter = 2 cm)

Note: 126-790B-10H-6, 140 cm, is correlative to 126-790C-1H-4, 57 cm.

bases of cores; excluding the uppermost coarse material, several cores are graded from coarser gravel at the base to finer gravel, pebbly sand, sand, or silt at the top. Some of this grading may be an artifact of drilling. A detailed correlation of Holes 790A and 790B (Fig. 11) indicates that some pebbly sand and gravel intervals may not be primary features of the sedimentary succession. For example, the pebbly sand bed in Sections 126-790A-1H-3 to 126-790A-1H-6 is unlike the sediment found in Cores 126-790B-1H and -2H at the same sub-bottom depth, and key-bed correlation indicates that the pebbly sand bed overlaps with sediment in Section 126-790A-2H-1. This overlap can only be explained by flow-in of the pebbly sand.

In downhole plots, thick vitric silt units are clearly marked by very low magnetic susceptibility values (Fig. 9) forming distinct intervals that can be correlated between Holes 790A and 790B, and that can also be traced to Site 791 (Fig. 15).

Crude parallel stratification in a few of the gravel and pebbly sand units, defined by concentrations of brown-black glass (Fig. 16), implies little drilling deformation in these intervals. Elsewhere, the unconsolidated nature of the gravels in cores makes it difficult to discriminate unequivocally between *in-situ* sediment, and cave-in or flow-in material.

In Hole 790B (Fig. 10), the intervals 6–20.5, 55–70, and 87–100 mbsf consist predominantly of two distinct sequences. The first is sharp-based, thin- to thick-graded beds (Fig. 17), consisting of a lower sand or silt division, overlain by beds of silty clay that contain scattered sand- and granule-size grains of pumice. The second sequence is characterized by millimeter- to centimeter-thick layers of white or dusky green ash (Fig. 18). The sands and silts appear black (N2) because of a predominance of brown glass, scoria, and dark mineral grains, as indicated by smear slide analysis. Where the sands have not been liquefied by drilling, they commonly show parallel lamination, in some cases above a basal division that is graded but otherwise massive. Some of these sand beds contain intraclasts of soft silty clay similar to the interbedded sediments.

Below 127 mbsf, there are distinctive tripartite units (triplets) (Fig. 19), each beginning with a sharp or erosional base. The lowest division of a triplet is a thin black sand or silt layer that is poorly graded or ungraded and may be plane-parallel laminated (Fig. 20) or burrowed (Fig. 21). The black sand/silt is overlain with a sharp contact by a subtly graded, gray, structureless vitric clayey silt. This second division is succeeded over a thin transition by an uppermost division of strongly burrowed and color mottled, greenish gray, nannofossil-rich clayey silt with scattered sand- to pebble-size clasts of pumice and scoria (Figs. 22 and 23). The nannofossil-rich clayey silt also contains widely spaced, white to dark green, silty to sandy ash layers, generally less than 5 cm thick (Fig. 24). Tripartite beds of this type are also found in the uppermost part of underlying Unit II (above 184 mbsf).

The composition of the pumiceous gravels and sands in Unit I is predominantly felsic, given the pale color of the pumice (clear in smear slides and thin sections), although 10%–20% of the sand-size grains consist of black basaltic fragments. Rare grains of olivine were also identified in the smear slides, although these may have been in beds partially mixed by drilling disturbance.

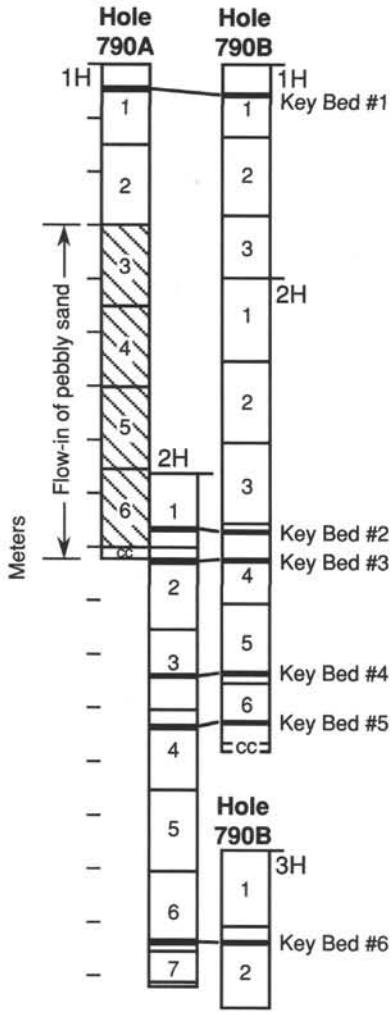

Figure 11. Correlation of sections in Cores 126-790A-1H to -2H with sections in Cores 126-790B-1H to -3H, based on positions of the bases of six key beds recognized in both holes. The apparent overlap between Cores 126-790A-1H and -2H is the result of flow-in of pebbly sand that is present at 4.5–6.0 mbsf in Core 126-790B-1H. Note scale in meters.

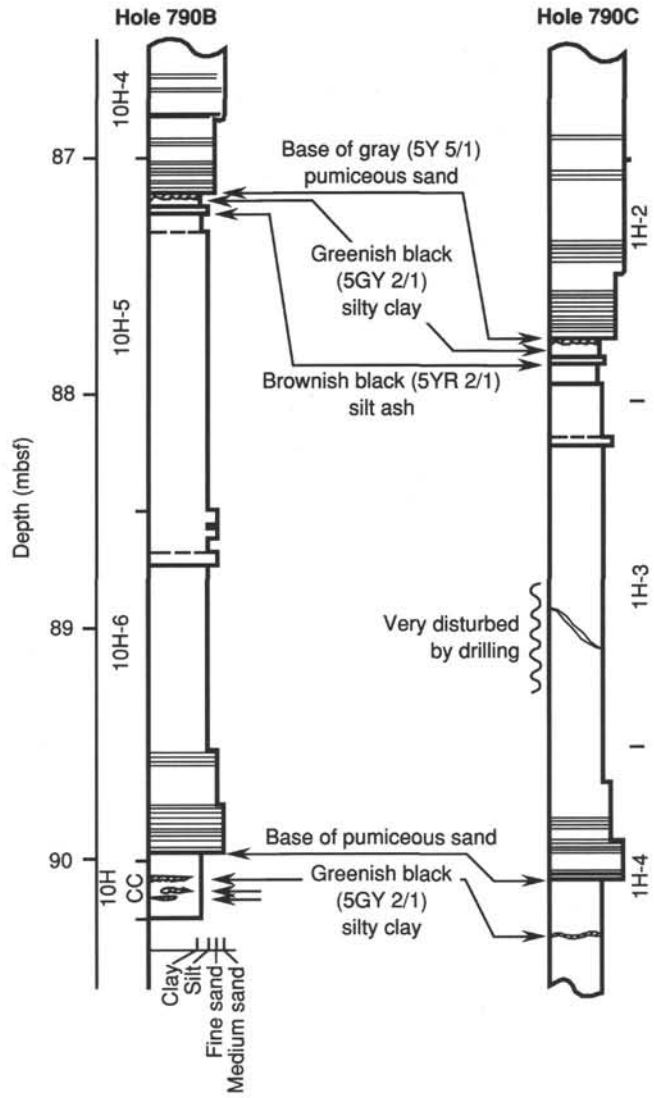

Figure 12. Graphic representation of the key elements in Sections 126-790B-10H-4 to -7 and Sections 126-790C-1H-2 to -4 that allow correlation between Holes 790B and 790C. Photographs of Key Bed #7, consisting of greenish black silty clay, are shown in Figure 13.

The black sands in the thinner-bedded intervals consist of dark brown glass, clinopyroxene, orthopyroxene, plagioclase, volcanic lithic grains, and rare olivine and epidote. A grain was tentatively identified as pumpellyite in Sample 126-790C-5H-4, 112 cm.

Unit II

Intervals: Core 126-790C-10X through Section 126-790C-20X-CC at 34 cm
Age: Quaternary
Depth: 165–266.6 mbsf

Unit II is entirely restricted to Hole 790C. The top of Unit II was not recovered, and its contact with Unit I is placed between Cores 126-790C-9X and -10X at 165 mbsf (Fig. 9), based upon the presence of massive sandy beds, magnetic susceptibility data, carbonate content, and comparison with the logging results for Site 791. The basal contact of Unit II with the igneous rocks of Unit III (see "Igneous Petrology" section, this chapter) was recovered in Core 126-790C-20X.

Unit II consists of 67% nannofossil clay and nannofossil-rich clay, 21% silty clay and clayey silt, 8% clay, 2% silt (vitric ash), and 1% each of sand and gravel. The nannofossil clays are concentrated in the interval 193.9–210 mbsf (Fig. 9). Nannofossil clays and nannofossil-rich clays are generally structureless except for widely spaced, very thin (<5 cm), medium-grained sand to silt beds of dark grayish green to white ash (Fig. 25).

From 184 mbsf to the top of Unit II at 165 mbsf, there are thin tripartite beds of black vitric sand/silt, light gray vitric silt, and burrowed nannofossil clayey silt like those found in the lower part of Unit I. These reflect an upward transition from the nannofossil clay and related sediment types of the lower part of Unit II to the coarser volcaniclastic section of Unit I.

Below 230 mbsf, grain size increases to clayey silt, and the sediment becomes greener in color. Burrowing is strong and marked by dark greenish gray (5G 4/1) mottles. Thin silty or sandy ash bands of the same color are common. The abundance and size of scattered felsic pumice and basaltic clasts increases downcore; the lower 3 m of Unit II, immediately above the igneous rocks of Unit III, contains pumice clasts with maximum diameters of 5 cm (Fig. 26). In this basal interval, color mottling

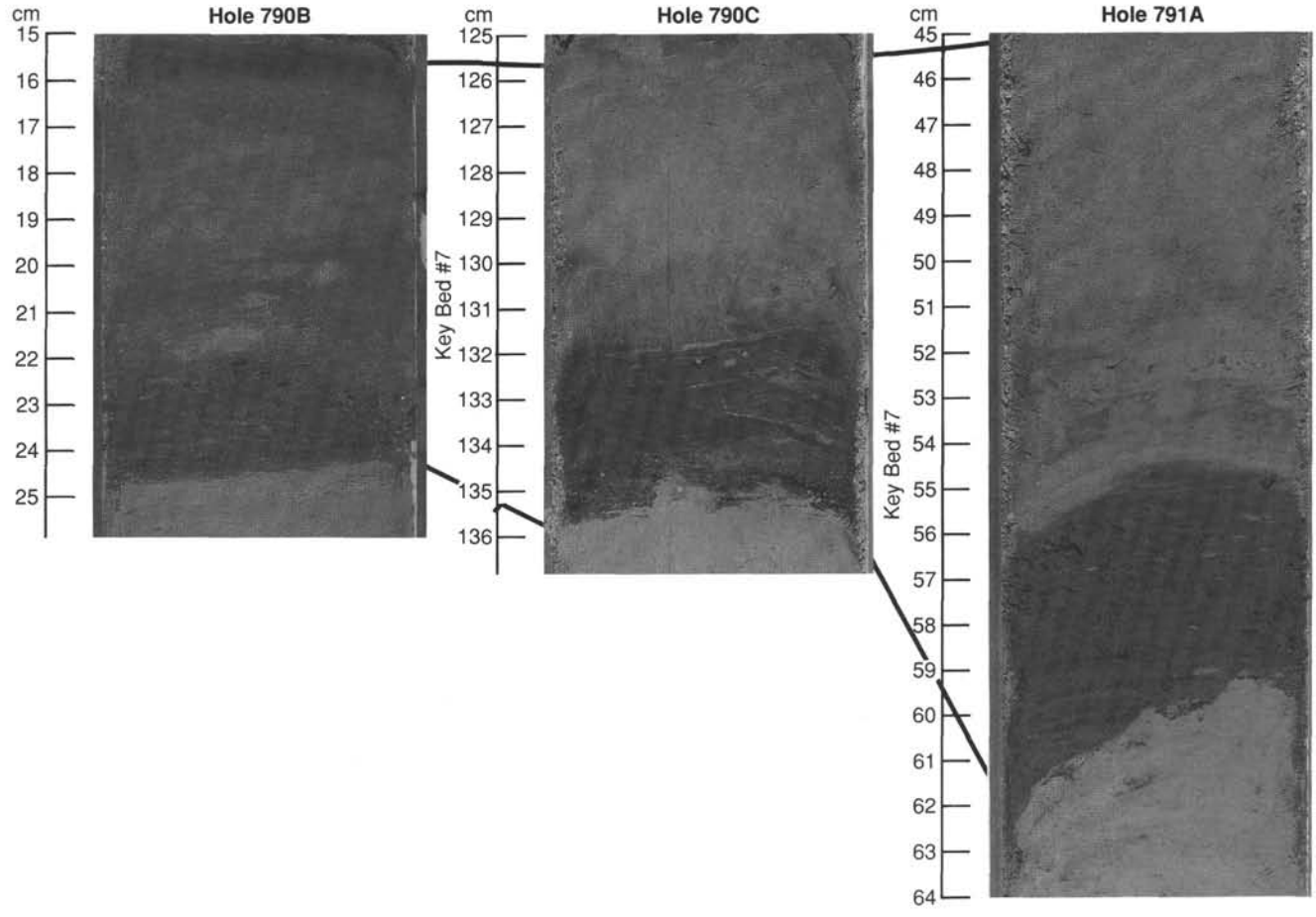

Figure 13. Key Bed #7, a greenish black silty clay bed, at Hole 790B (Interval 126-790B-10H-5, 15–25 cm, 87.25 mbsf), Hole 790C (Interval 126-790C-1H-2, 125–136 cm, 87.85 mbsf), and Hole 791A (Interval 126-791A-22H-6, 44–60 cm, 205.0 mbsf).

increases dramatically, and both sediment and pumice clasts contain secondary coloration in shades of grayish green (5GY 6/1, 10GY 5/2) and grayish yellow green (5GY 7/2).

Site 791

Two holes were drilled at Site 791. The recovery in these holes does not overlap, so the description below is made on the basis of a single column (Fig. 27) that comes from Holes 791A (0–419.1 mbsf) and 791B (463.3–1138.6 mbsf). Recovery of the sedimentary section in Hole 791B with the RCB was low (20%); recovery of sediments at Hole 791A with the XCB was even lower (3%). In contrast, APC recovery in the upper part of Hole 791A was very high (83%). The generally low recovery rates below 208 mbsf decrease the reliability of our description of the sedimentary succession in this interval.

The succession at Site 791 is divided into three lithologic units (Fig. 27). The upper two units are sedimentary and the lower one is igneous. Although part of the lithology for Unit III is shown in Figure 27, this material, including a 22-cm interval of silt and sandy silt in Core 126-791B-62R (igneous Unit 9), is described in a later section (see "Igneous Petrology" section, this chapter). Several lines of evidence (see "Correlation" section that follows) indicate that Unit I at this site is correlative both in time and in sedimentary facies with Unit I at Site 790, although it is much thicker.

In the interval of good recovery at Site 791 (Cores 126-791A-2H to -22H), Unit I consists mainly of very thick beds (up to 65 m thick) of pumiceous gravel with clasts up to 7.5 cm long, and thinner beds of sand, pumiceous pebbly sand, and vitric silt. Thin interbeds of clay, silty clay, and black vitric sand/silt like those in Unit I at Site 790 are present in this section but are much less common. The lower part of Unit I, characterized by very low recovery, consists mainly of vitric silt/siltstone and nannofossil-rich silty clay/claystone.

The top of Unit II is placed at a depth of 428.4 mbsf, based partly on seismic stratigraphic results (see "Seismic Stratigraphy" section, this chapter). Below this depth, most sediments are sufficiently lithified to be called "-stones," although some unlithified vitric silt beds are present even near the base of Unit II.

Unit II consists mainly of burrowed nannofossil-rich claystone and nannofossil claystone, both with scattered sand-size basaltic grains. Bedding dips increase gradually to 15°–20° at a depth of 600 mbsf. Dip then increases more rapidly and reaches values of 45° by a depth of 760–770 mbsf. Below this latter depth, the quantity of disseminated mafic grains, including dark glass and heavy minerals, increases markedly. The change in dip and variation in mafic content may be the result of faulting in the section.

Sediment types and sedimentary structures (Units I and II) are summarized in Table 6. Plots of the downhole distribution of total carbonate and magnetic susceptibility are shown in Figure 27. As at Site 790, peaks in magnetic susceptibility correlate with relative concentrations of ferromagnetic or paramagnetic minerals (e.g., magnetite, ilmenite, pyrrhotite, and hematite), either as solitary phases or as minute inclusions in basaltic glass.

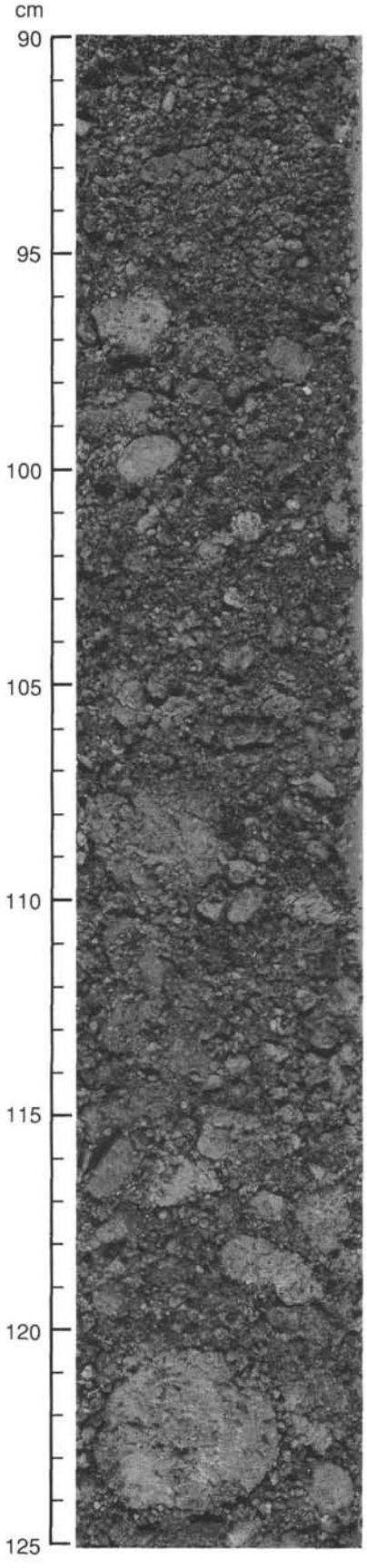

Figure 14. Poorly sorted pumiceous gravel of Unit I (Interval 126-790B-5H-4, 90–125 cm).

Unit I

Interval: Cores 126-791A-1H through -46X and Cores 126-791B-1R through -5R-2, 120 cm
Age: Quaternary
Depth: 0–428.4 mbsf

All sediment recovered in Hole 791A is assigned to Unit I. Cores 126-791B-1R through -5R also penetrated sediments of Unit I, but there was no recovery. Unit I consists of 44% pumiceous gravel; 30% pumiceous and vitric sand, granule sand, and pebbly sand; 14% vitric silt; 7% silty clay and clayey silt; 1.5% nannofossil-rich clay and nannofossil-rich silty clay; and 2% clay. The pumiceous gravel, pebbly sand, granule sand, and sand beds are similar in composition and texture to facies in Unit I at Site 790. Notable differences between these gravels and those of Site 790 are that they form a higher percentage of the succession at Site 791, are thicker (Figs. 9 and 27), and are generally coarser (Fig. 28) with clasts up to 7.5 cm in diameter. In some cores, the gravel has partly flowed within the core barrel, so that the true thickness of some units cannot be determined.

Sand and pebbly sand generally occur in structureless, very thick beds that are light in color from the pumice content (Fig. 29). In many cases, this material is strongly disturbed by drilling (flow-in). Intraclasts of vitric silt up to 7 cm in diameter are present locally (Fig. 30). Rarely, the vitric sand in Unit I is black (Fig. 31); smear slide analysis shows the sand consists of abundant brown glass and mafic minerals. This black sand occurs as the basal part of graded sand to silty clay couplets that characterize the thinner bedded intervals of Unit I. The sand lies with an erosional or sharp contact on burrowed silty clay, is in many cases plane-parallel laminated, and grades upward into silt and burrowed silty clay. Black sand also appears in widely spaced, crude laminae in the very thick pumiceous sand beds.

The vitric silt component is commonly very light colored and can form structureless beds up to 20 m thick (Fig. 27) or millimeter-thick beds within silty clay units. Very thin beds of dark silt (ash) also occur locally. One such bed, in Core 126-791A-22H-6, 55-60 cm (205.0 mbsf), has also been identified in Holes 790B (87.25 mbsf) and 790C (87.85 mbsf; Key Bed #7, Fig. 13).

Light-colored vitric silt, pumiceous and vitric sand, nannofossil-rich clay/claystone, and nannofossil-rich silty clay/claystone characterize the interval of poor recovery in Unit I below 206 mbsf. The biogenic-rich sediment types also contain variable amounts of siliceous microfossils (mainly diatoms and sponge spicules). These sediment types are similar to those present in the lower part of Unit I at Site 790. The contact between Units I and II at Site 791 is placed below the lowest recovered bed of pumiceous sand at 428.4 mbsf. The tripartite beds present in the lower part of Unit I and the upper part of Unit II at Site 790 were not recovered at Site 791. However, their presence in this interval is implied by peaks in the total gamma-ray logs (see "Downhole Measurements" section, this chapter) from 330 to 485 mbsf. These peaks may mark burrowed, nannofossil-rich clayey silts that form one division of the tripartite beds.

Unit II

Interval: Cores 126-791A-47X to -48X and Core 126-791B-5R-2, 120 cm to Section 126-791B-47R-1 at 44 cm
Age: Quaternary
Depth: 428.4–834 mbsf

The first recovery of sediment in Unit II is in Section 126-791B-9R-CC. Recovery in Unit II was low (25%, 34% below 599 mbsf). The sediments consist of 27% carbonate claystone, 22% carbonate-rich claystone, 28% carbonate-rich silty claystone, and 15% carbonate silty claystone, plus very minor amounts of unlithified, light-colored, carbonate-rich vitric silt and vitric silt (3%), carbonate-rich sandy mudstone (2%), silty

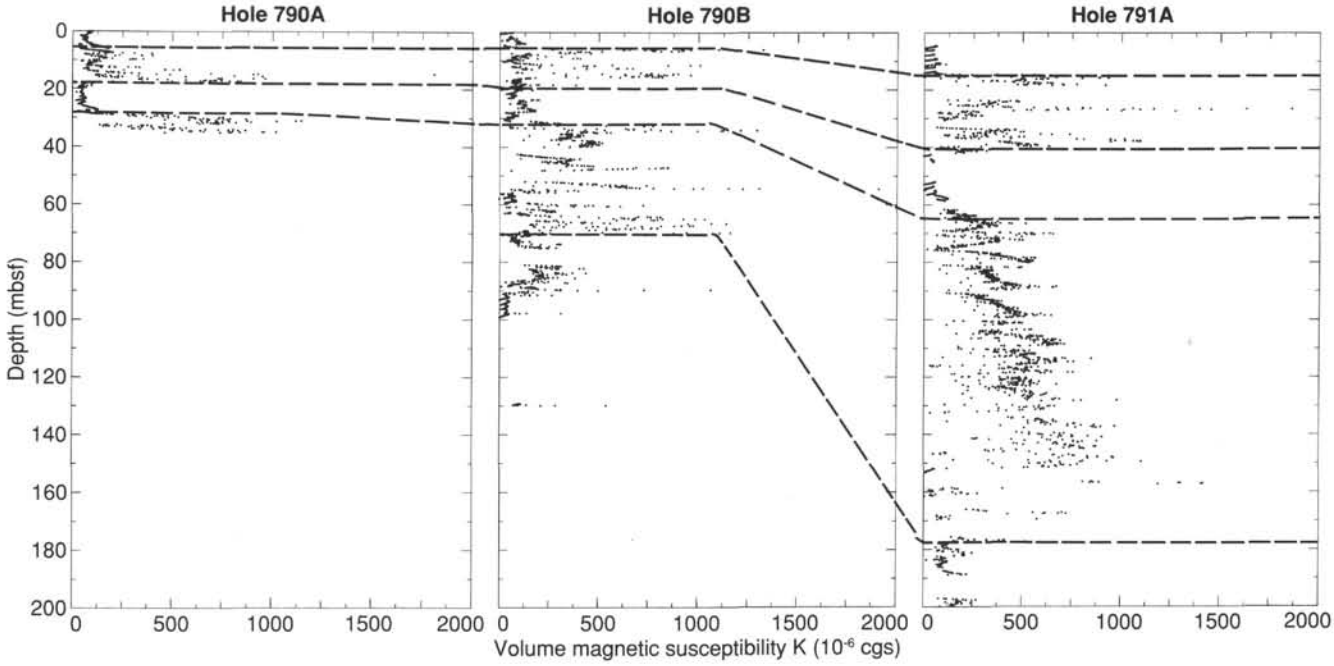

Figure 15. Plots of magnetic susceptibility for Holes 790A, 790B, and 790C. Dashed lines mark correlative sections.

claystone (1%), and chalk (1%). The carbonate component is primarily nannofossils, but some sediments contain 10%–20% foraminifers. Biogenic silica is present in all samples in minor amounts, mainly as diatoms, radiolarians, and sponge spicules. In some cores, scattered, white, elliptical masses, about 1 mm across, consist of clusters of sponge spicules, probably biologically pelletized.

The sediments of Unit II are generally burrowed by *Chondrites, Zoophycos,* and *Scolites* (Fig. 32). From 580 to 770 mbsf, secondary pyrite is common in burrows; other minor pyrite persists to the bottom of Unit II. Most burrowed sediments contain disseminated, black, sand-size basaltic rock fragments and scattered pumice clasts up to about 1.5 cm in diameter. The basaltic fragments are locally concentrated into dark disseminated bands, very thin beds, or burrows. Isolated basaltic clasts are as large as 2 cm. The abundance of basaltic fragments increases downward from a depth of about 695 mbsf toward the basalts of underlying Unit III; below 780 mbsf, the mean size of the basaltic clasts increases to a maximum of about 1–2 mm.

An important minor lithology in Unit II below 570 mbsf is very light to medium gray (N8–N6), locally parallel-laminated vitric silt beds, generally 1–10 cm thick (Fig. 33). The apparent original contacts of these soft beds were generally lost during drilling (Fig. 34). The bed thicknesses, therefore, are significantly reduced. In some cases, the soft vitric silt beds were squeezed to fill the core liner completely (the core diameter of lithified sediments is considerably less; Fig. 35).

At a depth of about 600 mbsf, bedding in Unit II dips at angles of 15°–20°. By 760 mbsf, dips are about 45° (Figs. 33 and 34). Two faults are present in the lower 15 m of Unit II (819–834 mbsf), just above the basalt contact (Fig. 36).

X-ray Diffraction Analysis

Site 790

The X-ray diffraction (XRD) results for Site 790 are summarized in Table 7. In Unit I, glass grains have fresh surfaces with only traces of clay alteration products. The XRD analyses of vitric silt and sand from Unit I show very high, broad backgrounds, reflecting abundant, amorphous volcanic glass. Smectite and chlorite are present in this material. Mica group minerals are present in small amounts in all vitric units. Light olive gray (5Y 6/1) to greenish gray (5GY 6/1) ash beds contain abundant calcite, reflecting the high contents of microfossils. Feldspars and quartz are present in all the sediments analyzed; clay minerals are present only in trace amounts (Fig. 37).

Diaspore (AlO[OH]) is common in Unit I, indicating the circulation of hydrothermal fluids with temperatures of 300°–400°C, a result not consistent with sediment pore-water geochemistry (see "Sediment/Fluid Geochemistry" section, this chapter). Handpicked, medium yellowish green (10GY 6/4) glass grains and dark yellowish green (10GY 4/4) ash beds show a strong, but unidentified, peak at 0.203 nm (Fig. 38) probably caused by a mineral containing reduced, divalent iron (Fe^{2+}).

A moderate, reddish brown (10R 4/6) pumice clast (Fig. 23; Sample 126-790C-5H-6 at 22 cm) contains quartz, feldspar, cristobalite, calcite, smectite, chlorite, the 0.203-nm unknown mineral, and amorphous volcanic glass. The presence of cristobalite indicates hydrothermal conditions and temperatures of 200°–300°C. Clasts of this color are exceedingly rare and are probably material incorporated from locally distinct rocks in the vicinity of the volcanic vent as accidental inclusions during eruptions.

In Unit I, dark greenish gray mottles in light olive gray sandy ash (Sample 126-790C-5H-6 at 6 cm) contain calcite, feldspar, quartz, pyrolusite ($Mn0_2$), pyrite (FeS_2), and the 0.203-nm unknown mineral. The characteristic peaks of pyrolusite and pyrite overlap, but they can be distinguished by high intensities at 0.314 (pyrolusite) and 0.163 nm (pyrite).

In Unit II, gritty, light olive gray nannofossil sandy mud (Samples 126-790C-20X-2, 80 cm, and 126-790C-20X-3, 46 cm and 90 cm) contains abundant calcite, feldspar, quartz, the unknown 0.203-nm mineral, and a trace of 1.4-nm clay minerals. Other clay minerals, such as mica group minerals, are very rare.

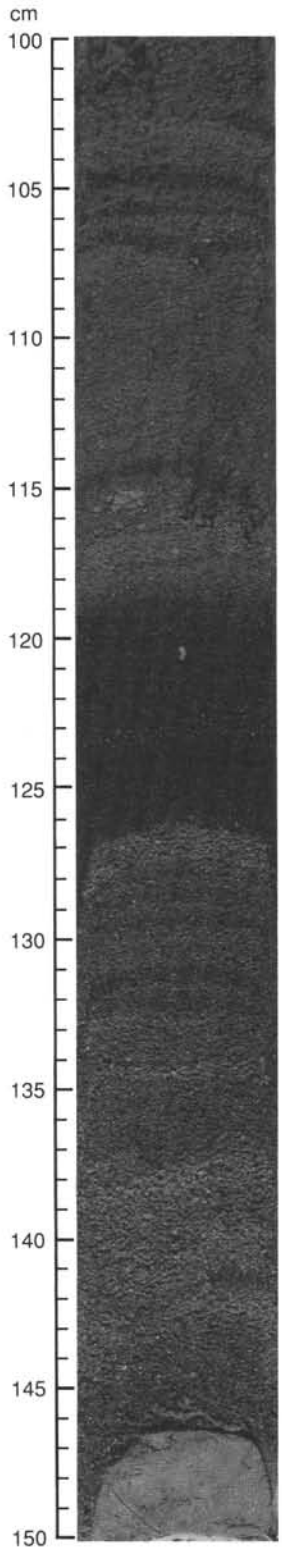

Figure 16. Basal, parallel-laminated part of a sharp-based, graded, pumiceous sand bed that is 120 cm thick (Interval 126-790B-10H-6, 100–150 cm). The pumice pebbles at 115 cm may mark a surface of amalgamation in the bed.

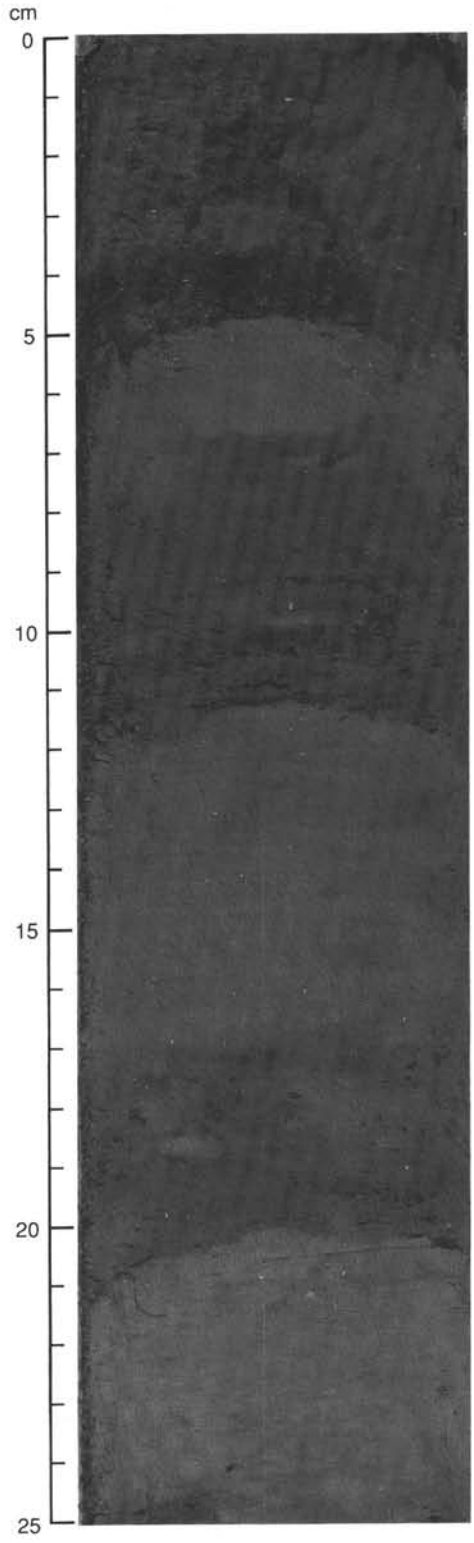

Figure 17. Thin, sharp-based, graded beds of silt to silty clay (Interval 126-790B-2H-3, 0–25 cm). The silty clay in this example is burrowed and contains scattered sand-size grains of pumice.

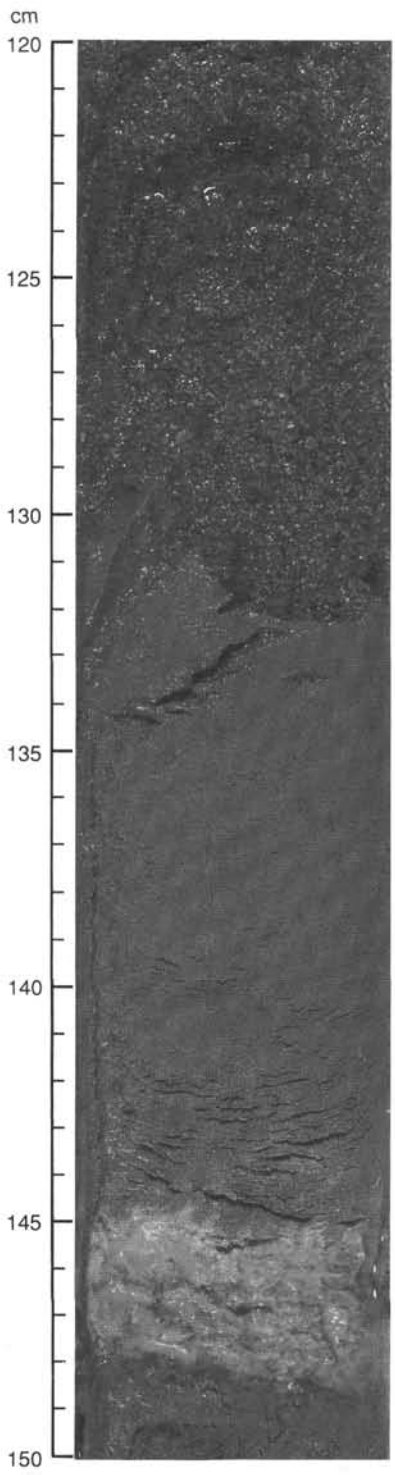

Figure 18. A 2.5-cm-thick bed of white ash (144–147 cm) within a silty clay bed (Interval 126-790B-7H-6, 120–150 cm). Above 131 cm, the photograph shows the lower part of a sharp-based, vitric sand bed of indeterminate thickness (upper part deformed by flow-in).

Site 791

The XRD results for Site 791 are summarized in Table 8. Vitric clay, vitric silt, and vitric sand in Unit I are characterized by abundant amorphous material (volcanic glass). Small amounts of smectite, chlorite, and mica group minerals are present in samples from Cores 126-791A-18H and -19H, whereas clay minerals are present in only trace amounts in Core 126-791A-20H. A trace of diaspore is present in all samples.

Samples from Core 126-791A-18H contain calcite and quartz as major mineral species; feldspar and an unknown mineral with a *d*-spacing of 0.209 nm are also present. The 0.209-nm peak corresponds to minerals containing Fe and/or Ni (e.g, FeS minerals troilite and mackinawite, both characteristic of reduced sediments; Berner, 1964). Abundances are so low, however, that additional peaks that discriminate between the various possible minerals in this group cannot be discerned. Also, poor crystallinity of the iron monosulfides may contribute to difficulties in identifying secondary peaks. Substitutions of small amounts of Mn, Zr, Ti, Co, and Si in the lattice of the unknown mineral would subtly affect its *d*-spacing. Identification of this mineral, as well as the mineral with the 0.2030-nm peak at Site 790, can only be achieved with chemical data using SEM-EDX and TEM-electron diffraction patterns.

In Unit II, calcite is abundant in sediments that contain nannofossils (e.g., Cores 126-791B-9R, -21R, and -22R). All cores contain large amounts of amorphous volcanic glass. Mica group minerals, chlorite, and quartz are major minerals, whereas feldspar and cristobalite are minor minerals in nannofossil-rich claystones.

In Section 126-791B-22R-1, thin lens-shaped masses of black (5G 2/1), vitric clayey silt contain abundant amorphous glass and pyrite and only traces of clay minerals, calcite, feldspar, and cristobalite. The pyrite and abundant glass indicate high sedimentation rates (see "Sediment Accumulation Rates" section that follows) associated with reducing conditions.

Pyrite crystals are scattered in the nannofossil-rich silty claystone in the Interval 126-791B-25R-2, 18–46 cm. Handpicked pyrite yields the characteristic peaks of pyrite (FeS_2) as well as peaks attributed to troilite (FeS), traces of calcite, quartz, and the 1.4-nm clay minerals (Fig. 39).

Foraminifer-nannofossil claystone just above the basalts of Unit III (Section 126-791B-47R-1) contains calcite and alunite ($KAl_3[SO_4]_2[OH]_6$). Alunite has characteristic peaks at 0.301, 0.190, and 0.175 nm, which indicates low-temperature hydrothermal alteration.

Sediment Accumulation Rates

Sedimentation rates for Sites 790 and 791 were determined from calcareous nannofossil and radiolarian datums and from paleomagnetic events (Table 9), which were used to construct the age-depth curve shown in Figure 40. Data from Hole 790C were used to construct the curve for Site 790. At Site 791 all the datums (except the ash-bed correlation) come from Hole 791B. A distinctive correlatable ash bed was found at Holes 790C and 791A (Fig. 13). The age of the ash bed in Hole 790C (0.091 Ma) was determined by dividing the sub-bottom depth (87 m) of the bed by the linear sedimentation rate for the interval (958 m/m.y.). This age was then used to constrain the age-depth curve even further for the top of Site 791.

Sedimentation rates at each site exhibit an exponential increase over the recovered interval. At Site 791, sedimentation rates increase from 344 m/m.y. at the base of Unit II (approximately 1 Ma) to over 2200 m/m.y. at the top Unit I. At Site 790, sedimentation rates increase from 90 m/m.y. around 1 Ma to ~1000 m/m.y. at present. Prior to the LO of *Pseudoemiliania lacunosa* (0.275 Ma), sedimentation rates at Site 791 were approximately four times those found at Site 790. Between 0.275 and 0.10 Ma, linear sedimentation rates at Site 791 were greater by a factor of 3, although this ratio declined to 2:1 over the past 0.10 Ma.

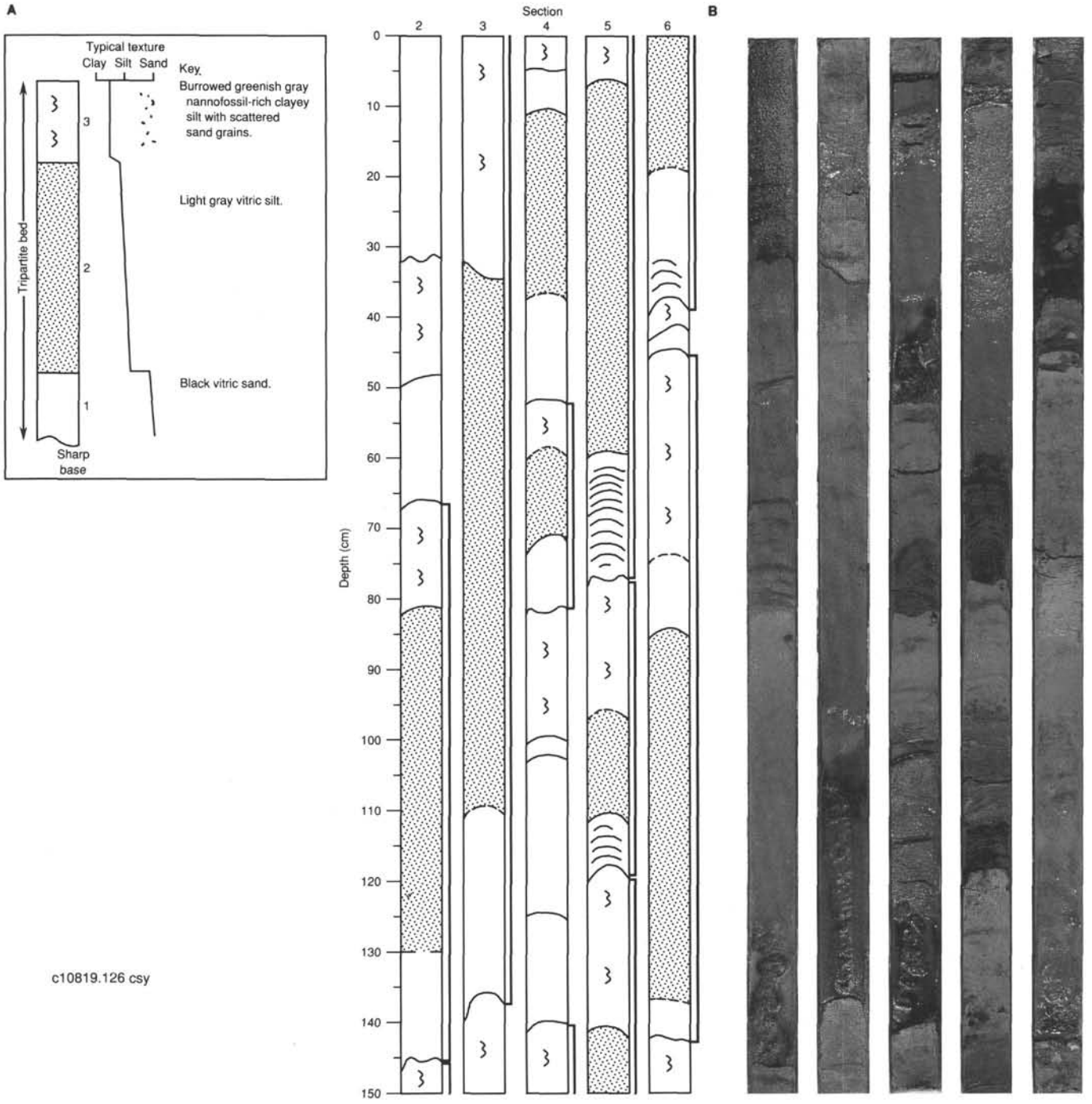

Figure 19. **A.** Positions and internal lithology of seven tripartite beds in Core 126-790C-6H. Note that the middle division of vitric silt (fine stipple) is generally considerably thicker than the lower division of black vitric sand (coarse stipple). Burrowed nannofossil-rich silty clays contain scattered sand- and granule-size pumice grains. **B.** Corresponding core photograph of the tripartite beds.

Correlation of Sites 790 and 791

Sites 790 and 791 are located on the western margin and in the central part of the eastern half-graben of the Sumisu Rift, respectively (Figs. 2–5). The recovery at both sites of the contact between the sedimentary sequence and the underlying basaltic rocks demonstrates that the sedimentary section at Site 791 is about three times thicker than the section at Site 790. The biostratigraphic and paleomagnetic data used to construct the age-depth curves at Sites 790 and 791 (Fig. 40 and Table 9) indicate that the successions at the two sites are essentially time equivalent.

Lithostratigraphic correlation between Sites 790 and 791 is made on the basis of the following characteristics: (1) lithology and sedimentary facies (Fig. 41); (2) identification of Key Bed #7 (volcanic ash) at both sites (Fig. 13); (3) bulk magnetic susceptibility (Fig. 15); (4) carbonate contents (Fig. 42); and (5) a correlatable seismic horizon. Correlation between the two sites

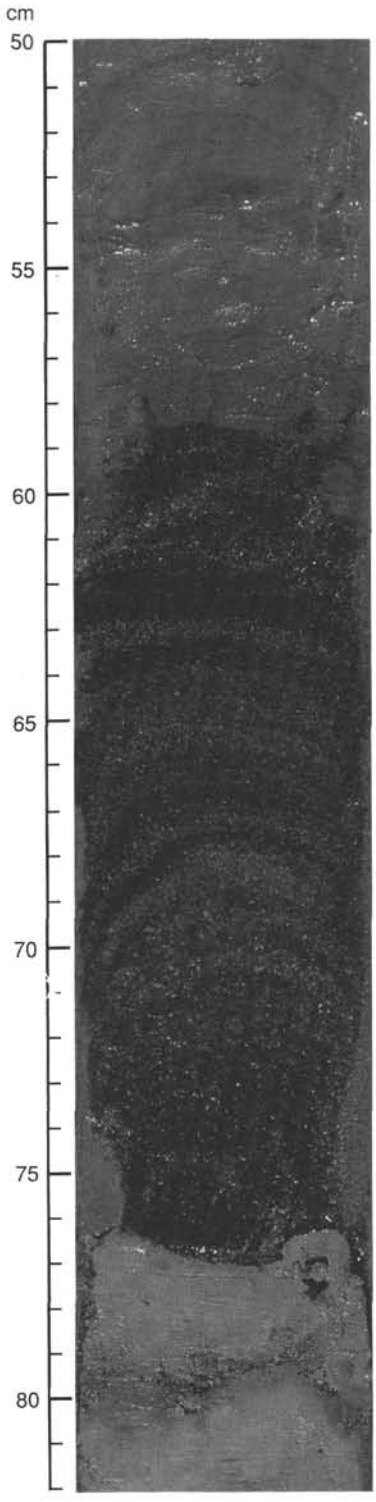

Figure 20. Parallel-laminated lower division of the tripartite bed illustrated in Figure 19 (Interval 126-790C-6H-5, 50–82 cm). The curvature of the laminae is a result of coring disturbance.

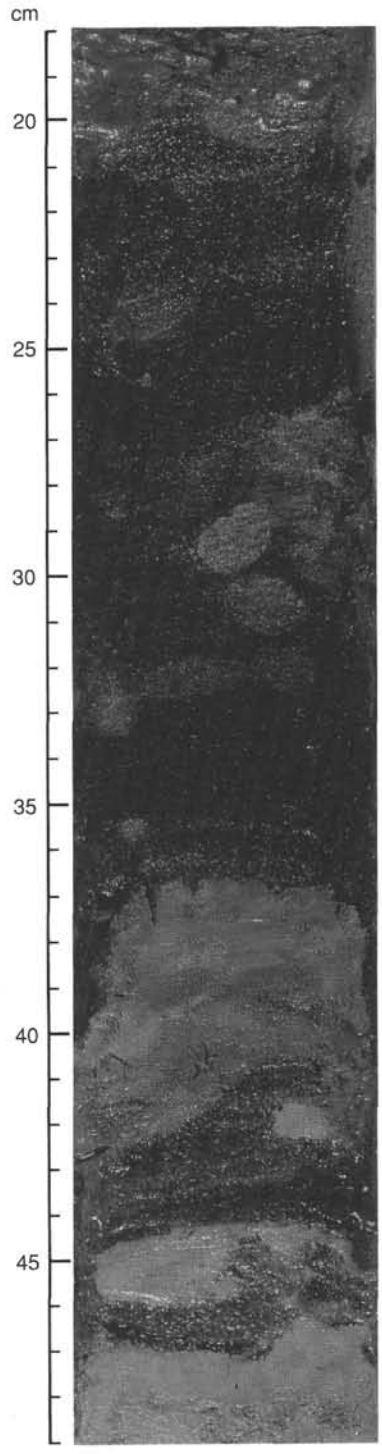

Figure 21. Cylindrical burrows in black vitric sand divisions of tripartite beds illustrated in Figure 19 (Interval 126-790C-6H-6, 18–49 cm). Burrows in the sand are filled with nannofossil-rich silty clay (29–31 cm, 42 cm), whereas burrows in the nannofossil-rich silty clay are filled with sand (45–47 cm).

is well constrained above Key Bed #7, based mainly on the marked differences in magnetic susceptibility between thick units of felsic vitric silt (volume magnetic susceptibility $< 125 \times 10^{-6}$) and thin- to thick-bedded intervals containing magnetic minerals and mafic grains of basaltic composition. These latter intervals include black vitric sand/silt beds and pumiceous gravels and pebbly sands (e.g., Site 791, 60–150 mbsf) that contain scattered scoria grains.

At Sites 790 and 791, there is a sharp lithologic contrast between Units I and II, with Unit I containing thick intervals of pumiceous gravel and pumiceous sand. The contact between the two units is reasonably well defined at Site 790, although the

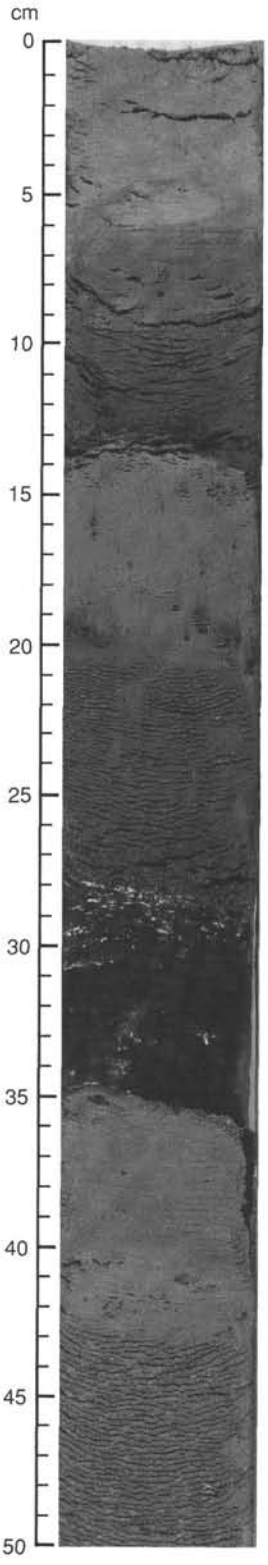

Figure 22. Scattered sand-size volcanic fragments in burrowed nannofossil-rich silty clay (14–20 cm) that forms the upper division of a tripartite bed from 14 to 35 cm (Interval 126-790C-5H-5, 0–50 cm). The basal division of vitric sand is saturated with water in this photograph as a result of coring-induced liquefaction.

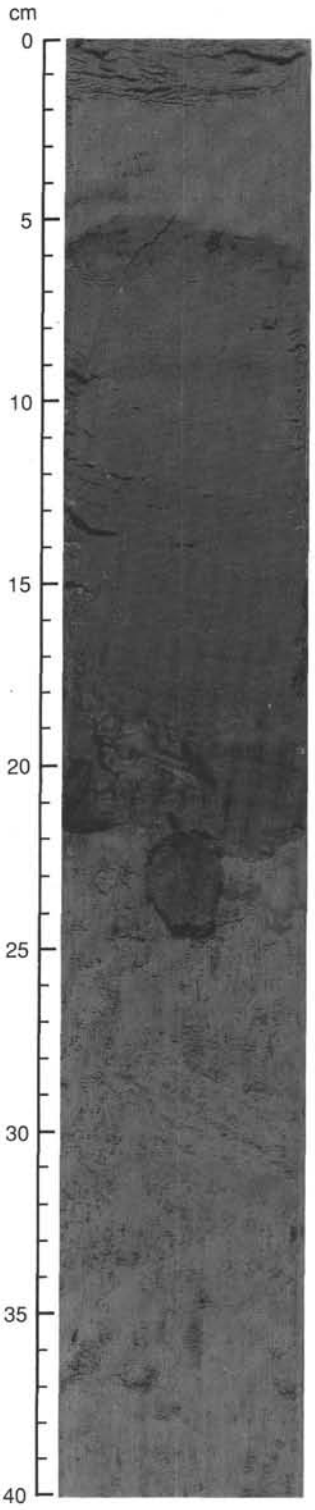

Figure 23. Scattered volcanic fragments (sand to pebble sizes) in burrowed nannofossil-rich silty clay (Interval 126-790C-5H-6, 0–40 cm). The 2-cm pebble is in the lowermost lithology, not in the overlying dark gray vitric silt.

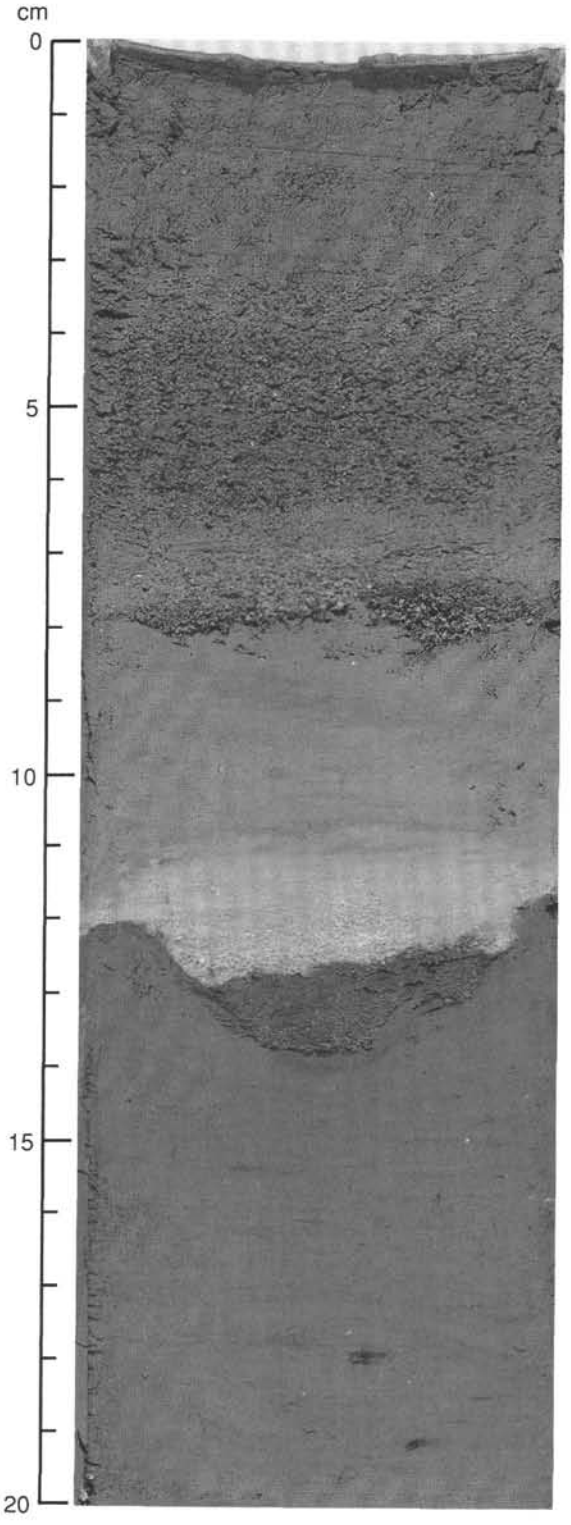

Figure 24. Photograph of a scour, filled partially by a light olive gray, 1-cm-thick vitric sand lens, and blanketed by a light gray, very fine, vitric sand (ash) bed (Interval 126-790C-11X-5, 0–20 cm).

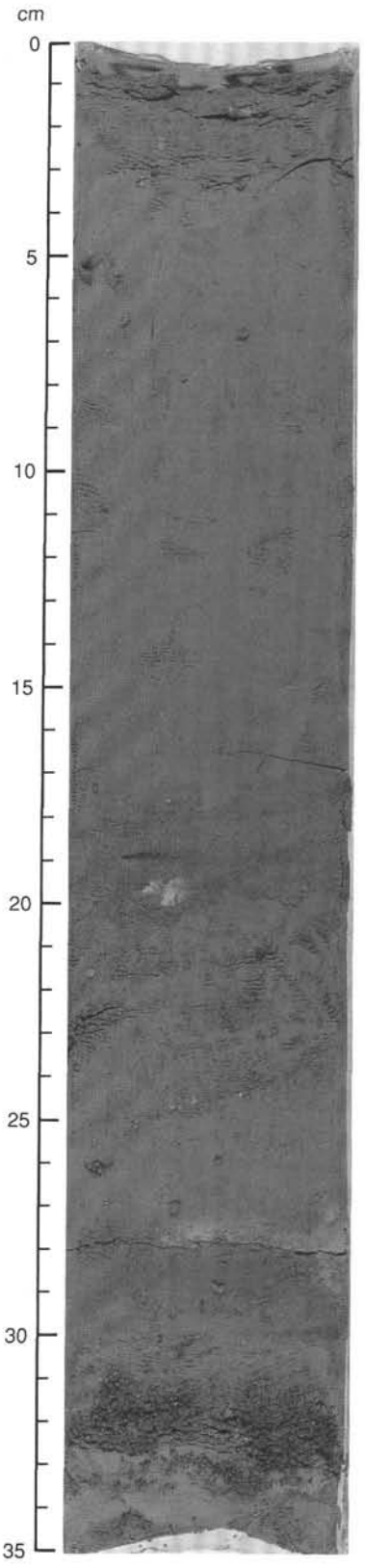

Figure 25. Dark grayish green (31–33 cm) and light gray (28 cm) ash beds in nannofossil-rich clay of Unit II (Interval 126-790C-17X-CC, 0–35 cm).

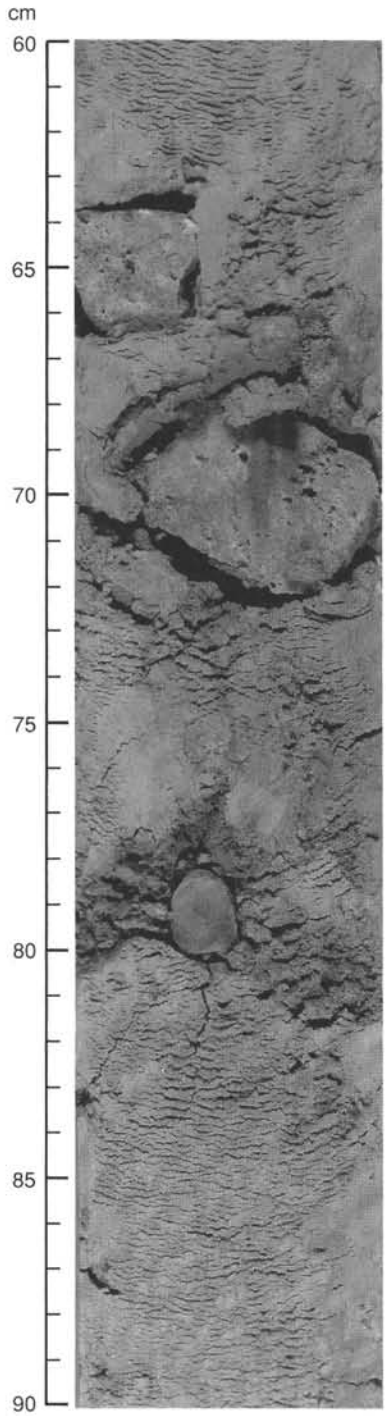

Figure 26. Dispersed, large pumice pebbles (64–66, 68–71, and 78–80 cm) near the base of Unit II (Interval 126-790C-20X-2, 60–90 cm).

contact itself was not recovered in the cores. At Site 791, however, very poor recovery does not allow a confident assessment of the position of the contact, given only the lithology. Therefore, we used three criteria to estimate the true depth of the contact between Units I and II at Site 791: (1) the age correlation as determined from the age-depth curves (Fig. 40); (2) a comparison of downhole trends in carbonate content at the two sites; and (3) seismic stratigraphic correlations (see "Seismic Stratigraphy" section, this chapter).

Poor recovery near the contact between Units I and II at Site 790 permits the contact to be placed anywhere in the interval from 155 to 165 mbsf. On the basis of the age-depth curves, the contact at Site 790 (155–165 mbsf) has the same age (about 0.2 Ma) as sediment at a depth of 415–430 mbsf at Site 791. To minimize the apparent difference in age between the base of Unit I at the two sites, the base at Site 790 is assigned its maximum possible depth of 165 mbsf, and the base at Site 791 is assigned to the bottom of Core 126-791A-46X.

At Site 790, Unit II has carbonate contents of 20%–40%, whereas Unit I has <20% carbonate (Fig. 42). The carbonate curve for Site 791 shows the same trend, with the upward transition from high to low carbonate values occurring at about 375–500 mbsf. This depth is consistent with the independent estimate of the position of the contact between Units I and II at 428.4 mbsf, but it is not sufficiently well defined in the carbonate curves to allow a more accurate definition of the contact (see "Physical Properties" section, this chapter, for further discussion of these data).

Interpretation

The sedimentary succession recovered at Sites 790 and 791 shows stratigraphic variation caused by changes in the amount, texture, and composition of volcaniclastic materials, and the amount of biogenic (pelagic) input to the backarc basin. Sites 790 and 791 have undergone differential subsidence, resulting in a thickening of the basin fill toward the eastern margin of the half-graben and the volcanic arc. The gravel material that characterizes the pumice units in Unit I at both sites also increases in grain size from west to east.

The volcanogenic components in the sediments are bimodal in composition, consisting of felsic pumice and dark grains of mafic glass, ferromagnesian minerals, and lithic fragments. This bimodal signature is present throughout the sedimentary history of the basin, although the relative amounts of the two end members has changed with time. In particular, the proportion of felsic material increased dramatically during the last 0.2 Ma (Fig. 40), whereas more mafic components are dominant in Unit II at both sites.

Some of the mafic volcanic material may have been produced within the backarc basin at volcanic centers like those that are found today along the transverse volcanic ridge to the north, or in the vicinity of Shadow Mountain to the south (Hochstaedter et al., in press). The felsic pumice, in contrast, was probably produced by explosive eruptions of submarine/subaerial volcanoes of the Izu-Bonin Arc to the east, like the Minami Sumisu and Sumisu calderas (see "Igneous Petrology" section, this chapter).

The sedimentary sequence at Sites 790 and 791 coarsens upward from the nannofossil-rich and nannofossil claystones of Unit II to the pumiceous gravels and sands of Unit I. This coarsening upward is not produced by a decrease in water depth or an encroachment of source areas but is the result, instead, of increased volcanic activity and the tectonic development of basin-margin and intrabasinal relief. Benthic foraminifers indicate that the entire sedimentary sequence was deposited in a bathyal setting ranging in depth from 1500 to >2000 m (see "Biostratigraphy" section, this chapter).

Limited paleontological data from a thin sedimentary unit within the basaltic section indicate that there is no significant time gap between the eruption of the underlying basalts and the deposition of the lowest sediments of Unit II. The sediments of Unit II, summarized in Figures 9 and 27, are predominantly fine grained and burrowed and contain 20%–40% biogenic carbonate. They were deposited in a low-energy environment where burrowers were able to rework the sediment continuously and

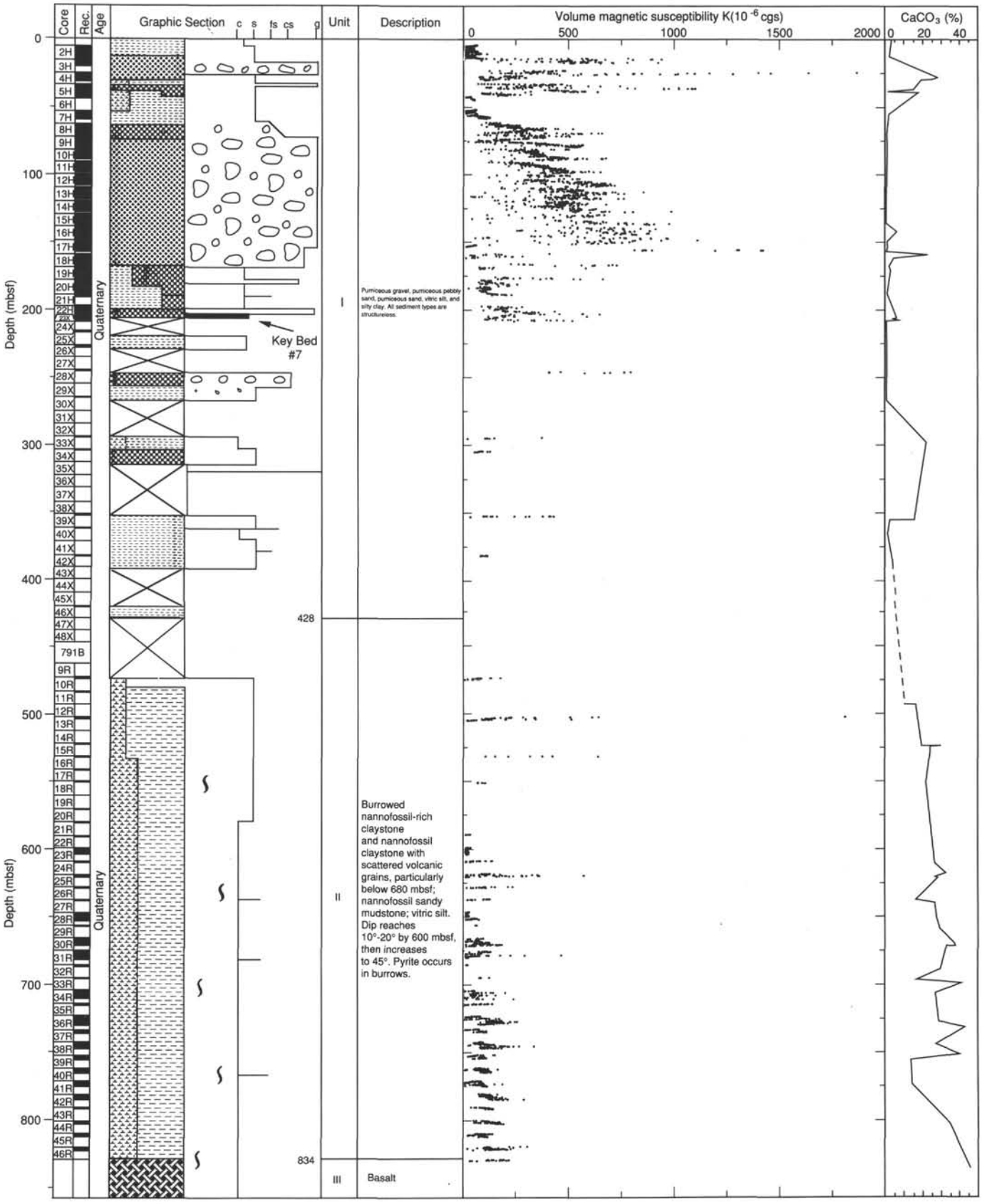

Figure 27. Composite stratigraphic succession for Site 791 showing unit boundaries and downhole variations in magnetic susceptibility and total carbonate. See Figures 6 and 9 for key to graphic lithology.

Table 6. Summary of lithology and sedimentary structures of units at Site 791.

Unit	Lithology	Sedimentary structures	Interval (mbsf)	Age	Occurrence
I	Pumiceous gravel, pumiceous pebbly sand and sand, vitric silt with minor clay, silty clay, and nannofossil-rich silty clay.	Generally structureless.	0–428.4	Quaternary	126-791A-1H to -46X 126-791B-1R to -5R-2, 120 cm
II	Nannofossil-rich claystone and nannofossil claystone with scattered volcanic grains, particularly below 680 mbsf; nannofossil sandy mudstone; vitric silt. Dip reaches 10°–20° by 600 mbsf, then increases to 45° by 760 m. Pyrite occurs in burrows.	Burrows of *Chondrites* and *Zoophycos* (1-cm burrows). Vitric silt beds may be parallel laminated.	428.4–834	Quaternary	126-791B-5R-2, 120 cm to -47R-1, 44 cm
III	Basalt, diabase, basaltic mousse, felsic ash to lapilli tuff, and rare dark vitric silt.		834–1145	Quaternary	126-791B-47R-1, 44 cm, to 126-791B-79R

destroy any primary physical structures. Nevertheless, depositional rates were high, about 90 (Site 790) to 345 m/m.y. (Site 791). At Site 791, burial of organic carbon at high sedimentation rates led to reducing conditions in the sediment and the precipitation of iron sulfides (troilite and pyrite) in burrows and as disseminations.

The high sedimentation rates demand a constant supply of fine-grained material to the basin and enhanced delivery of this material to areas with the highest subsidence rates. This material includes volcanogenic ash and clays as well as nannofossils. Because Unit II in the Sumisu Rift is not evenly draped across the basin, its deposition must have involved an interplay of processes that include settling from the overlying water column, supply from dilute density currents, and redistribution by weak bottom currents.

To provide a proper evaluation of the depositional processes for the fine-grained sediments of Unit II requires the determination of the mass budget of fine volcanogenic and biogenic carbonate materials within the basin and around the basin margins. It is known from dredging and seismic profiling that basement highs east of Sites 790 and 791 are covered only by a thin, discontinuous blanket of Holocene pelagic sediments and pumiceous clastic rocks. Also, Pleistocene to Pliocene sediments recovered from Site 788 (see "Lithostratigraphy and Accumulation Rates" section, "Site 788" chapter, this volume) are represented mainly by winnowed pumiceous gravel and conglomerates. At or near the seafloor, this gravel, unlike the pumiceous gravel at Sites 790 and 791, contains no mud matrix or nannofossils; some pumice clasts are coated by black manganese oxides, and others are oxidized.

We interpreted the features at Site 788 to be the result of winnowing by bottom currents that swept clays and microfossils away from the highs and into the adjacent basins. Fine clay and nannofossil particles are easily resuspended and may, in fact, never be deposited under strong bottom currents (Nowell and Hollister, 1985). Similar hydrodynamic conditions probably persisted throughout the Quaternary, carrying clay particles and nannofossils from bathymetric highs into the Sumisu Rift. Suspended fines from the highs around the rift may have traveled down into the basin as plumes of suspended material along density interfaces in the water column or as dilute lutite flows (McCave, 1972). These flows and plumes could then have fed a nepheloid layer above the basin floor from which clay and fine-silt particles settled to the seafloor. Because of severe bioturbation, we do not see evidence for density current deposits in Unit II; it is essential, however, that the depositional mechanism of these sediments involved control by bathymetry of the rift basin.

The foregoing discussion assumes that the recovered sediments at Site 791, where Unit II is thicker, are representative. This may not be true, because there are several examples in remnant cores of vitric silt beds that have been almost completely lost during drilling (Figs. 33 and 34). Preliminary interpretation of the total gamma-ray log for Site 791 is not inconsistent with the presence of about 20% vitric silt beds in the unrecovered intervals (see "Downhole Measurements" section, this chapter). If these vitric silt beds are much thinner at Site 790, then the degree to which the fine-grained, burrowed, carbonate-rich facies must thicken to the east may be less than assumed above. However, there must be significant eastward thickening of all sediments to account for the 400% increase in the thickness of Unit II from Sites 790 to 791.

An important characteristic of the nannofossil-rich and nannofossil claystones of Unit II at Site 791 is the presence of scattered basaltic sand grains that decrease in abundance away from the contact with the basalts. These mafic-rich intervals are also characterized by high smectite contents, implying that submarine, and possibly even subaerial, weathering and erosion of basaltic outcrops was prevalent during the earliest phase of rift sedimentation. These basaltic materials may have been transported from submarine volcanoes east and north of Sites 790 and 791. Alternatively, the basaltic grains in the lower part of Unit II may have been derived from the erosion of basalt from intrabasinal highs and from hyaloclastite-forming eruptions on the irregular floor of the embryonic rift.

Despite the relative abundance of the mafic component directly above basement, clear (felsic) glass shards are still present, indicating that bimodal volcanism prevailed in this region throughout the sedimentary history of the site. Light-colored, thin beds of felsic fine ash that occur throughout Unit II were probably derived from distant volcanic eruptions around the western Pacific rim.

The contact between syn-rift basalts and the sediments of Unit II was recovered at Site 790, but not at Site 791. Even at Site 791, however, the lowest-recovered sediments came from less than 10 m above the volcanic rocks. At neither site is there evidence for hydrothermal alteration (such as from the recrystallization of microfossils). The alunite present at Site 791 may be detrital.

The basaltic basement rocks that underlie the eastern half-graben near Sites 790 and 791 can account for some of the basaltic detritus in the lower part of Unit II, but similar detritus in younger sediments must have come from different volcanic centers. A possible source for basaltic detritus in the upper part of the basin fill is the basaltic fissure ridges north of the Minami Sumisu Basin (see "Igneous Petrology" section, this chapter).

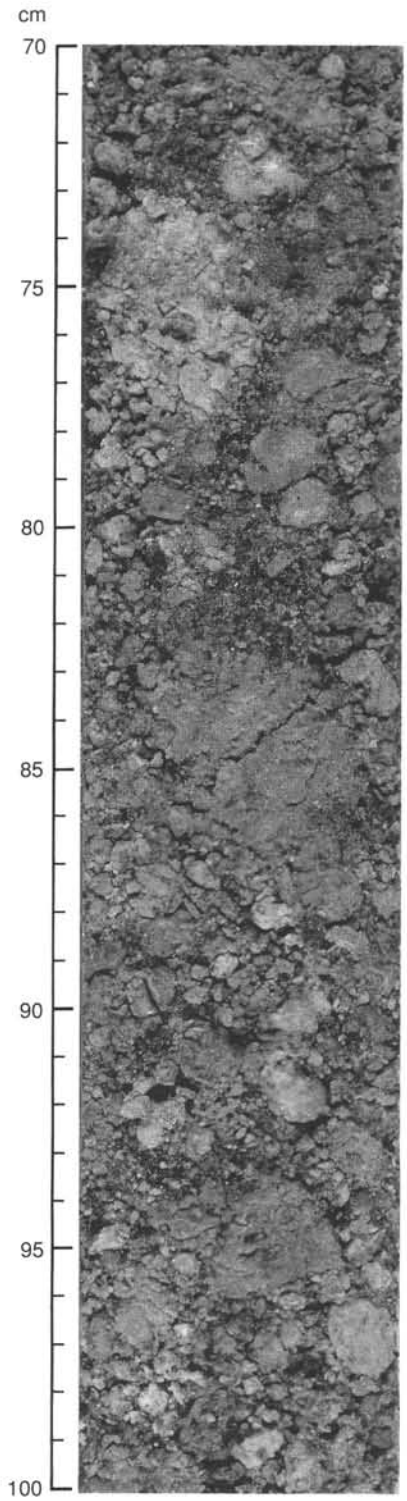

Figure 28. Structureless, poorly sorted, pumiceous gravel from the upper part of Unit I (Interval 126-791A-13H-4, 70–100 cm).

The upper part of Unit II contains decimeter-scale, tripartite beds of sharp-based, black sand/silt, thick vitric silt, and burrowed nannofossil-rich clayey silt that are interpreted as pyroclastic deposits because of their thick cap of glass shards (vitric silt). This facies, which typifies the transition between Units I and II, records the initial phase of the paroxysmic volcanic activity that characterizes Unit I.

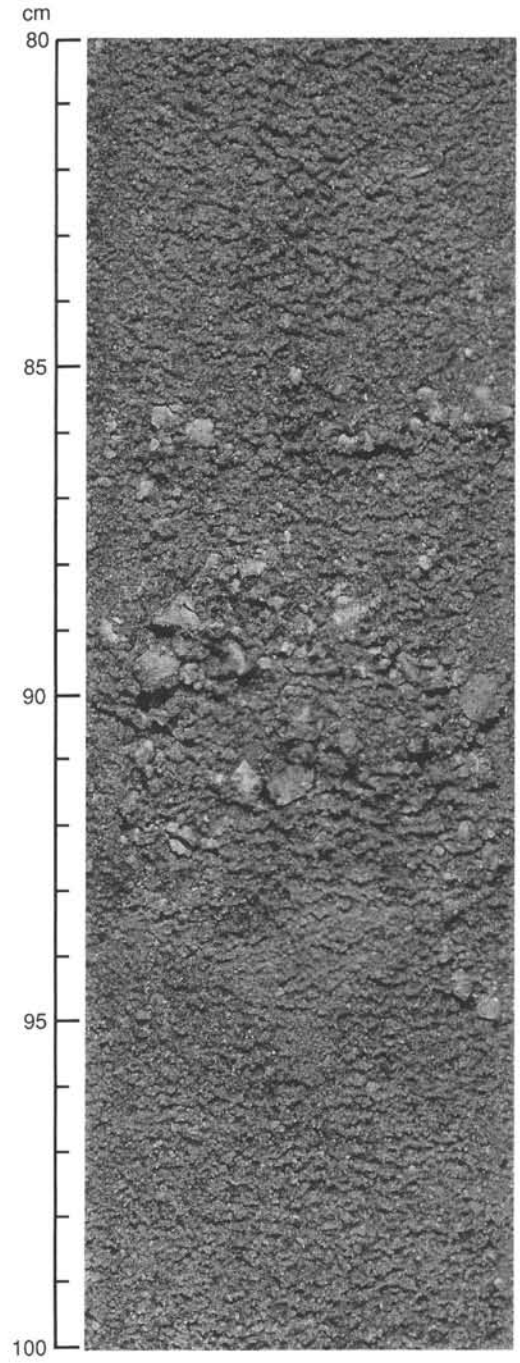

Figure 29. Pumiceous sand and pebbly sand of Unit I (Interval 126-791A-8H-5, 80–100 cm).

Unit I is characterized by a sequence of thick, coarse, silicic volcanogenic materials. Possible mechanisms to transport the volcanic ash and coarser ejecta include (1) air fall; (2) the rafting of floating pumice until it is water saturated; (3) an entire spectrum of mass movements (both hot and cold), including submarine slumps, debris flows, and turbidity currents; and (4) hyaloclastite-induced submarine density flows. The first three mechanisms would be predominantly associated with felsic eruptions in the nearby arc volcanoes, whereas the last process may be one of the agencies responsible for the mafic ash layers. The dramatic lateral thinning of the pumiceous gravels from Sites 791 to 790, the mounded reflectors that characterize these gravels in high-resolution air-gun records of the Geological Survey

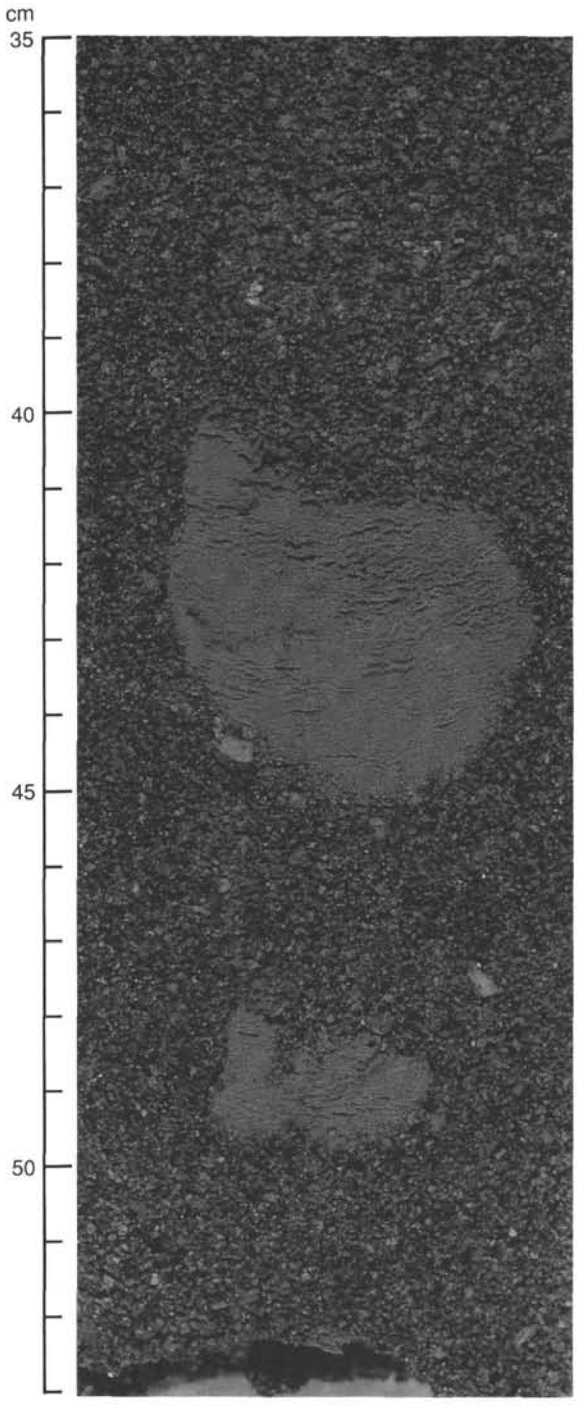

Figure 30. Vitric silt intraclasts in pumiceous sand of Unit I (Interval 126-791A-19H-7, 35–53 cm). Because this is an APC core, the intraclasts cannot be drilling biscuits.

of Japan, the presence of intraclasts of vitric silt, and the lack of coeval pumiceous gravels on the basin slopes, all favor resedimentation by debris flow for final emplacement of the gravels. The pumiceous gravel probably was initially deposited as blankets on the basin floor as well as metastably perched on adjacent basin slopes. Shortly after each was laid down, gravitational failure or seismic shaking remobilized the gravels on the basin slopes into debris flows that moved onto the basin floor, preferentially filling in the deeper parts of the half-graben.

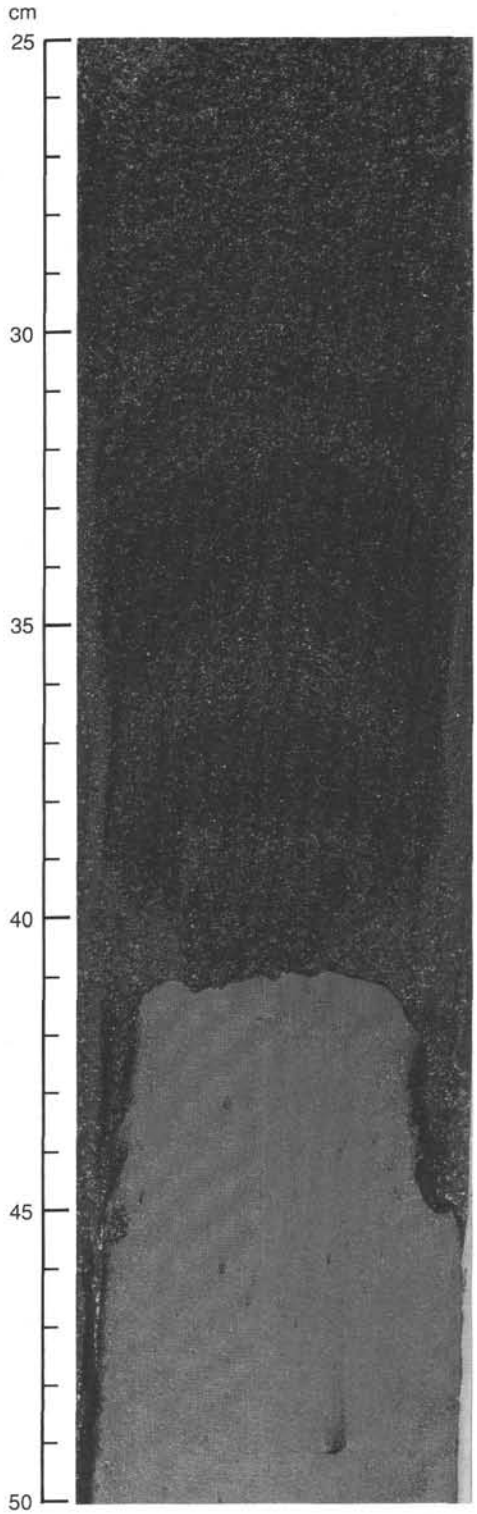

Figure 31. Sharp base of a faintly laminated black sand bed that is about 20 cm thick (Interval 126-791A-5H-3, 25–50 cm).

Explosive volcanism provided large thicknesses of pumiceous gravel five times during the deposition of Unit I. Figure 43 summarizes an attempt to date these occurrences. It assumes that the layers of strongly burrowed silty clay and clayey silt with variable amounts of biogenic carbonate were contributed to the

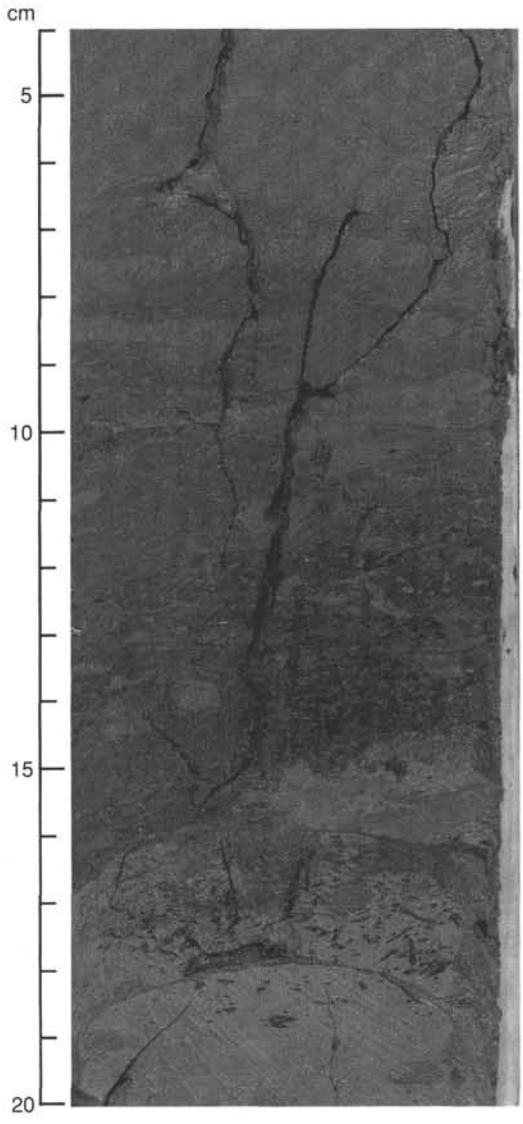

Figure 32. *Chondrites* (11–19 cm), *Zoophycos* (5–10 cm), and unidentified cylindrical burrows in Unit II (Interval 126-791B-13R-2, 4–20 cm).

basin at a fairly constant rate. Specifically, the 21.33 m of muddy sediment deposited in Unit I at Site 790 since the FO of the *Emiliania huxleyi* datum (275,000 yr ago) accumulated at a rate of about 77.5 mm/1000 yr. Applying this uniform rate, and treating each massive influx of pumice as an essentially instantaneous event, yields dates for the explosive eruptions of 194, 128, 122, 59, and 2 ka.

BIOSTRATIGRAPHY

Calcareous Nannofossils

Hole 790A

Samples 126-790A-1H-1, 0–1 cm, through 126-790A-4H-CC contain *Emiliania huxleyi* and are placed within Zone CN15. Rare reworked specimens of *Calcidiscus macintyrei* and *Pseudoemiliania lacunosa* are present in Cores 126-790A-1H, -2H, and -4H. Other species present include *Umbilicosphaera sibogae, Helicosphaera carteri, Rhabdosphaera clavigera,* and *Gephyrocapsa oceanica.*

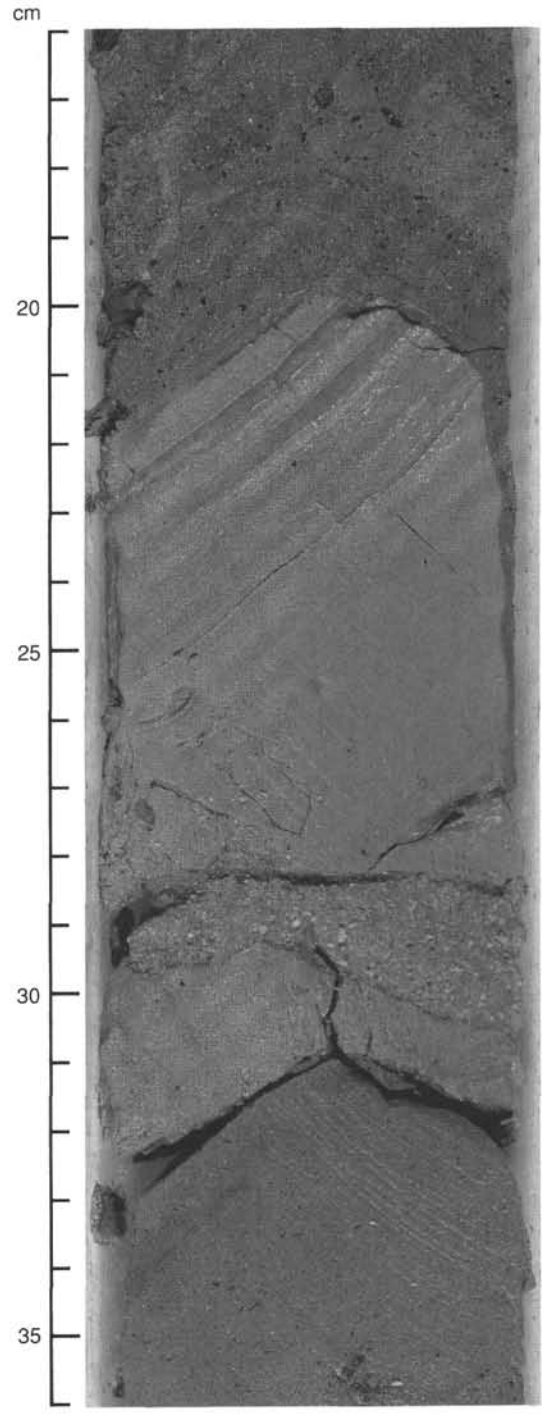

Figure 33. Dipping bed of predominantly vitric silt (20–30 cm), with 1–2-mm pumice grains at the base (Interval 126-791B-42R-1, 16–36 cm). The base is in a different drilling biscuit than the top of the bed, and its apparent dip is horizontal. The vitric silt is soft, and the top of the bed has been truncated during drilling.

Hole 790B

Samples 126-790B-1H-1, 3 cm, through 126-790B-15X-CC contain *E. huxleyi* and are placed within Zone CN15. Rare reworked specimens of *P. lacunosa* and *C. macintyrei* are present in most samples. One reworked specimen of the upper Miocene *Discoaster quinqueramus* was found in Sample 126-790B-15X-CC.

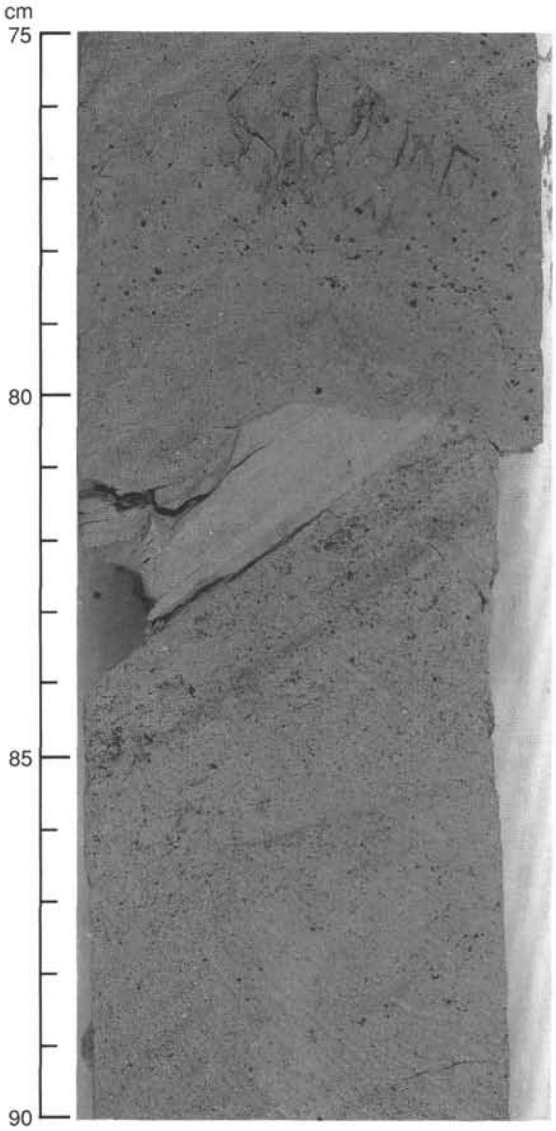

Figure 34. Remnant of a dipping bed of vitric silt (81–83 cm) that has been almost completely destroyed by drilling (Interval 126-791B-44R-2, 75–90 cm).

Hole 790C

Samples 126-790C-1H-CC through 126-790C-11X-CC contain *E. huxleyi* and are placed within Zone CN15. Samples 126-790C-12X-1, 120–121 cm, through 126-790C-15X-CC are located below the FO of *E. huxleyi* and above the LO of *P. lacunosa* and are assigned to Zone CN14b. Samples 126-790C-16X-1, 40–41 cm, through 126-790C-20X-CC contain *P. lacunosa* and *G. oceanica* and are assigned to Zone CN14a. Sample 126-790C-19X-1, 40–41 cm, contains the highest occurrence of common *Reticulofenestra* sp. A that marks the datum of Takayama and Sato (1987) and Sato et al. (1988) (about 0.83 Ma). *Reticulofenestra* sp. A commonly are present throughout Cores 126-790C-19X and -20X.

Samples 126-790C-21X-CC, 126-790C-23X-CC, 126-790C-32X-CC, and 126-790C-33X-CC consist of fragments of volcanic rocks (scoria) that had small particles of sediment stuck to them. These sediment particles contain *P. lacunosa, Gephyrocapsa* spp., *Calcidiscus* sp., and *Coccolithus pelagicus,* which would indicate assignment to Zone CN14a. However, these assemblages may be downhole contaminants.

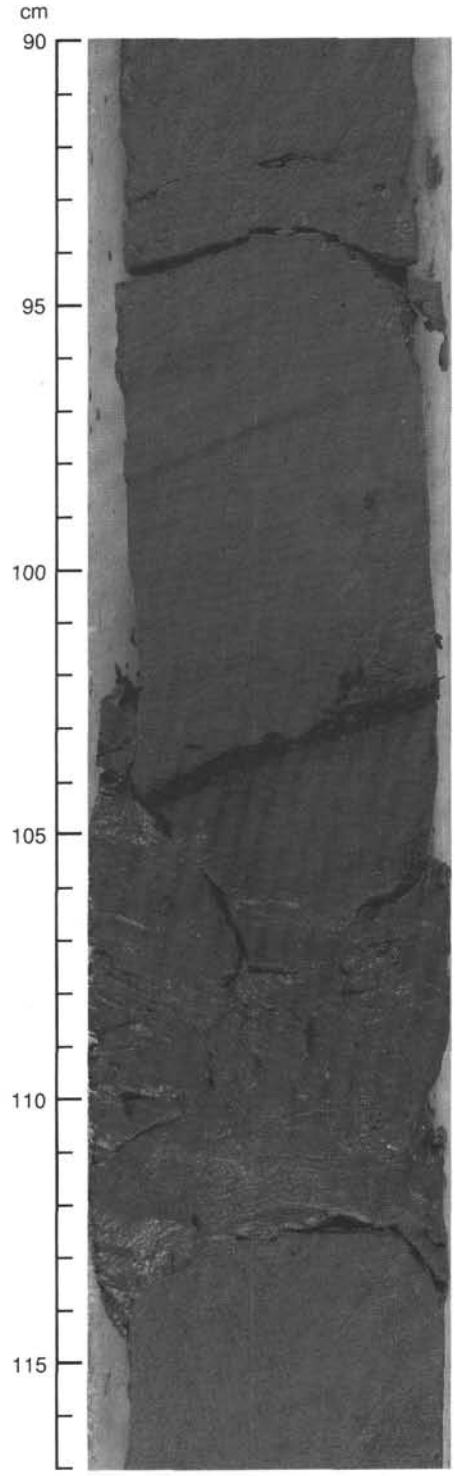

Figure 35. Squeezed and expanded bed of unlithified vitric silt (106–113 cm) sandwiched between hard, lithified sediments that form the bulk of Unit II (Interval 126-791B-25R-1, 90–117 cm).

Hole 791A

All core-catcher samples contain *E. huxleyi,* and are assigned to Zone CN15. Other species present in these samples include

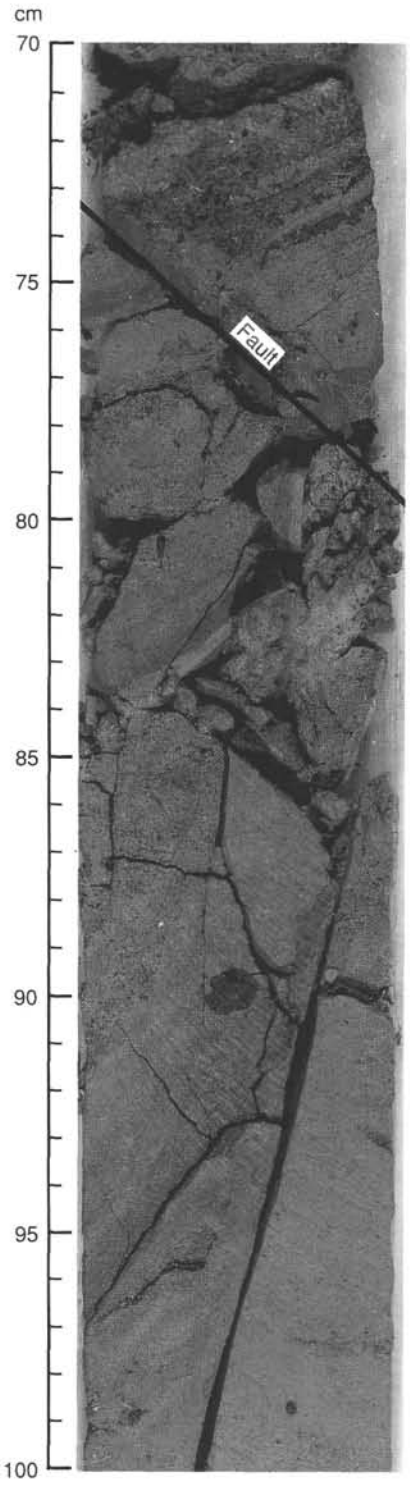

Figure 36. Fault with a dip of about 45°, left to right (73–78 cm), near the base of Unit II (Interval 126-791B-46R-1, 70–100 cm). Note the high concentration of sand-size basaltic rock fragments above 75 cm.

Umbilicosphaera sibogae, Coccolithus pelagicus, Gephyrocapsa spp., *Ceratolithus cristatus, Rhabdosphaera clavigera, Helicosphaera* spp., and *Thoracosphaera* sp.

Hole 791B

Samples 126-791B-5R-CC through 126-791B-11R-CC contain *E. huxleyi* and are assigned to Zone CN15. Samples 126-791B-13R-CC through 126-791B-28R-CC contain neither *E. huxleyi* nor *P. lacunosa,* but do contain *G. oceanica,* indicating placement in Subzone CN14b. Samples 126-791B-29R-CC through 126-791B-49R-CC contain *P. lacunosa* and *G. oceanica* and are placed within Subzone CN14a. The LO of common *Reticulofenestra* sp. A in Sample 126-791B-41R-CC indicates an age of about 0.83 Ma at this level (Takayama and Sato, 1987; Sato et al., 1988). Other species present throughout Hole 791B are *Calcidiscus leptoporus, R. clavigera, U. sibogae, Helicosphaera carteri, Scapholithus fossilis, Pontosphaera* spp., *Thoracosphaera* sp., and *Syracosphaera* spp.

Samples 126-791B-56R-1 (Pieces 1, 2, and 6), 126-791B-75R-CC, and 126-791B-78R-CC are barren of calcareous nannofossils.

Planktonic Foraminifers

Hole 790A

Samples 126-790A-1H, 1–2 cm, 2–4 cm, and 7–9 cm, contain *Globigerina calida, Globorotalia tumida* (sinistral), *Globorotalia truncatulinoides* (dextral), and *Globorotalia menardii* (sinistral), in addition to about 30 long-ranging, warm-water taxa, placing these samples in the upper Pleistocene Zone N23 (Blow, 1969). Samples 126-790A-1H-CC and 126-790A-2H-CC contain colder water faunas than the three topmost samples; dominant taxa include *Globigerina pachyderma* (dextral), *Globigerina hermanae* (dextral), *Globigerina cryophila, Globigerina quinqueloba, Globigerina bulloides, Globigerinita uvula,* and *Globorotalia scitula.*

Hole 790B

Samples 126-790B-3H-CC and 126-790B-7H, 98–102 cm, contain *Pulleniatina obliquiloculata* and other warm-water taxa, in addition to cool-water and eurythermal species such as *G. bulloides, G. quinqueloba, G. uvula, G. truncatulinoides, Globorotalia inflata, Globigerinoides gomitulus, Globoquadrina dutertrei-pachyderma* (dextral), *Globorotalia falconensis, Globorotalia crassaformis, Orbulina universa, Globigerinella aequilateralis,* and others, indicating that the sediments were deposited during interglacial periods. Samples 126-790B-10H-CC and 126-790B-11H-CC contain interglacial faunas, and the presence of *G. calida* and *Globigerina digitata* places these samples in upper Pleistocene Zone N23.

Hole 790C

Sample 126-790C-9H-CC contains only two juvenile specimens of warm-water species (*Globigerinoides ruber* s.s. white and *Globigerinoides trilobus sacculifer*) in an ash fall. Sedimentation rates were very high during the deposition of this ash bed and more than 99% of the fraction >63 μm is composed of volcanic ash. Sample 126-790C-13X-3, 104–106 cm, contains high percentages of cool-water dextral *G. pachyderma, G. quinqueloba, G. bulloides,* and *Globigerinita glutinata* as well as low percentages of warm-water *G. menardii, G. tumida,* and *P. obliquiloculata.* In Sample 126-790C-14X-CC, warm-water taxa (*Globigerinoides trilobus, Globigerinoides conglobatus, G. tumida,* and *P. obliquiloculata*) dominate the faunal assemblage. Samples 126-790C-15X-CC, 126-790C-18X-CC, and 126-790C-19X-CC contain transitional faunal assemblages (e.g., *G. gomitulus, G. dutertrei,* etc.). Sample 126-790C-20X, 36–41 cm, contains an interglacial warm-water fauna that is dominated by *Sphaeroidinella dehiscens, P. obliquiloculata, G. ruber, G. trilobus, G. conglobatus, G. sacculifer, G. tumida, G. menardii,* and others.

Hole 791A

Sample 126-791A-4H-3, 60–62 cm, contains cool- and warm-water species (e.g., *G. quinqueloba, Globigerina glutinata, Globigerina scitula, G. sacculifer, G. conglobatus, S. dehiscens,* etc.);

Table 7. X-ray diffraction data from Site 790.

Core, section, interval (cm)	Unit	Color	Sample description	Clay minerals			Minerals	Amorphous materials
				1.3 ~ 1.4 nm	1.0 nm	0.7 nm		
126-790A-								
1H-1, 1	I	10YR3/3	Green grains in clayey vitric silt	Trace	Trace		0.203 nm > Feldspar-diaspore	Abundant
3H-3, 90	I	5Y6/1	Vitric silt	Present		Present	0.209 nm > halite > diaspore, calcite, 0.203 nm > feldspar	Abundant
4H-1, 140	I	N5	Green grains in vitric medium to coarse sand	Trace		Trace	0.203 nm > diaspore	Abundant
126-790B-								
1H-1, 5	I	5YR3/4	Clayey vitric silt	Trace (chlorite)	Present	Present	Calcite > quartz > halite > 0.203 nm > feldspar, diaspore	Abundant
10H-5, 14	I	5Y5/1	Very fine sand (ash)	Trace	Trace	Trace	Halite > calcite > diaspore, 0.203 nm > feldspar, quartz	Abundant
10H-5, 20	I	5GY2/1	Silty clay	Trace	Trace	Trace	Halite, calcite > diaspore, 0.203 nm > feldspar, quartz	Abundant
10H-5, 24	I	5YR2/1	Silt (ash)	Present (smectite)	Trace	Trace	Halite > 0.203 nm, calcite > feldspar, quartz	Abundant
126-790C-								
2H-2, 150	I	5Y6/1	Vitric silt (ash)	1.65 nm (smectite) 1.41 nm (chlorite)	Trace	Present	Halite > 0.203 nm > calcite, quartz, feldspar, > diaspore	Abundant
5H-6, 22	I	5Y5/3	Reddish pumice in vitric clayey silt	Present		Present	Quartz, feldspar, cristobalite > calcite > 0.203 nm	Abundant
5H-6, 6	I	5Y5/3	Vitric silt (ash)	Trace			Pyrolusite, pyrite, 0.203 nm > calcite, feldspar > quartz	Abundant
11X-5, 10	II	5Y5/2	Very fine sand	Trace			Halite > calcite > 0.203 nm, feldspar > quartz, diaspore	Abundant
20X-2, 80	II	5G4/1	Pumice gravel-bearing nannofossil mud	Trace			Calcite > feldspar, quartz, halite, 0.203 nm	Abundant
20X-3, 46	II	5GY7/2	Pumice gravel-bearing nannofossil mud	Trace			Calcite > feldspar, quartz, halite, 0.203 nm	Abundant
20X-3, 90	II	5GY6/1	Pumice gravel-bearing nannofossil mud	Trace			Calcite ≫ feldspar, quartz, halite, 0.203 nm	Abundant

the presence of *G. calida* and *G. digitata* places this sample in Zone N23. Sample 126-791A-5H-3, 52–54 cm, contains specimens of *Globorotalia tumida flexuosa*. Cool-water elements dominate the assemblage in Sample 126-791A-16H-2, 95–97 cm. The presence of *G. calida* places this sample in Zone N23. Sample 126-791A-31X-CC contains cool- and warm-water faunas, including *G. truncatulinoides* (dextral), *G. pachyderma, G. falconensis, G. tumida, G. menardii, G. ruber, P. obliquiloculata,* and *G. trilobus*.

Hole 791B

Sample 126-791B-24R-CC contains cool-water foraminifers such as dextral *G. pachyderma,* dextral *G. hermanae, G. bulloides,* and *G. falconensis*. Cool foraminiferal elements including dextral *G. pachyderma,* dextral *G. hermanae,* dextral *G. cryophila, G. bulloides,* and *G. glutinata* are present in Samples 126-791B-30R-CC and 126-791B-32R-CC. Sample 126-791B-37R-CC (just above the Brunhes/Matuyama boundary; see "Paleomagnetics" section, this chapter) contains a transitional fauna and is dominated by *G. glutinata, G. aequilateralis, G. dutertrei,* dextral *G. pachyderma, G. scitula,* and *G. gomitulus*. Sample 126-791B-38R-CC, immediately below the Brunhes/Matuyama boundary, contains a predominantly warm-water foraminiferal fauna (e.g., *G. trilobus, G. ruber, S. dehiscens, P. obliquiloculata,* and *G. tumida*). Sample 126-791B-39R-CC is characterized by high percentages of cool-water taxa (dextral *G. pachyderma* complex, *G. bulloides, G. glutinata, G. crassaformis,* and *G. uvula*) deposited during a period henceforth termed the Matuyama *G. pachyderma* acme Zone 1. The estimated age of this event is about 780 ka, based on the paleomagnetic stratigraphy of Hole 791B. Sample 126-791B-45R-CC, deposited during the Jaramillo Event about 920 ka, contains warm-water species (e.g. *G. menardii, G. tumida, G. sacculifer, G. trilobus, S. dehiscens, P. obliquiloculata,* and *G. ruber*). Sample 126-791B-46R-CC contains mostly cool-water taxa characterized by the dominance of the *G. pachyderma* dextral complex and accompanied by *G. quinqueloba, G. glutinata,* and *G. falconensis*. The fauna was deposited during a period henceforth termed the Matuyama *G. pachyderma* acme Zone 2. The estimated age of this event is about 1 Ma, based on the paleomagnetic stratigraphy of Hole 791B and extrapolated sedimentation rates below the base of the Jaramillo event in Hole 791B. Sample 126-791B-47R-1, 41–43 cm, at the contact with the underlying basalt, contains both cool- and warm-water species such as dextral *G. pachyderma, G. falconensis, G. gomitulus, G. ruber, G. crassaformis, G. tumida, G. menardii, S. dehiscens, P. obliquiloculata,* and *G. ruber.* This sample is placed in lower Pleistocene Zone N22.

Benthic Foraminifers

Quaternary strata at Sites 790 and 791 may be subdivided biostratigraphically into six biozones based on benthic foraminifers (Fig. 44). Water mass depths are estimated mainly on the

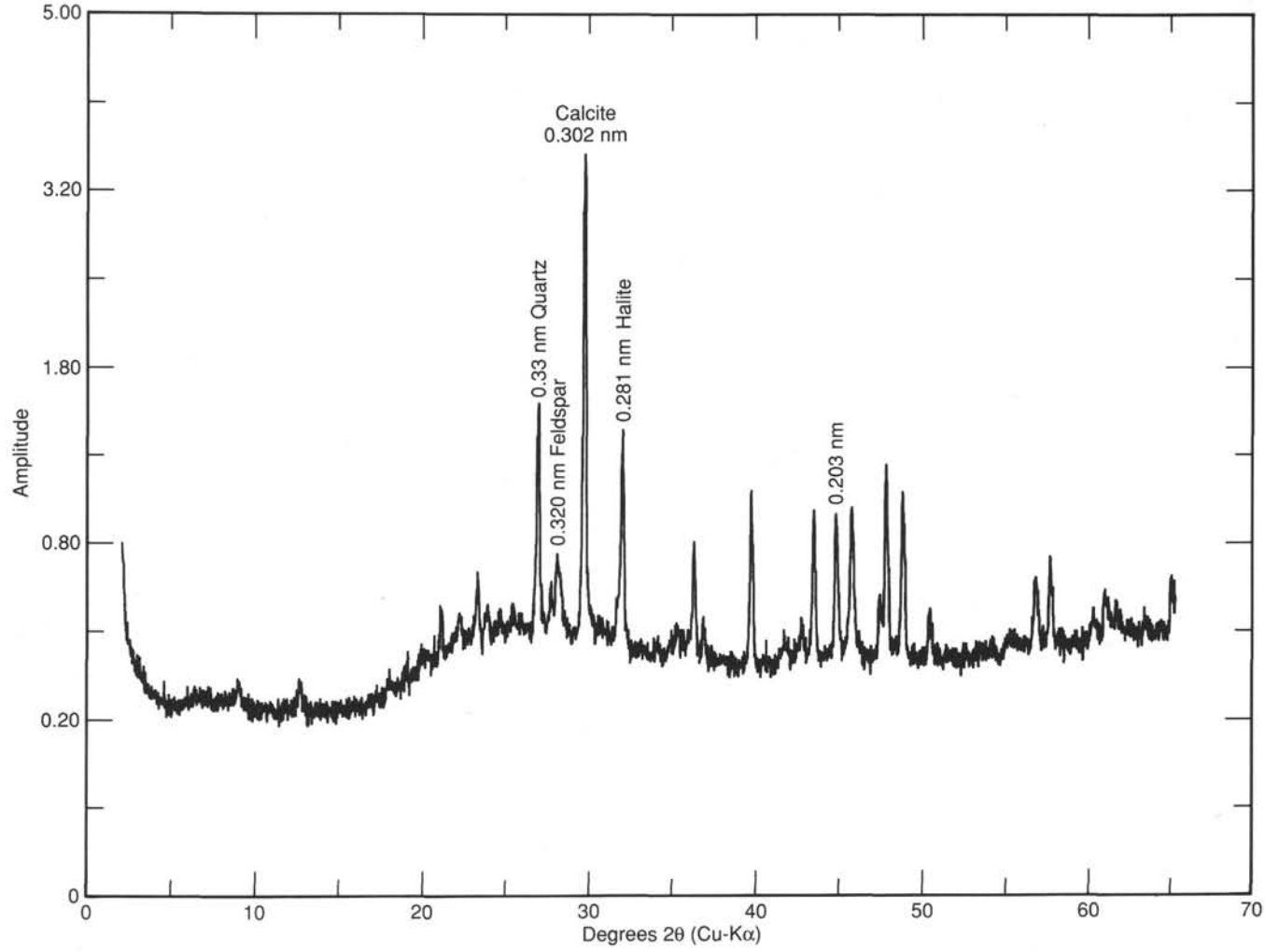

Figure 37. X-ray diffraction chart of brown vitric clayey silt (Sample 126-790B-1H-1, 5 cm) showing high calcite abundance, with quartz, feldspar, halite (from pore water), diaspore, and small amounts of clay minerals.

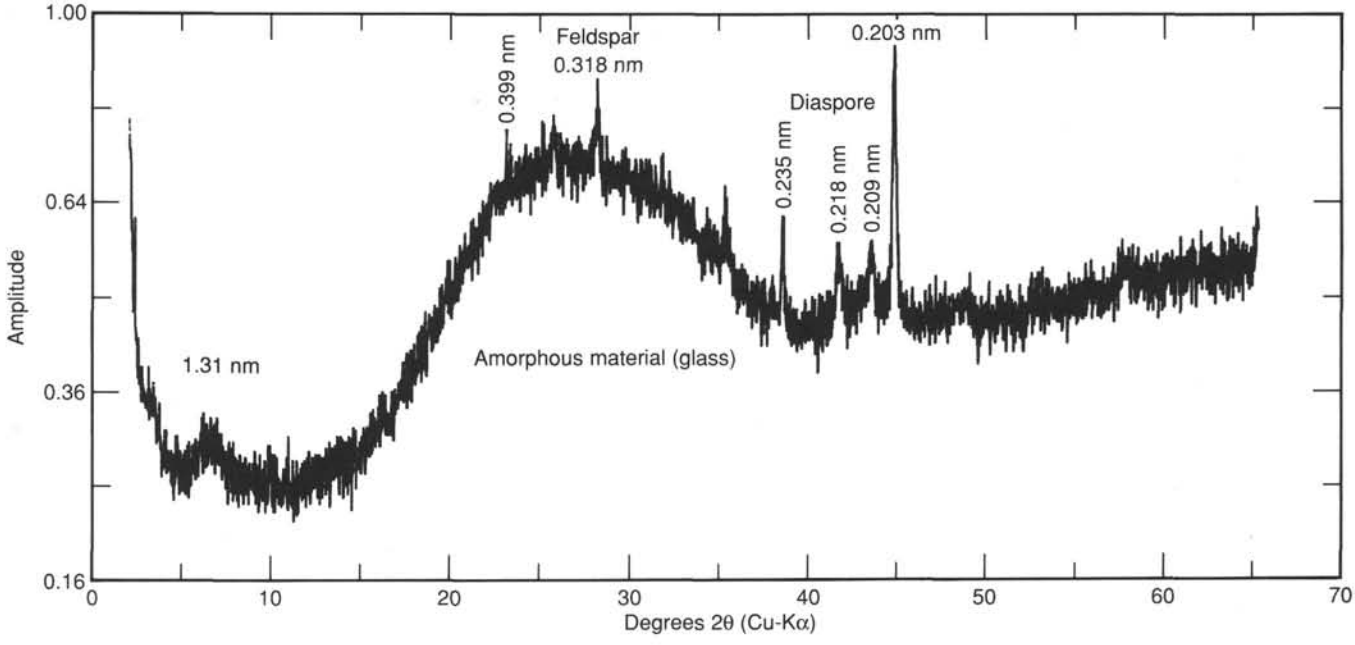

Figure 38. X-ray diffraction chart of handpicked green grains in clayey vitric silt (Sample 126-790A-1H-1, 1 cm), showing abundant amorphous material with traces of 1.31-nm minerals, feldspar, diaspore, and the unknown 0.203-nm mineral.

Table 8. X-ray diffraction data from Site 791.

Core, section, interval (cm)	Unit	Color	Sample description	Clay minerals			Minerals	Amorphous material
				1.4 nm	1.0-nm Mica	0.7-nm Chlorite		
126-791A-								
18-1, 40	I	N4	Silty clay	1.66 nm (smectite) 1.40 nm (chlorite)	—	—	Calcite > quartz > 0.209-nm > feldspar > diaspore	Abundant
18-2, 100	I	5Y4/1	Clayey silt	Present	Common	Present	Calcite > quartz > feldspar, 0.209 nm > diaspore	Abundant
19-7, 43	I	5Y5/2	Gravel-rich sand	Present	Trace	Present	Halite > quartz, feldspar, calcite > diaspore	Abundant
20H-2, 92	I	5Y6/1	Graded fine sand	Trace	—	—	Halite > quartz, feldspar, calcite > diaspore	Abundant
126-791B-								
9R-CC, 20	II	5Y2/1	Nannofossil-rich silty claystone	1.43 nm (chlorite)	Common	Common	Calcite > quartz > feldspar	Abundant
21R-CC, 8	II	5Y4/2	Claystone	1.40 nm (chlorite)	Common	Common	Calcite > quartz > feldspar	Abundant
22R-1, 10	II	5Y4/1	Claystone	Trace	Common	Common	Calcite > quartz > feldspar cristobalite	Abundant
22R-1, 30	II	5G4/1	Claystone	1.77 nm (smectite) 1.44 nm (chlorite)	Common	Common	Calcite > quartz > feldspar	Abundant
22R-1, 51	II	5G4/1	Claystone	1.71 nm (smectite) 1.43 nm (chlorite)	Common	Common	Quartz > calcite > feldspar, cristobalite	Abundant
22R-1, 53	II	5G2/1	Vitric clayey silt	Trace	Trace	Present	Pyrite > quartz > calcite, cristobalite > feldspar	Abundant
22R-1, 58	II	5G4/1	Vitric clayey silt	Trace	—	Present	Quartz > calcite > feldspar, cristobalite	Abundant
22R-1, 60	II	5G2/1	Vitric clayey silt	Trace	—	Present	Quartz > calcite, feldspar	Abundant
22R-1, 70	II	5G4/1	Vitric clayey silt	1.65 nm (smectite) 1.40 nm (chlorite)	Common	Common	Calcite > quartz ≫ feldspar, cristobalite	Abundant
25R-2, 18	II	5Y3/2	Pyrite grains	Trace	—	—	Pyrite ≫ troilite > calcite, quartz	Abundant
25R-2, 46	II	5Y3/2	Pyrite grains	—	—	—	Pyrite ⋙ calcite > quartz	Abundant
42R-3, 70	II	5Y6/1	Nannofossil silty claystone	Trace	Trace	—	Calcite ⋙ quartz, feldspar	Abundant
47R-1, 43	II	5GY6/1	Nannofossil-foraminifer claystone	Trace	—	Trace	Calcite ⋙ alunite, quartz, feldspar > cristobalite	Abundant

basis of benthic foraminiferal data from Shizuoka and Shikoku, southwest Japan (Akimoto, 1989; Yasuda, 1989).

These six biozones are as follows:

1. *Pleurostomella* spp.–*Stilostomella* spp. assemblage zone

Definition: This assemblage zone is marked by the joint occurrence of *Pleurostomella* spp. and *Stilostomella* spp.

Characteristic species: *Uvigerina hispidocostata, Oridorsalis umbonatus, Cibicidoides wellerstorfi, Stilostomella* spp., *Melonis barleeanus, Melonis pompilioides, Pullenia bulloides,* and *Pleurostomella* spp.

Samples: 126-790C-20X-CC through 126-790C-18X-CC, and 126-791B-47R-1, 41–43 cm, through 126-791B-37R-CC

Depositional water depth: 2000–3500 mbsl

Dissolved oxygen: high

Environment: deep open ocean, or basin with open-ocean access

2. *Bulimina aculeata* assemblage zone

Definition: This zone corresponds to an interval from the LO of *Pleurostomella* spp. to the base of the acme zone of *Uvigerina proboscidea.*

Characteristic species: *U. hispidocostata, Bulimina aculeata, O. umbonatus,* and *M. barleeanus*

Samples: 126-790C-17X-CC and 126-791B-36R-CC

Original water-mass depth (this depth may be the depth of a sill surrounding the basin): 1600–2300 mbsl

Dissolved oxygen: medium to high

Event: slight shallowing or closing of the basin started

3. *Uvigerina proboscidea* acme zone

Definition: This zone corresponds to the acme zone of *Uvigerina proboscidea.*

Characteristic species: *Hoeglundina elegans, U. proboscidea, Bulimina striata, B. aculeata, M. barleeanus, M. pompilioides, P. bulloides, Sphaeroidina bulloides,* and *O. umbonatus*

Samples: 126-790C-15X-CC through 126-790C-13X-3, 104–106 cm, and 126-791B-35R-CC through 126-791B-25R-CC

Original water-mass depth (this depth may be the depth of a sill surrounding the basin): 1000–1800 mbsl

Dissolved oxygen: low-medium to partly low. Low oxygen in Samples 126-790C-14X-2, 61–63 cm, 126-790C-13X-CC, 126-791B-29R-CC, and 126-791B-28R-CC because of the occurrence of *Globobulimina pacifica* and low ratios of aerobic forms

Event: closing of the basin probably occurred and dissolved oxygen decreased in this basin. A shallower fauna entered into this basin and faunal change occurred

4. *Bulimina striata–Bulimina aculeata* assemblage zone

Definition: This zone represents a body of strata characterized by the joint occurrence of *B. striata* and *B. aculeata*

Characteristic species: *U. hispidocostata, H. elegans, B. aculeata, B. striata, O. umbonatus, M. barleeanus,* and *M. pompilioides*

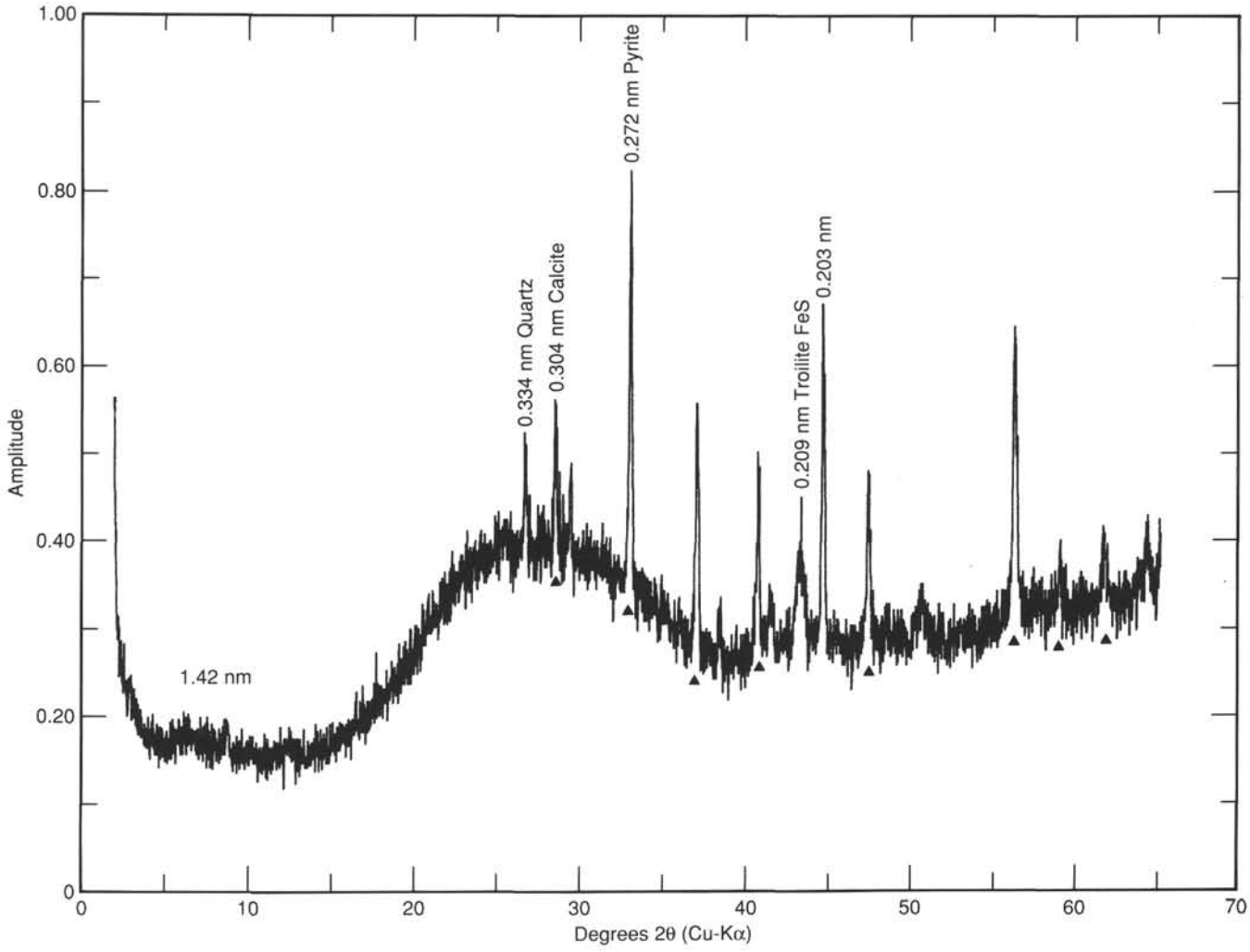

Figure 39. X-ray diffraction analysis of handpicked pyrite grains from Sample 126-791B-25R-2, 18 cm (nannofossil-rich silty claystone) showing pyrite (filled triangle) and troilite with traces of quartz, calcite, and 1.42-nm clay minerals.

Samples: 126-790C-12X-CC through 126-790B-10H-CC, and 126-791B-24R-CC through 126-791A-38X-CC

Original water-mass depth: 1000–1800 mbsl

Dissolved oxygen: medium

Event: closed environment still continued but dissolved oxygen increased

5. *Bulimina aculeata–Uvigerina hispidocostata* assemblage zone

Definition: The present zone represents a body of strata characterized by the joint occurrence of *B. aculeata* and *U. hispidocostata.*

Characteristic species: *U. hispidocostata, M. barleeanus, O. umbonatus, B. aculeata, P. bulloides, Pyrgo murrhina,* and *Tosaia hanzawai*

Samples: 126-790B-8H-6, 29–31 cm, through 126-790B-7H-CC, and 126-791A-33X-1, 6–8 cm, through 126-791A-16H-6, 58–60 cm

Original water-mass depth: 1600–2300 mbsl

Dissolved oxygen: medium

Event: sill depth probably deepened. Thick volcanic ash was deposited above the present zone and faunal change occurred.

6. *Chilostomella oolina–Uvigerina hispidocostata* assemblage zone

Definition: The zonal base is defined by a rapid increase in the abundance of *Chilostomella oolina.*

Characteristic species: *Chilostomella oolina, U. hispidocostata, M. barleeanus,* and *Globobulimina pacifica*

Samples: 126-790B-3H-1, 0–2 cm, through 126-790A-1H-1, 7–9 cm, 126-791A-5H-3, 52–54 cm, and 126-791A-4H-3, 60–62 cm

Original water-mass depth: 1600–2300 mbsl

Dissolved oxygen: low-medium to partly low. Low oxygen in Samples 126-790A-2H-3, 98–100 cm, 126-790A-2H-1, 129–131 cm, 126-791A-5H-3, 52–54 cm, and 126-791A-4H-3, 60–62 cm, because of occurrences of *C. oolina* and *G. pacifica* and the low ratios of aerobic forms.

Event: anaerobic fauna increased

A deep, open-ocean benthic foraminiferal fauna (>2000 mbsl) was distributed in this area between 1.0 and 0.7 Ma. The appearance of the low-to-medium-oxygen shallower fauna (1000–2000 mbsl) between 0.7 to 0.5 Ma implies that a closing of the basin may have started at this time, while dissolved oxygen decreased. After a part of the deep, open ocean fauna became extinct, a shallower fauna entered into the basin and the low-to-medium-oxygen fauna survived. The slight change of the fauna at 0.4 Ma indicates that dissolved oxygen increased slightly. The minor change to a deeper fauna at 0.2 to 0.1 may imply a slight

Table 9. Biostratigraphic, paleomagnetic, and other correlatable horizons used to construct the age-depth curve in Figure 40.

Chronostratigraphic event	Core, section, interval (cm)	Depth (mbsf)	Age (Ma)
Nannofossils:			
	Hole 790C		
FO *E. huxleyi*	11X-CC to 12X-CC	181.6–193.9	0.275
LO *A. angelinum*	14X-CC to 15X-CC	207.3–222.8	0.410
LO *P. lacunosa*	15X-CC to 19X-1, 40	213.6–224.6	0.460
Reticulofenestra sp. A	18X-CC to 19X-1, 40	248.5–253.3	0.830
	Hole 791B		
FO *E. huxleyi*	13R-CC to 15R-CC	504.9–531.0	0.275
LO *A. angelinum*	23R-CC to 24R-CC	604.1–618.1	0.410
LO *P. lacunosa*	28R-CC to 29R-CC	652.5–666.0	0.460
Reticulofenestra sp. A	41R-3 to 41R-CC	774.7–781.3	0.830
Paleomagnetics:			
	Hole 790C		
Blake	Between 2H-6 and 2H-7	103.5	0.108
Brunhes/Matuyama	Between 17X-CC and 18X-1	241.7–245.3	0.730
Top of Jaramillo	Between 19X-3 and 19X-4	256.2–257.4	0.910
Bottom of Jaramillo	Between 19X-6 and 20X-1	260.0–265.9	0.980
	Hole 791B		
Brunhes/Matuyama	38R-4, 40	747.8–752.2	0.730
Top of Jaramillo	Between 43R-CC and 44R-1	792.6–807.5	0.910
Bottom of Jaramillo	46R-1, 80	820.8–827.6	0.980
Other:			
Ash bed 126-790C-1H-2, 132–135 126-790B-10H-5, 22–24	22H-6, 55–60	205.0	0.091

Note: See text for discussion of ash-bed correlation.

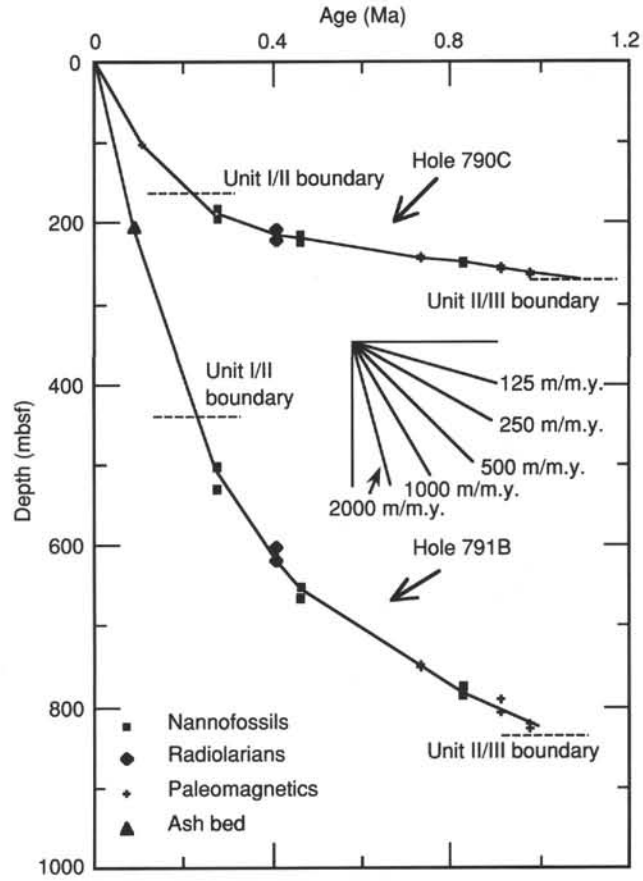

Figure 40. Age-depth curves for Sites 790 and 791. See text and Table 9 for details of the chronostratigraphic horizons. Two points at any given event (age) indicate the possible depth range for the event.

deepening of the sill water depth. After a thick pile of volcanic ash was deposited at about 0.06 Ma, a low-oxygen fauna occupied the basin.

Radiolarians

Well-preserved radiolarians are present in many samples and indicate a late Pliocene to Recent age for the sediments cored at Sites 790/791. The abundance of radiolarians is variable, and they are often diluted by volcanic ash. Preservation is generally good. A diverse radiolarian assemblage that includes *Didymocyrtis tetrathalamus, Lamprocyclas maritalis maritalis, Theocorythium trachelium dianae, Stylochlamydium asteriscus, Botryostrobus aurita/australis* group, *Porodiscus* sp., *Amphirhopalum ypsilon, Eucyrtidium* spp., *Tetrapyle octacantha,* and *Spongaster tetras* are found in samples throughout all of the holes drilled at Sites 790/791. The common occurrence of *T. trachelium dianae* indicates a late Pliocene age, at the oldest.

Specimens of *Druppatractus acquilonius* are present in Sample 126-790C-12X-CC and in samples below this level. This species is also observed at Site 791 in and below Sample 126-791B-17R-CC. The occurrence of *D. acquilonius* indicates an age greater than 0.3 Ma (Foreman, 1981) for samples deeper than 184.2 mbsf at Site 790 and more than 540.9 mbsf at Site 791. Specimens of *Axoprunum angelinum* are present in Sample 126-790C-15X-CC. This species is first observed downhole at Site 791 in Sample 126-791B-24R-CC. The LO of *A. angelinum* was dated at 0.41 Ma (Foreman, 1981), and its presence indicates an age greater than this for samples below 213.2 mbsf at Site 790 and below 608.4 mbsf at Site 791. More precise dating using radiolarians was not possible as published upper Quaternary zonations are based on the occurrence of rare equatorial forms (Sanfilippo et al., 1985), which were not observed at Sites 790 and 791.

Summary

A summary of biostratigraphic and benthic foraminifer results for Sites 790 and 791 is presented in Figures 44, 45, and 46. Hole 790C ends at about 1.1 Ma, whereas the bottom sediments of Hole 791B are estimated to have an age of 1 Ma on the basis of the extrapolated sedimentation rates (Fig. 40).

Calcareous nannofossils are generally common to abundant in the samples studied. Three nannofossil datums are identified: the FO of *Emiliania huxleyi* (0.275 Ma), the LO of *Pseudoemiliania lacunosa* (0.46 Ma), and the LO of the acme of *Reticulofenestra* sp. A (0.83 Ma).

The abundance of planktonic foraminifers in the Pleistocene and Holocene sediments ranges from rare to very abundant, and their preservation ranges from poor to excellent. Based on preliminary data, three planktonic foraminiferal datum levels are recognized. In an upward sequence these are (1) the Matuyama *Globigerina pachyderma* acme II zone, about 1 Ma, marking the first major late Neogene global cold event; (2) the Matuyama *G. pachyderma* acme I zone, deposited about 780 ka; and (3) the *Globigerina calida–Globigerina digitata* Zone (Blow, 1969; N23) ranging between the Holocene and the base of the Brunhes Epoch (Blow, 1969: Berggren et al., 1985). Confirmation of these correlations must await additional faunal data as well as stable isotope analyses and absolute age determination.

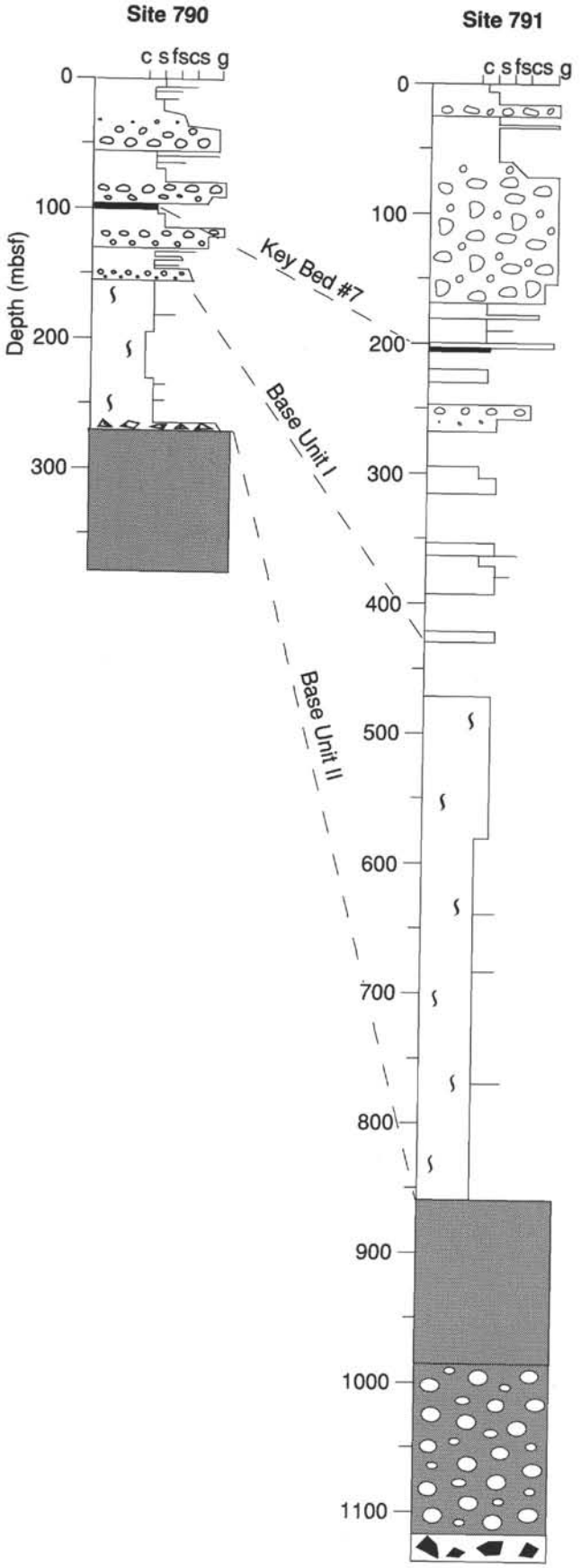

Figure 41. Detailed correlation between stratigraphic summary sections for Sites 790 (Fig. 9) and 791 (Fig. 27).

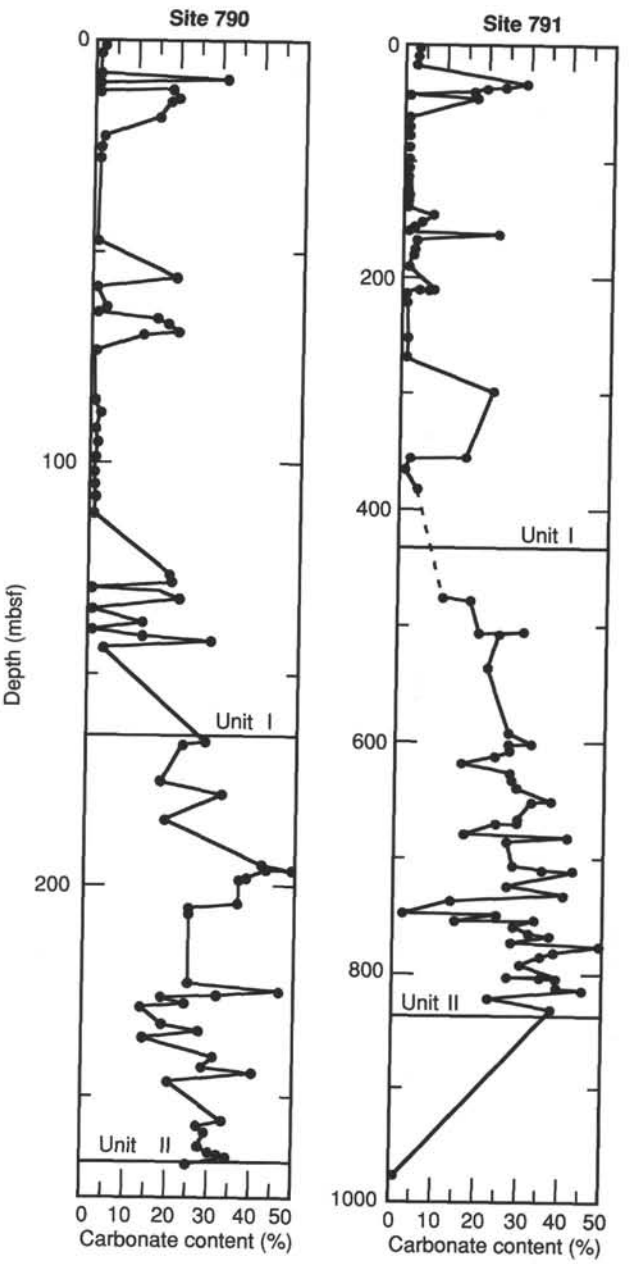

Figure 42. Downhole plots of carbonate content for Sites 790 and 791. Note that the depth scale is different in each plot.

Radiolarians are generally common to abundant in the examined samples except when diluted by volcanic ash. Preservation is typically moderate to good. Two radiolarian datums are recognized: the last appearance of *Druppatractus acquilonius* at 300 ka and the last appearance of *Axoprunum angelinum* at 410 ka (Foreman, 1981). Diatoms and silicoflagellates are also common in many samples.

The benthic foraminifer fauna indicates that a deep ocean (>2000 m) or a basin with open-ocean access existed between 1.0 and 0.7 Ma. The appearance of a low-to-medium-oxygen shallower fauna (1000–2000 mbsl) between 0.7 and 0.5 Ma implies that the basin may have started closing at this time and is continuing to close at present.

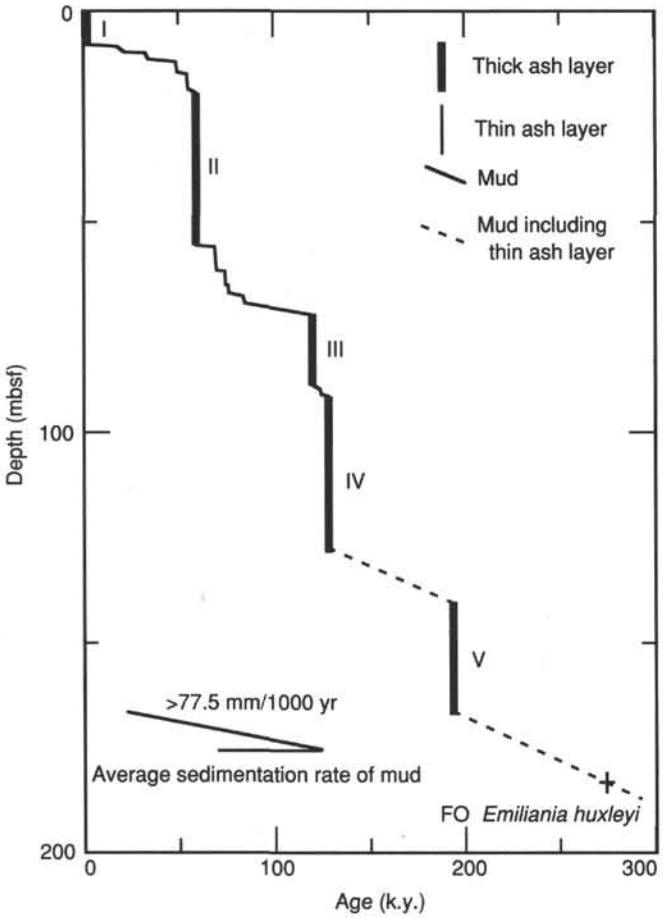

Figure 43. Plot of age vs. depth for Unit I sediments recovered at Holes 790B and 790C, illustrating the periodicity of explosive pumice eruptions as recorded by five thick pumiceous beds (I–V). Eruption and deposition of pumice is treated as an instantaneous event.

PALEOMAGNETICS

Introduction

Paleomagnetic measurements were carried out on all archive halves of cores from Sites 790 and 791 that were not composed only of unconsolidated gravel or coarse sand or were not highly disturbed by drilling, or where the segments of recovered sample were long enough not to have rotated vertically during drilling. For cores that contained igneous rocks, only longer segments were measured after transfer to separate fiberglass boats, to eliminate the signals from short segments that may have rotated vertically. Alternating field (AF) demagnetization levels were adjusted according to the expected magnetic hardness of the various sampled sediment types, as coarser-grained intervals generally were less resistant to AF demagnetization.

In addition to the pass-through core measurements on the cryogenic magnetometer, a large number of discrete samples were measured with the fully automatic spinner (FAS) magnetometer (see "Explanatory Notes" chapter, this volume). The discrete samples were taken at specific zones of interest as well as at regular intervals to serve as a backup and check of the continuous core measurements. The use of AF values >15 mT was often essential in determining the true polarity of the primary remanence, and the stable "end point" direction of magnetization that characterizes the field direction at the time of primary remanence acquisition.

Magnetostratigraphy

Holes 790A and 790B

Magnetostratigraphic determinations on cores from these two holes were severely hampered by large ambient fields (up to thousands of gammas) in the region of the AF demagnetization coils within the cryogenic magnetometer shield assembly. We realized that an apparent polarity reversal in Core 126-790A-4H, and the large number of apparent polarity reversals in the first 11 cores of Hole 790B were inconsistent with the late Pleistocene nannofossil assemblages present throughout this interval (see "Biostratigraphy" section, this chapter).

We then noted that the reversed zones of magnetization generally corresponded to the coarse-grained (i.e., magnetically "soft") sediment types, and that the negative inclinations had appeared only after AF demagnetizations of the cores. Subsequently, a number of discrete samples from the apparent reversed intervals were measured and demagnetized on the spinner magnetometers and the Schonstedt sample demagnetizer, and they retained their positive inclinations throughout the demagnetization process.

Measurement of the ambient field in the region of the cryogenic system's AF coils with the Applied Physics Systems APS 520 fluxgate magnetometer revealed that the strong ambient field was directed upcore. Therefore, reversed inclinations in the coarse sediment types most likely resulted from the acquisition of an anhysteretic remanent magnetization (ARM). From this point on, the mu-metal shielding that surrounds the cryogenic measuring system was periodically demagnetized with degaussing coils already built into the shielding. With repetitive degaussing the field level in the AF coil region was reduced to <100 gammas; however, frequent monitoring of the field indicated that fields of >1000 gammas could build up in a period of several hours.

The cause of the instabilities in the mu-metal shielding is currently unknown. It may have been the result of metal degradation from heat generated by the AF coils, or from exposure to cold helium during instrument filling. The consistent magnetostratigraphic results obtained for Hole 787B indicated that a substantial ambient field was not present during measurement and demagnetization at that location. This may have been a fortuitous circumstance, as the shielding was not disassembled or in any other way disturbed between drilling at Site 787 and at the following sites.

Hole 790C

The first 17 cores from this hole were magnetized mostly in a normal sense, even after AF demagnetization. A short reversed-polarity interval revealed after AF demagnetization in Section 126-790C-2H-7 (~104 mbsf) may represent the Blake Event (~0.108 Ma), which has been recorded in sediments from Japan and the Pacific, including the Marianas region (C. Helsley, pers. comm., 1989). Another short reversed-polarity interval was recorded in Section 126-790C-13X-4 (198.5 mbsf), possibly corresponding to the Biwa II excursion, which has been recorded in deposits from Lake Biwa, Japan, dating to 0.295 Ma (Tarling, 1983).

The first major reversed-polarity zone occurred at the very bottom of Sections 126-790C-17X-7 and 126-790C-17X-CC (241.8 mbsf) and continued into Core 126-790C-19X (Fig. 47). Although the continuous core measurements did not reveal a consistent polarity for Sections 126-790C-19X-1 and 126-790C-19X-3 even after AF demagnetization to 15 mT, measurements on discrete samples indicated that a reversed polarity characterizes these sections (Table 10).

The measurement of Section 126-790C-19X-4 (~256–258 mbsf) was hampered by the extreme variation of remanence in-

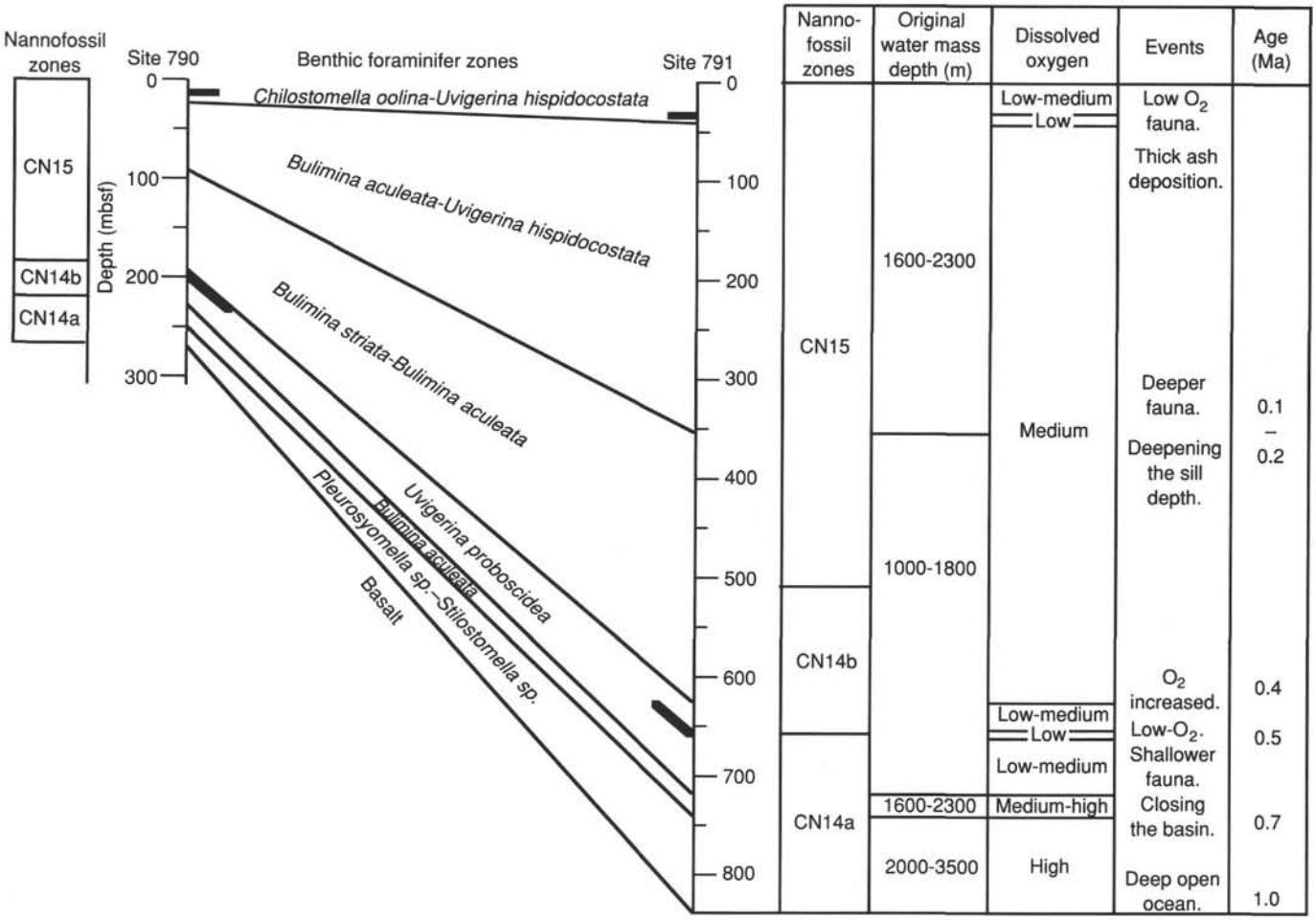

Figure 44. Quaternary benthic foraminiferal biozones at Sites 790 and 791.

tensity in the section, with the signal from the bottom of the section (pumiceous gravel) exceeding the range of the cryogenic magnetometer. However, measurements on a discrete clay sample (126-790C-19X-4, 52 cm) from above the gravel bed (Table 10) confirmed that this section marked a return to normal polarity. Positive inclinations also characterized Sections 126-790C-19X-5 and 126-790C-19X-6, whereas reversed inclinations returned at the bottom of Core 126-790C-19X (261.4 mbsf; Fig. 47).

Although the bottom sections of Core 126-790C-20X (beginning at about 263.5 mbsf) exhibited predominantly positive inclinations when measured on the cryogenic pass-through system (Fig. 47), higher AF demagnetizations of discrete samples taken from this same pumiceous interval revealed an underlying reversed primary magnetization (Table 10).

Because the paleontology indicated only Quaternary faunal assemblages in the above cores (see "Biostratigraphy" section, this chapter), we identified the polarity transition recorded at the bottom of Core 126-790C-17X as the Brunhes/Matuyama boundary (0.73 Ma), and the subsequent short normal-polarity zone at 256.2–261.4 mbsf as the Jaramillo interval (0.91–0.98 Ma). The base of the sedimentary section in this hole corresponds to an age of ~1.1 Ma, based on extrapolation of the age-depth curve (see Fig. 40 in "Lithostratigraphy and Accumulation Rates" section, this chapter).

Holes 791A and 791B

Magnetostratigraphic results from Hole 791A were inconsistent, apparently because of the unconsolidated and soupy nature of the sediments. Although the more consolidated sections generally indicated normal polarities, as expected for upper Quaternary sediments, many of the less-coherent sections displayed a highly inclined reversed magnetization before and after AF demagnetization. The almost vertical nature of their remanence implies that it was acquired during drilling, probably in the field associated with the drill string.

Fortunately, the magnetic signal associated with the cores from Hole 791B, which began recovery just below the bottom depth of Hole 791A, seemed more representative of the predrilling remanence signal in the sediments. This probably resulted from the more lithified nature of these deeper strata. Cores 126-791B-10R through -38R were consistently magnetized in a normal sense. A sharp transition to reversed polarity, revealed only after AF demagnetization, took place near the bottom of Section 126-791B-38R-4 (747.8 mbsf; Fig. 48B), and the reversed polarities continued from this point until the top of Core 126-791B-44R, where another normal polarity zone began at 800.7 mbsf. The normal polarities persisted over this and the following core and ended at the base of Section 126-791B-46R-1 (820.9 mbsf; Fig. 48C).

The next sedimentary and igneous cores that were measured were reversely magnetized for the most part or trended toward reversed polarity with AF demagnetization (e.g., Core 126-791B-47R at ~830 mbsf). Cores 126-791B-72R, -73R, -75R, and -76R (from ~1070 to ~1110 mbsf) consisted of basaltic "mousse" (see "Igneous Petrology" section, this chapter) and displayed indeterminate polarities. Subsequent measurements on discrete samples taken from the "mousse" indicate wide variations in in-

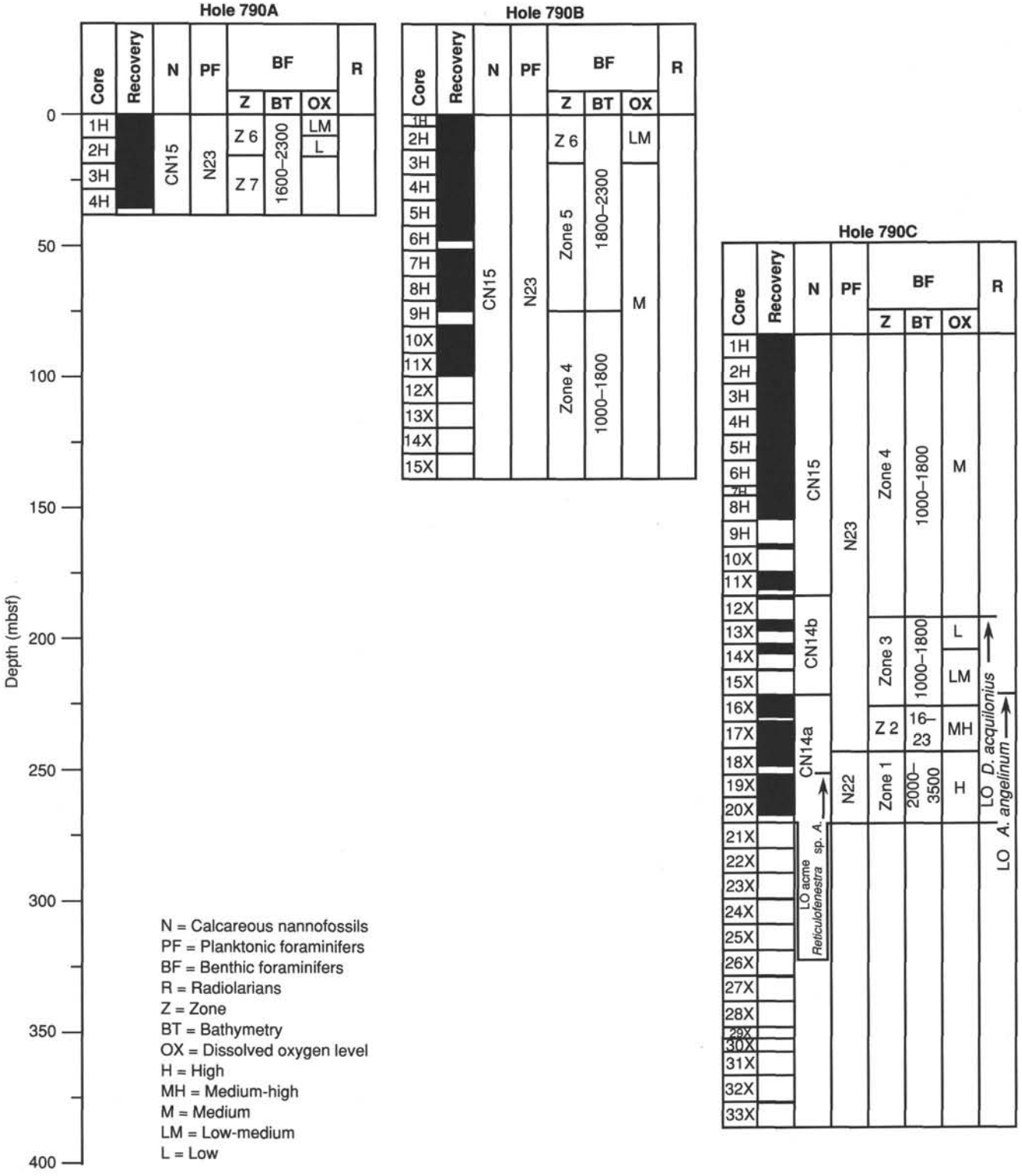

Figure 45. Biostratigraphic summary chart for Site 790.

clination, implying that separate cooling units of the mousse moved with respect to each other after welding.

The next two cores also had indeterminate polarities and contained tuff, basalt, and diabase intruded by gypsum veins (see "Igneous Petrology" section, this chapter). However, the final core obtained from the hole (Core 126-791B-79X; 1137.6–1145 mbsf), which consisted of lapilli tuff and diabase, could again be characterized as reversely magnetized (Fig. 48D).

As with Hole 790C, the restriction of the fossil assemblages in the sedimentary portions of this hole to the Quaternary allows us to label with confidence the transition in Core 126-791B-38R as the Brunhes/Matuyama boundary, with the following short normal-polarity interval corresponding to the Jaramillo zone. By extrapolation of the age-depth curve (see Fig. 40 in "Lithostratigraphy and Accumulation Rates" section, this chapter), the initiation of sediment accumulation began at 1

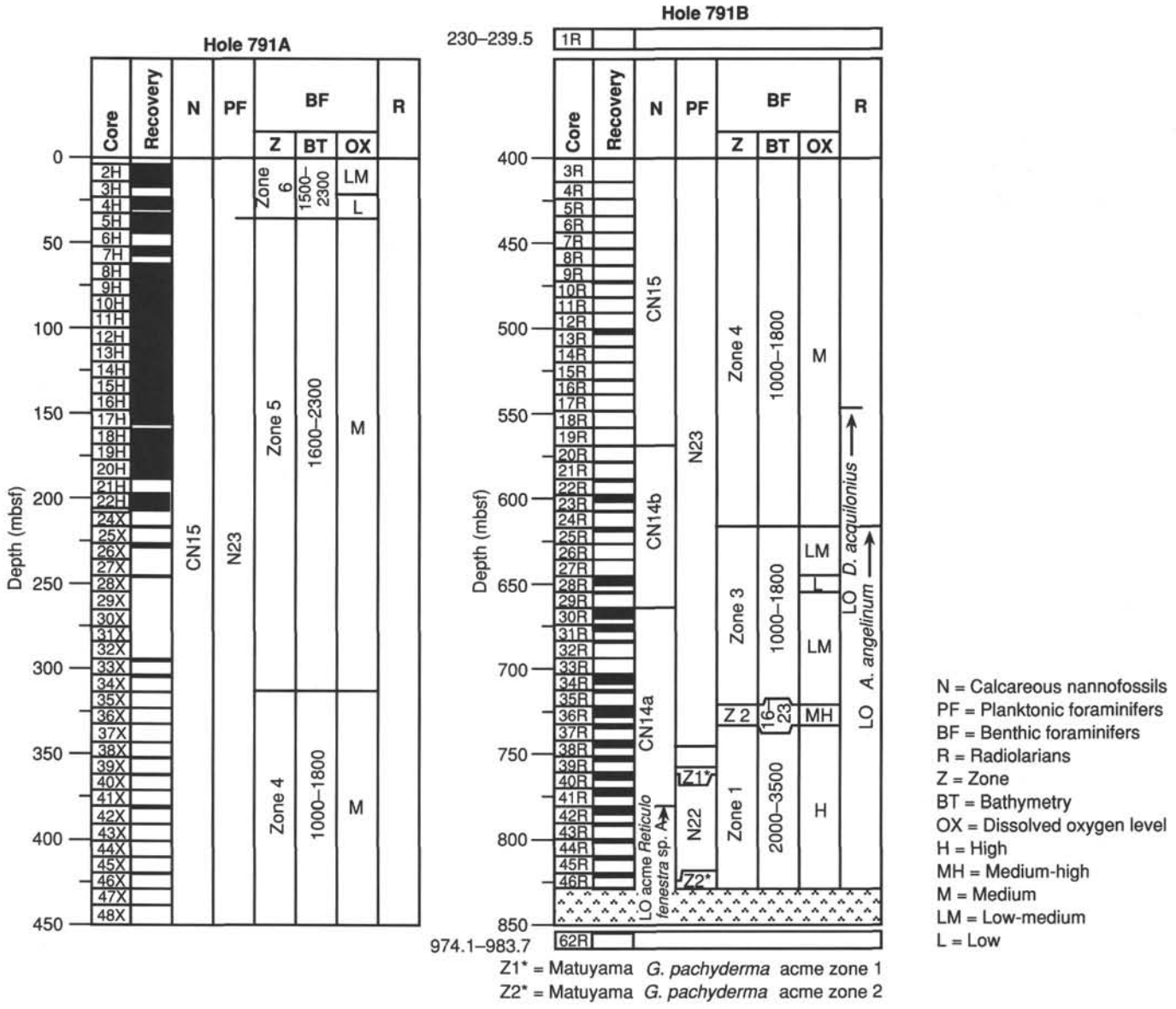

Figure 46. Biostratigraphic summary chart for Site 791.

Ma, implying that the sediment recovered from the bottom of Hole 790C was ~0.1 Ma older than that recovered above the igneous units in Hole 791B.

The higher sedimentation rate at Site 791 compared with Site 790 is illustrated by the length of the normal polarity zone identified as the Jaramillo and the overlying reversed (Matuyama) zone, which in Hole 791B occupies more than seven cores, compared with only two cores in Hole 790C (Fig. 49). This indicates a sedimentation rate increase by almost a factor of 4 (344 vs. 90 m/Ma) between the bottom portions of Hole 791B and 790C (see Fig. 40 in "Lithostratigraphy and Accumulation Rates" section, this chapter).

Brunhes/Matuyama Reversal Record

In Holes 790C and 791B, sedimentary sections containing the Brunhes/Matuyama polarity transition were recovered from nannofossil-rich clayey silt and claystone, respectively. Despite the high sedimentation rates for Hole 791B, the observed change from negative to positive inclination is very sharp, occurring over an interval of only a few centimeters. A pronounced decrease in remanence intensity that accompanies the reversal spans only about 20 cm (Fig. 50).

If the average sedimentation rate is applied to these intervals, then the change from positive to negative inclination occurred in perhaps as little as 100 yr, with the pronounced demise of dipole intensity limited to ~600 yr. However, the ~35% recovery rate in Hole 791B for the interval between the Brunhes/Matuyama reversal and the bottom of the Jaramillo zone could mean that the actual sedimentation rate across the reversal was up to one third lower than the average rate, or ~100 m/Ma, if the unrecovered portions of these cores consisted entirely of rapidly deposited pumice and volcanic ash. However, in Hole 790C, ~75% recovery was achieved in the same stratigraphic interval with only minor recovery of rapidly deposited pumiceous gravel (see "Lithostratigraphy and Accumulation Rates" section, this chapter).

Continuous pass-through measurements on the archive core halves that record the reversal were supplemented by extensive sampling across the reversal as well as in the sections of core immediately beneath the boundary. Although the ~100% recov-

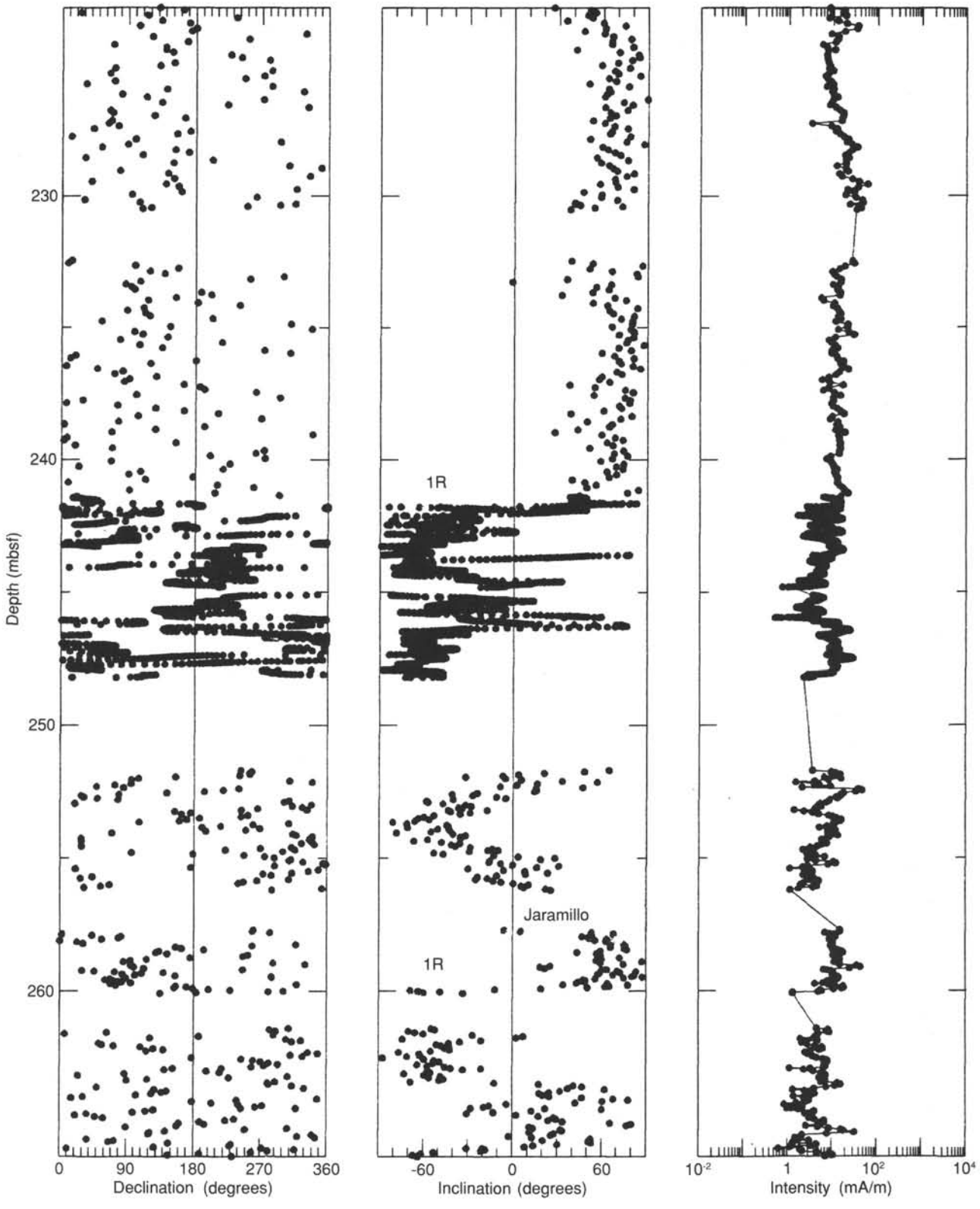

Figure 47. Paleomagnetic results vs. depth (mbsf) for Cores 126-790C-16X through -20X, after maximum AF demagnetization. Identifications of polarity chrons are indicated above inclination polarity changes.

Table 10. Remanence properties, before and after 35-mT AF demagnetization, of selected discrete samples from Hole 790C.

Core, section, interval (cm)	NRM ($\times 10^{-3}$ mA/m)	Inclination (degrees)	AF(35 mT) ($\times 10^{-3}$ mA/m)	Inclination (degrees)
126-790C-				
19X-1, 12	4.8	−31	4.4	−32
19X-1, 64	4.5	−16	3.4	−34
19X-1, 104	18.3	−67	16.4	−73
19X-3, 25	14.1	−37	4.2	−48
19X-3, 83	3.3	+18	0.4	−57
19X-4, 52	5.9	+83	1.5	+60
20X-3, 75	3.7	+44	1.7	−36
20X-3, 133	5.0	+24	0.8	−6

ery in Core 126-790C-17X indicates a near-continuous record of the magnetic field before and after the reversal, 55% recovery in Core 126-791B-38R leaves open the possibility of a significant hiatus in the magnetic record before and/or after the transition. However, in this case, recovery in the immediate vicinity of the reversal seems to be complete, with no severe drilling disturbance, except for horizontal rotation of drilling biscuits (Fig. 51).

In general, AF demagnetization of discrete samples taken near the reversal boundary revealed a high degree of directional stability after the removal of a soft normal component of magnetization at the lowest demagnetization step (Fig. 52). This indicates that an accurate representation of the behavior of the magnetic field can be obtained from these sediments around the time of the polarity transition.

Although the cores from these holes were not oriented by azimuth, the high dips (20°–45°) of the vitric silt beds near the reversal plane in Hole 791B, combined with the easterly dip directions apparent from the seismic profiles at shallower depths (see Fig. 7 in "Seismic Stratigraphy" section, this chapter), allowed for estimates of true declinations for discrete samples taken near to highly dipping laminations (Fig. 51B). Figure 53 shows the migration of the field vector derived in this manner for the polarity transition recorded in Core 126-791B-38R-4. These data indicate a far-sided pole path for the reversal.

For both holes, the core catcher is present just below the sections that include the polarity transition. The core catchers for each hole record a brief reverse-normal-reverse polarity event preceding the final reverse to normal transition (Fig. 50). Given the average sedimentation rate, the complete sequence of reversals appears to have taken place over a >1,000-yr period. Okada and Niitsuma (1989), in an examination of rapidly deposited sediments on the Boso Peninsula, Japan, which also record the Brunhes/Matuyama boundary, have found evidence for rapid, multiple reversals of inclination associated with a longer-term polarity transition.

IGNEOUS PETROLOGY

Highly vesicular, sparsely phyric volcanic rocks were drilled at the base of two sites in the Sumisu Rift. At Site 790, these rocks lay 256.9–387 mbsf below sediment estimated to be 1.1 Ma in age (see "Lithostratigraphy and Accumulation Rates" section, this chapter). Only 1.03 m of scoriaceous basalt was recovered, all in core catchers (Fig. 54). At Site 791, the volcanic rocks are similar in composition to those at Site 790 but were found much deeper (834–1145 mbsf). Altogether, 27.83 m (8.9% recovery) of basalt lava, basalt "mousse" (see below), diabase, and felsic crystal-lithic tuffs were recovered below sediments also estimated to be 1.1 Ma in age (Fig. 55).

Alteration increases downsection from fresh to zeolite or lower greenschist facies. Below about 1110 mbsf all rocks have been sheared, hydrothermally altered, and metamorphed. Consequently, it is unclear if the metamorphism is a result of greater burial or hydrothermal alteration. The transition in metamorphic grade is gradual and begins within basalt units interpreted as syn-rift in origin rather than as arc basement, based on their petrography and chemical composition. The ubiquitous and extensive vesiculation of these basalts, despite an inferred deep-water site of eruption (see "Biostratigraphy" section, this chapter), is attributed to high, pre-eruption water contents. The origin of the volcaniclastic felsic rocks at the base of the hole is rendered ambiguous by their alteration, but they are more similar in texture and some immobile trace elements to rocks from the arc than from the rift. Whether they were deposited on the arc before rifting or within the basin during rifting is not constrained by petrology.

At Site 791, the volcanic rocks lie immediately beneath lithologic Unit II (Section 126-791B-62R-1, 18 cm). No contact was recovered, but the overlying sediments are nonvolcanogenic (see "Lithostratigraphy and Accumulation Rates" section, this chapter). The underlying rocks were divided on the basis of macroscopic texture and mineralogy into 29 units: 7 basalt flows, 2 basalt breccias, 3 units of enigmatic frothy basalt that we called "basaltic mousse" in a fit of gastronomic deprivation, 7 diabase intrusives, 7 units of intermediate to felsic ash to lapilli tuffs, 1 unit of interlava sediment, and 2 units of fault gouge (Fig. 55). Chemical analyses show that the basalt flows are of two types (see "Igneous Geochemistry" section, this chapter), the more differentiated (Unit 2) above the more mafic (Units 3, 5, and 7). The three basaltic mousse units (Units 11, 12, and 14) constitute the thickest deposit encountered, spanning 135 m (from 980 mbsf in Core 126-791B-62R to 1115 mbsf in Section 126-791B-76R-2), and may represent one lava type and perhaps one eruption event. The diabase intrusions are variable in mineralogy and composition, ranging from olivine-rich and as mafic as any basalt at this site (Units 15 and 23) to Fe-Ti-oxide-rich and more differentiated than any basalt at this site (Units 4 and 29).

The ash and lapilli tuffs at the base of Hole 791B (Units 16, 18–22, and 28) are interpreted as a sequence of hot pyroclastic flows. With the exception of Units 16 and 22, all of the tuffs exhibit strong flattening of pumice shards and development of eutaxitic texture. Even the coarsest lapilli tuffs, with lava clasts up to 30 mm, contain pronounced fiamme. The pyroclastic sequence as a whole contains clasts of andesite, which, combined with the evidence of coarse-grained lapilli tuffs and hot eruptions, indicates that it was produced in close proximity to the volcanic source. In light of the apparent propinquity of hot ash flows to calderas, it could be concluded that the felsic sequence is a manifestation of arc volcanism. Hence, the sequence may represent pre-rift arc-basement to the Sumisu Rift system. However, the effects of alteration on texture, mineralogy, and bulk composition, render this conclusion speculative. Unit 20, a crystal-lithic ash tuff, also shows the development of a weak metamorphic fabric. This runs at an angle of approximately 45° to the eutaxitic fabric and can only be recognized as an alignment of chlorite fibers in cross-polarized light.

The age range of the basement rocks is unknown, but all cores are reversely magnetized except for the gypsum-filled veins, which are normally magnetized (see "Paleomagnetism" section, this chapter). The similarity of all basaltic rocks to each other, and to basalts from the rift wall dated from 1.1 to 1.4 Ma (Hochstaedter et al., in press), implies emplacement in a short time interval prior to 1.1 Ma at both sites. The underlying tuffs could be older-arc basement, but present information is inconclusive.

The characteristics of the individual units are discussed below. The basement lithostratigraphy of Sites 790 and 791 is illustrated in Figures 54 and 55, respectively.

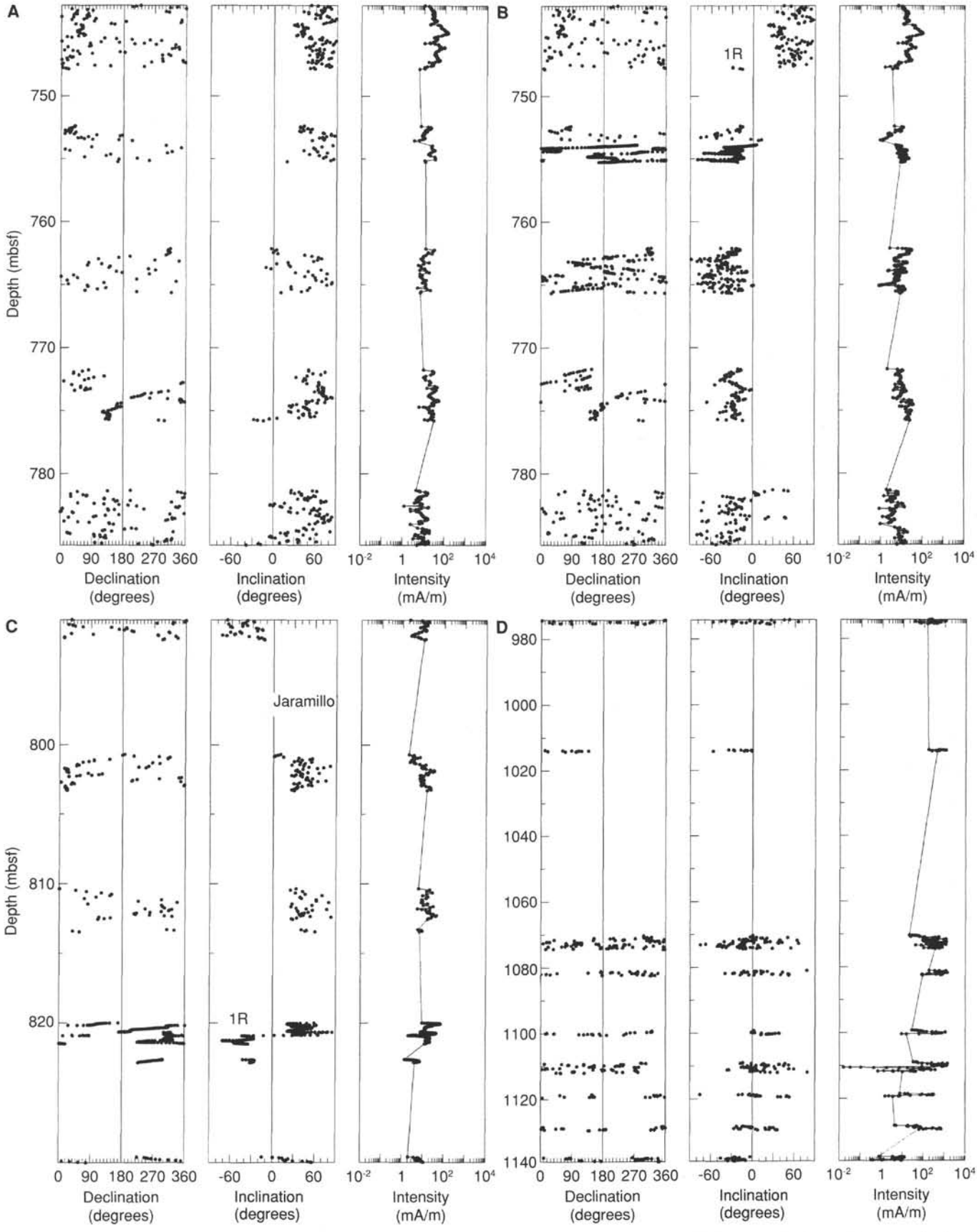

Figure 48. Paleomagnetic results vs. depth (mbsf) for Hole 791B. **A** and **B.** Cores 126-791B-38R to -42R before and after AF demagnetization. **C.** Cores 126-791B-43R to -47R after AF demagnetization. **D.** Cores 126-791B-62R to -79R after AF demagnetization.

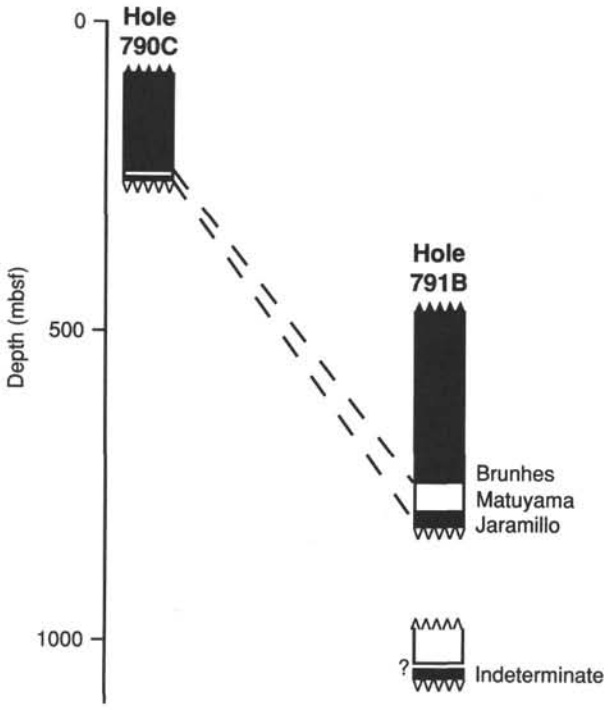

Figure 49. Polarity zones vs. depth (mbsf) for Holes 790C and 791B. Note increased thickness of polarity zones in Hole 791B.

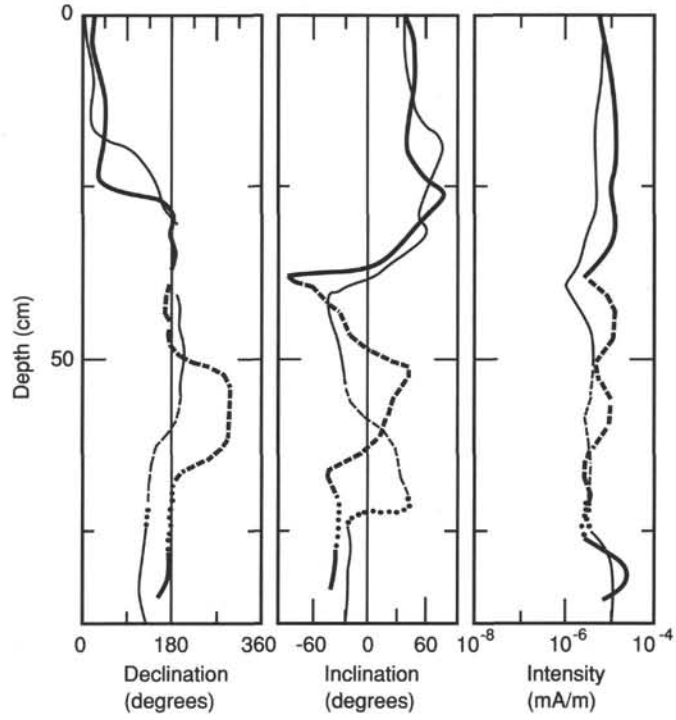

Figure 50. Paleomagnetic results for archive half of cores from Holes 790C and 791B, which include the Brunhes/Matuyama polarity transition. Thick line = Core 126-790C-17X-7 and core catcher. Thin line = Core 126-791B-38R-4 and core catcher. Declination segments were adjusted to eliminate rotations between core segments. Dashed lines indicate core-catcher data. Dotted lines are interpolations to the underlying core.

Site 790

Unit 1

Description: basalt
Intervals: Cores 126-790C-18X through -28X

The pieces and gravel are highly vesicular (20%–50%), nearly aphyric, basalt scorias. They contain microphenocrysts of olivine and plagioclase in an intersertal groundmass. Typical modal proportions, morphology, and sizes of the phenocrysts are 1% euhedral, 0.1–0.2-mm-diameter olivine and 5% euhedral, 0.1–0.3-mm-diameter plagioclase. One comparatively dense piece (126-790C-21X-CC, Piece 2) is an exception as clinopyroxene is present as both phenocrysts (1% euhedral, 0.1 mm diameter) and in the groundmass. The groundmass in all the samples consists of plagioclase laths in partially devitrified glass. The vesicles are round and range from 0.2 to 0.3 mm in size. Yellow translucent crystals occur on the vesicle walls and exposed surfaces.

Site 791

Unit 1

Description: basalt breccia
Interval: Section 126-791B-47R-1 at 45–150 cm

Vesicular olivine-plagioclase-clinopyroxene basalt clasts, 0.5–2.0 cm in diameter, lie in a matrix of glass shards, olivine and plagioclase crystals, and smaller basaltic fragments. In the 1.03 m recovered from Unit 1, a distinct visual difference is apparent between the upper 40 cm and the lower 75 cm. In thin section, the upper part has a glassy matrix, which is isotropic, but difficult to confirm as being either a mass of fine shards or a continuous "liquid" matrix. If the matrix is continuous, the style of this flow may be similar to that of the basaltic mousse described below in Unit 11, the key physical difference being the lack of microvesiculation in Unit 1.

The lower part is composed of fragmental vitric material. It is layered with bands of dark clast-rich material and concentrations of pale glass shards. This lower section may be a hyaloclastite, a vitric debris flow, or a hot pyroclastic flow.

The entire unit contains olivine, plagioclase, and clinopyroxene as phenocrysts in the clasts and as crystals in the matrix (Table 11). This three-phase assemblage is similar to the underlying Unit 2 basalt.

Unit 2

Description: glomeroporphyritic basalt
Intervals: Cores 126-791B-48R through -53R

Unit 2 is a vesicular olivine-plagioclase-clinopyroxene basalt with fresh phenocrysts that are characteristically in large glomeroporphyritic clots. The presence of clinopyroxene contrasts with its absence from the next lower basalt, which is more mafic, thus reflecting the more differentiated character of Unit 2. The vesicles are up to 3 mm in diameter. They have thin, blue smectite linings at the top of the unit but become increasingly filled with smectite and calcite toward the base. Exotic pebbles are present only at the top of cores and may have fallen from higher units rather than represent interbedded material. One is a silt-rich foraminiferal nannofossil chalk at the top of Core 126-791B-49R; another is a greenish (10GY) lapilli tuff at the top of Core 126-791B-52R. A total of 1.38 m was recovered from 58 m of cored interval.

Unit 3

Description: vesicular, sparsely phyric, olivine-plagioclase basalt
Intervals: Cores 126-791B-54R through -56R

Glomeroporphyritic clots are present but are less common than in Unit 2. Clinopyroxene phenocrysts are absent. Vesicle abundance, size, and filling are similar to Unit 2. We recovered

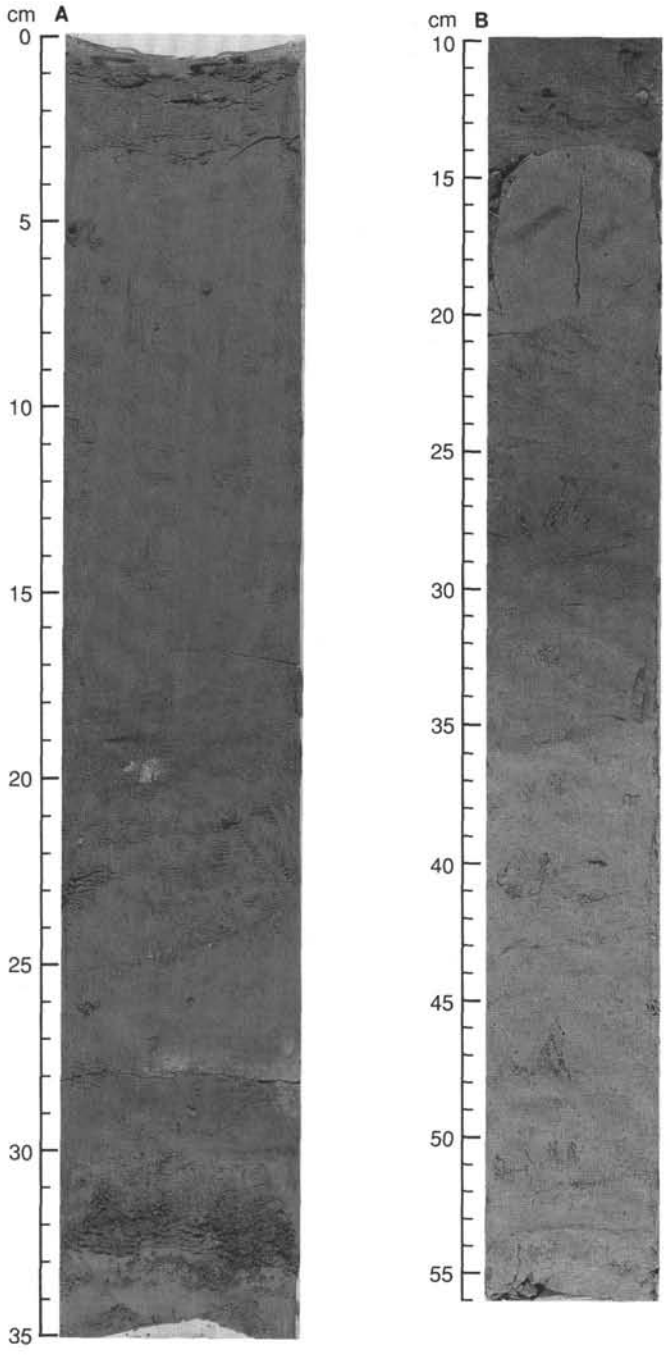

Figure 51. Photographs of core intervals from Holes 790C and 791B, which include the Brunhes/Matuyama polarity transition. **A.** Interval 126-790C-17X-CC (0–35 cm). **B.** Interval 126-791B-38R-4, 10–56 cm.

1 piece from each of Cores 126-791B-54R and -55R and 11 pieces from Core 126-791B-56R, for a total of 0.30 m.

Unit 4

Description: diabase
Intervals: Sample 126-791B-56R-1, Pieces 8 and 10, to 126-791B-57R-1 at 22 cm

Unit 4 is a fine-grained, mostly holocrystalline dike or sill (no contacts recovered) of differentiated basaltic material containing plagioclase, clinopyroxene, olivine, and magnetite. There is devitrified glass and microvesicles, even in this more intrusive rock. Only 0.30 m of core was recovered.

Unit 5

Description: vesicular, sparsely phyric, olivine-plagioclase basalt
Intervals: Sample 126-791B-57R-1 at 22 cm to 126-791B-58R-1, Piece 1

This unit is similar to Unit 3 and may be the lower portion of a single flow unit cut by the diabase. Alteration is more evident in the middle of Core 126-791B-57R, where brownish halos surround a spherical grey interior. However, the two areas are almost indistinguishable in thin section. A total of 0.85 m of core was recovered.

Unit 6

Description: basalt
Intervals: Sample 126-791B-58R-1, Piece 2, to 126-791B-60R-1, Piece 1

Unit 6 is a vesicular, sparsely phyric, olivine-plagioclase basalt similar to Units 3 and 5. A glassy margin, possibly a chilled contact, separates it from Unit 5. In comparison with Unit 5, Unit 6 is less vesicular (10% vs. 25%); however, the phenocryst content and texture are similar, so it may be only a different lava flow of the same magma type. In Sample 126-791B-50R-1 (Piece 8), the basalt invades a xenolith of basalt breccia similar to Unit 2, but is not chilled against it. A total of 0.74 m of core was recovered.

Unit 7

Description: basalt
Interval: Samples 126-791B-60R-1, Pieces 2 through 13

Unit 7 is a vesicular, sparsely phyric, olivine-plagioclase basalt similar to Units 3, 5, and 6. It is distinguished from the latter by being more vesicular, but its similarity in mineralogy and composition indicate that it, too, belongs to the same magma type, if not the same flow. A total of 0.15 m of core was recovered. Altogether, 2.0 m of this basalt type was recovered from 59 m of cored interval, interrupted by one diabase intrusion. Thus, potentially, a similar thickness ($\leq$60 m) of more mafic basalt (Units 3, 5, 6, and 7) underlies a less mafic basalt (Unit 2).

Unit 8

Description: diabase
Intervals: Core 126-791B-61R

Unit 8 is a fine-grained, equigranular, plagioclase-clinopyroxene-olivine rock. Its flow-aligned plagioclase laths, glass, and microvesicularity indicate a shallow level of emplacement. A similar pebble occurs at the top of Core 126-791B-62R.

Unit 9

Description: sediment
Interval: Section 126-791B-62R-1 at 0–28 cm

A bedded sand-clay-gravel/sand sequence of volcanic clasts is interpreted to be air-fall deposit. The lowest lapilli may be accretionary, but identification is inconclusive (see "Lithostratigraphy and Accumulation Rates" section, this chapter).

Unit 10

Description: basalt
Interval: Sample 126-791B-62R-1, Piece 1

Unit 10 consists of one clast of vesicular basalt with only plagioclase phenocrysts, often in clots. Because it lies below the sediment and no similar material was recovered higher in the core, it is considered a separate lava.

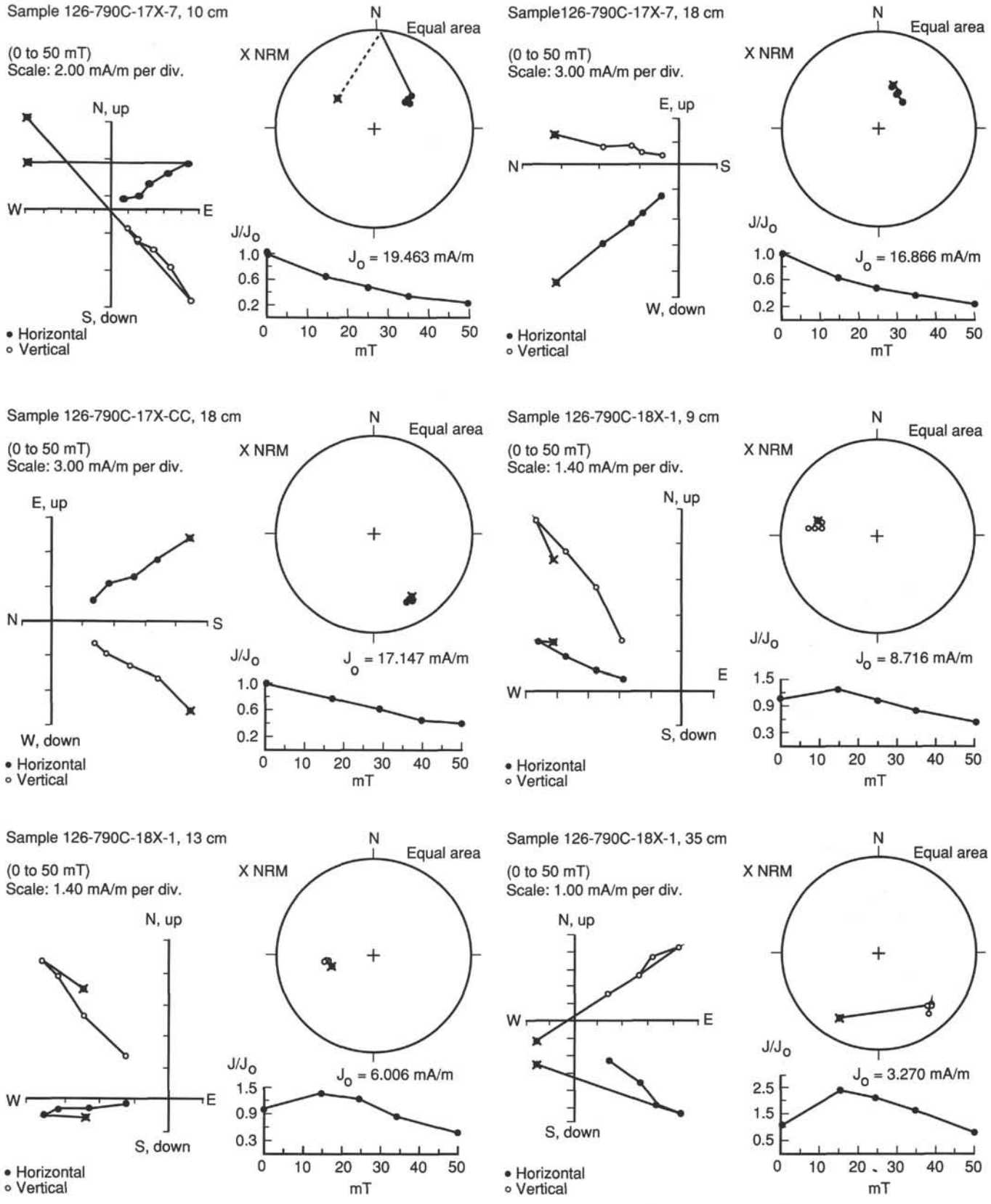

Figure 52. Orthogonal component field vector directions, and remanence intensities, as a function of AF demagnetization, for discrete samples taken across the Brunhes/Matuyama boundary interval (from ~65 cm below to ~35 cm above the inclination reversal horizon) in Hole 790C.

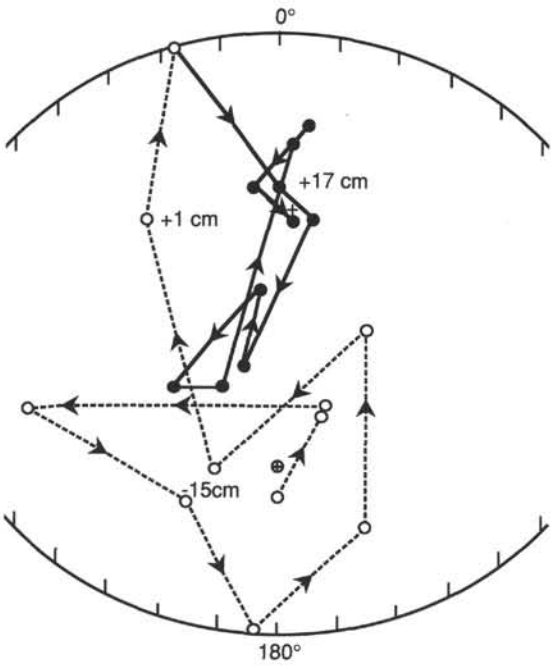

Figure 53. Field-vector directions (after AF demagnetization to 35 mT) as a function of distance below (−) and above (+) the Brunhes/Matuyama reversal plane recovered in Core 126-791B-38R-4. Upper hemisphere (negative inclination) paths are plotted as dashed lines. Azimuthal directions were determined from the directions of dipping laminations. + and (+) represent the present normal (reversed) dipole field direction for this latitude. All field vectors are corrected for bedding dips. Samples from the core catcher were not included in this plot.

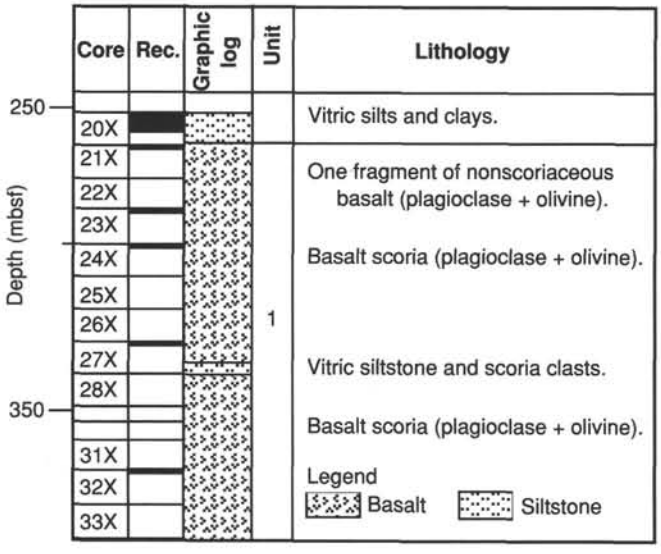

Figure 54. Lithostratigraphy of Hole 790C basement.

Unit 11

Description: basalt mousse
Samples 126-791B-62R-1, Pieces 2 through 11, through Core 126-791B-74R

This 135-m-thick unit is enigmatic and exotic. Macroscopically, it looks like a breccia of vesicular grey basalt clasts in a greenish matrix. However, in detail, "clasts" and "matrix" are very similar, and both consist primarily of highly expanded basaltic glass. Thus, the texture is like that of a mousse. The unit is interpreted as the product of a large-volume, deep-submarine eruption of gas-rich basalt. Its youth and very rapid burial have preserved it from collapse.

Most "clasts" are sparsely olivine-plagioclase phyric. The olivines contain spinel inclusions. Both minerals are euhedral and fresh near the top of the section. The plagioclases are optically zoned. The two minerals commonly form glomeroporphyritic clots that are set in a microvesicular groundmass of devitrified glass. The total vesicle content in the "clasts" is about 30%–40%, so that the glass usually consists of vesicle walls <0.5 mm thick. The measured porosity is also 35%–45% (see "Physical Properties" section, this chapter).

The vesicles are round and open at the top of the section, and some have thin linings of blue smectite. In some "clasts," the rim is less vesicular than the interior, as in a pillow (e.g., Sample 126-791B-73R-2, Piece 1B). However, the "clast" margins are not dense glass but are like scoria margins, that is, highly angular and irregular because of burst vesicles. Near the base of the section, plagioclase-clinopyroxene clasts appear infrequently. The clinopyroxene is subhedral; olivine is absent. Why clinopyroxene is present, or olivine is absent, in some clasts or at some depths but not at others is not yet clear.

All of the above description applies equally to the mousse "matrix" as well. The only difference is that the glass in the matrix is fresher. Throughout Unit 11 the matrix glass is fresh and isotropic, lending a greenish hue to hand specimens. This is especially evident around the glomeroporphyritic clots, where microvesiculation is absent. Again, the vesicles near the top of the section are empty except for occasional thin smectite linings (Figs. 56 and 57). The matrix glass vesicle walls may be thicker adjacent to "clasts," and vesicle walls as thin as 0.1 mm are often "clast" margins. These are the only characteristics that indicate a difference in strength between the components, perhaps as a result of the cooling history prior to their intermingling.

Both clasts and matrix become more altered with depth, resulting in smectite forming along cracks in olivine, and vesicles filling with thicker smectite, calcite, or zeolite(?). Plagioclase minerals remain fresh throughout. The glass becomes more devitrified, but it always is fresher in the matrix than in the clasts, preserving a color contrast in hand specimens.

Unit 12

Description: basalt mousse
Intervals: Samples 126-791B-74R-1, Piece 2, through 126-791B-75R-1, Piece 10

These pieces are similar to an uncommon clast type found near the base of Unit 11. They contain only plagioclase phenocrysts, usually in clots. Clinopyroxene is visible in the groundmass, whereas it is small or absent in most of Unit 11. Most pieces are partially rimmed by thin, greenish, microvesicular "mousse matrix." This, plus the similarity in bulk composition to Unit 11 (see "Igneous Geochemistry" section, this chapter) and the resumption of two-component mousse in Unit 14, may mean that Units 11, 12, and 14 are one flow unit. However, it is unclear whether the magma type is homogeneous. Unit 12 is the most different of the three units.

Unit 13

Description: fault gouge
Intervals: Sample 126-791B-75R-1, Piece 12

Unit 13 is a smectite-feldspar-rich clay.

Unit 14

Description: basalt mousse
Intervals: Samples 126-791B-75R-1, Piece 13, through 126-791B-76R-2, Piece 7

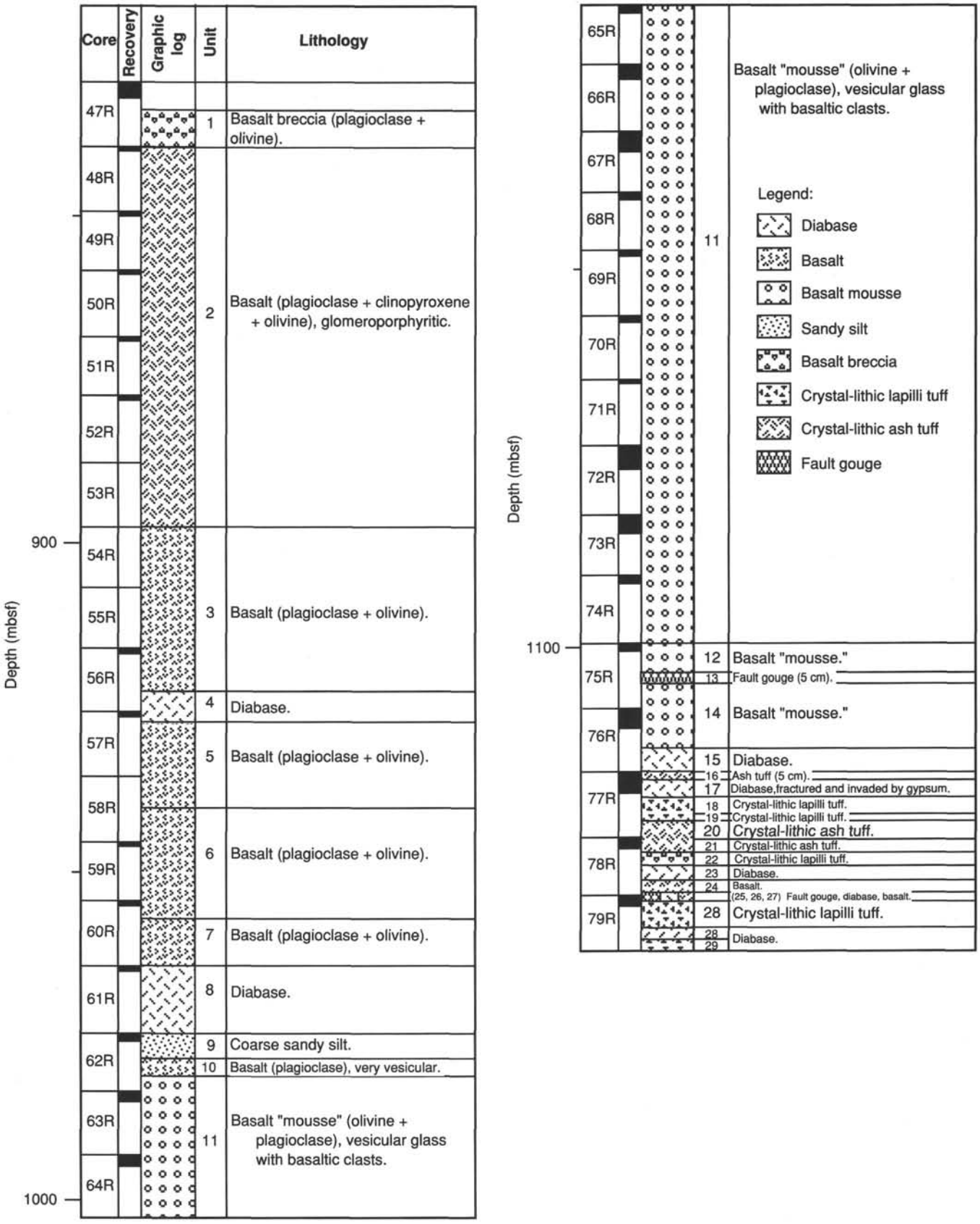

Figure 55. Lithostratigraphy of Hole 791B basement.

Table 11. Summary of phenocryst percentages observed in shipboard thin sections.

Core, section, piece no.	Rock type	Olivine	Plagioclase	Cpx	Others	Alteration
47R, 3	Breccia	1	3	0		
47R, 10	Breccia	2	2	5	Cr-sp	
47R, 17		2	3	0		
48R, 9	Glom basalt	2	4	2		
53R, 5	Glom basalt	1	3	2		
55R, 1	Basalt	3	5	0	sp	
56R, 2	Basalt	2	5	0	sp	
56R, 13	Diabase	3	60	15		
57R, 4	Basalt	5	10	0	sp	
59R, 5	Basalt	3	3	0	sp	
60R, 13	Basalt	1	3	0	sp	
61R, 1	Diabase	0	12	3		
62R, 1B	Plag basalt	0	5	0		
62R, 5B	Mousse C and M	2	5	0	sp	fresh gl and ol
63R, 13B	C and M	2	4	0		devit and fresh gl ves filled smec excell M/C
64R-1, 13	C	0	2	0.5		devit xline gms
64R-2, 1	C and M	1	5	0	sp	gl alt ves more filled
65R, 17	C and M	3	5	0		ol alt
67R-1, 5	C and M	2	4	0	sp	
67R-2, 9	C and M	2	4	0		ol alt, gl fresg ves open
68R, 9	C	0.5	2	0		
70R, 10	C and M	0	2	0		C gl alt M gl fresh ves filled smec
72R-1, 18	C and M	2	4	0		M gl devit ves filled zeol
72R-3, 2A	C and M	2	4	0		M gl devit ves filled zeol
73R-3, 10	C	1	6	0		
75R, 10	C	1	10	0		ol alt calcite
76R-1, 12	C and M(?)	4	4	0		ol pseudo gl alt ves filled
76R-2, 6B	C and M(?)	4	10	1		ol pseudo gl alt ves filled
76R-3, 4A	Diabase	2	40	30		
77R-1, 1	Tuff		+			
77R-1, 7	Diabase	2	60	10		
77R-2, 2A	Tuff	0	3	1	qtz, ox	
77R-2, 6A	Tuff	0	8	0	qtz, ox	
77R-3, 1A	Tuff	0	5	1		
78R, 2	Tuff	0	15	0	ox	
78R, 3B	Diabase	5	60	5		
78R, 8	Basalt	2	2	0		
78R, 10A	Diabase	5	60	10		
78R, 12A	Basalt	0	65	1		
79R, 3	Tuff	0	30	0		
79R, 6	Tuff	0	40	0		
79R, 7	Diabase	7	65	5		

Note: Cr-sp = chromium spinel, sp = spinel, alt = alteration/altered, gl = glass, ol = olivine, devit = devitrified, ves = vesicles, smec = smectite, zeol = zeolite, cpx = clinopyroxene, qtz = quartz, C = clast, M = matrix, xline = crystalline, gms = groundmass, Glom = glomeroporphyritic, pseudo = pseudomorphs, and ox = oxides.

This unit is a more altered version of Unit 11. Compared with Unit 11, the vesicles in the "clasts" are less abundant but larger. The glomeroporphyritic clots are larger (to centimeter scale) and have cumulate textures. The margins between clast and matrix are more convoluted. Olivine is largely pseudomorphed by chlorite, vesicles are largely filled with smectite and calcite, and the glass is more devitrified and iron stained. Plagioclase remains fresh.

Unit 15

Description: diabase
Intervals: Sample 126-791B-76R-2, Piece 8, through Section 126-791B-76R-3

This intrusive rock has 40% euhedral plagioclase <0.5 mm in size, 30% euhedral clinopyroxene as large as 1 mm in size, and around 30% glass and oxides. The glass and 2% euhedral olivine (0.5 mm in size) are altered to smectite. A total of 0.76 m of core was recovered.

Unit 16

Description: crystal-lithic tuff
Interval: Sample 126-791B-77R-1, Piece 1

This unwelded pyroclastic rock could be a drop-in as it is the first piece in the core. However, because nothing like it occurs higher in the sequence, it is treated as a new unit, the first of a fundamentally different kind that constitutes the base of the core. The contact with the mousse was not recovered. The piece contains 5% partially sericitized plagioclase and 10% lithic lava fragments replaced by various assemblages, including calcite and hematite. Of the original vitric shards, 85% are altered to chlorite. The rock may represent an air-fall deposit because there is no evidence for crushing of the pumice shards. A total of 0.03 m of core was recovered.

Unit 17

Description: diabase
Interval: Samples 126-791B-77R-2, Pieces 3 through 8

The diabase is fine grained with a subophitic and intersertal texture and is very similar to the diabase in Unit 15. The phenocrysts in this rock are as large as 1 mm in size and predominantly plagioclase (60%). All of the glass (30%) and olivine (2%) are altered to chlorite. Gypsum veins cut the pieces. A total of 0.80 m of core was recovered.

Unit 18

Description: gypsum-mineralized fracture breccia in lapilli tuff
Interval: Samples 126-791B-77R-2, Pieces 1A through 1E

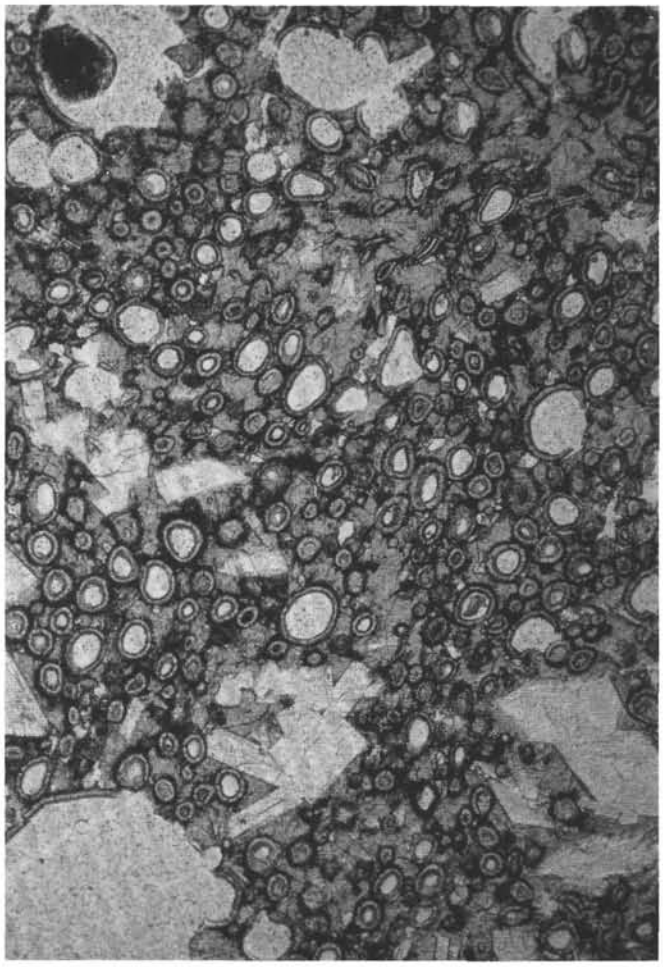

Figure 56. Basalt mousse (Unit 11). Microvesicular basalt glass with glomeroporphyritic clots of plagioclase and olivine. Vesicle walls are lined with smectite (95× magnification, plane-polarized light, Sample 126-791B-62R-1, Piece 13).

Figure 57. Basalt mousse (Unit 11). Glomeroporphyritic texture with clots of plagioclase and olivine. Birefringent haloes mark the smectite-lined microvesicles (95× magnification, cross-polarized light, Sample 791B-62R-1, Piece 13).

This rock consists of large fracture blocks (0.5–4.0 cm in size) randomly aligned. The clasts are crystal-lithic lapilli tuff and welded, lithic-vitric lapilli tuff. The fractures in the rock are filled with gypsum. The breccia is caused by fault plane movement followed by fracturing and infilling of fluid-precipitated gypsum. A sharp basal contact with the unbrecciated Unit 19 is present.

Unit 19

Description: crystal-lithic lapilli tuff
Interval: Samples 126-791B-77R-2, Pieces 1E through 4

The rock is a eutaxitic, welded, well-sorted tuff (Fig. 58). It consists of 50% vitric fragments that are present mainly as compressed flattened pumice with fiamme, 40% lithic fragments, and 10% crystals (quartz, calcite, and magnetite). The vitric rocks are completely altered to chlorite. The rock shows two fabrics: an igneous eutaxitic one with flattened pumice, and a metamorphic overprint with chlorite aligned 45° to the igneous one. A total of 0.45 m of core was recovered.

Unit 20

Description: crystal-lithic tuff
Interval: Samples 126-791B-77R-2, Pieces 5–6, through Samples 126-791B-77R-3, Pieces 1–2

This welded tuff has the same compositional characteristics as Unit 19, but a much finer grain size (<2 mm), and hence is a new flow unit. This rock consists of 70% compressed and flattened pumice altered to chlorite. Minor amounts of calcite are also present (Fig. 59). The metamorphic fabric resulting from chlorite alignment is more pronounced in this unit. A total of 0.45 m of core was recovered.

Unit 21

Description: crystal-lithic tuff
Interval: Sample 126-791B-77R-3, Pieces 3–4

The difference between Units 20 and 21 is that the Unit 21 pumices are not flattened as in Unit 20. A total of 0.15 m of core was recovered.

Unit 22

Description: lithic lapilli tuff
Sample 126-791B-77R-3, Piece 6, through Sample 126-791B-78R-1, Piece 2

This is a poorly sorted, unwelded rock. Altered andesitic lava constitutes the lithic fragments. The clinopyroxenes are replaced by epidote. A total of 0.10 m of core was recovered.

Figure 58. Crystal lithic lapilli tuff (Unit 19). Semiflattened scoriaceous pumice shards, in a matrix of vitric, lithic, and crystal fragments (95× magnification, plane-polarized light, Sample 126-791B-77R-2, Piece 2).

Figure 59. Crystal-lithic tuff (Unit 20). Flattened, elongate pumice shards compacted around crystal and lithic fragments in a eutaxitic texture (95× magnification, plane-polarized light, Sample 126-791B-77R-2, Piece 6A).

Unit 23

Description: diabase
Interval: Sample 126-791B-78R-1, Piece 3

This diabase has an intersertal, subophitic texture similar to that of the other diabases. The only difference is that this rock has slightly more olivine (5%), the crystals are smaller, and it contains gypsum. A total of 0.09 m of core was recovered.

Unit 24

Description: basalt
Interval: Samples 126-791B-78R-1, Pieces 4 through 8

This basalt is plagioclase phyric with an intersertal, vesicular texture. It is highly altered and composed of plagioclase and chlorite. It contains rounded vesicles filled with radially grown chlorite. The vesicles contain tiny laths of plagioclase in a glassy matrix, which could imply that the vesicles are filled with differentiated melt. A total of 0.4 m of core was recovered.

Unit 25

Description: felsic clast and fault gouge
Interval: Sample 126-791B-78R-1, Piece 9

A silicic rock, mineralized with pyrite and containing an epidote vein, was recovered in the same interval as green fault gouge. Pyrite also is disseminated in the rock, which consists of plagioclase and some chlorite in a fine-grained groundmass. The XRD patterns from the fault gouge showed the presence of chlorites and quartz. A total of 0.04 m of core was recovered.

Unit 26

Description: diabase
Interval: Samples 126-791B-78R-1, Pieces 10 to 11, through Sample 126-791B-79R-1, Piece 1

This diabase unit has essentially the same characteristics as Unit 23. It is mineralized in fractures with pyrite, calcite, and gypsum. The alignment of plagioclase laths may be the result of shearing. A total of 0.14 m of core was recovered.

Unit 27

Description: basalt
Interval: Sample 126-791B-78R-1, Piece 12

This rock has a porphyritic texture with partly altered plagioclase phenocrysts and epidote resembling clinopyroxene pseudomorphs. Plagioclase is the dominant phenocryst (65%), with 1% clinopyroxene. The secondary mineralogy consists of smectite, chlorite, and quartz. A total of 0.09 m of core was recovered.

Unit 28

Description: welded crystal-lithic tuff
Interval: Sample 126-791B-79R-1, Pieces 2 through 6 and Piece 11

This deposit has variable composition and variable vesicularity of the lithic fragments and pumice, implying a difference in competence. Part of the plagioclase and all of the crushed pumice and glass shards are altered to smectite and chlorite. A total 0.80 m of core was recovered.

Unit 29

Description: diabase
Interval: Samples 126-791B-79R-1, Pieces 7 through 10

This diabase has a mineralogy similar to that of the other diabases, but it is more extensively altered. All of the clinopyroxene is altered to chlorite and parts of the plagioclase are altered to sericite. This unit is mineralized with secondary calcite, pyrite, and gypsum as in Unit 26. A total of 0.20 m of core was recovered.

X-ray Diffraction Results

The XRD results are summarized in Table 12. In Units 1–11, samples from vesicle walls have very high, broad backgrounds that reflect abundant amorphous glass as well as large amounts of smectite. This blue clay alteration product coats vesicle interiors. Greenish, elongated crystals in vesicles are calcite with traces of 1.4-nm minerals (chlorite or smectite) and feldspar also present.

The matrix of the basalt mousse in Unit 11 (Sample 126-791B-65R-1, Piece 13) contains abundant smectite together with feldspar, augite, glass, and halite. The smectite is an alteration product of the glass and seawater. The white, vein-filling material in Cores 126-791B-76R to -79R was confirmed as gypsum ($CaSO_4 \cdot 2H_2O$) with characteristic peaks at 0.76, 0.43, 0.38, and 0.306 nm (Fig. 60). The tuff of Unit 20 in Sample 126-791B-77R-3 (Piece 1) contains calcite, quartz, and chlorite, together with lesser amounts of mica group minerals, feldspar, and glass, but no smectite (Fig. 61).

Two types of fault gouge are present. The one within the basalt mousse (Unit 13, Sample 126-791B-75R-1, Piece 12) contains smectite and feldspar (Fig. 62). In contrast, the gouge associated with a felsic clast within the lapilli tuff section is rich in chlorites and quartz. The different mineral suites show that the rock being faulted affects the gouge mineralogy.

IGNEOUS GEOCHEMISTRY

We analyzed 4 samples from Site 790 and 20 from Site 791 by X-ray fluorescence (XRF) for major elements; all except 2 were also analyzed for 12 trace elements (Table 13). One basalt scoria from Hole 790A and one rhyolite pumice from Hole 791B were from Unit I. The rest were from Unit III, the basement (see "Lithostratigraphy and Accumulation Rates" section, this chapter).

The basement rocks of Units 1–15 are predominantly basaltic. Their high TiO_2 with respect to MgO, low Ba contents (<30 ppm), and Ti/V ratios closer to 20 than 10, distinguish them from basalts and andesites of the Izu-Bonin Arc (Fig. 63). Consequently, the younger basement volcanism is inferred to be syn-rift in origin.

In detail, the basement basalts are more similar to those from the rift wall, dated at 1.1–1.4 Ma, and from seamounts in the outer rift, than to basalts from the 250-ka en echelon pillow ridges of the inner rift (Hochstaedter et al., in press). That is, the basement volcanics have 17% vs. 16% Al_2O_3, 1.0% vs. 0.85% TiO_2, 11% vs. 12% CaO, 2.5% vs. 2.0% Na_2O, 0.2% vs. 0.1% P_2O_5, and 60–70 vs. 40–50 ppm Zr at 7%–8% MgO. These contrasts indicate percent fusion increases with time. The higher Ca/Al_2O_3 ratios in younger basalts implies that clinopyroxene has remained a residual phase, as it also is during MORB genesis. This contrasts with the more extensive melting and refractory harzburgite beneath the arc.

The basement basalts also have higher Fe with respect to Mg, implying higher pressure fusion (e.g., Klein and Langmuir, 1987). Taken together, these intra-rift comparisons indicate that the crust has thinned, allowing the mantle to rise closer to the surface and, therefore, melt more extensively during the last million years, at least beneath the en echelon ridges. One observation inconsistent with this idea is that the basement basalts apparently become saturated in clinopyroxene at a later stage of differentiation (between 7% and 6% MgO) than do the younger rift basalts, making them more similar to MORB and implying lower-pressure conditions of fractionation.

The basement basalts at Site 791 have lower concentrations of Ba, Rb, and perhaps Ce than do those at Site 790 or the younger rocks of the inner rift. Indeed, Ba and Rb concentrations in Site 791 basalts are as low as in MORB. Previously, such low concentrations have been found only in the basalts of well-evolved backarc basins such as the Lau and West Philippine Basins (Hawkins and Melchior, 1985; Mattey et al., 1981). In the Sumisu Rift, such differences occurred at approximately the same time, only 1 km apart, early in the basin history. The more depleted variant erupted in deeper water.

At Hole 791B, the volcanic rock stratigraphic units can be subdivided into four types. The most mafic is sparsely olivine-plagioclase phyric and has about 8% MgO, 100 ppm Ni, and 250–300 ppm Cr. This also characterizes the least-differentiated lavas from the major en echelon pillow ridges of the inner rift between the North and South Sumisu basins (Hochstaedter et al., in press). It applies to petrologic Units 3, 5, 6, and probably

Table 12. X-ray diffraction analysis of Site 791 rocks.

Core, section, piece no.	Unit	Sample description	Clay minerals			Minerals	Amorphous materials
			1.4 nm	1.0-nm Mica	0.7-nm Chlorite		
126-791B-							
47R-1, 4	1	Basalt breccia	1.73 nm (smectite)	—	—	Feldspar	Abundant
53R-1, 7	2	Hand-picked green grains in a vesicle of basalt	Trace	—	—	Calcite > feldspar	Abundant
65R-1, 13	11	Hand-picked coating materials in vesicles of basalt breccia	1.68 nm (smectite)	—	—	Feldspar	Abundant
65R-1, 13	11	Matrix of basalt breccia	1.69 nm (smectite)	—	—	Feldspar > halite > augite	Abundant
75R-1, 12	13	Fault gouge	1.65 nm (smectite)	—	Trace	Feldspar >>> quartz	Abundant
76R-1, 12	14	White part of vein in basaltic mousse	—	—	—	Gypsum	—
76R-2, 10A	15	White parts in diabase	—	—	—	Gypsum	—
791B-77R-3, 1	20	Welded coarse-ash tuff	1.456 nm (chlorite)	Present	Common	Calcite > quartz >> feldspar	Present
791B-78R-1, 9	25	Fault gouge	1.42 nm (chlorite)	Present	Common	Quartz >>> feldspar	Present

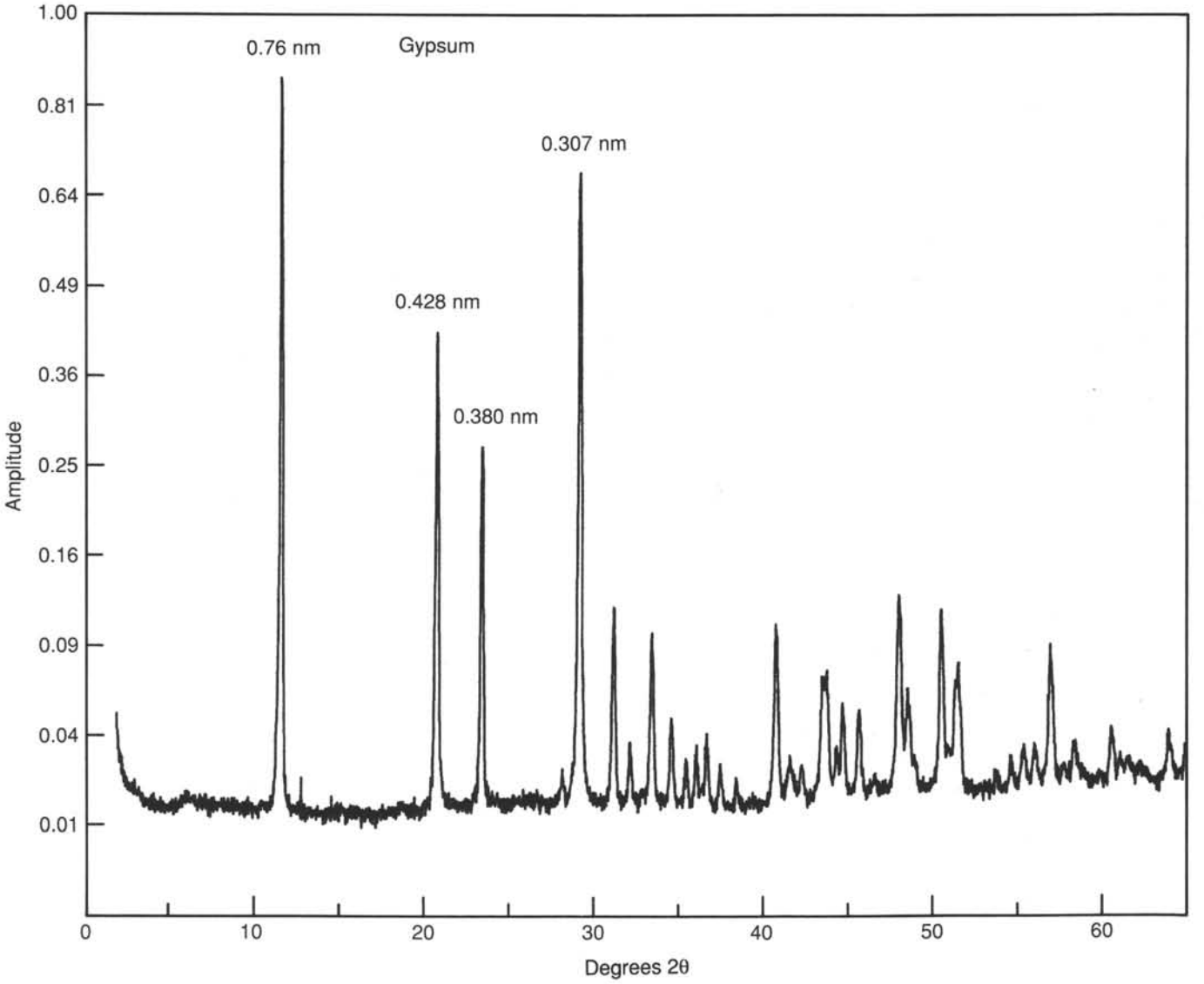

Figure 60. XRD analysis of gypsum in Sample 126-791B-76R-2 (Piece 10A).

7 (see "Igneous Petrology" section, this chapter). Although these four units are scattered over 68 m of section and are intruded at least twice by diabase, they are remarkably similar.

The second type contains clinopyroxene, in addition to olivine and plagioclase, and has about 6.5% MgO, 50 ppm Ni, and 110 ppm Cr. This is the most typical level of differentiation in the young basalts of the inner rift and characterizes petrologic Unit 2 of this site. The underlying basalt mousse is similarly mafic but has lower high-field-strength element (HFSE) concentrations, higher Ti/Zr ratios, and more erratic K, Rb, and P concentrations. This type may also characterize Units 24 and 27, which are interspersed with the tuffs near the base of the hole, but alteration makes assignment of those basalts ambiguous.

Diabases constitute the third rock type. They range in composition from being as mafic as type I (Unit 15), to being similar to type II (Unit 8), to being more differentiated than type II (Units 4 and 29). The TiO_2 contents increase regularly in that order from 1.1% to 1.9%, although Zr remains oddly constant at about 60–70 ppm.

Finally, the tuffs and lapilli tuffs at the base of the section in Units 16–22 and 28 appear broadly intermediate to felsic in nature, but they are too fine grained and altered for clear shipboard interpretation. Magnesium, calcium, sodium, and potassium are especially erratic, reflecting the chloritization. Nonetheless, the tuff (Unit 20) is roughly andesitic, and the basal lapilli tuff (Unit 28) has a broadly basaltic bulk composition. However, the chloritic alteration of both is strong, yielding K_2O/CaO ratios greater than 2.0, loss on ignition (LOI) of 4%–5%, and generally erratic alkali and alkaline earth concentrations. In both, nevertheless, the ratios of the most immobile trace elements have strong island-arc characteristics (e.g., Ti/Zr = 195; Ti/V = 12; and Zr/Y = 1.5), and the basalt plots together with data from the modern Bonin Arc in the Ba-Zr and Ti-V diagrams of Figure 63. Thus, the eutaxitic textures, which imply proximity to the eruption site, and the preliminary bulk geochemistry suggest that Units 16–28 are an arc basement of unknown age. However, Units 24 and 27 are intercalated yet similar in composition and mineralogy to the overlying syn-rift basalts. Consequently, the provenance of the tuffs remains ambiguous.

SEDIMENT/FLUID GEOCHEMISTRY

Eleven 10-cm long, whole-round samples from Holes 790A, 790B, and 790C and 15 whole-round samples from Holes 791A

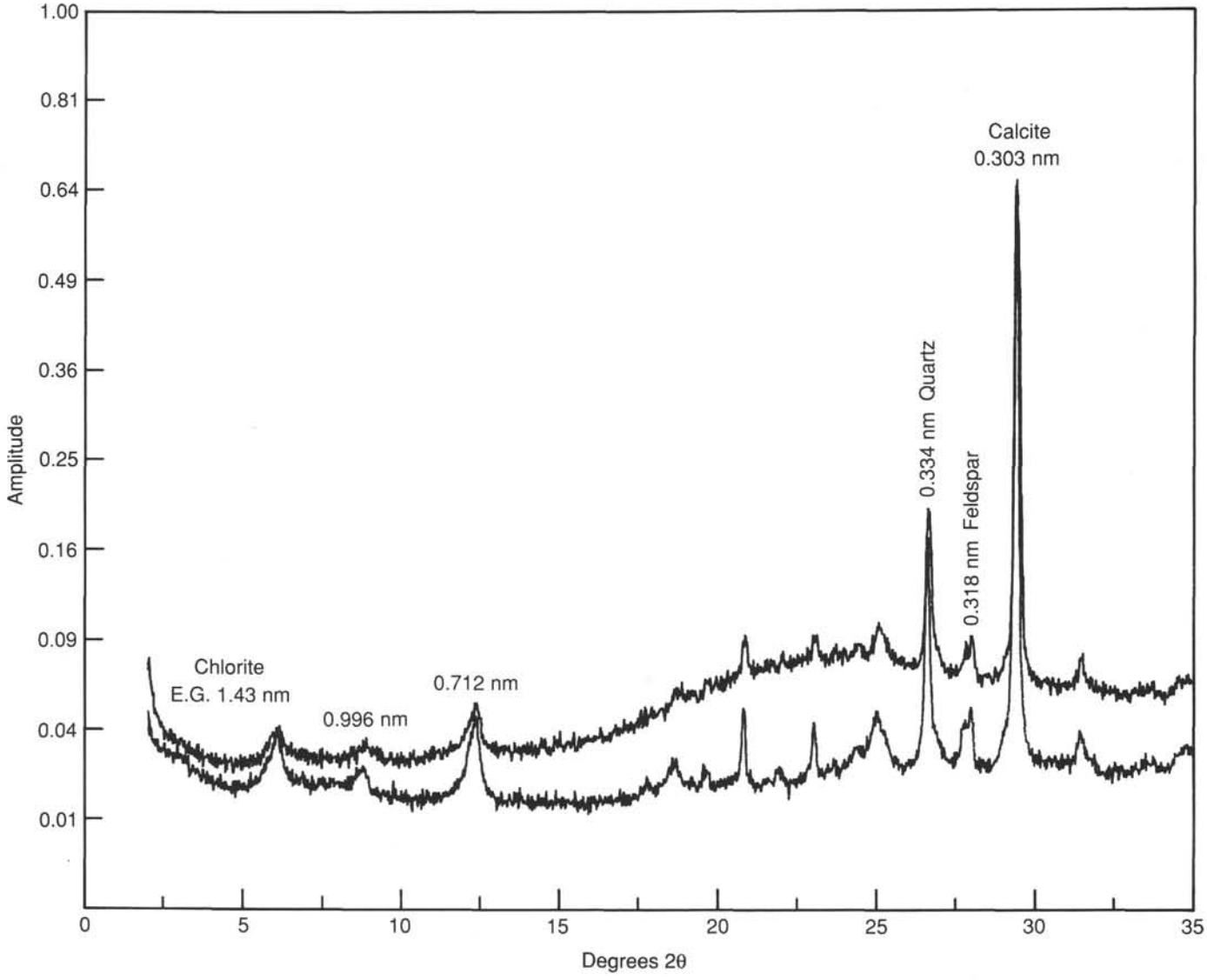

Figure 61. XRD analysis of ash tuff showing chlorite, mica group minerals, quartz, feldspar, calcite, and amorphous glass in Sample 126-791B-77R-3 (Piece 1) before (bottom) and after glycolation (EG).

and 791B were obtained for electrical resistivity measurements, pore-water squeezing, and sediment and fluid analyses.

Sediment Resistivity

The formation factors calculated from the resistivity measurements vary between 2.0 and 7.5 (Table 14). The sample from Core 126-790B-6H consists of coarse sand, and the high formation factor (5.5) is caused by water draining away from the electrodes during measuring. At Site 791, the same phenomenon precluded recording of meaningful data on Cores 126-791A-9H, -12H and -15H. There is a tendency for slightly higher formation factors in the lower parts of the holes, consistent with the more compacted nature of these sediments (Fig. 64). The magnitude of the formation factors is the same as determined by other investigations on similar sediments at the same stage of compaction (e.g., Manheim and Waterman, 1974).

Sediment Geochemistry

Sediments from Sites 790 and 791 were analyzed on board ship for inorganic carbon, total carbon, nitrogen, and sulfur (see "Explanatory Notes" chapter, this volume). Sulfur was not determined quantitatively because vanadium pentoxide was not added to the samples for capacity reasons. Analytical results are presented in Table 15. The distribution pattern of organic carbon at the two sites shows the same features, with low values in the upper part of the holes and a broad maximum in the lower half (Fig. 65).

Despite a three-fold difference in the rate of sediment accumulation, the concentration of organic carbon at the two sites is not very different. The concentration of organic carbon is positively correlated with sedimentary carbonate. This probably relates to the fact that sections with high concentrations of sedimentary carbonate (mainly nannofossils) represent periods with high planktonic productivity and/or reduced input of clastic material. However, for samples with high concentrations of carbonate, the correlation may be enhanced by the method used for determining the concentration of organic carbon, which involves subtracting inorganic carbon and total carbon (see "Explanatory Notes" chapter, this volume).

The concentration of total nitrogen varies from less than the detection limit to 0.2%. Although most of the nitrogen is organically bound, there is no significant correlation between or-

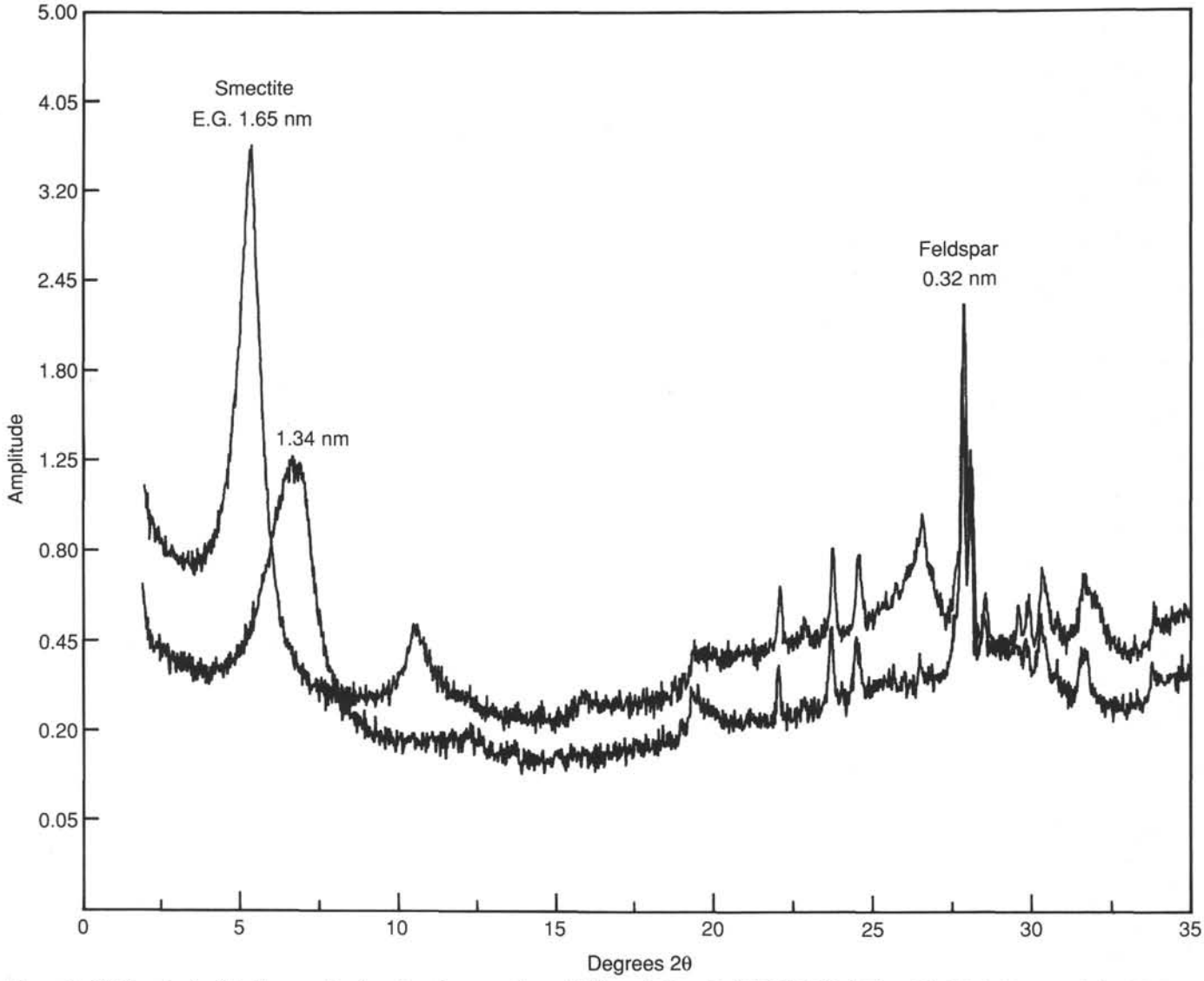

Figure 62. XRD analysis of fault gouge showing abundant smectite and feldspar in Sample 126-791B-75R-1 (Piece 12). The 1.34-nm peak is shifted to 1.65 by glycolation. (EG)

ganic carbon and sedimentary nitrogen. Except for Core 126-790A-2H, sulfur could only be detected between 88 (Core 126-790C-1H) and 247 mbsf (Core 126-790C-18X) at Site 790. The fact that sulfur is more abundant in the part of the hole where sulfate reduction is taking place (see discussion that follows) attests to its biogenic origin.

Fluid Geochemistry

The headspace hydrocarbon analyses did not show any gases above background level and are not reported. Special attention was paid to possible contamination of the pore water by drilling-mud filtrate because of the extensive use of mud while drilling Holes 790A, 790B, 790C, 791A, and 791B. The composition of the mud filtrate is given in Table 16. Uniform chloride concentrations at typical seawater levels (Table 16) indicate that none of the samples were measurably contaminated by drilling-mud filtrate.

Concentrations of sodium, magnesium, and strontium in pore waters recovered from Holes 790A, 790B, and 790C deviate little from concentrations in seawater of similar chlorinity. Concentrations of potassium decrease to about 50% of its seawater level at 100 mbsf (Core 126-790C-2H) and increase to normal seawater concentrations at 254 mbsf (Core 126-790C-18X; Table 16). A similar trend is observed at Site 791.

At Site 790, the concentration of lithium exhibits a pronounced subsurface maximum of 63 μM at 100 mbsf (Core 126-790C-2H; Fig. 66), whereas at Site 791 the highest lithium concentration is recorded at 37 mbsf (Core 126-791A-5H). Very few sources of lithium other than high-temperature alteration of volcanic material have been identified. However, Gieskes (1983) proposed that lithium can be enriched in pore waters during dissolution and recrystallization of biogenic silica.

At Site 790, alkalinity remains at about 4 mM down to 131 mbsf (Core 126-790C-5H) and then increases to about 9.3 mM in Cores 126-790C-13X through -16X (197–227 mbsf), below which it decreases to 6.0 mM at 255 mbsf (Core 126-790C-2X; Fig. 66). The concentration profile of calcium mirrors the alkalinity profile (Fig. 66) and shows calcium concentrations only slightly higher than in seawater in Cores 126-790C-2H and -5H. The alkalinity maximum and calcium minimum coincide with the minimum in the sulfate concentration profile between 197 and 227 mbsf. Evidently, the concentration of calcium is af-

Table 13. Shipboard X-ray fluorescence analyses of rocks from Sites 790 and 791.

Hole, core	790A-4H	790C-21X	790C-24X	790C-24X	791B-9R	791B-48R	791B-53R	791B-55R	791B-56R	791B-57R	791B-59R
Section, interval (cm)	2, 57–59	CC, 3–8	CC, 8–10	15–72	CC, 2–3	1, 46–49	1, 10–12	1, 2–5	1, 69–71	1, 31–34	1, 41–44
Piece number	—	2	2A	2B	—	9	4	1	13	4	5
Depth (mbsf)	32.1	275	305	305	472	845	890	910	922	930	950
Petrologic unit	1	1	1	1	1	2	2	3	4	5	6
Lithology[a]	basalt	basalt	basalt	basalt	pumice	basalt	basalt	basalt	diabase	basalt	basalt
Major elements:											
SiO_2	49	51.43	48.71	49.61	73.08	49.22	50.08	49.2	48.81	48.55	48.91
TiO_2	1.07	1.35	0.97	0.97	0.4	1.2	1.24	1.06	1.74	1/-8	1
Al_2O_3	16.4	16.89	17.57	17.21	13.36	16.84	17.36	17.33	15.12	16.78	17.46
Fe_2O_3	11.21	10.9	9.64	10.62	3.55	11.27	10.35	11.1	14.63	10.59	10.7
MnO	0.16	0.16	0.13	0.15	0.13	0.13	0.15	0.14	0.17	0.14	0.13
MgO	8.1	4.69	7.8	8.49	0.84	6.81	5.85	8.03	5.65	6.45	8.53
CaO	10.87	10.14	11.63	10.44	2.98	10.71	10.77	10.9	9.63	12.35	10.54
Na_2O	2.44	3.23	2.44	2.49	4.97	2.85	2.93	2.53	2.93	2.67	2.68
K_2O	0.37	0.54	0.4	0.56	0.91	0.26	0.28	0.31	0.2	0.41	0.2
P_2O_5	0.19	0.25	0.27	0.14	0.07	0.23	0.24	0.17	0.27	0.17	0.16
LOI	0	0.24	0.21	0.49	0.38	0.56	0.15	0.35	0.24	2.14	1.39
Total	99.81	99.58	99.56	100.68	100.29	99.52	99.25	100.77	99.15	99.18	100.31
Trace elements:											
P	828.59	1090.25	1177.47	610.54	305.27	1003.03	1046.64	741.37	1177.47	741.37	697.76
Zr	61.4	90.5			92.1	75.8	79	69.8	67.9	68.5	61.1
Y	21.2	29			47	26.8	26.5	23.1	26.4	22.1	20.7
Rb	4.9	7.9			9.9	2.4	3.1	3.6	0.3	7.3	2.6
Sr	222	287			162	243	260	237	258	356	246
Ba	42	38			162	8	13	20	24		11
V	291	663				336	356	320	516	279	300
Nb	3.4	2.1			1.3	2.1	1.6	1.8	1.5	1.2	1.2
Ni	102	12			1	45	51	98	8	116	124
Cr	920	21				106	118	278		266	261
Zn	68	120			112	114	116	101	131	95	91
Cu	67	35			4	48	46	47	50	48	35
Ce	26	10			11		5	1		3	
Mg#	61.4	48.64	64.04	63.76	34.25	57.08	55.44	61.42	45.95	57.27	63.7

Note: Major elements in wt%, trace elements in ppm.
[a] Msse = mousse, c = clast, m = matrix, lap = lapilli.

fected by precipitation of calcium carbonate in response to the increase in alkalinity resulting from bacterial sulfate reduction. Further evidence for bacterial activity in this interval is provided by the ammonium profile exhibiting a pronounced maximum between 197 and 227 mbsf (Fig. 67).

The ammonium profile also shows that the pore water from the coarse sand in Core 126-790B-6H probably has been severely mixed with seawater. At Site 791, the low concentrations of ammonium in Cores 126-791A-5H, -9H, and -12H probably reflect the same phenomenon.

There are several interpretations of the minimums in the sulfate profile at 197 (Core 126-790C-13X) and 651 mbsf (Core 126-791B-28R): (1) contamination of deeper samples by surface seawater used during drilling, (2) subsurface flow of seawater, and (3) nonsteady-state sulfate reduction. Contamination cannot be entirely excluded. However, at Site 790 the whole rounds taken for squeezing were thoroughly examined, and all of them consisted of continuous, undisturbed, coherent sediments.

Given the distribution of sedimentary sulfur and organic carbon, and the young age of these sediments, the nonsteady-state interpretation is preferred. Circulation of seawater in the basement is also a possibility, but in this case, a less likely interpretation. At Site 791, the quality of the cores was low, and some contamination of the deeper samples by seawater may have occurred. However, it is interesting to note that the sulfate minimum at Site 791 is present at about the same age as at Site 790 (0.32 Ma).

High calcium and low magnesium concentrations in the pore waters recovered from Cores 126-791A-2H and -5H are the only direct indications of ongoing low-temperature alteration of volcanogenic material at these two sites, despite the abundance of pyroclastic material. It is speculated that this is related to the very high sedimentation rates, which give the reactions too little time to impose their signal on the pore-water composition.

PHYSICAL PROPERTIES

Introduction

Multisensor track (GRAPE and *P*-wave) logging, thermal conductivity, index property, and Hamilton Frame (HF) sonic velocity measurements were completed on sediments from all three holes at Site 790 (see "Explanatory Notes" chapter, this volume). In addition, vane shear strength was measured on sections of Holes 790B and 790C that appeared the least disturbed. Velocity measurements were completed on one igneous sample recovered from the base of Hole 790C.

The full suite of physical property measurements were attempted on cores recovered from Hole 791A. However, because of the nature of the material, many intervals of poor recovery, and extensive drilling disturbance, sample spacing is variable. See the individual sections below for details. Multisensor track (MST) logging, thermal conductivity, index property, and velocity measurements were performed on cores throughout the sedimentary section at Hole 791B. Within the igneous section at Hole 791B, velocity and index property analyses were obtained on discrete samples; four igneous samples were measured for thermal conductivity. Because of disturbance resulting from rotary drilling, no vane shear strength analyses were made on any of the material recovered in Hole 791B. In addition, *P*-wave logging and GRAPE measurements were suspended at the base of the sedimentary section.

Samples of hard rock used for physical property analyses were removed from the cores at different time intervals. Some

Table 13 (continued).

791B-61R	791B-62R	791B-64R	791B-67R	791B-72R	791B-73R	791B-75R	791B-77R	791B-77R	791B-78R	791B-78R	791B-79R	791B-79R
1, 1-4	1, 88-92	1, 8-81	1, 61-63	3, 14-17	3, 112-115	1, 57-59	1, 92-95	2, 128-130	1, 79-82	1, 113-115	1, 17-20	1, 94-97
1	5B	13	5	2A	10	10	7	5B	8	12A	3	7
967	982	1001	1025	1077	1088	1103	1121	1125	1133	1137	1139	1143
8	11	11	11	11	11	12	17	20	24	27	28	29
diabase	mousse-c	mousse-c	mousse-m + c	mousse-c + m	mousse-c	mousse-c	diabase	lap-tuff	basalt	basalt	lap-tuff	diabase
50.14	48.59	48.94	49.76	50.21	49.61	49.68	48.51	60.66	52.62	51.59	51.04	49.09
1.17	0.96	0.99	1.04	0.92	1.01	0.98	1.09	0.96	1	1.05	0.68	1.59
17.69	16.99	16.89	17.58	16.56	16.59	17.11	18.6	15.66	17.09	17.98	18.78	16.9
10.45	10.67	12.16	12.02	10.94	10.79	10.13	11.69	8.92	10.12	10.48	11.16	14.96
0.13	0.15	0.16	0.18	0.17	0.12	0.11	0.2	0.12	0.09	0.14	0.21	0.22
5.97	8.25	9.17	8.72	10.83	7.95	8.94	7.82	7.22	9.58	8.71	8.98	5.43
11.66	12.11	10.02	8.43	4.78	10.17	10.74	10.05	1.64	6.6	7.59	1.67	5.9
2.63	2.28	2.12	2.41	4.52	2.9	2.41	2.6	1.76	3.02	2.82	3.96	5.15
0.3	0.15	0.3	0.54	1.15	0.52	0.15	0.15	3.26	0.47	0.22	3.41	0.73
0.18	0.48	0.07	0.07	0.1	0.23	0.19	0.15	0.24	0.23	0.21	0.06	0.16
0.64	1.49	1.56	6.32	6.4	2.1	1.95	1.5	4.48	2.94	2.45	4.32	3.34
100.32	100.63	100.82	100.75	100.18	99.89	100.44	100.86	100.44	100.82	100.79	99.95	100.13
784.98	2093.28	305.27	305.27	436.1	1003.03	828.59	654.15	1046.64	1003.03	915.81	261.66	697.76
71.7	46.8	45.7	46.3	40.1	47.5	43.9	56.1	84.3	62.4	63.9	20.9	59.6
25	29.1	16.2	15.9	16.7	26.2	18.7	20.1	45.5	20.3	16.4	13.8	20.9
5.3	2	3.1	4.8	5.5	1.4	1.1	0.9	71.3	3.3	1.4	26.3	9.7
242	260	183	172	227	275	203	220	59	256	286	292	358
5	1	25		25	22		3	147	43	37	209	33
455	353	321	355	165	387	361	123	306	327	352	419	
1.9	0.9	0.7	1.1	0.7	1.2	1.2	1.1	1.6	2	2.3	0.4	1.1
55	43	56	52	55	40	53	97	5	58	51	22	0
167	186	164	181	165	167	180	226	1	166	160	26	6
103	106	102	95	88	99	99	92	164	98	95	100	111
51	55	58	54	47	52	49	50	12	48	62	27	18
4	11		7		12	11	7		1	4		3
55.7	62.99	62.4	61.49	68.54	61.86	66.01	59.55	64.05	67.57	64.66	63.91	44.41

were taken and measured immediately after the cores were split; others were taken after all pieces had their surface dried for labeling (approximately 2–3 hr after core splitting). The largest group of samples were taken 2–4 days after the cores had been retrieved.

Even in these relatively short time periods, a significant loss of pore fluid may have occurred (e.g., Hay, Sibuet, et al., 1984) and permanent alteration of the rock resulted, induced by changes in the hydration and crystallographic states of the minerals. Attempts to resaturate these samples in seawater did, indeed, increase the amount of water in the rock, but the resulting material properties may have little relation to those of the *in-situ* rock. Consequently, those samples measured directly after splitting are the most reliable indicators of the original state and properties of the rock.

Site 790

Index Properties

Trends in wet-bulk density and grain density roughly parallel each other throughout the entire sedimentary section. Throughout lithologic Unit I (see "Lithostratigraphy and Accumulation Rates" section, this chapter), both properties are characterized by high variability and no real systematic downhole trends. Values in Unit II increase fairly regularly from approximately 160 to 250 mbsf, at which point both parameters again become highly variable (Fig. 68 and Table 17).

Gravimetrically determined wet-bulk densities range from approximately 1.4 to 2.0 g/cm^3, averaging 1.61 g/cm^3 in Unit I and 1.69 g/cm^3 in Unit II. This downhole increase is primarily the result of increased consolidation from the weight of overburden. However, a distinct change at the Unit I/II boundary (Fig. 68) implies that higher calcium carbonate contents within Unit II are also influencing the wet-bulk densities, probably through their effect on grain densities (see below).

GRAPE wet-bulk density values correlate very well in the overlapping intervals between Holes 790A and 790B and between Holes 790B and 790C (Fig. 69). Slight offsets may be attributed to small variations in the cored interval (see "Lithostratigraphy and Accumulation Rates" section, this chapter) and/or coring disturbance.

In general, agreement between GRAPE and gravimetrically determined wet-bulk density values is good throughout Holes 790A, 790B, and 790C. With the exception of the upper 20 m of Hole 790B, gravimetric bulk density measurements fall within 0.1 g/cm^3 of the GRAPE values (Fig. 69). Gravimetric bulk density values in the upper 20 m of Hole 790B display significantly greater scatter than either those in Hole 790A or GRAPE-generated values. These discrete samples are from thin layers with extreme bulk density values, such as vitric sand and silt beds. When the GRAPE data are averaged (over 20-cm intervals), much of the scatter in the data is minimized.

The downhole increase in wet-bulk density is mirrored by decreases in water content and porosity. Porosity data range from 50% to over 80%, and average 68% and 66% in Units I and II, respectively. Water contents generally fall between approximately 30% and 110% and average 79% and 68% in Units I and II, respectively (Table 17 and Fig. 68). Variability in water content and porosity decreases near the lithologic boundary, similar to the trend in wet-bulk density and grain density.

Grain density values in the upper unit range from 2.1 to ~3.0 g/cm^3, with a mean of 2.57 g/cm^3. Intervals of high grain density in Unit I correspond to beds with high calcium carbonate contents (11–28 and 55–70 mbsf; Fig. 68; see discussion that follows). Grain density values in Unit II display less variability, averaging 2.66 g/cm^3. This increase in grain density from Units I to II is related to higher calcium carbonate contents below 130–150 mbsf.

The magnitude and trends of the gravimetrically determined index properties agree well in the depth overlaps between the

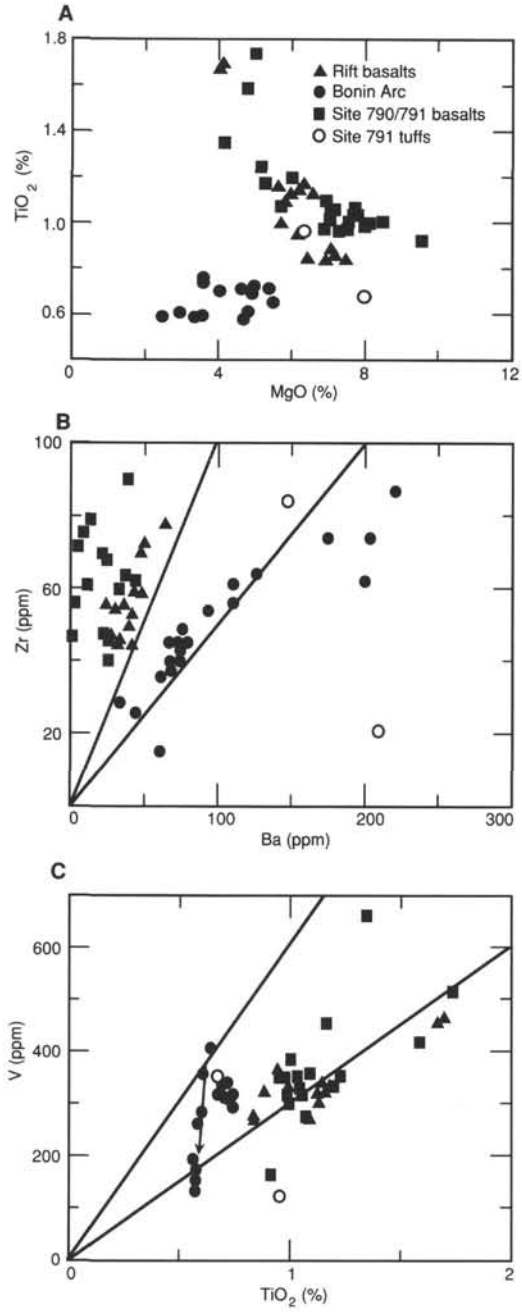

Figure 63. **A.** TiO_2 vs. MgO. The rift basalts are representatives of the 0.6–0.05 Ma basalts dredged and sampled by ALVIN (Hochstaedter et al., in press; Fryer et al., in press). The Bonin Arc samples are basalt to andesites from Tori Shima, Sumisu Jima, and Oshima (Y. Zhang, pers. comm., 1989; Wood et al., 1980). The two Site 791 tuffs are from Units 20 and 28. Note the slightly higher TiO_2 content of the younger "rift" vs. older Site 790/791 basalts. **B.** Ba vs. Zr. Symbols and data as above. Lines of constant Ba/Zr ratios of 1 and 2 are shown for reference. Arc lavas generally have Ba/Zr >1; MORB and oceanic-island basalt (OIB) ratios are about 0.15 and 0.8, respectively. The Site 790/791 shipboard Ba data are tentative, but unquestionably <50 ppm, indicating Ba/Zr ratios intermediate between MORB and the arc, but overlapping OIB. **C.** TiO_2 vs. V. Symbols and data as above. Lines of constant Ti/V ratios of 10 and 20 are shown for reference. Arc lavas generally have Ti/V of 10–20 vs. 20–25 in MORB and >30 in OIB. The arrow shows the differentiation path of Tori Shima lavas, implying a low Ti/V parent and early magnetite fractionation.

Table 14. Sediment resistivity, measurement temperature, and pore-water resistivity at 25°C and formation factor of sediments from Sites 790 and 791.

Core, section, interval (cm)	Depth (mbsf)	R_s (ohm-m)	Temperature (°C)	R_{pw} (ohm-m)	F
126-790A-					
2H-3, 140–150	13.25	0.675	10.0	0.200	2.4
3H-5, 140–150	25.75	0.704	10.9	0.200	2.5
126-790B-					
6H-3, 140–150	46.95	1.445	13.1	0.200	5.5
8H-5, 140–150	69.05	0.709	13.7	0.198	2.7
9H-2, 140–150	74.25	0.657	13.6	0.198	2.5
126-790C-					
2H-4, 140–150	100.45	0.530	11.9	0.196	2.0
5H-5, 140–150	130.95	0.761	14.9	0.198	3.0
10X-1, 101–111	165.96	0.717	14.3	0.197	2.8
13X-2, 140–150	196.85	0.662	15.3	0.196	2.7
16X-3, 140–150	227.25	0.791	15.3	0.197	3.2
18X-2, 140–150	254.65	0.695	18.7	0.198	3.0
126-791A-					
2H-5, 140–150	11.95	0.619	11.1	0.196	2.3
5H-3, 140–150	37.45	0.856	13.8	0.193	3.4
18H-6, 90–100	166.95	0.886	13.3	0.195	3.5
22H-6, 140–150	205.85	0.902	14.2	0.194	3.6
126-791B-					
10R-1, 86–96	474.21	1.253	14.5	0.199	5.0
13R-1, 140–150	503.55	0.964	14.9	0.196	4.2
23R-3, 115–125	602.9	0.790	14.6	0.198	5.0
28R-3, 140–150	651.05	1.049	16.1	0.198	4.3
34R-3, 140–150	709.05	1.246	16.4	0.199	5.1
39R-1, 140–150	753.85	0.872	14	0.198	3.4
42R-2, 0–10	782.85	0.951	15.6	0.198	3.9
45R-2, 140–150	813.2	1.864	15.8	0.199	7.5

Note: R_s = sediment resistivity, R_{pw} = pore-water resistivity, and F = formation factor.

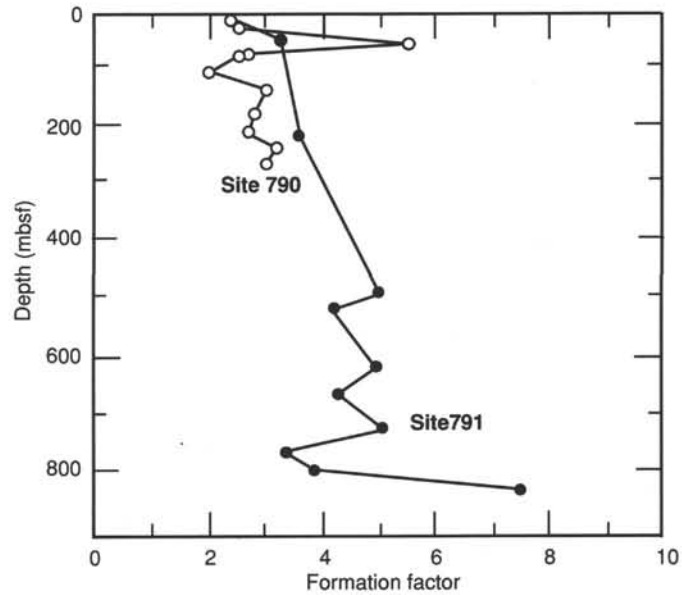

Figure 64. Formation factor of sediments from Sites 790 and 791.

Table 15. Concentration of organic carbon and total nitrogen and sulfur in sediments from Sites 790 and 791.

Core, section, interval (cm)	Depth (mbsf)	Inorg. carbon (%)	$CaCO_3$ (%)	Total carbon (%)	Org. carbon (%)	Tot N (%)	Tot S (%)
126-790A-1H-1, 52–54	0.52	0.22	1.8	0.40	0.18	0.09	
126-790B-1H-1, 62–65	0.62	0.29	2.4	0.50	0.21	0.08	
126-790A-1H-2, 87–89	2.38	0.18	1.5	0.33	0.15		
126-790B-1H-2, 106–109	2.58	0.13	1.1	0.26	0.13		
126-790B-1H-3, 22–25	3.23	0.13	1.1	0.28	0.15	0.08	
126-790A-1H-3, 23–25	3.23	0.15	1.2	0.32	0.17		
126-790B-2H-2, 53–56	6.55	0.16	1.3	0.32	0.16	0.06	
126-790A-1H-6, 25–27	7.76	0.15	1.2	0.28	0.13		
126-790B-2H-3, 113–116	8.65	3.71	30.9	4.97	1.26	0.17	
126-790A-2H-1, 84–85	9.64	0.07	0.6	0.17	0.10	0.01	0.04
126-790B-2H-4, 88–91	9.90	1.95	16.2	2.82	0.87	0.13	
126-790A-2H-2, 71–73	11.02	2.35	19.6	3.11	0.76	0.06	
126-790B-2H-5, 61–64	11.13	0.11	0.9	0.20	0.09		
126-790B-2H-6, 36–39	12.37	2.38	19.8	3.29	0.91	0.13	
126-790A-2H-3, 122–123	13.02	2.22	18.5	3.00	0.78	0.09	
126-790A-2H-3, 140–150	13.25	2.04	17.0	2.87	0.83	0.13	
126-790A-2H-6, 132–133	17.62	1.77	14.7	2.45	0.68	0.11	
126-790A-3H-2, 102–104	20.83	0.23	1.9	0.43	0.20	0.08	
126-790A-3H-4, 40–42	23.21	0.18	1.5	0.34	0.16	0.07	
126-790A-3H-5, 140–150	25.75	0.16	1.3	0.30	0.14	0.06	
126-790A-3H-6, 57–59	26.38	0.14	1.2	0.29	0.15		
126-790B-6H-3, 140–150	46.95	0.05	0.4	0.11	0.06		
126-790B-7H-3, 72–76	55.74	2.32	19.3	3.08	0.76	0.13	
126-790B-7H-4, 62–65	57.14	0.10	0.8	0.30	0.20		
126-790B-7H-5, 24–27	58.26	0.05	0.4	0.18	0.13		
126-790B-8H-1, 134–135	62.94	0.34	2.8	0.59	0.25	0.09	
126-790B-8H-2, 132–134	64.33	0.05	0.4	0.16	0.11	0.05	
126-790B-8H-3, 130–132	65.91	1.83	15.2	2.42	0.59	0.11	
126-790B-8H-4, 10–12	66.21	2.07	17.2	2.63	0.56	0.10	
126-790B-8H-5, 140–150	69.05	2.52	21.0	3.22	0.70	0.13	
126-790B-8H-6, 47–49	69.58	1.37	11.4	1.99	0.62	0.12	
126-790B-9H-1, 124–126	72.55	0.07	0.6	0.17	0.10	0.07	
126-790B-9H-2, 140–150	74.25	0.20	1.7	0.15	-0.05	0.06	
126-790B-9H-3, 13–15	74.44	0.05	0.4	0.14	0.09	0.05	
126-790B-10H-4, 57–60	86.09	0.05	0.4	0.12	0.07		
126-790B-10H-5, 81–84	87.83	0.26	2.2	0.42	0.16	0.07	
126-790C-1H-3, 34–36	88.32	0.27	2.2	0.40	0.13	0.08	0.14
126-790B-10H-6, 96–99	89.48	0.10	0.8	0.20	0.10	0.05	
126-790B-11H-1, 114–117	91.86	0.13	1.1	0.24	0.11	0.05	
126-790B-11H-2, 89–92	93.11	0.18	1.5	0.34	0.16	0.08	
126-790C-1H-6, 107–109	93.58	0.17	1.4	0.27	0.10	0.06	0.11
126-790B-11H-4, 114–117	96.36	0.16	1.3	0.31	0.15	0.07	
126-790C-2H-2, 106–109	97.08	0.08	0.7	0.15	0.07	0.06	0.08
126-790B-11H-6, 15–18	98.37	0.15	1.2	0.25	0.10	0.07	
126-790C-2H-5, 0–5	100.53	0.08	0.7	0.16	0.08		
126-790C-2H-6, 79–82	102.81	0.07	0.6	0.23	0.16	0.07	
126-790C-3H-3, 62–65	107.84	0.08	0.7	0.21	0.13		
126-790C-3H-6, 38–41	112.10	0.06	0.5	0.28	0.22		0.17
126-790C-5H-3, 81–84	127.33	2.26	18.8	2.76	0.50	0.11	0.08
126-790B-15X-1, 10–13	129.42	2.38	19.8	2.80	0.42	0.09	
126-790B-15X-1, 45–47	129.76	0.07	0.6	0.18	0.11		
126-790C-5H-5, 59–61	130.10	0.04	0.3	0.13	0.09	0.07	0.40
126-790C-5H-5, 140–150	130.95	1.86	15.5	2.23	0.37		
126-790C-5H-6, 91–94	131.93	2.58	21.5	3.18	0.60	0.11	
126-790C-6H-1, 126–129	134.47	0.05	0.4	0.13	0.08	0.13	
126-790C-6H-2, 91–93	135.62	0.09	0.7	0.19	0.10		
126-790C-6H-4, 88–92	138.60	1.57	13.1	1.88	0.31	0.09	0.14
126-790C-6H-5, 62–65	139.84	0.08	0.7	0.13	0.05	0.03	0.09
126-790C-6H-6, 67–69	141.38	1.66	13.8	2.07	0.41	0.10	
126-790C-6H-7, 22–25	142.44	3.42	28.5	4.03	0.61	0.12	0.11
126-790C-7H-2, 25–28	144.47	0.36	3.0	0.55	0.19		
126-790C-10X-1, 101–111	165.96	3.38	28.2	4.28	0.90	0.12	
126-790C-10X-2, 36–39	166.78	2.71	22.6	3.38	0.67	0.14	
126-790C-11X-1, 103–106	175.65	2.06	17.2	2.57	0.51	0.11	
126-790C-11X-3, 52–54	178.13	3.87	32.2	4.48	0.61	0.13	0.12
126-790C-11X-5, 42–45	181.04	2.96	24.7	4.09	1.13	0.20	0.24
126-790C-12X-1, 43–45	184.64	2.22	18.5	2.82	0.60	0.15	0.14
126-790C-12X-2, 6–8	185.77	4.76	39.7	5.19	0.43	0.12	0.12
126-790C-13X-1, 115–116	195.06	5.07	42.2	5.60	0.53	0.11	
126-790C-13X-2, 99–100	196.39	5.88	49.0	6.45	0.57	0.14	
126-790C-13X-2, 140–150	196.85	5.16	43.0	5.70	0.54	0.08	
126-790C-13X-3, 100–101	197.91	4.60	38.3	5.40	0.80	0.14	0.10
126-790C-13X-4, 14–16	198.55	4.38	36.5	5.18	0.80	0.15	0.14
126-790C-14X-1, 127–128	204.88	4.38	36.5	5.20	0.82	0.14	
126-790C-14X-2, 125–126	206.36	2.93	24.4	3.73	0.80	0.17	0.13

Table 15 (continued).

Core, section, interval (cm)	Depth (mbsf)	Inorg. carbon (%)	$CaCO_3$ (%)	Total carbon (%)	Org. carbon (%)	Tot N (%)	Tot S (%)
126-790C-14X-3, 35–36	206.96	3.02	25.2	3.68	0.66	0.15	
126-790C-16X-1, 90–91	223.71	2.93	24.4	3.54	0.61	0.16	
126-790C-16X-2, 104–105	225.35	5.63	46.9	6.43	0.80	0.19	
126-790C-16X-3, 68–69	226.49	3.77	31.4	4.56	0.79	0.15	
126-790C-16X-3, 140–150	227.25	2.16	18.0	2.58	0.42	0.09	
126-790C-16X-4, 109–110	228.40	2.87	23.9	3.46	0.59	0.13	
126-790C-16X-5, 91–92	229.72	1.62	13.5	2.18	0.56	0.12	0.17
126-790C-17X-1, 101–103	233.42	2.22	18.5	2.63	0.41	0.12	
126-790C-17X-2, 74–77	234.66	3.31	27.6	4.15	0.84	0.14	
126-790C-17X-3, 111–113	236.52	1.69	14.1	2.09	0.40	0.75	0.16
126-790C-17X-4, 14–16	237.05	1.79	14.9	2.42	0.63	0.10	0.15
126-790C-17X-6, 105–108	240.97	3.73	31.1	4.26	0.53	0.12	0.19
126-790C-18X-2, 35–38	243.97	3.35	27.9	3.86	0.51	0.12	
126-790C-18X-2, 140–150	245.05	4.91	40.9	5.35	0.44	0.08	
126-790C-18X-4, 82–85	247.44	2.37	19.7	2.69	0.32	0.07	0.16
126-790C-19X-2, 44–47	253.66	6.97	58.1	6.59		0.09	
126-790C-19X-3, 115–118	255.87	4.02	33.5	4.56	0.54	0.11	
126-790C-19X-4, 124–127	257.46	3.26	27.2	3.75	0.49	0.10	
126-790C-19X-5, 72–73	258.43	3.52	29.3	3.94	0.42	0.08	
126-790C-20X-1, 112–114	262.53	3.29	27.4	3.72	0.43	0.09	
126-790C-20X-2, 57–59	263.48	3.58	29.8	3.90	0.32	0.08	
126-790C-20X-3, 38–41	264.78	4.09	34.1	4.07		0.07	
126-790C-20X-3, 38–41	264.80	3.84	32.0	4.07	0.23	0.07	
126-790C-20X-4, 12–15	266.04	3.02	25.2	3.32	0.30	0.07	
126-791A-2H-1, 81–84	5.31	0.33	2.7	0.54	0.21		
126-791A-2H-2, 92–95	6.92	0.23	1.9	0.39	0.16		
126-791A-2H-5, 140–150	11.90	0.23	1.9	0.42	0.19		
126-791A-2H-6, 48–51	12.48	0.21	1.7	0.36	0.15		
126-791A-4H-3, 96–97	27.46	3.37	28.1	4.46	1.09	0.16	0.10
126-791A-4H-4, 119–120	29.19	2.92	24.3	3.98	1.06	0.15	0.13
126-791A-4H-5, 55–56	30.05	2.33	19.4	3.32	0.99	0.13	0.08
126-791A-5H-2, 120–121	35.70	1.91	15.9	2.76	0.85	0.14	
126-791A-5H-3, 56–57	36.56	1.80	15.0	2.18	0.38	0.10	
126-791A-5H-3, 140–150	37.40	0.12	1.0	0.24	0.12	0.05	0.07
126-791A-5H-4, 23–24	37.73	0.11	0.9	0.24	0.13	0.07	0.20
126-791A-5H-5, 73–74	39.73	2.05	17.1	2.74	0.69	0.11	0.11
126-791A-7H-3, 62–65	55.62	0.14	1.2	0.30	0.16	0.07	
126-791A-7H-4, 134–137	57.84	0.14	1.2	0.30	0.16	0.07	
126-791A-8H-4, 70–72	66.80	0.07	0.6	0.16	0.09		0.08
126-791A-9H-6, 140–150	80.20	0.07	0.6	0.15	0.08		
126-791A-12H-5, 140–150	107.80	0.04	0.3	0.15	0.11		
126-791A-15H-6, 25–35	137.25	0.04	0.3	0.11	0.07	0.04	0.08
126-791A-16H-2, 74–76	141.44	0.82	6.8	1.17	0.35	0.09	
126-791A-16H-5, 60–63	145.80	0.44	3.7	0.63	0.19	0.07	0.13
126-791A-17H-1, 81–83	149.61	0.09	0.7	0.20	0.11	0.06	
126-791A-17H-3, 86–88	152.66	0.14	1.2	0.21	0.07	0.04	0.08
126-791A-17H-6, 79–81	157.09	0.04	0.3	0.11	0.07		0.09
126-791A-18H-1, 46–49	158.96	2.75	22.9	3.26	0.51	0.14	
126-791A-18H-2, 102–104	161.02	0.41	3.4	0.61	0.20	0.07	
126-791A-18H-6, 90–100	166.90	0.20	1.7	0.27	0.07		
126-791A-19H-1, 107–109	169.17	0.36	3.0	0.59	0.23	0.09	
126-791A-19H-6, 123–125	176.83	0.22	1.8	0.43	0.21	0.07	
126-791A-20H-2, 110–112	180.30	0.19	1.6	0.39	0.20	0.10	
126-791A-20H-6, 76–79	185.96	0.07	0.6	0.22	0.15	0.07	
126-791A-22H-6, 140–150	205.80	0.40	3.3	0.54	0.14	0.08	0.10
126-791A-22H-7, 16–19	206.06	0.90	7.5	1.27	0.37	0.11	
126-791A-23H-2, 72–75	207.76	0.04	0.3	0.10	0.06		0.08
126-791A-25X-CC, 15–217	0.18	0.12	0.5	0.06	0.50		
126-791A-28X-1, 68–70	246.68	0.09	0.7	0.25	0.16	0.04	
126-791A-28X-CC, 25–247	0.17	0.12	0.4	0.05	0.40		
126-791A-30X-CC, 15–265	0.12	0.03	0.7	0.09	0.70		
126-791A-33X-1, 16–18	294.46	2.62	21.8	3.20	0.58	0.11	
126-791A-39X-1, 12–13	352.42	1.88	15.7	2.74	0.86	0.13	
126-791A-39X-1, 42–45	352.72	0.22	1.8	0.43	0.21	0.09	
126-791A-40X-1, 2–3	362.02	0.13	1.1	0.26	0.13		
126-791A-42X-1, 10–11	381.50	0.45	3.7	0.71	0.26	0.09	
126-791B-10R-1, 34–35	473.64	1.24	10.3	1.80	0.56	0.06	0.07
126-791B-10R-1, 86–96	474.16	1.98	16.5	2.40	0.42	0.04	
126-791B-13R-1, 46–50	502.56	2.29	19.1	2.79	0.50	0.06	0.17
126-791B-13R-1, 140–150	503.50	3.59	29.9	4.14	0.55	0.05	0.06
126-791B-13R-2, 44–47	504.04	2.91	24.2	3.40	0.49	0.04	0.11
126-791B-16R-1, 23–25	531.43	2.58	21.5	3.23	0.65	0.05	0.14
126-791B-18R-1, 4–7	550.64	0.56	4.7	0.68	0.12	0.02	0.21
126-791B-22R-1, 69–71	589.69	3.14	26.2	4.12	0.98	0.08	0.05
126-791B-23R-1, 77–79	599.47	3.90	32.5	4.92	1.02	0.09	0.14
126-791B-23R-2, 84–86	601.04	3.18	26.5	4.18	1.00	0.10	0.21
126-791B-23R-3, 115–125	602.85	3.32	27.7	4.37	1.05	0.03	
126-791B-23R-CC, 2–4	603.91	3.26	27.2	4.05	0.79	0.08	0.43

Table 15 (continued).

Core, section, interval (cm)	Depth (mbsf)	Inorg. carbon (%)	$CaCO_3$ (%)	Total carbon (%)	Org. carbon (%)	Tot N (%)	Tot S (%)
126-791B-24R-1, 54–56	608.94	2.81	23.4	3.43	0.62	0.06	0.02
126-791B-25R-1, 25–27	618.35	1.86	15.5	2.40	0.54	0.07	0.13
126-791B-25R-2, 13–15	619.73	3.22	26.8	3.86	0.64	0.07	0.78
126-791B-26R-1, 4–6	627.74	3.27	27.2	3.81	0.54	0.04	0.03
126-791B-27R-1, 37–39	637.37	3.46	28.8	4.23	0.77	0.07	0.03
126-791B-28R-1, 120–121	647.80	4.46	37.2	5.25	0.79	0.08	0.07
126-791B-28R-3, 81–83	650.41	4.53	37.7	5.32	0.79	0.08	0.02
126-791B-28R-3, 140–150	651.00	3.86	32.2	4.74	0.88	0.07	0.10
126-791B-30R-1, 146–147	667.46	3.51	29.2	4.11	0.60	0.05	
126-791B-30R-3, 107–108	670.07	2.85	23.7	3.45	0.60	0.06	0.04
126-791B-31R-1, 83–84	676.43	1.98	16.5	2.48	0.50	0.06	0.05
126-791B-31R-3, 70–71	679.30	4.93	41.1	5.45	0.52	0.05	0.03
126-791B-32R-1, 30–32	685.60	3.17	26.4	3.75	0.58	0.05	0.08
126-791B-34R-1, 116–118	705.76	3.38	28.2	4.05	0.67	0.06	0.07
126-791B-34R-3, 37–39	707.97	5.12	42.6	5.79	0.67	0.06	
126-791B-34R-3, 140–150	709.00	4.21	35.1	4.91	0.70	0.05	0.22
126-791B-34R-4, 68–70	709.78	5.17	43.1	5.70	0.53	0.05	
126-791B-36R-1, 28–30	723.88	3.18	26.5	3.84	0.66	0.07	0.02
126-791B-36R-4, 134–136	729.44	4.86	40.5	5.31	0.45	0.04	
126-791B-37R-2, 66–67	735.36	1.62	13.5	2.06	0.44	0.04	0.03
126-791B-38R-2, 8–10	744.38	4.01	33.4	4.49	0.48		0.06
126-791B-38R-4, 15–18	747.45	2.46	20.5	2.56	0.10		0.04
126-791B-39R-1, 9–11	752.49	4.03	33.6	4.51	0.48		0.04
126-791B-39R-1, 140–150	753.80	1.72	14.3	1.86	0.14	0.02	0.05
126-791B-39R-2, 108–109	754.98	3.42	28.5	3.82	0.40	0.04	
126-791B-40R-1, 9–11	762.19	3.78	31.5	4.12	0.34	0.04	0.04
126-791B-40R-3, 50–52	765.60	4.53	37.7	4.98	0.45	0.05	
126-791B-41R-1, 17–19	771.87	3.41	28.4	3.88	0.47	0.05	
126-791B-41R-3, 72–74	775.42	6.03	50.2	6.47	0.44	0.05	
126-791B-42R-1, 36–38	781.66	4.59	38.2	5.03	0.44	0.04	
126-791B-42R-2, 0–10	782.80	4.24	35.3	4.76	0.52		
126-791B-43R-1, 9–11	791.09	3.64	30.3	4.14	0.50	0.07	
126-791B-44R-1, 40–41	801.10	4.66	38.8	5.17	0.51	0.04	
126-791B-44R-1, 98–99	801.68	4.22	35.2	4.53	0.31	0.03	
126-791B-44R-2, 97–98	803.17	3.25	27.1	3.62	0.37	0.04	
126-791B-45R-2, 96–99	812.76	4.74	39.5	5.18	0.44	0.04	
126-791B-45R-2, 140–150	813.20	5.46	45.5	5.95	0.49		
126-791B-46R-1, 43–45	820.43	2.70	22.5	3.07	0.37	0.04	
126-791B-46R-2, 15–18	821.65	4.88	40.7	5.31	0.43	0.04	

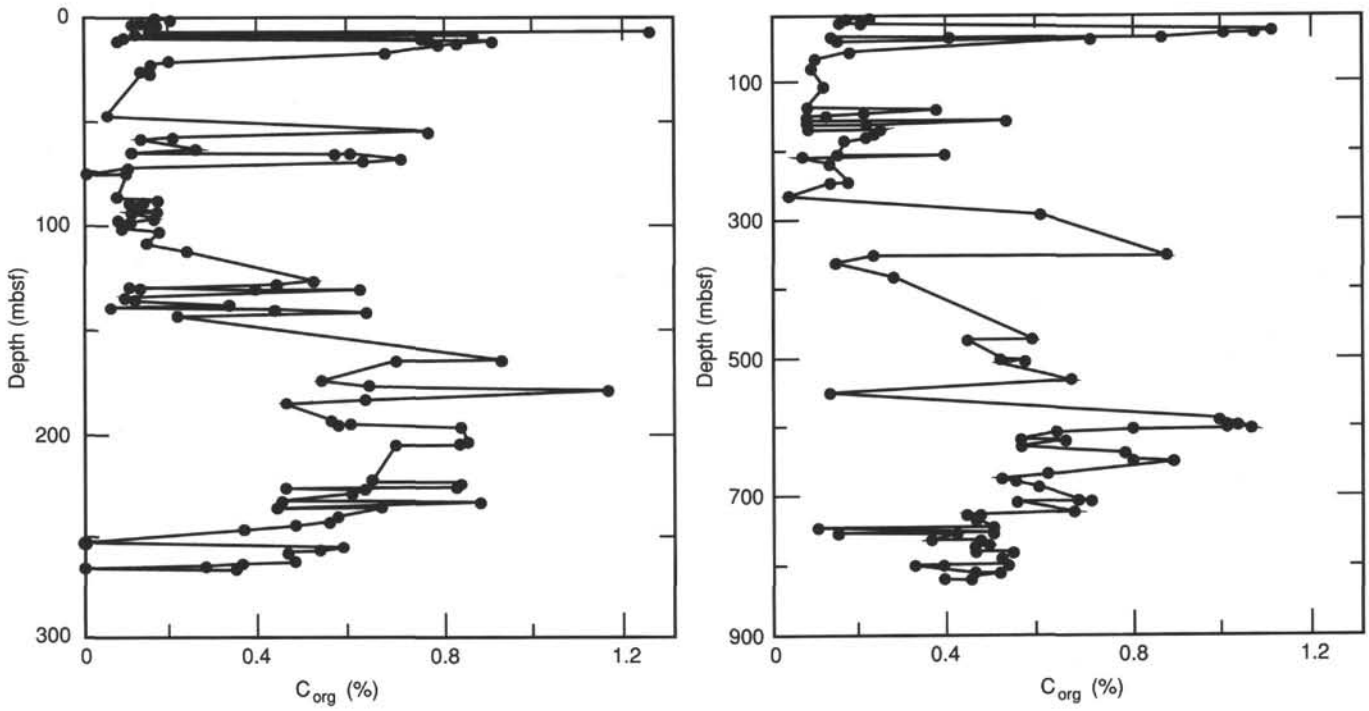

Figure 65. Concentrations of organic carbon, Sites 790 (left) and 791 (right).

Table 16. Composition of pore water and drilling mud filtrate at Sites 790 and 791.

Core, section, interval (cm)	Depth (mbsf)	pH	Alk. (mM)	Sal. (g/kg)	Cl^- (mM)	SO_4^{2-} (mM)	Na (mM)	Mg^{2+} (mM)	Ca^{2+} (mM)	K (mM)	Li (μM)	Sr (μM)	Fe (μM)	Mn (μM)	SiO_2 (μM)	NH_4 (μM)
126-790A																
2H-3, 140–150	13.25	7.66	4.46	35.5	554	27.9	474	53.5	9.7	10.2	25.1	90	9	39	677	271
3H-5, 140–150	25.75	7.62	3.94	35.0	553	27.4	470	53.1	10.2	9.3	25.1	90	7	28	477	197
126-790B																
6H-3, 140–150	46.95	7.93	2.70	35.0	555	27.8	478	53.0	10.8	9.2	23.3	89	7	13	239	56
8H-5, 140–150	69.05	7.64	4.79	35.0	560	27.6	475	52.2	9.6	8.0	35.9	97	12	25	823	695
9H-2, 140–150	74.25	7.56	4.90	35.5	561	27.2	485	52.6	10.3	6.5	39.4	98	7	22	500	733
126-790C																
2H-4, 140–150	100.45	7.69	3.99	36.5	563	26.8	483	53.8	11.7	5.4	62.8	100	43	19	392	572
5H-5, 140–150	130.95	7.62	3.40	35.5	567	25.3	478	51.9	11.0	6.7	50.2	98	12	24	718	894
10X-1, 101–111	165.96	7.45	5.68	35.5	563	21.2	472	52.3	9.5	7.1	48.4	105	6	10	956	1234
13X-2, 140–150	196.85	7.36	9.29	35.0	560	15.1	472	52.0	5.6	8.1	30.5	111	11	9	962	1468
16X-3, 140–150	227.25	7.39	9.40	35.0	560	18.2	473	51.9	5.7	8.7	30.5	103	11	10	942	1425
18X-2, 140–150	254.65	7.4	5.99	35.0	560	22.9	478	50.0	7.5	9.9	30.2	98	16	7	1003	752
126-791A-																
2H-5, 140–150	11.95	7.47	4.11	36.0	569	28.5	487	45.8	19.2	6.8	80.7	105	88	74	284	281
5H-3, 140–150	37.45	7.56	3.01	36.0	576	27.5	493	44.3	19.7	7.3	93.5	103	35	40	576	331
9H-6, 140–150	80.25	7.86	3.19	36.0	563	28.1	478	52.8	12.0	9.5	40.4	95	LD	27	269	175
12H-5, 140–150	107.85	7.77	3.54	35.5	558	28.8	473	52.1	12.3	8.8	42.2	95	LD	34	338	271
15H-6, 25–35	137.30	7.82	3.72	36.0	565	26.6	478	52.8	10.9	8.3	45.9	95	4	21	263	266
18H-6, 90–100	166.95	7.77	4.66	36.5	570	26.9	484	53.0	10.8	6.6	55.0	95	LD	14	506	440
22H-6, 140–150	205.85	7.53	4.55	36.0	571	26.5	486	52.7	10.8	6.6	64.2	95	1	22	487	415
126-791B																
10R-1, 86–96	474.21	7.53	3.76	36.0	557	27.6	484	48.7	15.7	5.8	60.5	99	2	26	717	536
13R-1, 140–150	503.55	7.48	2.39	36.0	566	26.8	483	49.5	16.1	5.6	51.4	96	3	36	850	417
23R-3, 115–125	602.90	7.33	4.58	36.0	561	25.5	481	49.5	15.7	5.7	53.2	107	LD	33	1001	811
28R-3, 140–150	651.05	7.34	3.98	35.5	562	24.2	491	47.9	14.2	6.3	58.7	121	2	12	1049	1110
34R-3, 140–150	709.05	7.39	3.77	36.0	558	25.9	469	49.6	13.1	9.6	36.7	103	2	23	947	310
39R-1, 140–150	753.85	7.45	4.10	36.0	561	26.2	481	50.4	13.0	9.7	40.4	109	13	12	856	398
42R-2, 0–10	782.85	7.32	3.33	36.5	562	26.1	480	50.3	13.2	10.2	40.4	107	3	16	999	196
45R-2, 140–150	813.20	7.48	2.32	36.5	558	26.7	483	49.6	12.5	10.6	27.5	99	1	12	682	47
Drilling mud filtrate		9.01	0.87		267	14.3	251	5.4	6.0	4.0	23.8	93	LD	LD	16	LD
Surface seawater		8.05	2.67		563	28.6	475	53.3	10.7	10.0	31.2	29	LD	LD	2	LD

Note: LD = less than the detection limit.

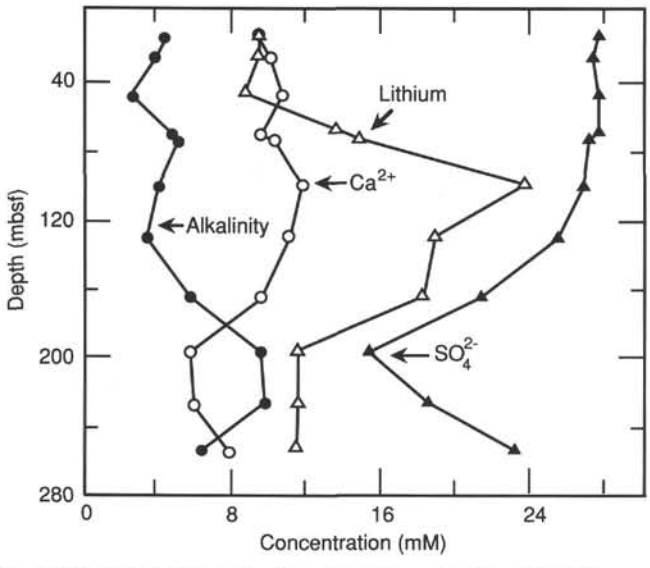

Figure 66. Composition of sedimentary pore water from Site 790.

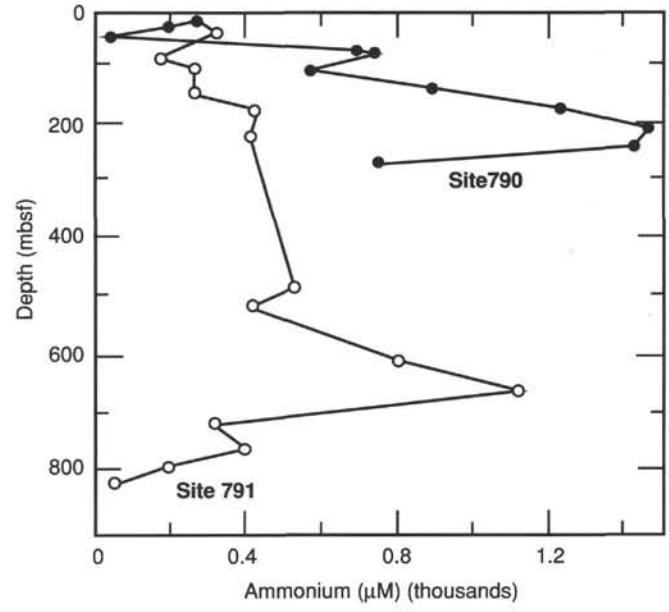

Figure 67. Concentrations of ammonium in pore waters from Sites 790 and 791.

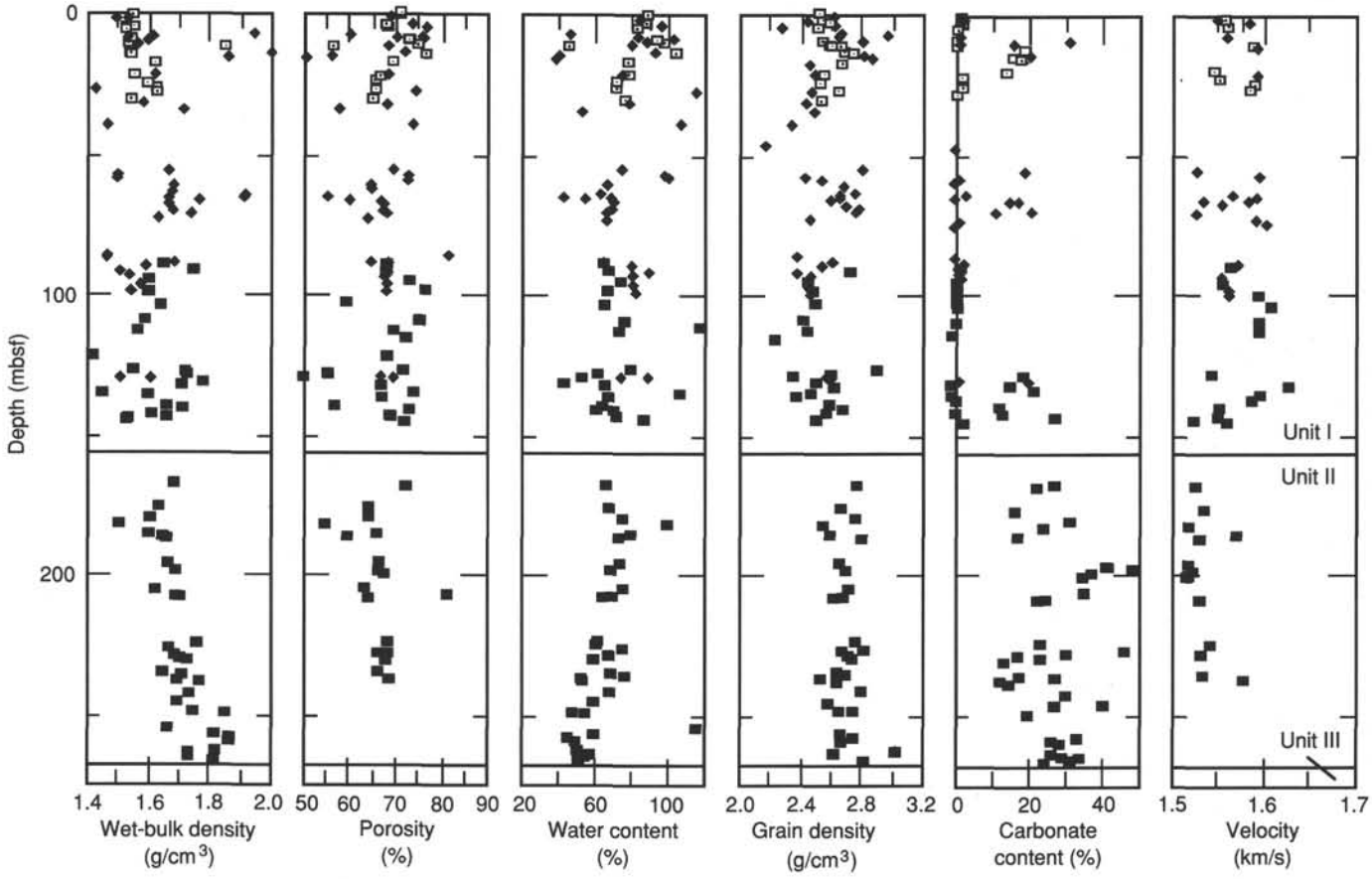

Figure 68. Downhole plots of index properties, carbonate content, and velocity for Holes 790A (open squares with dots), 790B (diamonds), and 790C (closed squares). Horizontal lines indicate Unit I, II, and III boundaries.

three holes. Particularly good correlation is observed in the grain density values. It is likely that grain density is the parameter least changed by drilling disturbance.

Calcium Carbonate

The upper 140 m of Unit I at Site 790 is characterized by low calcium carbonate contents, generally <2–3 wt% (Fig. 68). These low values are usually associated with thick beds of silt- to gravel-size volcanogenic material rich in pumice (see "Lithostratigraphy and Accumulation Rates" section, this chapter). Thinner layers, 5–10 m thick, in which $CaCO_3$ contents reach 30%, are also present within this unit. Dilution of pelagic carbonate sedimentation by thick, sporadic, geologically instantaneous volcanogenic sediment input is the probable cause of these variations.

At the transition to Unit II, average carbonate contents increase to approximately 30%. The magnitude of the carbonate content fluctuations increases in Unit II, ranging from a low of 13.5% to a high of 49%.

Vane Shear Strength

Vane shear strength measurements in Holes 790B and 790C range from <5 to 110 kPa; values in the sediments above 240 mbsf never exceed 65 kPa (Fig. 70). Trends in the shear strength measurements between 80 and 240 mbsf correlate well with those in water content. A fairly consistent inverse trend between the two parameters is observed (Tables 17 and 18). Much of the variation in shear strength, water content, and other index properties may be attributed to lithologic and mineralogical variations such as grain size, carbonate content, degree of consolidation, and changes in the clay mineral assemblages (see "Lithostratigraphy and Accumulation Rates" section, this chapter). However, the effects of coring disturbance and other artifacts attributed to the sampling procedure cannot be disregarded (e.g., Becker, Sakai, et al., 1988, "Sites 677 and 678" chapter).

Sonic Velocity

Sonic velocity measurements were performed on discrete samples from Site 790 (Holes 790A, 790B, and 790C) with the HF method (Table 17 and Fig. 68). In addition, all cores from Holes 790A and 790B and Cores 126-790C-1H through -20X were passed through the MST and sonic velocity measurements were obtained (Fig. 71). The MST *P*-wave data, obtained at 2.5-cm intervals, were filtered to remove low signal strengths and then averaged over 10-cm intervals to reduce the number of data points to a manageable size. A comparison of HF and MST velocity measurements shows good correlation of these data for the upper parts of the APC holes (Figs. 71 and 72). The MST values obtained deeper in the section are faster than those given by the HF method. Because variable contact with the core liner from XCB coring (reduced core diameters) should result in a lower MST velocity, the cause of these higher MST velocity values is problematic.

Drilling three separate holes at Site 790 provided means for an independent check on velocity measurements in the overlapping regions of Holes 790A and 790B and Holes 790B and 790C. Velocity measurements at the same depth below seafloor in different holes produced almost identical values, indicating that (1) similar sediments were present and (2) there is a high degree of precision in these measurements between holes and be-

Table 17. Physical properties (index, velocity, and carbonate) data for Site 790.

Core, section, interval (cm)	Depth (mbsf)	Wet-bulk density (g/cm^3)	Dry-bulk density (g/cm^3)	Porosity (%)	Water content (%)	Grain density (g/cm^3)	Void ratio	Velocity (km/s)	Carbonate (%)
126-790A-									
1H-1, 52–54	0.52	1.54	0.84	71	88.9	2.52	2.43	1.56	1.8
1H-2, 92–94	2.42	1.52	0.84	69	87.3	2.61	2.25	1.57	1.5
1H-3, 23–25	3.23	1.54	0.86	69	83.9	2.54	2.19	[a]1.89	1.2
1H-6, 25–27	7.75	1.54	0.82	73	94.4	2.55	2.73		1.2
2H-1, 82–84	9.62	1.55	0.81	75	97.7	2.61	2.98	1.59	0.6
2H-2, 70–72	11.00	1.85	1.30	56	45.1	2.67	1.28		19.6
2H-3, 123–125	13.03	1.54	0.78	76	103.9	2.73	3.24	[a]1.50	18.5
2H-3, 140–150	13.20								17.0
2H-6, 134–136	17.64	1.62	0.94	69	77.5	2.67	2.24	1.55	14.7
3H-2, 102–104	20.82	1.56	0.90	67	78.2	2.53	2.02	1.55	1.9
3H-4, 39–41	23.19	1.60	0.95	66	72.9	2.53	1.92	1.59	1.5
3H-5, 140–150	25.70								1.3
3H-6, 56–58	26.36	1.63	0.97	66	71.1	2.63	1.94		1.2
4H-1, 140–142	29.20	1.55		66	76.7	2.53	1.90		
126-790B-									
1H-1, 62–65	0.62	1.53	0.74	68	84	2.60	2.15	1.55	2
1H-2, 106–109	2.56	1.49	0.81	69	89	2.45	2.19	1.59	1
1H-3, 23–25	3.23	1.52	0.80	73	96	2.63	2.70		1
2H-1, 51–53	5.01	[a]1.4	[a]0.64	[a]76.6	[a]127.6	[a]2.27	[a]3.27		
2H-2, 53–55	6.53	[a]1.94	[a]1.35	[a]59.3	[a]45.5	[a]2.97	[a]1.46	1.56	1
2H-3, 112–115	8.62	1.53	0.78	75	103	2.65	3.07	1.51	31
2H-4, 89–92	9.89	1.59	0.87	73	88	2.79	2.65	1.51	16
2H-5, 61–64	11.11	1.56	0.89	68	81	2.60	2.15	1.59	1
2H-6, 36–39	12.36	1.54	0.83	72	92	2.66	2.55	1.51	20
3H-1, 39–41	14.39	2.00	1.45	56	40	2.80	1.27		
3H-1, 139–140	15.39	1.85	1.26	50	39	2.86	1.01		
3H-3, 76–78	17.76	[a]1.44	0.77	[a]67	[a]92	2.46	2.06		
3H-5, 121–123	21.21	1.62	0.95	68	1	2.49	2.09	1.59	
4H-3, 75–77	27.25	[a]1.43	[a]0.69	[a]74	[a]113	2.47	[a]2.88		
4H-6, 101–103	32.01	[a]1.58	[a]0.91	[a]67	[a]77	2.43	[a]2.09		
5H-1, 108–110	34.08	[a]1.71	[a]1.15	[a]56	[a]51	2.49	[a]1.32		
5H-4, 88–90	38.38	[a]1.46	[a]0.73	[a]73	[a]106	2.34	[a]2.73		
6H-1, 61–62	43.11	[a]1.38	[a]0.58	[a]80	[a]147	[a]2.15	[a]4.09		
6H-3, 140–150	46.90								0
7H-3, 74–76	55.74	1.66	0.98	69	74	2.80	2.21	1.53	19
7H-4, 62–64	57.12	1.50	0.78	73	98	2.41	2.65	1.60	1
7H-5, 25–27	58.25	1.49	0.77	73	99	2.53	2.65		0
7H-CC, 9–11	61.09	1.68	1.04	65	65	2.67	1.83		
8H-1, 134–135	62.94	1.68	1.04	65	65	2.74	1.83	1.57	3
8H-2, 132–134	64.42	1.92	1.38	55	42	2.64	1.22	1.59	0
8H-3, 123–134	65.92	1.67	1.02	66	68	2.61	1.92	1.54	15
8H-4, 9–11	66.19	1.76	1.17	60	53	2.65	1.48	1.59	17
8H-4, 94–96	67.04	1.67	1.01	67	69	2.67	2.00	1.55	
8H-5, 140–150									21
8H-6, 42–44	69.52	1.68	1.02	66	68	2.78	1.98	1.52	11
8H-6, 110–112	70.20	1.74	1.07	68	67	2.74	2.11	1.53	
9H-1, 124–126	72.54	1.53	1.00	64	66	2.45	1.75	1.59	1
9H-3, 13–16	74.43								0
10H-4, 58–60	86.08	[a]1.46	[a]0.66	[a]81	[a]131	2.35	[a]4.30		0
10H-5, 81–83	87.81	1.68	1.05	64	64	2.61	1.78	1.57	2
10H-6, 96–98	89.46	1.59	0.92	69	79	2.54	2.19		1
11H-1, 114–116	91.84	[a]1.51	[a]0.82	[a]68	[a]87	2.37	[a]2.18		1
11H-2, 90–93	93.10	1.53	0.88	67	80	2.46	1.99	1.58	2
11H-4, 112–115	96.32	1.57	0.90	68	80	2.43	2.11	1.56	1
11H-6, 16–19	98.36	1.54	0.87	68	82	2.46	2.11	1.57	1
15X-1, 12–15	129.40	1.60	0.94	67	75	2.58	2.02		20
15X-1, 46–48	129.76	1.51	0.83	69	88	2.56	2.25		1
126-790C-									
1H-3, 34–36	88.34	1.65	1.02	64	66	2.61	1.79	1.57	2.2
1H-4, 63–65	90.13	1.75	1.07	69	67	2.71	2.18		
1H-6, 107–109	93.57	1.60	0.95	66	74	2.45	1.98	1.56	1.4
2H-2, 107–109	97.07	1.60	0.98	64	68	2.48	1.74	1.59	0.7
2H-5, 0–5	100.50								0.7
2H-6, 80–82	102.80	1.64	1.01	63	65	2.51	1.72	1.61	0.6
3H-3, 62–65	107.82	1.59	0.93	67	76	2.42	2.04	1.60	0.7
3H-6, 39–41	112.09	1.57	0.92	66	75	2.45	1.90	1.60	0.5
4H-1, 60–62	114.50	[a]1.32	[a]0.60	[a]72	[a]127	[a]2.23	[a]2.57		
4H-5, 71–73	120.61	[a]1.43	[a]0.67	[a]75	[a]118	[a]1.71	[a]3.11		
5H-2, 38–40	125.38	1.56	0.89	68	80	2.91	2.10		
5H-3, 81–83	127.31	1.72	1.08	65	63	2.61	1.84	1.55	18.8

Table 17 (continued).

Core, section, interval (cm)	Depth (mbsf)	Wet-bulk density (g/cm³)	Dry-bulk density (g/cm³)	Porosity (%)	Water content (%)	Grain density (g/cm³)	Void ratio	Velocity (km/s)	Carbonate (%)
126-790C- (Cont.)									
5H-4, 35–38	128.35	[a]1.75	[a]1.15	[a]59	[a]53	[a]2.35	[a]1.47	[a]1.49	
5H-5, 59–61	130.09	1.79	1.26	54	44	2.50	1.16	1.63	0.3
5H-5, 104–150	130.90								15.5
5H-6, 91–94	131.91	1.71	1.05	66	66	2.62	1.96		21.5
6H-1, 125–127	134.45	1.46	0.73	74	108	2.47	2.84	1.60	0.4
6H-2, 91–94	135.61	1.60	0.99	63	68	2.39	1.72	1.59	0.7
6H-4, 88–91	138.58	1.66	1.03	64	65	2.59	1.76	1.56	13.1
6H-5, 63–66	139.83	1.71	1.08	64	62	2.67	1.75	1.50	0.7
6H-6, 67–70	141.37	1.61	0.95	66	73	2.57	1.94	1.56	13.8
6H-7, 22–25	142.42	[a]1.67	[a]0.99	[a]67.7	[a]71		[a]2.10	1.53	28.5
7H-2, 25–27	143.94	1.53	0.84	70	88	2.50	2.30	1.56	3.0
10X-1, 101–111	165.91								
10X-2, 36–39	166.37	1.69	1.05	65	66	2.78	1.89	1.53	28.2
11X-1, 103–106	175.63	1.64	1.01	64	67	2.67	1.81	1.54	22.6
11X-3, 51–55	178.11	1.62	0.95	68	76	2.78	2.14	1.52	17.2
11X-5, 42–45	181.02	1.51	0.79	74	99	2.55	2.78	1.52	32.2
12X-1, 43–47	184.63	1.60	0.92	70	80	2.61	2.27	1.57	24.7
12X-CC, 6–9	185.66	1.65	0.98	68	73	2.82	2.15	1.53	18.5
13X-1, 116–118	195.06	1.68	0.99	70	74	2.66	2.32	1.52	42.2
13X-2, 99–100	196.39	[a]1.24	[a]1.01	[a]23.8	[a]24.4	[a]2.68			49.0
13X-2, 140–150	196.80								43.0
13X-3, 97–99	197.87	1.69	1.02	68	71	2.69	2.17	1.53	38.3
13X-4, 14–16	198.54	[a]1.86	[a]1.00	[a]65	[a]68	[a]2.69		1.52	36.5
14X-1, 126–128	204.86	1.63	0.95	69	76	2.72	2.17	1.52	36.5
14X-2, 122–124	206.32	1.70	1.02	69	71	2.65	2.18	1.52	24.4
14X-3, 32–34	206.92	1.69	1.04	66	66	2.68	1.91	1.53	25.2
16X-1, 91–93	223.71	1.76	1.12	66	62	2.76	1.90	1.54	24.4
16X-2, 104–106	225.34	1.68	0.98	71	76	2.82	2.41	1.52	46.9
16X-3, 67–71	226.49	1.69	1.06	64	63	2.71	1.78	1.53	31.4
16X-3, 140–150	227.20		1.05						18.0
16X-4, 99–101	228.29	1.71		67	68	2.71	2.07	1.53	23.9
16X-5, 91–93	229.71	1.74	1.11	64	61	2.75	1.79		13.5
17X-1, 101–103	233.41	1.65	0.99	67	71	2.67	2.02	1.54	18.5
17X-2, 74–77	234.64	1.71	0.93	72	76	2.70	2.60	1.52	27.6
17X-3, 111–113	236.51	1.70	1.12	59	54	2.52	1.41	1.58	14.1
17X-4, 13–16	237.03	1.77	1.17	61	54	2.64	1.55		14.9
17X-6, 105–108	240.95	1.74	1.06	69	68	2.79	2.18		31.1
18X-2, 35–38	243.95	1.70	1.08	63	61	2.47	1.67		27.9
18X-2, 140–150	245.00								40.9
18X-4, 82–85	247.42	1.86	1.26	61	50	2.75	1.54		19.7
18X-4, 126–129	247.86	1.75	1.14	62	57	2.66	1.63		
19X-2, 43–46	253.63	[a]1.67	[a]0.80	[a]87	[a]116	[a]2.22	[a]6.92		
19X-3, 115–118	255.85	1.82	1.16	67	60	2.66	2.02		33.5
19X-4, 124–127	257.44	1.87	1.27	58	46	2.75	1.37		27.2
19X-5, 72–73	258.42	1.87	[a]1.21	61	50	2.68	1.54		29.3
20X-1, 111–115	262.51	[a]1.82	1.13	[a]60	[a]52	[a]3.04	1.55		27.4
20X-2, 57–60	263.47	1.73	[a]1.10	61	56	2.63	1.56		29.8
20X-3, 38–41	264.78	[a]1.74	1.22	[a]59	[a]54	[a]3.03	[a]1.49		33.0
20X-4, 12–15	266.02	1.82	1.30	61	52	2.81	1.57		25.2
33X-CC, 9–11	378.30							4.26	

[a] Results are of uncertain quality.

tween the two techniques (HF and MST; Fig. 72). The HF velocity data at this site exhibit minimal variation, with a total range of 1.51–1.63 km/s in the entire recovered section.

A general increase in velocity is observed from the seafloor down to about 155 mbsf (Unit I). Velocity measurements in this unit average 1.57 km/s (HF). A good correlation is observed between the velocity data obtained by both methods, although there is a wider range of scatter in the MST velocity data. A small (~40 m/s), but distinct, velocity inversion occurs between Units I and II (Figs. 68 and 71).

Within Unit II, velocity data average 1.54 km/s, are relatively uniform, and show a slight increase downhole to 266.7 mbsf. The HF and MST methods within Unit II show similar trends, but the MST measurements are consistently higher. This offset may result from the effect of XCB coring methods used over this interval, which can result in a lack of sediment contact with the core liner. A scoriaceous basalt (Unit III) lies beneath Unit II. Because of the low recovery, only one velocity measurement was performed, yielding a velocity of 4.26 km/s (Section 126-790C-33X-CC; 378.30 mbsf).

Thermal Conductivity

Thermal conductivity values of sediments from Holes 790A and 790B (Fig. 73 and Table 19) generally increase downhole. Values in Unit I (especially in the upper 50 m) are variable, averaging 0.902 W/m · K and ranging up to 1.06 W/m · K. This variability may be related to lithologic changes, with higher values in carbonate-rich sediments and lower values in carbonate-poor sands and gravels. Within Unit II, values tend to increase downhole and exhibit less overall variability than in Unit I. Ther-

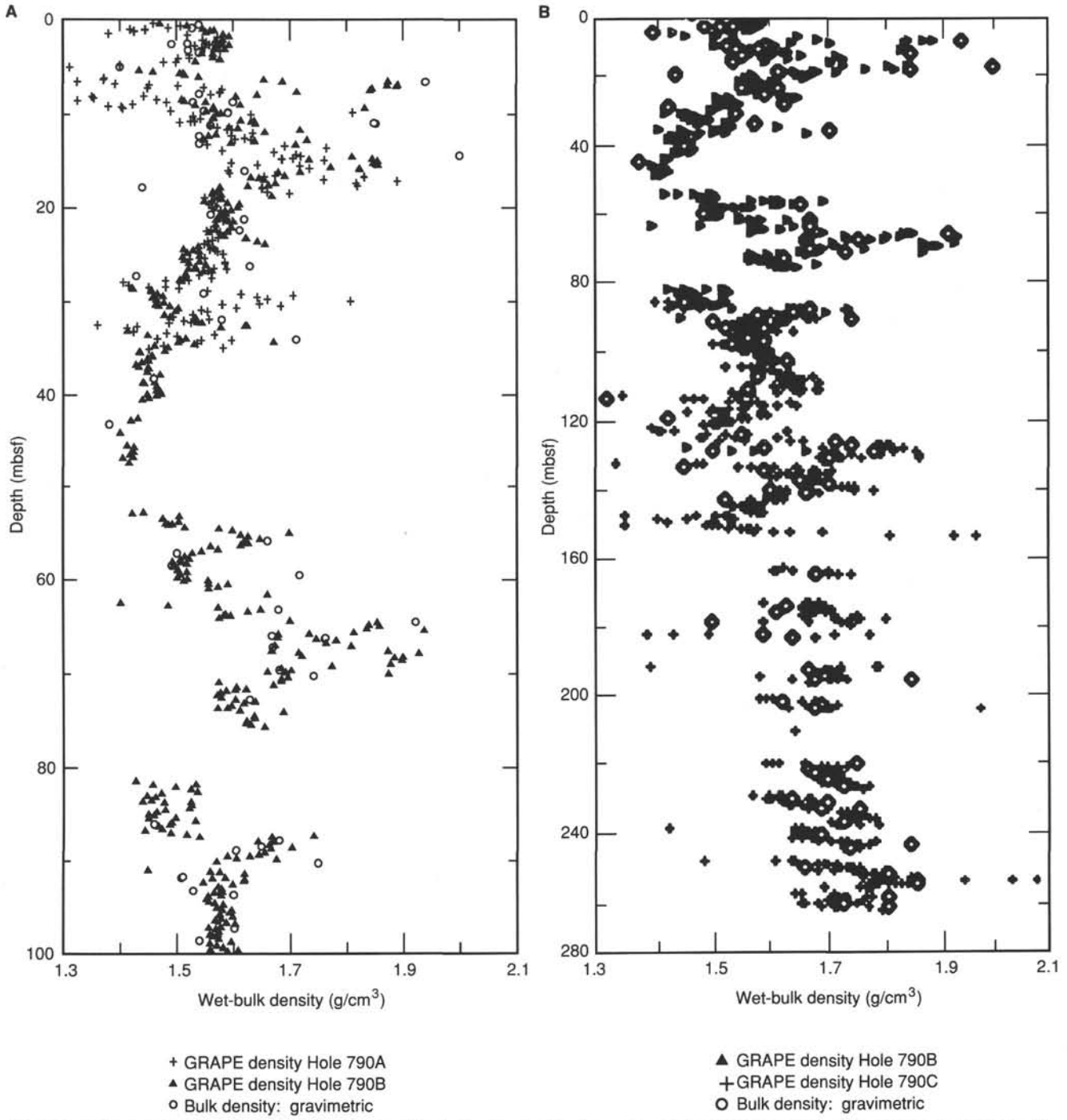

Figure 69. Comparison of gravimetric and GRAPE wet-bulk density. **A.** Overlap region of Holes 790A and 790B. **B.** Overlap region of Holes 790B and 790C.

mal conductivity values in this unit are higher than in Unit I and average 1.069 W/m · K (with a range of 0.983 – 1.183 W/m · K).

Thermal conductivity measurements are made before cores are split, not allowing assessment of coring disturbance prior to making the measurements. Because lower thermal conductivity values may result from coring disturbance (e.g., an increase in water content), we suspect that the higher values are more representative of *in-situ* conditions. Because of the low recovery, no thermal conductivity measurements were conducted on Unit III rocks.

Site 791

Index Properties

As at Site 790, wet-bulk density and grain density at Site 791 increase with depth. Mean values in Unit I are 1.64 and 2.52 g/cm^3 (Fig. 74), respectively. Unit II wet-bulk and grain density

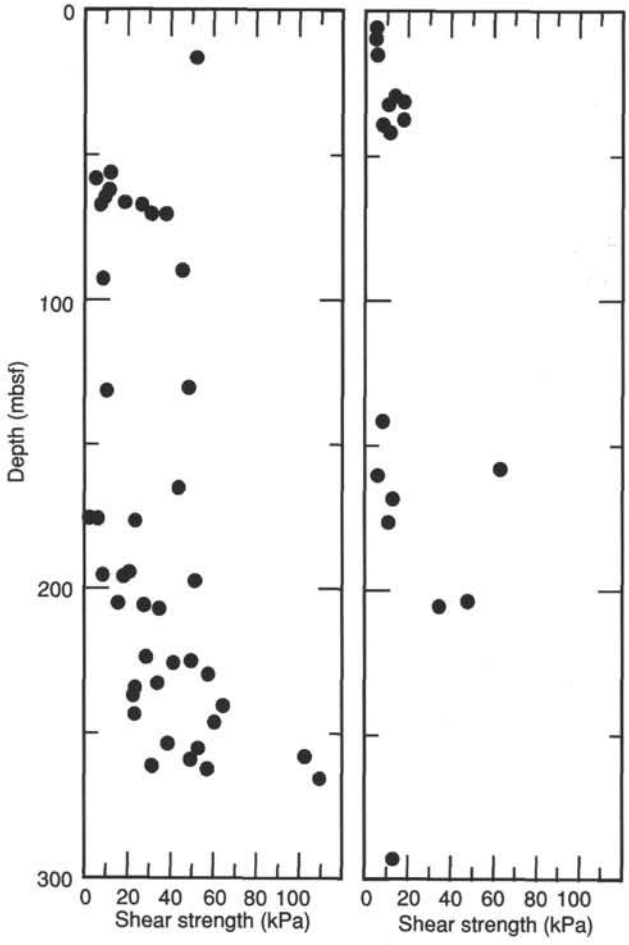

Figure 70. Plots of shear strength vs. depth, Sites 790 (left) and 791 (right).

averages are 1.86 and 2.7 g/cm^3, respectively. Concurrent decreases in porosity (averages of 65.9% in Unit I and 59.1% in Unit II) and water content (averages of 73.6% in Unit I and 48.8% in Unit II) are also noted (Table 20 and Fig. 74). With the exception of grain density, the majority of these downhole changes can be attributed to increased consolidation with depth.

Because the first eight cores in Hole 791B had essentially no recovery, no samples were taken for index properties. Therefore, a gap of about 80 m occurs in the data and no information on the overlap in the cored intervals exists. However, trends observed in Hole 791A appear to continue, at least in a general way, in Hole 791B.

Variations in wet-bulk density and grain density, especially within Hole 791A (Unit I), may be related to the sporadic input of pumice-rich material derived from volcanic eruptions (see "Lithostratigraphy and Accumulation Rates" section, this chapter). Porosity and water content trends are similar in shape, but inverse to the bulk-density trends. However, the majority of index properties measured within these pumice-rich layers are suspect. The coarse, unconsolidated nature of this material makes it especially prone to coring disturbance. Therefore, most measured properties may not be representative of the *in-situ* state of the sediment. The parameter that is expected to most resemble the *in-situ* value is grain density. Grain density variations display a strong similarity to those of $CaCO_3$. This is the case even below 450 mbsf where both properties are highly variable (Fig. 74).

Table 18. Shear strength data from Site 790.

Core, section, interval (cm)	Depth (mbsf)	Shear strength (kPa)
126-790B-		
3H-2, 40	15.9	52.2
7H-3, 72	55.7	12.2
7H-5, 27	58.3	5.0
8H-1, 132	62.9	11.1
8H-2, 135	64.5	9.7
8H-3, 136	66.0	18.3
8H-4, 7	66.2	8.2
8H-4, 92	67.0	27.1
8H-6, 42	69.5	30.7
8H-6, 113	70.2	38.1
11H-2, 129	93.5	8.9
126-790C-		
1H-4, 63	90.1	48.7
5H-5, 106	130.6	10.5
5H-6, 58	131.6	43.4
10X-2, 30	166.3	2.3
11X-2, 12	176.2	6.1
11X-2, 28	176.4	23.3
11X-2, 115	177.3	19.8
13X-1, 121	195.1	8.4
13X-2, 90	196.3	18.2
13X-2, 103	196.4	50.8
13X-3, 96	197.9	15.9
14X-1, 125	204.9	28.0
14X-2, 121	206.3	34.7
14X-3, 31	206.9	28.4
16X-1, 87	223.7	49.2
16X-2, 101	225.3	41.0
16X-3, 66	226.5	56.9
16X-5, 95	229.8	34.0
17X-1, 98	233.4	22.9
17X-2, 77	234.7	22.2
17X-3, 114	236.5	64.4
17X-6, 108	241.0	23.6
18X-2, 32	243.9	60.6
18X-4, 80	247.4	39.2
19X-2, 39	253.6	52.7
19X-3, 121	255.9	102.6
19X-5, 121	258.9	49.4
19X-6, 70	259.9	30.9
20X-1, 103	262.4	57.0
20X-2, 50	263.4	109.4

Index property variability is damped within Unit II (Hole 791B). Except for anomalous points that result from coring disturbance and measurement errors, the range of values in the sediments of these four index properties is much less below 450 mbsf (wet-bulk density: 1.64–2.0 g/cm^3; grain density: 2.56–2.89 g/cm^3; porosity: 30%–75%; water content: 21%–75%; Table 20). The unfortunate coincidence of the change in lithologic unit and the change of coring technique makes unequivocal interpretation impossible. However, a comparison with Site 790, which was not rotary cored, but which does display similar index property trends over these stratigraphic intervals, indicates that much of the decrease in variability between Units I and II is real. The difference in the rate of change in the index properties in Unit II of Site 791 compared with Site 790 (approximately 3×10^{-4} g/cm^3/m at Site 791 vs. 1.7×10^{-3} g/cm^3/m at Site 790 for wet-bulk density) may be related to greater depth higher overburden stresses, and a more advanced state of consolidation in Unit II at Site 791.

The correlation between GRAPE and gravimetrically determined wet-bulk densities in Hole 791A is excellent (Fig. 75). Even in the XCB drilled holes below 200 mbsf, where recovery

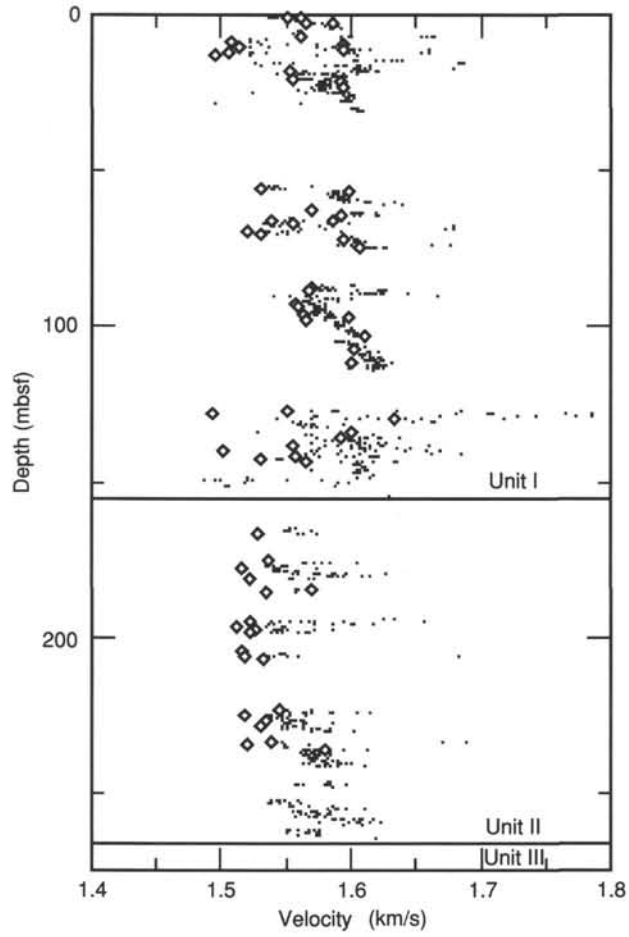

Figure 71. Comparison of sonic velocity determined by Hamilton Frame (diamonds) and multisensor track (small dots) methods for Site 790. Horizontal lines indicate lithologic unit boundaries.

was low and coring disturbance increased, values from the two data sets match extremely well. In contrast, the situation in rotary-drilled Hole 791B is the opposite. Virtually all the gravimetrically derived bulk densities are greater than those determined by the GRAPE, as expected from rotary-drilled sections. The GRAPE volume calculations assume that the core fills the liner. The real core diameter is less than this because of drilling effects. Consequently, the core volume is overestimated and the density underestimated.

An analogous situation was noted in the rotary-drilled section at Site 787 (see "Physical Properties" section, "Site 787" chapter, this volume). However, the dissimilarity between the trends in the two types of measurements is unexpected. Although the GRAPE data is characterized by a high degree of scatter, not even well-defined trends seen in the gravimetric bulk density are observed in the GRAPE data (e.g., compare the densities between 650 and 770 mbsf in Fig. 75). The probable cause of this discrepancy is from variations in the way that the two measurements are made; specifically, differences in the true and GRAPE-estimated volumes of the cores.

A sharp, but not unexpected, change in all measured physical properties occurs at the transition from sediment to igneous rocks (Fig. 74). In general, bulk and grain density values increase, and porosity and water content values decrease. However, these properties are by no means constant within the hard-rock section. Some variability may be attributed to measurement errors related to differences in the sampling times (see "Explanatory Notes" chapter, this volume), but most appears to be related to the inherent properties of the rocks (see "Igneous Petrology" section, this chapter).

After filtering out anomalous data points that are obviously erroneous, some clear-cut trends emerge. The basaltic "mousse," a mixture of vesicular glass matrix and basaltic clasts, is characterized by lower wet-bulk density values and higher porosity values and water contents than the other igneous units. Porosity values as high as 44% were measured in this unit, with a mean value of approximately 36%. Porosity data in the other igneous units in Hole 791B rarely exceed 25% (Table 21). The properties of the clast vs. matrix material in the "mousse" indicate that the porosity and water content of the clasts is lower and the bulk density higher than those of the matrix glass. Samples composed of a mixture of both tend to exhibit intermediate values (Table 21).

Variations in porosity and density values between the various units are linked closely with the mineralogy and chemistry of the different rocks. This is supported by the high grain density of the diabase in Sample 126-791B-57R-1, 7 cm (926 mbsf). The high iron content of this unit (see "Igneous Geochemistry" section, this chapter) is probably the cause of this extreme value (the highest measured). In contrast, the sample with the lowest grain density is that of Sample 126-791B-76R-2, 108 cm (within the diabase; Unit 15), which contained a large amount of low-density gypsum in veins.

In general, the diabase units display low porosity values, ranging from 13.7% in Unit 4 to 17.2% in Unit 17. Again, this variation in properties appears to be tied to chemical and mineralogical changes, not to such variations in compaction as those common in the sedimentary section.

The lowest measured porosity values are found in the deepest recovered unit, a lapilli tuff. Three samples, taken within 50 cm of each other, exhibit an average porosity of 8.5%. These samples are from an upward-fining sequence. A slight positive correlation between porosity and grain size is observed.

Generally, agreement between the visual petrographic estimate of vesicle pore space and the gravimetrically determined porosity data is good (see "Igneous Petrology" section, this chapter). The greatest discrepancies between the two determinations is found in the denser, low-porosity units, such as the diabase units. Although the gravimetric and visual porosity trends are the same, the gravimetrically determined absolute values are often significantly greater in these samples.

Grain density values range from a low of 2.6 g/cm^3 to a high of 3.03 g/cm^3 in the igneous section. Values exhibit a high degree of scatter throughout the hard-rock sequence and may be related to variations in composition.

Calcium Carbonate

The basic trend of low calcium carbonate content in Unit I and increased values in Unit II noted at Site 790 was also observed at Site 791 (Fig. 74). Average $CaCO_3$ contents and small-scale variability increase significantly at the Unit I/II boundary. A more pronounced trend is indicated in Unit I at Site 791. Calcium carbonate values at the base of the sedimentary section at Site 791 are somewhat higher than those at Site 790.

Vane Shear Strength

Unfortunately, poor recovery and drilling disturbance resulted in only a small number of vane shear strength measurements, most of which fall below 15 kPa. Increased values at 36 mbsf and isolated peaks below 150 mbsf are probably related to an increase in grain size (Fig. 70 and Table 22).

Sonic Velocity

Sonic velocity measurements were performed on discrete samples from Holes 791A and 791B with the HF method (Table 20 and Fig. 74). In addition, Cores 126-791A-1H through -42X and

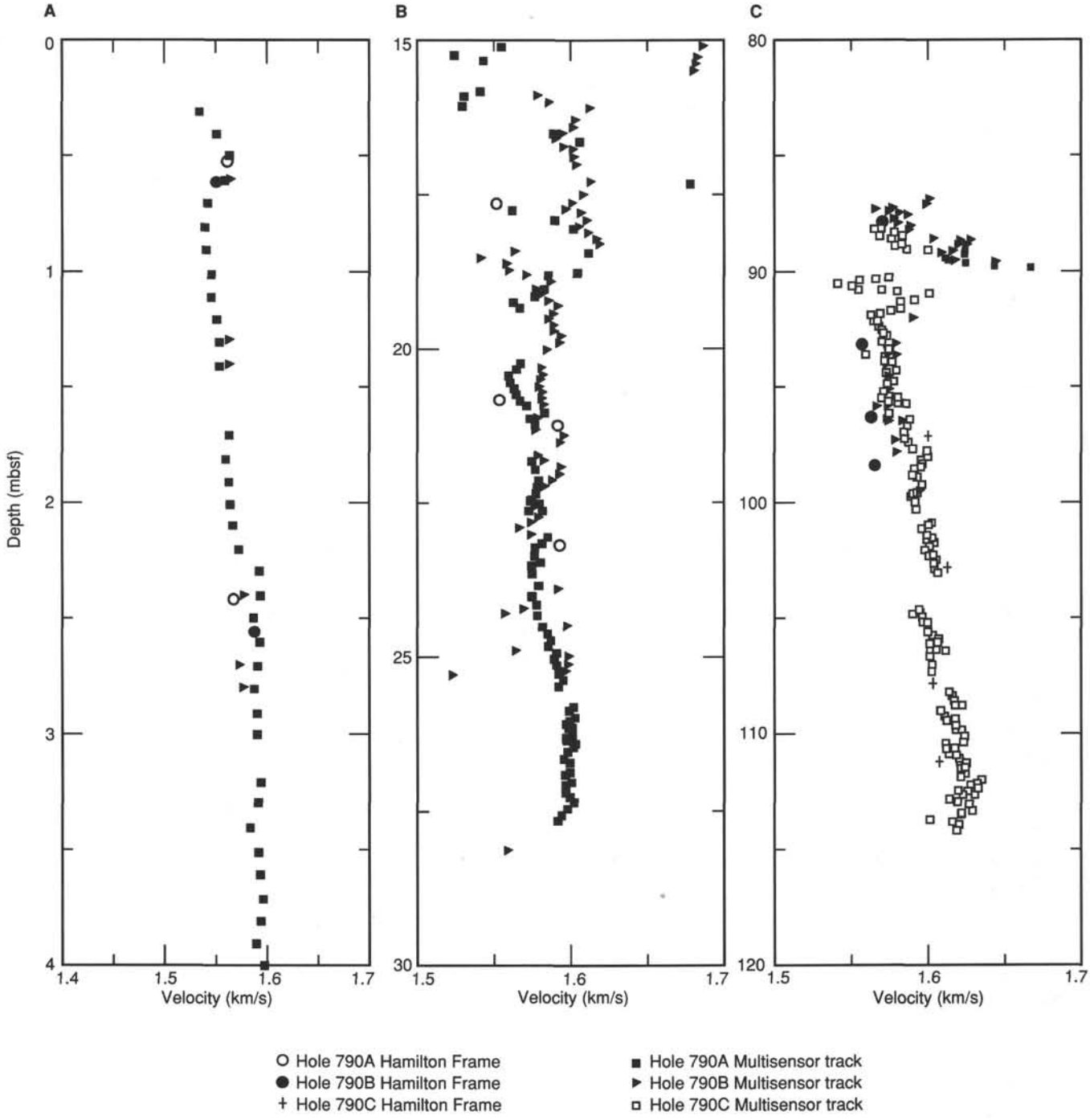

Figure 72. Detailed comparison of sonic velocity measurements between overlapping holes and methods of measurement. **A.** and **B.** Overlap of Holes 790A and 790B. Note that the vertical scales for each graph are different. **C.** Overlap of Holes 790B and 790C.

126-791B-1R through -46R were passed through the MST, and sonic velocity measurements were obtained with the sonic wave (*P*-wave) logger (Fig. 76).

Velocity values in Unit I (0–425 mbsf) range from 1.53 to 1.61 km/s and average 1.58 km/s. Several distinct velocity lows are observed between 27–37 and 158–168 mbsf and are seen in the HF and MST data (see Fig. 76). Both methods show similar values and trends in this unit.

Unit II is characterized by average sonic velocity values of 1.70 km/s with a range from 1.61 to 1.84 km/s. A distinct increase in velocity with depth was observed, with the highest sediment velocity measurements (~1.8 km/s) just above basement. This increase is mainly a result of increased induration.

In Unit III, velocity data range from 2.60 to 5.22 km/s and average 3.80 km/s. Unit III is characterized by two relative highs (~830–900 and >1100 mbsf). This wide variation in velocity

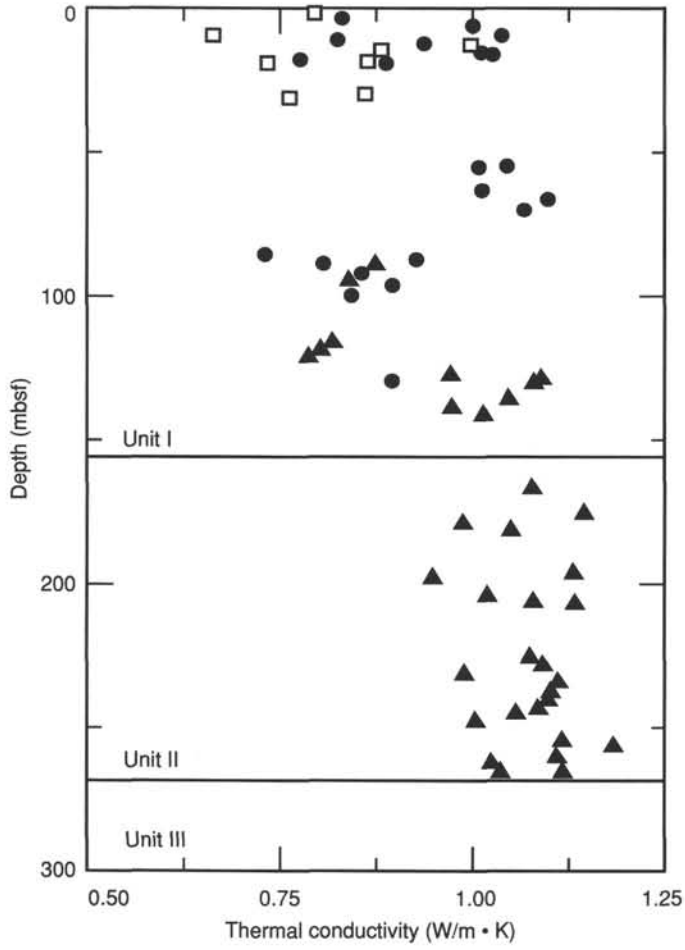

Figure 73. Plot of thermal conductivity, Site 790. Horizontal lines indicate lithologic unit boundaries. Open square = Hole 790A; closed circle = Hole 790B; closed triangle = Hole 790C.

(similar to that observed in the index properties) is probably caused by the variability of igneous rocks in Unit III (see "Igneous Petrology" section, this chapter; a summary of igneous rock types and physical property measurements is given in Table 21). The large velocity and density contrast is responsible for the strong reflection observed between 4.0 and 4.2 s on seismic Line BON II-4 (see "Site Survey" chapter, this volume, and "Seismic Stratigraphy" section, this chapter). The fastest velocity measured was 5.22 km/s in a gypsum vein within a diabase unit.

Thermal Conductivity

Thermal conductivity measurements were performed on as many undisturbed cores as possible from the sedimentary column, as well as on four igneous rock samples (with the half-space method) from below 830 mbsf (Fig. 77 and Table 23). Thermal conductivity values show a distinct increase with depth to the basement, at which point the values drop off slightly. Thermal conductivity data show distinct correlations with index property data. Within Unit I, thermal conductivity data average 0.913 W/m · K. Unit II exhibits higher conductivity values, with an average of 1.193 W/m · K. Unit III is characterized by slightly lower values that average 1.133 W/m · K.

DOWNHOLE MEASUREMENTS

At Hole 791B, the drill pipe became stuck during hole-conditioning procedures in preparation for downhole measurements.

Table 19. Thermal conductivity data from Site 790.

Core, section, interval (cm)	Depth (mbsf)	Thermal conductivity (W/m · K)
126-790A-		
1H-1, 28–29	0.28	0.817
1H-2, 15–16	1.65	0.793
1H-3, 57–58	3.57	[a]2.017
1H-5, 101–102	7.01	[a]2.317
2H-1, 51–52	9.31	[a]0.660
2H-3, 99–100	12.79	0.994
2H-5, 43–44	15.23	0.877
2H-7, 19–20	17.99	0.857
3H-1, 82–83	19.12	[a]0.730
3H-5, 63–64	24.93	0.881
3H-7, 53–54	27.83	1.041
4H-2, 72–73	30.02	0.855
4H-3, 33–34	31.13	0.758
126-790B-		
1H-1, 27–28	0.27	0.8212
1H-3, 11–12	3.11	0.8291
2H-2, 40–41	6.40	0.9972
2H-4, 43–44	9.43	1.0331
2H-5, 24–25	10.74	0.8216
2H-6, 50–51	12.50	0.9362
3H-1, 105–106	15.05	1.0086
3H-2, 41–42	15.91	1.0212
3H-3, 81–82	17.81	0.7763
3H-4, 20–21	18.70	0.8854
7H-2, 119–120	54.69	1.0397
7H-3, 48–49	55.48	1.0039
8H-2, 96–97	64.06	1.008
8H-4, 74–75	65.84	1.097
8H-6, 80–81	69.90	1.065
10H-4, 65–66	86.15	[a]0.7268
10H-5, 82–83	87.82	0.9232
10H-6, 49–50	88.99	0.8022
11H-2, 44–45	92.64	0.8528
11H-4, 87–88	96.07	0.8919
11H-6, 72–73	98.92	0.8382
15X-1, 53–54	129.83	0.8924
126-790C-		
1H-3, 46–47	88.46	0.8695
1H-5, 67–68	91.67	[a]1.45652
1H-7, 27–28	94.27	0.8395
4H-2, 53–54	115.93	0.8119
4H-4, 30–31	118.70	0.8003
4H-6, 41–42	121.81	0.7839
5H-3, 64–65	127.14	0.9686
5H-4, 81–82	128.81	1.0798
5H-6, 75–76	131.75	1.075
6H-2, 34–35	135.04	1.0456
6H-4, 83–84	138.53	0.9691
6H-6, 62–63	141.32	1.0105
10X-2, 25–26	166.26	1.0738
11X-1, 53–54	175.13	1.139
11X-3, 66–67	178.26	0.9824
11X-5, 56–57	181.16	1.0438
13X-2, 77–78	196.17	1.1263
13X-3, 72–73	197.62	0.945
14X-1, 80–81	204.40	1.0157
14X-2, 81–82	205.91	1.0727
14X-3, 28–29	206.88	1.1311
16X-2, 46–47	224.76	1.0692
16X-4, 73–74	228.03	1.0876
16X-6, 16–17	230.46	0.9833
17X-2, 39–40	234.29	1.1076
17X-4, 76–77	237.66	1.1009
17X-6, 83–84	240.73	1.0944
18X-1, 77–78	242.87	1.0821
18X-2, 73–74	244.33	1.0514
18X-4, 101–102	247.61	0.9982
19X-2, 63–64	253.83	1.1138
19X-4, 63–64	256.83	1.1806
19X-6, 56–57	259.76	1.1036
20X-1, 130–131	262.70	1.0221
20X-3, 42–43	264.82	1.1142
20X-4, 27–28	266.17	1.0258

[a] Results are of uncertain quality.

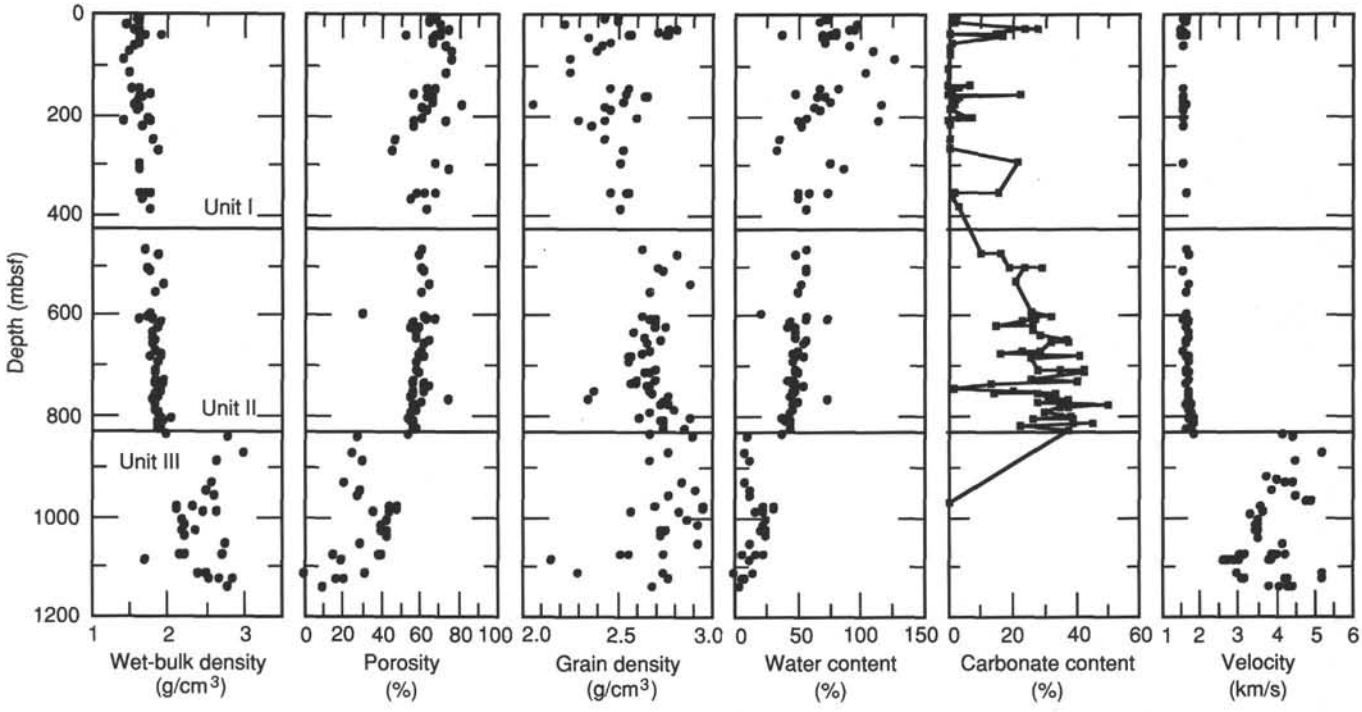

Figure 74. Downhole plots of index properties, carbonate content, and velocity for Site 791. Horizontal lines indicate lithologic unit boundaries.

This resulted in a decision to reduce the program to the deployment of the geochemical combination, the only one with the capability of recording measurements through the drill pipe. This series of measurements provides quantitative assessments of the natural gamma radiation (specifically K, Th, and U) emanating from the formation, together with the relative proportions of the elements Si, Ca, Fe, S, H, Cl, and Al (determined from neutron capture and activation). A detailed description of the geochemical measurements is given in the "Explanatory Notes" chapter (this volume). Further processing onshore may enable the extraction of two additional elements (Ti and Gd).

The base of the drill string was located at a depth of 830 mbsf (i.e., 315 m above the total depth of the hole). This depth coincides with the depth to the top of basement. Data was acquired solely on the uphole run of the combination, at a speed of approximately 450 ft/hr (137 m/hr) starting at a depth of 811.67 mbsf.

Data Quality

The geochemical combination is designed for use in open-hole conditions. When run inside the drill pipe, the quality of the data pertaining to the formations is inevitably degraded in comparison with data obtained in an open hole. The natural gamma-ray measurements suffer from attenuation in the pipe through Compton Scattering, whereas the measurement of the remaining elements is affected by the pipe in terms of the outward passage of neutrons from the tool to the formation as well as the return of the generated gamma rays to the detector from the formation through the drill pipe. The natural gamma-ray measurement technique uses five windows in the spectrometric determination of the contributions of Th, U, and K. Of the measured energy spectrum, the lower energy gamma rays are preferentially attenuated in passing through the wall of the drill pipe and, consequently, the measured spectrum is unfairly weighted toward the higher energies. This has a pronounced effect on the quality of the acquired data, since only 10% of the spectrum (in terms of counting rates) is derived from this higher energy region (Schlumberger, 1983).

In addition to the inevitable decrease in signal-to-noise ratio, the drill pipe itself provided additional input in terms of the chemical signals observed; this was expected particularly for iron and the other elements that compose the drill pipe. These effects were not constant throughout the hole but varied with the thickness of the pipe, the pipe collars, the BHA, and other special components. Because there were no additional measurements made in the borehole other than the geochemical analyses, there is no quantitative determination of borehole size or physical state.

Given the conditions encountered in terms of hole instability and the presence of the drill pipe, the quality of the acquired data was surprisingly good. Careful analysis of the relative variations of individual elemental yields allowed us to identify large- and small-scale sedimentary features that correlate well with the sediments recovered from Holes 790B, 790C, 791A, and 791B. It was also possible to identify sections of the hole that were most affected by the presence of the drill string.

All of the signals received (Figs. 78 and 79) showed responses that were strongly modified with respect to those expected in open-hole conditions. With the exception of the Fe (and possibly S) responses, which were positively increased by the drill-string effect, the remaining signals were all heavily attenuated. The relative values for the elements determined from the neutron bombardment of the formation (Si, Fe, S, Ca, H, Cl, and Al) appeared to be the most severely affected and did not show much variation with depth. No corrections for this attenuation were applied to the data, and no processing of the responses to remove the effects of variations in the contribution of pipe and pipe collars was attempted. Depth shifting was not necessary for this single downhole-measurements experiment.

Geochemical Variations with Depth

Hydrogen and Chlorine

Hydrogen and chlorine values (Fig. 78) provided estimates of the total amount of seawater in the formation as well as between the detector and the formation. Consequently, high values may

Table 20. Physical properties (index, velocity, and carbonate) data for Site 791.

Core, section, interval (cm)	Depth (mbsf)	Wet-bulk density (g/cm^3)	Dry-bulk density (g/cm^3)	Porosity (%)	Water content (%)	Grain density (g/cm^3)	Void ratio	Carbonate content (%)	Velocity (km/s)
126-791A-									
2H-1, 82–85	5.32	1.63	0.96	68	75	2.50	2.11	2.7	1.60
2H-2, 92–95	6.92	1.59	0.95	65	72	2.43	1.87	1.9	1.59
2H-5, 140–150	11.90							1.9	
2H-6, 49–52	12.49	1.64	1.01	65	67	2.50	1.83	1.7	1.61
3H-2, 73–74	16.23	[a]1.47	[a]0.76	[a]71	[a]98	[a]2.23	[a]2.45		
4H-3, 101–102	27.51	1.58	0.84	75	95	2.78	3.03	28.1	[a]1.52
4H-4, 120–122	29.20	1.62	0.88	75	90	2.81	3.00	24.3	[a]1.52
4H-5, 56–58	30.06	1.62	0.92	71	81	2.72	2.41	19.4	1.53
5H-2, 120–122	35.70	1.64	0.93	71	80	2.57	2.46	15.9	1.53
5H-3, 59–61	36.59	1.65	0.96	69	75	2.58	2.24	15.0	1.53
5H-3, 140–150	37.40							1.0	1.61
5H-4, 28–30	37.78	1.93	1.41	53	39	2.76	1.12	0.9	
5H-5, 71–73	39.71	1.69	1.02	68	70	2.78	2.11	17.1	1.55
6H-2, 77–78	44.77	1.65	0.99	66	70	2.35	1.95		
7H-3, 62–63	55.62	1.64	0.98	67	71	2.46	2.00	1.2	
7H-4, 135–136	57.85	1.58	0.86	73	90	2.42	2.72	1.2	1.60
8H-4, 72–73	66.82	[a]1.49	0.73	[a]75	[a]109	[a]2.40	[a]3.12	0.6	
9H-6, 140–150	80.20							0.6	
10H-3, 79–80	84.79	[a]1.41	0.65	[a]77	[a]126.4	[a]2.26	[a]3.35		
12H-5, 140–150	107.80							0.3	
13H-2, 68–70	112.28	[a]1.49	[a]0.75	[a]73	[a]103	[a]2.26	[a]2.83		
15H-6, 25–35	137.25							0.3	
16H-2, 74–76	141.44	1.62	0.99	63	67	2.56	1.73	6.8	1.58
16H-4, 63–65	144.33	[a]1.54	[a]0.86	[a]68	[a]83	[a]2.46	[a]2.14		
16H-5, 60–63	145.80							3.7	
17H-1, 81–83	149.61							0.7	
17H-3, 86–88	152.66							1.2	
17H-6, 80–82	157.10	[a]1.77	[a]1.20	[a]56	[a]48	[a]2.55	[a]1.30	0.3	
18H-1, 48–50	158.98	1.67	1.03	64	65	2.65	1.80	22.9	1.55
18H-2, 103–107	161.03	1.63	0.97	66	72	2.66	1.96	3.4	1.57
18H-6, 99–100	166.90							1.7	
19H-1, 108–110	169.18	1.60	0.93	67	76	2.53	2.06	3.0	1.54
19H-6, 123–126	176.83	[a]1.57	[a]0.75	[a]82	[a]115	[a]2.05	[a]4.63	1.8	1.61
20H-2, 110–112	180.30	1.62	1.01	62	64	2.43	1.62	1.6	1.59
20H-6, 78–80	185.98	1.61	0.98	64	69	2.46	1.77	0.6	1.59
22H-6, 71–73	205.11	1.73	1.12	61	57	2.60	1.57	6.1	1.59
22H-6, 140–150	205.80							3.3	
22H-7, 16–18	206.06	1.76	1.20	57	50	2.44	1.34	7.5	
23H-2, 73–75	207.77	[a]1.42	[a]0.68	[a]74	[a]114	[a]2.30	[a]2.86	0.3	
25X-CC, 13–16	217.84	1.68	1.12	56	52	2.36	1.29	0.5	
28X-1, 68–70	246.68							0.7	1.56
28X-CC, 21–23	247.16	1.82	1.35	48	37	2.43	0.91	0.4	
30X-CC, 12–14	265.42	1.88	1.43	46	34	2.54	0.86	0.7	
33X-1, 17–19	294.47	1.62	0.95	68	75	2.52	2.10	21.8	1.56
34X-1, 5–8	304.05	[a]1.65	[a]0.53	[a]74	[a]85	[a]4.28	[a]2.91		
39X-1, 12–15	352.42	1.64	1.19	68	73	2.57	2.08	15.7	
39X-1, 42–45	352.72	1.76	1.09	59	52	2.55	1.42	1.8	1.61
39X-CC, 11–12	353.40	1.70	0.97	62	60	2.47	1.66		
40X-1, 2–3	362.02	[a]1.66	[a]1.11	[a]55	[a]51	[a]1.48	[a]1.23	1.1	
42X-1, 10–11	381.50	1.77	1.14	63	58	2.52	1.73	3.7	
126-791B-									
9R-CC, 19–21	463.79	1.72	1.12	61	57	2.63	1.56	10.3	1.61
10R-1, 34–36	473.64	1.87	1.28	60	49	2.81	1.48	16.5	1.71
13R-1, 46–48	502.56	1.75	1.14	61	56	2.72	1.58	19.1	3.14
13R-1, 140	503.50							29.9	
13R-2, 46–48	504.06	1.77	1.14	63	58	2.75	1.71	24.2	1.58
16R-1, 23–24	531.43	1.94	1.30	65	52	2.89	1.84	21.5	1.72
18R-1, 5–7	550.65	1.83	1.17	61	51	2.67	1.54		1.64
22R-1, 69–71	589.69	[a]1.76	[a]1.46	[a]30	[a]21	[a]3.37	[a]0.44	26.2	1.63
23R-1, 75–77	599.45	1.75	1.13	63	58	2.63	1.67	32.5	1.64
23R-2, 82–84	601.02	1.64	0.97	67	73	2.70	2.07	26.5	1.61
23R-3, 115–125	602.85							27.7	
23R-CC, 3–6	603.92	1.81	1.18	64	56	2.68	1.74	27.2	1.60
24R-1, 57–59	608.97	1.91	1.34	57	44	2.70	1.33	23.4	1.69
25R-1, 27–29	618.37	1.87	1.33	55	43	2.71	1.23	15.5	1.67
25R-2, 14–17	619.74	1.88	1.34	60	49	2.76	1.50	26.8	1.67
26R-1, 6–9	627.76	1.81	1.24	58	49	2.59	1.38	27.2	1.69
27R-1, 35–37	637.35	1.81	1.24	58	48	2.65	1.36	28.8	1.71
28R-1, 129–131	647.89	1.84	1.20	65	57	2.73	1.85	37.2	1.65
28R-3, 81–83	650.41	1.82	1.20	63	54	2.66	1.67	37.7	1.63
28R-3, 140–150	651.00							32.2	
30R-1, 145–148	667.45	1.85	1.24	61	51	2.68	1.59	29.2	1.59

Table 20 (continued).

Core, section, interval (cm)	Depth (mbsf)	Wet-bulk density (g/cm^3)	Dry-bulk density (g/cm^3)	Porosity (%)	Water content (%)	Grain density (g/cm^3)	Void ratio	Carbonate content (%)	Velocity (km/s)
126-791B- (Cont.)									
30R-3, 104–108	670.06	1.91	1.32	60	47	2.64	1.49	23.7	
31R-1, 81–83	676.41	1.91	1.30	62	50	2.56	1.62	16.5	1.69
31R-3, 67–69	679.27	1.79	1.17	63	56	2.58	1.67	41.1	1.67
32R-1, 28–30	685.58	1.88	1.30	58	46	2.56	1.39	26.4	1.72
34R-1, 116–118	705.76	1.85	1.28	59	48	2.71	1.41	28.2	1.64
34R-3, 37–39	707.97	1.86	1.27	60	49	2.65	1.49	42.6	1.64
34R-3, 140–150	709.00							35.1	
34R-4, 68–69	709.78	1.85	1.26	60	50	2.68	1.53	43.1	1.67
36R-1, 27–29	723.87	1.95	1.39	57	42	2.70	1.30	26.5	1.72
36R-3, 134–136	727.94	1.83	1.26	58	47	2.61	1.35		
36R-4, 86–88	728.96	1.95	1.33	63	50	2.58	1.71		
36R-4, 134–136	729.44	1.83		58	47	2.61	1.35	40.5	1.65
37R-2, 8–10	734.78	1.92		62	49	2.68	1.64		
37R-2, 65–67	735.35	1.91	1.26	65	54	2.66	1.88	13.5	
38R-2, 8–10	744.38	1.92	1.31	62	49	2.68	1.64	33.4	1.70
38R-4, 16–18	747.46	1.88	1.31	58	46	2.38	1.35	20.5	
39R-1, 10–12	752.50	1.84	1.28	57	46	2.69	1.32	33.6	1.70
39R-1, 140–150	753.80							14.3	
39R-2, 107–109	754.97	1.88	1.32	56	44	2.77	1.27	28.5	1.72
40R-1, 10–13	762.20	[a]1.80	[a]0.82	[a]74	[a]73	[a]2.35	[a]2.92	31.5	1.73
40R-3, 50–53	765.60	1.85	1.25	61	50	2.74	1.53	37.7	1.73
41R-1, 17–20	771.87	1.83	1.28	56	46	2.73	1.29	28.4	1.66
41R-3, 71–74	775.41	1.86	1.28	58	47	2.78	1.40	50.2	1.76
42R-1, 35–38	781.65	1.85	1.27	58	47	2.80	1.37	38.2	1.74
42R-2, 0–10	782.80							35.3	
43R-1, 9–11	791.09	1.87	1.32	56	44	2.68	1.26	30.3	1.75
44R-1, 38–41	801.08	1.90	1.36	55	42	2.62	1.20	38.8	1.74
44R-1, 98–100	801.68	2.04	1.49	56	39	2.89	1.25	35.2	1.84
44R-2, 96–99	803.16	1.89		57	44	2.74	1.30	27.1	1.79
44R-2, 97–99	803.17	1.96	1.41	56	41	2.73	1.25	39.5	
45R-2, 17–19	811.97	1.89		57	45	2.86	1.32	39.5	
45R-2, 96–99	812.76	1.89	1.33	57	44	2.74	1.30	22.5	1.84
45R-2, 140–150	813.20							45.5	
46R-1, 43–45	820.43	1.92	1.35	58	44	2.75	1.36		1.66
46R-2, 17–19	821.67	1.89	1.33	57	45	2.86	1.32		1.77
47R-1, 41–42	830.01	1.99	1.45	54	39	2.68	1.18	37.99	1.87
47R-1, 88–90	[b]830.48					2.94			4.20
48R-1, 31–33	[b]839.51	2.78		28	11	2.90	0.38		4.45
51R-1, 5–9	[b]868.35	[a]3.01		[a]25	[a]9	[a]2.78	[a]0.34		5.19
53R-1, 15–23	[b]887.75	2.67		30	13	[a]2.68	0.44		4.53
56R-1, 25–31	916.55								3.71
56R-1, 4–6	921.30								4.04
57R-1, 6–8	925.96								4.22
57R-1, 7–8	925.97	2.80		14		3.03			4.26
57R-1, 55–64	926.45	2.59	2.39	21	9	2.84	0.26		4.46
59R-1, 36–38	945.56	2.51	2.21	30	14	2.92	0.42		3.90
60R-1, 16–19	[b]954.96	2.63		27	12	2.78	0.37		4.50
61R-1, 43–45	[b]964.93	3.19		15		2.83			4.81
62R-1, 5–7	974.15	2.13	1.65	49	31	2.96	0.97	0.71	
62R-1, 97–99	975.07	2.34	1.90	44	24	2.71	0.79		3.57
63R-1, 49–51	984.19	2.48	2.05	44	22	[a]2.65	0.78		3.65
63R-1, 76–79	[b]984.46	2.67		36	16	2.83	0.57		3.67
64R-1, 37–44	[b]993.37					[a]2.70			3.33
65R-1, 55–56	1003.25	2.21	1.84	43	25	2.87	0.75		3.56
66R-1, 65–67	[b]1013.05	2.22	1.81	41	23	2.93	0.69		3.49
66R-2, 46–48	[b]1014.24					[a]2.56			3.52
67R-1, 62–64	1022.72								3.52
67R-1, 90–91	1023.00	2.19	1.76	43	25	2.73	0.76		3.46
67R-2, 26–28	1023.86	2.20	1.79	42	24	2.76	0.71		3.45
67R-3, 24–26	[b]1025.34	2.37		40	21	2.73	0.68		3.46
68R-1, 49	1032.29	2.23	1.83	43	24	2.73	0.74		
68R-2, 60–65	1038.80								3.52
70R-1, 0–4	[b]1051.1	2.76		29	12	2.93	0.41		4.14
72R-1, 120–126	[b]1071.6	2.23		15	7	2.74	0.17		3.07
72R-2, 116–118	[b]1073.06	2.13		35		2.75			3.19
72R-2, 117–119	1073.07								3.87
72R-2, 135–140	[b]1073.25	2.73		39	17	[a]2.57	[a]0.64		4.21
72R-3, 35–37	1073.75	2.23	2.12	23		2.60			4.05
73R-2, 20–24	[b]1081.3					2.79			2.93
73R-2, 77–79	1081.87								2.69
73R-2, 77–79	1081.87								3.89
73R-2, 87–89	1081.97	2.00		42		2.75			2.71
73R-2, 87–89	1081.97								2.60
73R-2, 87–89	1081.97								2.69
73R-3, 18–21	[b]1082.7	2.09		37		2.72			3.02
73R-3, 18–21	[b]1082.7								2.76

Table 20 (continued).

Core, section, interval (cm)	Depth (mbsf)	Wet-bulk density (g/cm³)	Dry-bulk density (g/cm³)	Porosity (%)	Water content (%)	Grain density (g/cm³)	Void ratio	Carbonate content (%)	Velocity (km/s)
126-791B- (Cont.)									
73R-3, 72–74	1083.24	[a]1.69		[a]19.2	[a]13	[a]2.15	[a]0.24		3.82
76R-1, 117–120	[b]1110.17					2.75			2.96
76R-2, 37–38	1110.87	2.41	2.10	32	16	2.75	0.47		2.94
76R-2, 106–109	[b]1111.56	[a]2.52				[a]2.29			5.22
77R-1, 58–64	[b]1119.18	[a]2.85		[a]16.3	[a]6	[a]2.77	0.19		4.35
77R-1, 85–89	1119.45	2.68	2.51	17	7	2.78	0.21		4.21
77R-2, 43–45	1120.04								5.21
77R-2, 93–95	[b]1120.54					2.71			3.16
77R-2, 131–134	1120.92	2.54	2.33	21	10	3.21	0.27		3.09
79R-1, 19–21	[b]1137.79	[a]2.79		[a]9	[a]4	[a]2.69	[a]0.10		4.31
79R-1, 21–24	[b]1137.81	2.64		8		2.79			4.11
79R-1, 21–24	[b]1137.81								4.12
79R-1, 40–42	[b]1138.00	2.59	8.00			2.74			4.12
79R-1, 41–42	[b]1138.00								3.81
79R-1, 72–74	[b]1138.32	2.61	9.00			2.76			4.41
79R-1, 73–76	[b]1138.32								4.45

[a] Results are of uncertain quality.
[b] Samples that were not measured immediately after cores were split.

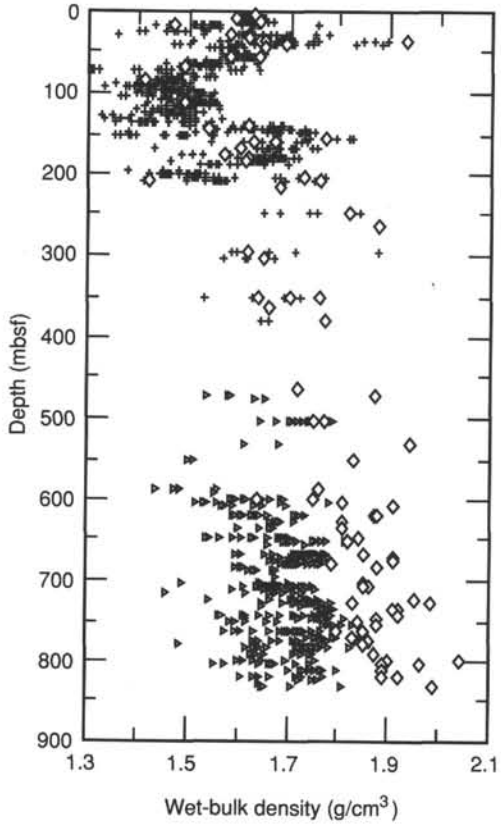

Figure 75. Comparison of gravimetric and GRAPE wet-bulk density data for Holes 791A and 791B. Open diamond = gravimetric bulk density; closed triangle = Hole 791B GRAPE density.

indicate either high porosities or the possibility of large hole conditions existing outside the pipe. Several distinct intervals are present (Fig. 78):

1. 0–42 mbsf: very high values; variable H and Cl values indicate bad hole conditions with a seawater pool developed around the pipe as a result of erosion of sediments through drill-string action (Fig. 78, 0–150 mbsf).

2. 42–182 mbsf: high values; fairly constant H and Cl values over this depth interval indicate either a higher *in-situ* porosity compared with the zone below (Fig. 78, 0–300 mbsf) or an oversized hole.

3. 182–560 mbsf: constant values; low values of H and Cl indicate that the best hole conditions were encountered within this hole.

4. 560–710 mbsf: variable values; H and Cl values imply variable lithology.

The high values correspond to zones of low Si and Fe, but high Th, U, and K (Fig. 78).

Natural Gamma-Ray Components

The total gamma-ray signal exhibits detailed variation downhole. Although the signal strength was particularly low throughout the section and was particularly affected by the pipe, the variations appeared to be lithologically related. The quantitative nature of the individual spectrometric determinations is, however, questionable because of the bias resulting from the differential attenuation of gamma rays at different energy levels. All three elements (Th, U, and K) contributed to the natural gamma-ray signal.

Silicon, Iron, Calcium, Sulfur, and Aluminum

All five of these elements showed little gross variation over the logged section (Fig. 78). There were variations evident, however, in the Fe, Si, Al, and S traces, which appeared to correlate with the main features of the hole described below. Calcium, however, did not show any substantial variation downhole; this is in contrast to the substantial variation exhibited by laboratory measurements of calcium carbonate on individual samples. With the exception of Fe and S (which increased because of contributions from the drill pipe), the measured signal strengths are very low when compared with the levels obtained in an open hole.

Stratigraphic Observations from Downhole Geochemical Data

Major Features

Three clearly separate units or zones were identifiable from the downhole data, selected on the basis of comparable geochemical signatures.

Table 21. Synthesis of physical property data from igneous rock samples from Hole 791B.

Core, section, interval (cm)	Depth (mbsf)	Wet-bulk density (g/cm³)	Porosity (%)	Grain density (g/cm³)	Velocity (km/s)	Rock type and unit	Comments
126-791B-							
47R-1, 89	830.49	—	—	2.94	4.20	Basalt breccia, Unit 1	Days; no salt correction
48R-1, 32	839.52	2.78	27.8	2.90	4.45	Vesicular basalt, Unit 2	Days
51R-1, 7	868.35	[a]3.01	[a]25.4	[a]2.78	5.19	Vesicular basalt, unit 2	Days; numerous large vesicles
53R-1, 20	887.80	[a]2.67	[l]30.4	[a]2.68	4.53	Vesicular basalt, Unit 2	Days
57R-1, 7	925.97	2.80	13.7	3.03	4.26	Diabase, Unit 4; high Fe content	Days; no salt correction
57R-1, 55	926.45	2.59	20.7	2.84	4.46	Basalt, Unit 5	Minutes
59R-1, 37	945.57	2.51	29.6	2.92	3.90	Basalt, Unit 6	Minutes
60R-1, 18	954.98	2.63	27.1	2.78	4.50	Basalt, Unit 7	Days
61R-1, 44	964.94	[a]3.19	[l]14.5	[l]2.83	4.90	Diabase, Unit 8	Days; no salt correction
62R-1, 98	975.08	2.34	44.1	2.71	3.57	Basaltic "mousse," Unit 11	Hours
63R-1, 50	984.20	2.48	43.9	2.65	3.65	Basaltic "mousse," Unit 11	Hours; mixture
63R-1, 78	984.48	2.67	36.3	2.83	3.67	Basaltic "mousse," Unit 11	Days; clast with large vesicles
64R-1, 40	993.40	—	—	2.70	3.33	Basaltic "mousse," Unit 11	Days; mixture; no salt correction
65R-1, 55	1003.25	2.21	42.9	2.87	3.56	Basaltic "mousse," Unit 11	Minutes; mixture
66R-1, 66	1013.05	2.22	40.7	2.93	3.49	Basaltic "mousse," Unit 11	Minutes; mixture
66R-2, 47	1014.24	—	—	[a]2.56	3.52	Basaltic "mousse," Unit 11	Days; matrix; no salt correction
67R-1, 90	1023.00	2.19	43.2	2.73	3.46	Basaltic "mousse," Unit 11	Minutes; mixture
67R-2, 27	1023.87	2.20	41.6	2.76	3.45	Basaltic "mousse," Unit 11	Minutes; mixture
67R-3, 25	1025.35	2.37	40.4	2.73	3.46	Basaltic "mousse," Unit 11	Days; mixture
68R-1, 50	1032.30	2.23	42.6	2.73		Basaltic "mousse," Unit 11	Minutes; mixture
70R-1, 2	1051.12	2.76	29.2	2.93	4.14	Basaltic "mousse," Unit 11	Days; clast ("dense")
72R-1, 124	1071.64	2.23	14.7	2.74	3.07	Basaltic "mousse," Unit 11	Days; matrix
72R-2, 117	1073.00	2.13	35.5	2.75	3.19	Basaltic "mousse," Unit 11	Days; mixture; no salt correction
72R-2, 138	1073.28	[a]2.73	[a]38.9	[a]2.57	4.21	Basaltic "mousse," Unit 11	Days; clast
72R-3, 37	1073.77	2.23	23.1	2.60	4.05	Basaltic "mousse," Unit 11	Hours; matrix; no salt correction
73R-2, 22	1081.32	—	—	2.79	2.93	Basaltic "mousse," Unit 11	Days; mostly matrix; no salt correction
73R-2, 89	1081.98	2.00	42.4	2.75	2.60	Basaltic "mousse," Unit 11	
73R-3, 20	1082.70	2.09	36.7	2.72	2.76	Basaltic "mousse," Unit 11	Days; mixture; no salt correction
73R-3, 73	1083.23	[a]1.69	[l]19.2	[a]2.15	3.82	Basaltic "mousse," Unit 11	Hours; clast
76R-1, 119	1110.19	—	—	2.75	2.96	Basaltic "mousse," Unit 14	Days; no salt correction; "not mousse"
76R-2, 37	1110.87	2.41	31.9	2.75	2.94	Basaltic "mousse," Unit 14	Hours; clast
76R-2, 108	1111.58	[a]2.52	—	[l]2.29	5.22	Diabase, Unit 15	Days; diabase with gypsum veins
77R-1, 60	1119.18	[a]2.85	[a]16.3	[a]2.77	4.35	Diabase, Unit 17	Days; sheared, slickensided
77R-1, 87	1119.47	2.68	17.2	2.78	4.21	Diabase, Unit 17	Minutes
77R-2, 94	1120.54	—	—	2.71	3.16	Lapilli tuff, Unit 19	Days; coarse grained
77R-2, 132	1120.92	2.54	21.4	[a]3.21	3.09	Ash tuff, Unit 20	Minutes
79R-1, 20	1137.80	[a]2.79	[a]9.2	[a]2.69	4.31	Lapilli tuff, Unit 28	Days; coarse grained
79R-1, 23	1137.83	2.64	8.3	2.79	4.11	Lapilli tuff, Unit 28	Days; no salt correction
79R-1, 41	1138.01	2.59	8.5	2.74	4.12	Lapilli tuff, Unit 28	Days; no salt correction
79R-1, 73	1138.33	2.61	8.6	2.76	4.41	Lapilli tuff, Unit 28	Days; no salt correction

Notes: Days, hours and minutes refer to the approximate amount of time between splitting and sampling. The term "mixture" in the basaltic "mousse" unit refers to a sample composed of both matrix and clast material. "No salt correction" = values have not been corrected for 35 ppt salt content in the pore fluid.

[a] Denotes suspicious values.

Table 22. Shear strength data from Site 791.

Core, section, interval (cm)	Depth (mbsf)	Shear strength (kPa)
126-791A-		
2H-1, 95	5.45	5.4
2H-2, 94	6.94	5.1
2H-6, 41	12.41	4.7
4H-3, 96	27.46	13.9
4H-4, 122	29.22	12
4H-5, 58	30.08	17.6
5H-2, 116	35.66	17.9
5H-3, 54	36.54	18.2
5H-4, 27	37.77	8.2
5H-5, 69	39.69	11.2
16H-2, 70	141.4	8.6
18H-1, 44	158.94	62
18H-2, 109	161.09	5.8
19H-1, 104	169.14	12.4
19H-6, 120	176.8	10.7
22H-6, 72	205.12	47.3
22H-7, 16	206.06	33.8
33X-1, 16	294.46	12.8

Unit A starts at the mud line, is approximately 42 m thick, and is contained within the depth limits of lithologic Unit I (see "Lithostratigraphy and Accumulation Rates" section, this chapter). It is characterized by very low values of Th, U, K, Fe, Si, and Al; these elements increase with depth over the interval observed (Fig. 79, 0–150 mbsf). Some of the observations may be explained by the large hole size below the mud line, where sediment eroded by the action of the drill string formed a seawater pool in the immediate vicinity of the pipe. This observation was supported by higher than average values of H and Cl over this interval (Fig. 78, 0–150 mbsf).

This section of hole, however, contains two compatible sets of observations that support the separation of this unit from the one below. First, this zone is one of high magnetic susceptibility (see "Lithostratigraphy and Accumulation Rates" section, this chapter, Fig. 9). Second, the recovered material from Holes 790B and 791A, for comparable depths (after correcting for variations in sedimentation rates), is described as a pumiceous sandy gravel; shipboard measurements of porosity for recovered cores are on the order of 60%–80%.

Unit B is also contained within lithologic Unit I. It starts at approximately 42 mbsf and is 140 m thick. It is characterized by low values of Th, U, K, Fe, Si, and Al (Fig. 79, 0–150 mbsf).

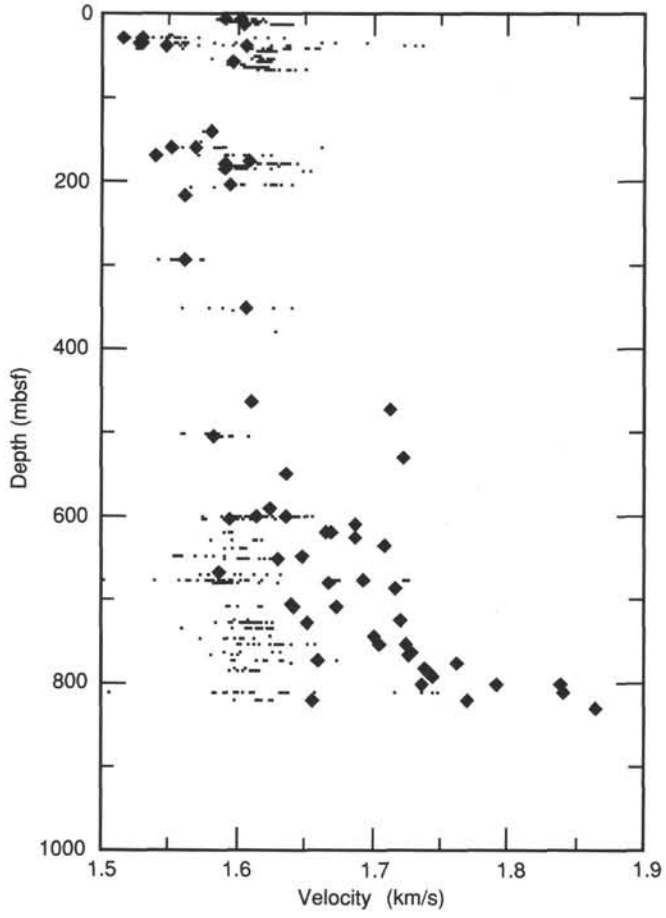

Figure 76. Comparison of sonic velocity determined by Hamilton Frame and multisensor track methods for Site 791. Dots = multisensor track; closed diamond = Hamilton Frame.

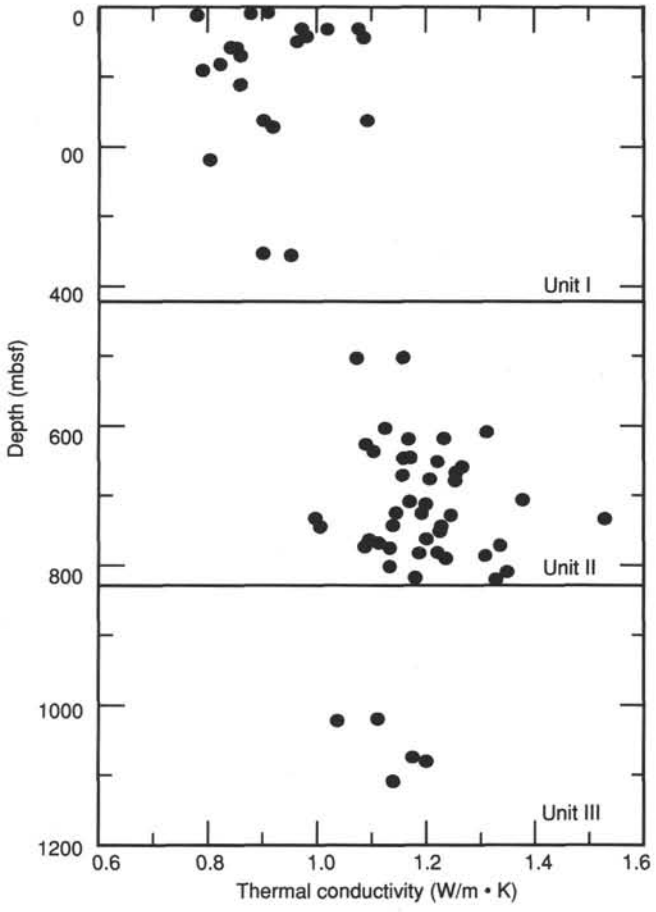

Figure 77. Plot of thermal conductivity, Site 791. Horizontal lines indicate lithologic unit boundaries.

The overall decrease in most of the elements studied might be a result of the increase in hole size. However, this section corresponds to a zone of steadily increasing magnetic susceptibility (see "Lithostratigraphy and Accumulation Rates" section, this chapter), reflected by a gradual increase in Fe content. Descriptions of recovered core material indicate that this interval is predominantly pumiceous sandy gravel and pebbly sand.

Unit C starts at 182 mbsf. It is characterized by a constant value of Al and a gradual increase in Th, Si, and K with depth (Fig. 79, 0–300 mbsf). The base of the unit is indistinct, however, within the terms of the present analysis. Consequently, it extends over parts of lithologic Units I and II. Toward the base of this unit, a narrow zone from 585 to 600 mbsf is characterized by high Th and U and low Fe, Al, and Si values. It may be possible to subdivide the unit by placing a boundary at either 471 or 534 mbsf on the basis of the trends described above (Fig. 79, 150–650 mbsf).

High Gamma Ray Horizons

Throughout the borehole we observed a series of narrow zones with high readings of natural gamma rays (Fig. 79). For example, the base of Unit A is defined by three of these horizons at 33, 38, and 43 mbsf (Fig. 79, 0–150 mbsf), which correlate with clay beds associated with black sand/silt beds recovered in Holes 790B (Core 126-790B-3H) and 791A (Core 126-791A-5H). The occurrence of these high natural gamma log features increases with depth.

Presence of Pyrite

Sulfur values increase toward the base of the analyzed section and correlate well with observations of pyrite in recovered cores. Between 585 and 685 mbsf, the Fe and S responses are effectively parallel. Unfortunately, further detailed analysis of this trend is hampered, at present, by the use of sulfur in the drillstring composition.

Nongeological Observations

At 645 mbsf (Figs. 78 and 79, 650–800 mbsf), a noticeable increase in iron results from the increased thickness in the wall of the drill string just above the BHA, where a 60-m-long section of 5½-in.-diameter drill pipe is present. At 710 mbsf, a massive increase in measured iron and a decrease in total natural gamma rays occur. This continues to the bottom 115 m of the logged portion of the hole, which is the length of the BHA.

Conclusions

This report is a preliminary assessment of the downhole geochemical data obtained in Hole 791B during Leg 126. The data are of good quality, given the difficult conditions encountered in the hole. Initial appraisals indicate that (1) it is possible to identify three major zones or units within the section studied, which may be either lithologically or hole-condition related; (2) high Fe concentrations are found in zones exhibiting high magnetic susceptibility values; (3) high gamma-ray values are found where clay beds are associated with black sands; (4) in lithologic

Unit I, low gamma-ray values are associated with unrecovered pumice gravels; and (5) the presence of pyrite in the lower part of the section is shown by a positive correlation between S and Fe.

Further detailed analysis can only be accomplished after the data have been evaluated for the effects of both attenuation and modification caused by the presence of the drill string.

REFERENCES

Akimoto, K., 1989. Recent foraminifera from Enshunada. *In* Takayanagi, Y., and Ishizaki, K. (Eds.), *Collected Papers on Foraminifera from the Japanese Islands:* Sendai (Toko Press), 93–104.

Becker, K., Sakai, H., et al., 1988. *Proc. ODP, Init. Repts.*, 111: College Station, TX (Ocean Drilling Program).

Berggren, W. A., Kent, D. V., Flynn, J. J., and Van Couvering, J. A., 1985. Cenozoic geochronology. *Geol. Soc. Am. Bull.*, 96:1407–1418.

Berner, R. A., 1964. Iron sulfides formed from aqueous solution at low temperatures and atmospheric pressure. *J. Geol.*, 72:293–306.

Blow, W. H., 1969. Late middle Eocene to Recent planktonic foraminiferal biostratigraphy. *In* Renz, H. H., and Brönniman, P. (Eds.), *Proceedings of the First International Conference on Planktonic Microfossils:* Leiden (E. J. Brill), 1:199–422.

Ericson, D. B., and Wollin, G., 1968. Pleistocene climates and chronology in deep-sea sediments. *Science,* 162:1227–1234.

Foreman, H. P., 1981. Radiolaria. *In* Emiliani, C. (Ed.), *The Sea* (Vol. 7): *The Oceanic Lithosphere:* New York (Wiley-Interscience), 1121–1144.

Fryer, P., Taylor, B., Langmuir, C., and Hochstaedter, A. G., in press. Petrology and geochemistry of lavas from the Sumisu and Torishima backarc rifts. *Earth Planet. Sci. Lett.*

Gieskes, J. M., 1983. The chemistry of interstitial waters of deep sea sediments: interpretation of deep sea drilling data. *In* Riley, J. P., and Chester, R. (Eds.), *Chemical Oceanography* (Vol. 8): London (Academic Press), 221–269.

Hawkins, J. W., and Melchior, J. T., 1985. Petrology of Mariana Trough and Lau Basin basalts. *J. Geophys. Res.*, 90:11,431–11,468.

Hay, W. W., Sibuet, J.-C., et al., 1984. *Init. Repts. DSDP,* 75, Pts. 1 and 2: Washington (U.S. Govt. Printing Office).

Hochstaedter, A. G., and Gill, J. B., in press. Petrology and geochemistry of lavas from the Sumisu Rift: an incipient back-arc basin. *Earth Planet. Sci. Lett.*

Klein, E. M., and Langmuir, C. H., 1987. Global correlations of ocean ridge chemistry with axial depth and crustal thickness. *J. Geophys. Res.*, 92:8089–8115.

Manheim, F. T., and Waterman, L. S., 1974. Diffusimetry (diffusion constant estimation) on sediment cores by resistivity probe. *In* von der Borch, C. C., Sclater, J. G., et al., *Init. Repts. DSDP,* 22: Washington (U.S. Govt. Printing Office), 663–670.

Mattey, D. P., Marsh, N. G., and Tarney, J., 1981. The geochemistry, mineralogy, and petrology of basalts from the West Philippine and Parece Vela basins and from the Palau-Kyushu and West Mariana ridges, Deep Sea Drilling Program Leg 59. *In* Kroenke, L., Scott, R. B., et. al., *Init. Repts. DSDP,* 59: Washington (U.S. Govt. Printing Office), 753–796.

McCave, I. N., 1972. Transport and escape of fine-grained sediment from shelf areas. *In* Swift, D.J.P, Duane, D. B., and Pilkey, O. H. (Eds.), *Shelf Sediment Transport: Process and Pattern:* Stroudsburg, PA (Dowden, Hutchinson and Ross), 225–248.

Niitsuma, N., 1982. Paleomagnetic results, Middle America Trench off Mexico, Deep Sea Drilling Project Leg 66. *In* Watkins, J. S., Moore, J. C., et al., *Init. Repts. DSDP,* 66: Washington (U.S. Govt. Printing Office), 737–770.

Nishimura, A., and Murakami, F., 1988. Sedimentation of the Sumisu Rift, Izu-Ogasawara Arc. *Bull. Geol. Surv. Jpn.*, 39:39–61.

Nowell, A.R.M., and Hollister, C. D. (Eds.), 1985. Deep ocean sediment transport—preliminary results of the High Energy Benthic Boundary Layer Experiments. *Mar. Geol.,* Spec. Issue, No. 66.

Okada, H., and Bukry, D., 1980. Supplementary modification and introduction of code numbers to the "Low-latitude coccolith biostratigraphic zonation" (Bukry, 1973; 1975). *Mar. Micropaleontol.*, 5: 321–325.

Sanfilippo, A., Westberg-Smith, M. J., and Reidel, W. R., 1985. Cenozoic radiolaria. *In* Bolli, H. M., Saunders, J. B., and Perch-Nielson, K. (Eds.), *Plankton Stratigraphy:* Cambridge (Cambridge Univ. Press), 631–712.

Sato, T., Takayama, T., Kato, M., Kudo, T., and Kameo, K., 1988. Calcareous microfossil biostratigraphy of the uppermost Cenozoic formations distributed in the Coast of the Japan Sea—Part 4: Conclusion. *J. Jpn. Assoc. Petrol. Tech.*, 53:13–29.

Schlumberger, 1983. *Natural Gamma Ray Spectrometry: Essentials of NGS Interpretation:* Houston (Schlumberger).

Takayama, T., and Sato, T., 1987. Coccolith biostratigraphy of the North Atlantic Ocean, Deep Sea Drilling Project Leg 94. *In* Ruddiman, W. F., Kidd, R. B., Thomas, E., et al., *Init. Repts. DSDP,* 94, Pt. 2: Washington (U.S. Govt. Printing Office), 651–702.

Tarling, D. H., 1983. *Palaeomagnetism, Principles and Applications in Geology, Geophysics and Archaeology:* London (Chapman and Hall).

Taylor, B., Brown, G., Fryer, P., Gill, J., Hochstaedter, A., Hotta, H., Langmuir, C., Leinen, M., Nishimura, A., and Urabe, T., in press. ALVIN-SeaBeam studies of the Sumisu Rift, Izu-Bonin Arc. *Earth Planet. Sci. Lett.*

Taylor, B., Brown, G., Hussong, D., and Fryer, P., 1988a. SeaMARC II sidescan acoustic imagery, Sumisu and Torishima rifts, Izu-Ogasawara Island Arc, 1:200,000. *Mar. Geol. Map Ser.,* Tsukuba (Geol. Surv. Jpn.), No. 31.

_____, 1988b. SeaMARC II bathymetry, Sumisu and Torishima rifts, Izu-Ogasawara Island Arc, 1:200,000. *Mar. Geol. Map Ser.,* Tsukuba (Geol. Surv. Jpn.), No. 31.

Wood, D. A., Joron, J.-L., Marsh, N. G., Tarney, J., and Treuil, M., 1980. Major- and trace-element variations in basalts from the North Philippine Sea drilled during Deep Sea Drilling Program Leg 58: a comparative study of back-arc-basin basalts with lava series from Japan and mid-ocean ridges. *In* Klein, G. deV., Kobayashi, K., et al., *Init. Repts. DSDP,* 58: Washington (U.S. Govt. Printing Office), 873–894.

Yasuda, H., 1989. Benthic foraminifers and sedimentary facies of the lower slope basin off Shikoku, Japan. *In* Takayanagi, Y., and Ishizaki, K. (Eds.), *Collected Papers on Foraminifera from the Japanese Islands:* Sendai (Toko Press), 83–92.

Ms 126A-108

NOTE: All core description forms ("barrel sheets") and core photographs have been printed on coated paper and bound as Section 3, near the back of the book, beginning on page 421.

Table 23. Thermal conductivity data from Site 791.

Core, section, interval (cm)	Depth (mbsf)	Thermal conductivity (W/m · K)
126-791A-		
2H-1, 52	5.02	0.907
2H-3, 95	8.45	0.777
2H-4, 66	9.66	0.874
4H-3, 56	27.06	0.970
4H-4, 122	29.22	1.072
4H-5, 49	29.99	1.013
5H-3, 96	36.96	0.974
5H-4, 19	37.69	1.075
5H-6, 106	41.56	0.958
7H-4, 16	56.66	0.848
7H-5, 14	58.14	0.837
8H-3, 30	64.90	0.856
8H-4, 17	66.27	[a]1.950
9H-6, 34	79.14	0.815
10H-6, 37	88.87	0.787
11H-4, 87	96.07	[a]0.158
11H-6, 68	98.88	0.125
12H-6, 50	108.40	0.854
18H-1, 52	159.02	1.089
18H-2, 82	160.82	0.899
19H-1, 73	168.83	0.914
25X-1, 17	217.27	0.803
39X-1, 35	352.65	0.899
39X-1, 82	353.12	0.953
126-791B-		
10R-1, 28	473.58	[a]1.190
13R-1, 83	502.93	1.156
13R-2, 48	504.08	1.071
16R-1, 18	531.38	[a]1.1724
23R-1, 82	599.52	[a]1.204
23R-3, 51	602.21	1.123
23R-4, 52	603.72	[a]0.805
24R-1, 36	608.76	1.303
25R-1, 117	619.27	1.164
25R-2, 47	620.07	1.229
26R-1, 8	627.78	1.086
27R-1, 44	637.44	1.101
28R-1, 33	646.93	1.160
28R-3, 24	649.84	1.154

Table 23 (continued).

Core, section, interval (cm)	Depth (mbsf)	Thermal conductivity (W/m · K)
126-791B- (Cont.)		
28R-4, 49	651.59	1.217
30R-1, 70	666.70	1.255
30R-2, 79	668.29	1.245
30R-3, 102	670.02	1.156
31R-1, 118	676.78	1.201
31R-3, 63	679.23	0.285
31R-4, 24	680.34	1.249
34R-1, 90	705.50	1.373
34R-3, 80	708.40	1.170
34R-5, 24	710.84	1.197
36R-1, 110	724.70	1.192
36R-2, 91	726.01	1.142
36R-3, 118	727.78	1.245
37R-1, 70	733.90	1.000
37R-2, 26	734.96	1.524
38R-1, 99	743.79	1.141
38R-3, 55	746.35	1.011
39R-1, 42	752.82	1.222
39R-2, 88	754.78	1.215
38R-4, 98	767.28	1.112
40R-1, 25	762.35	1.198
40R-2, 83	764.43	1.095
40R-3, 40	765.50	1.114
41R-1, 35	772.05	1.329
41R-2, 127	774.47	1.134
41R-3, 70	775.40	1.086
42R-1, 62	781.92	1.188
42R-2, 50	783.30	1.215
42R-3, 59	784.89	1.304
43R-1, 28	791.28	1.234
44R-1, 87	801.57	1.136
45R-2, 76	812.56	1.344
46R-1, 90	820.90	1.178
46R-2, 35	821.85	[a]2.2924
46R-CC, 18	822.80	1.323
67R-1, 40	1022.5	1.114
67R-2, 115	1024.8	1.042
72R-2, 85	1075.8	1.1731
73R-3, 32	1083.3	1.2007
76R-1, 128	1110.3	1.1365

[a] Results are of uncertain quality.

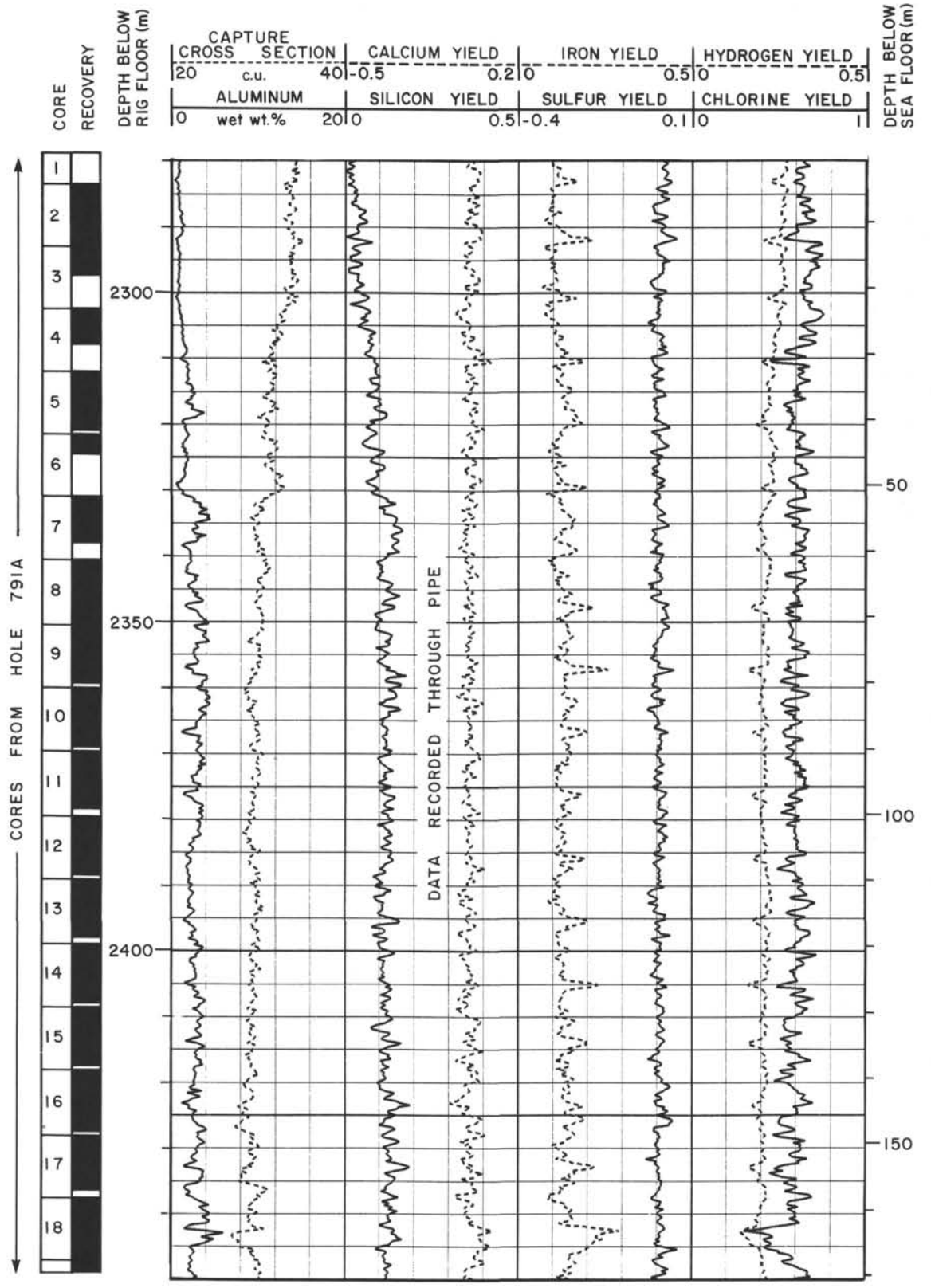

Figure 78. Summary log for hydrogen and chlorine (far right) obtained with the aluminum clay tool (ACT) for the interval from 0 to 830 mbsf. Also shown are the plots for aluminum, calcium, silicon, iron, and sulfur.

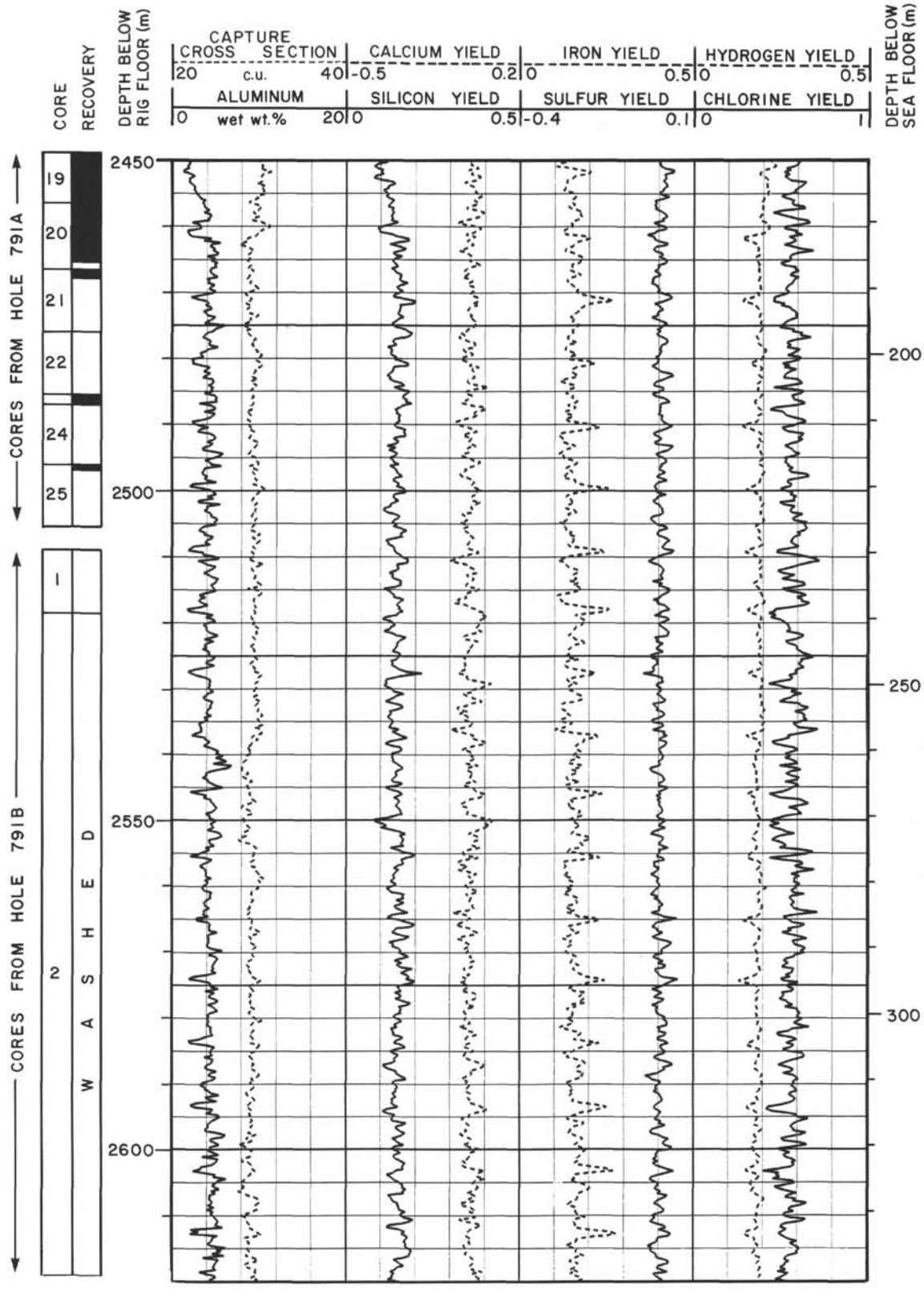

Figure 78 (continued).

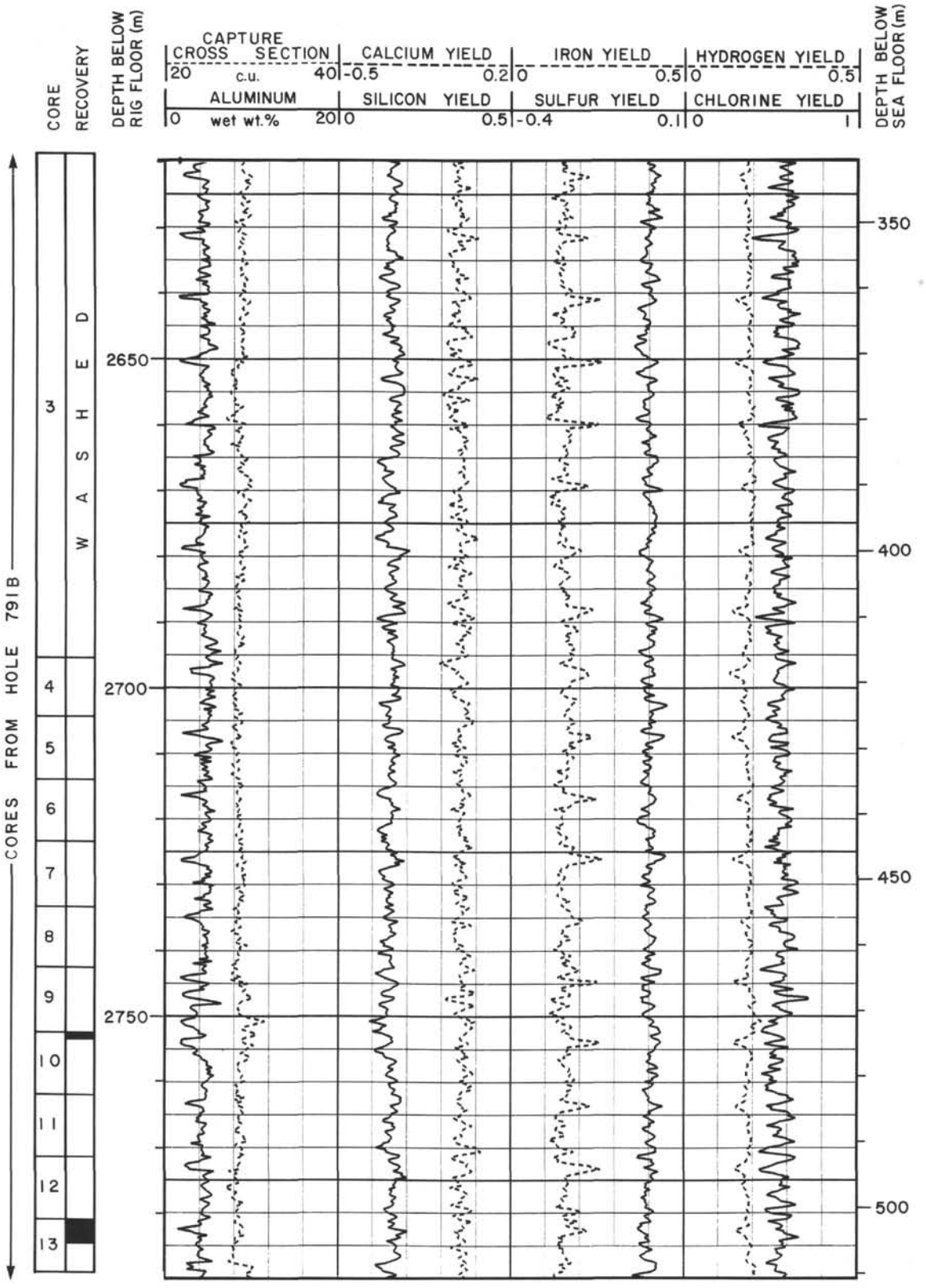

Figure 78 (continued).

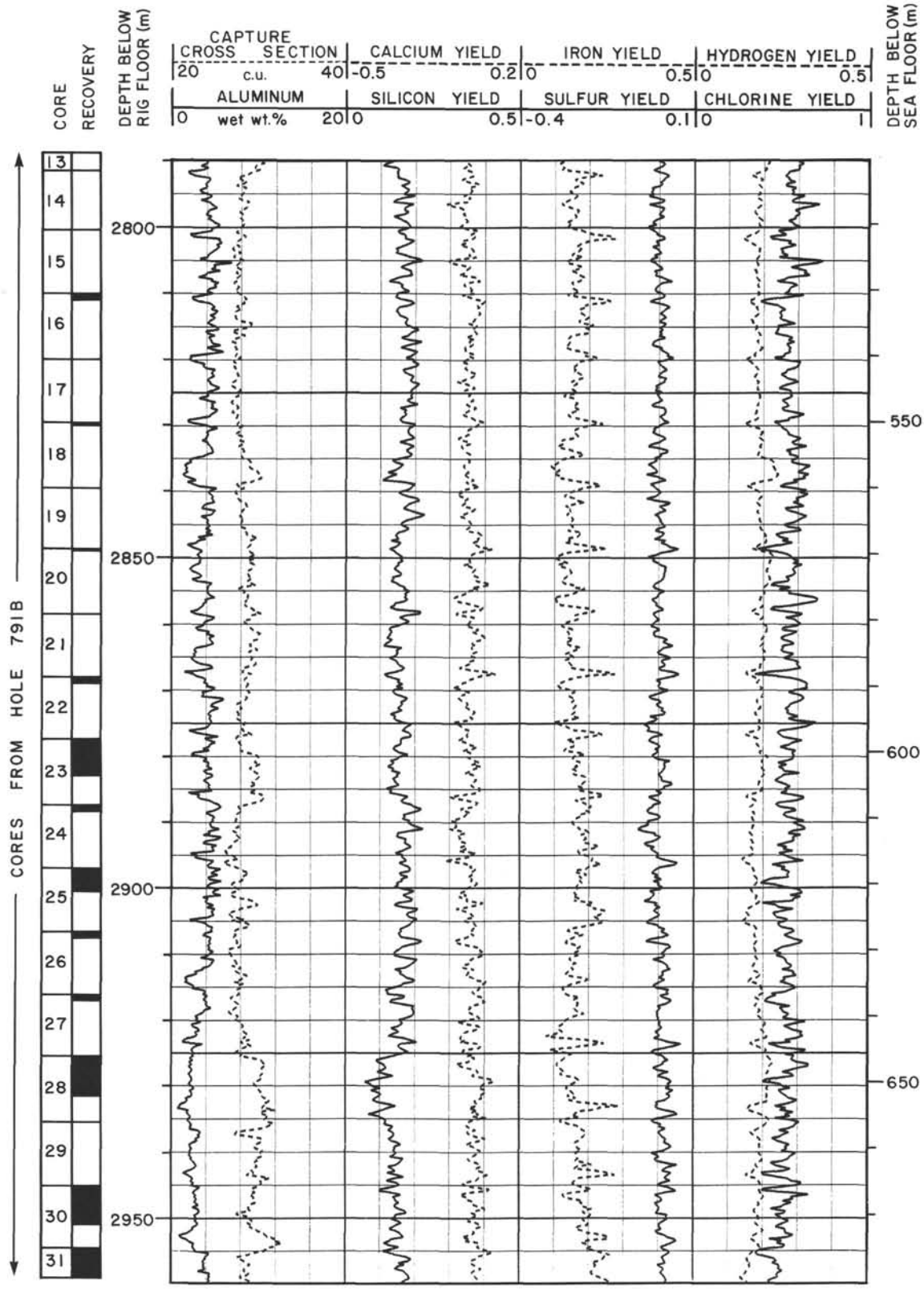

Figure 78 (continued).

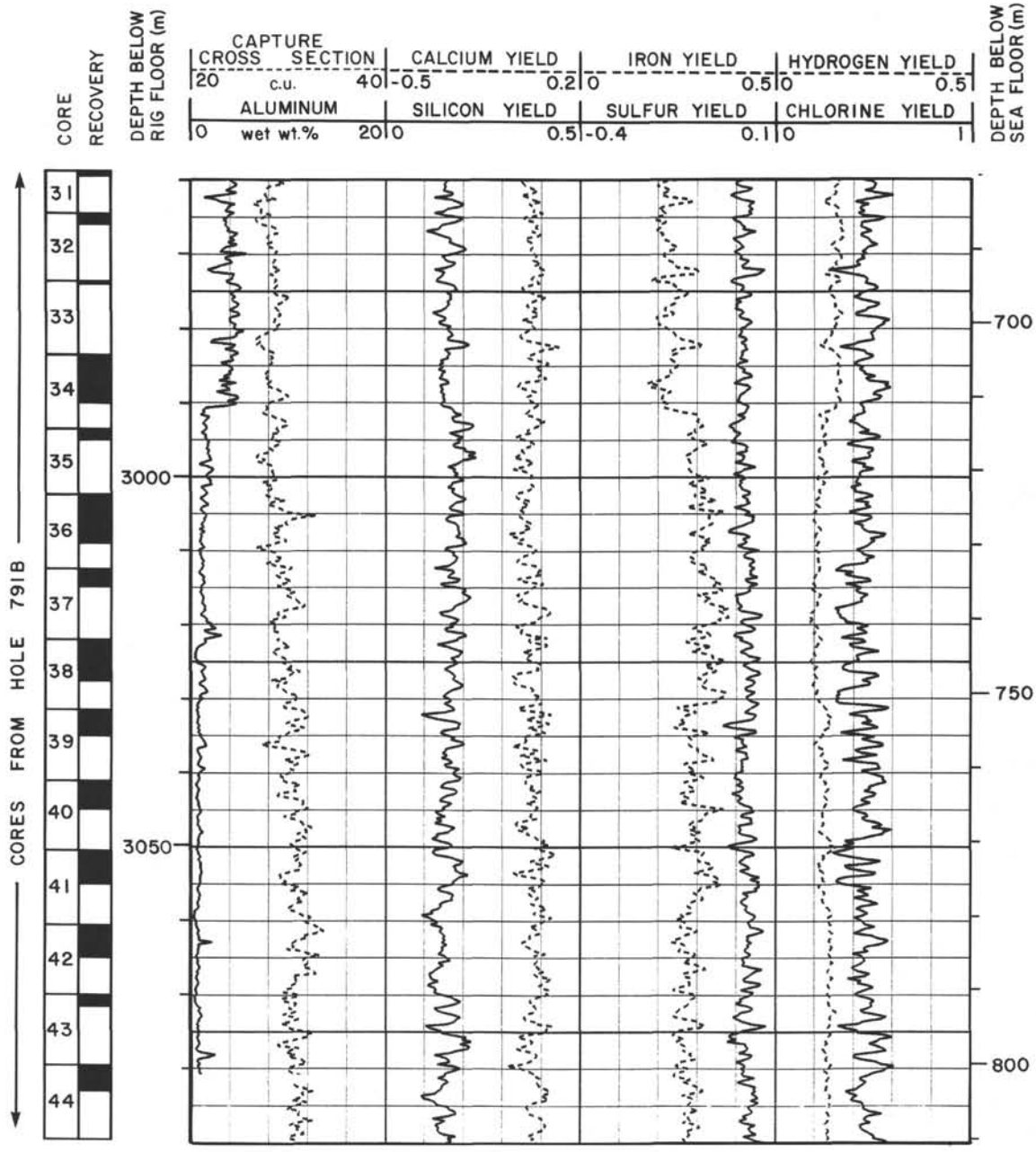

Figure 78 (continued).

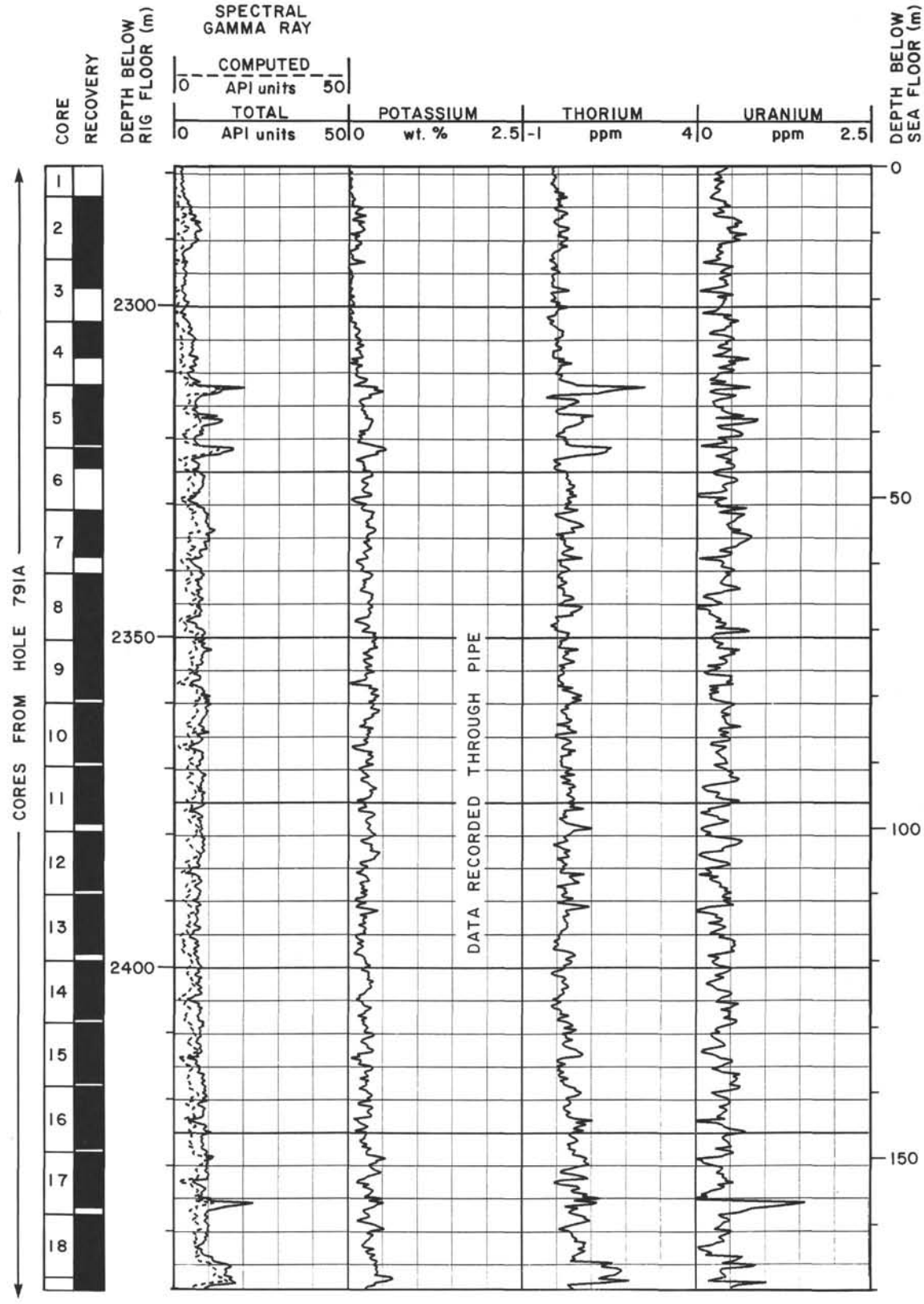

Figure 79. Summary log for potassium, thorium, and uranium obtained with the natural gamma-ray tool (NGT) for the interval from 0 to 830 mbsf. Also shown is the plot for spectral gamma-ray measurements.

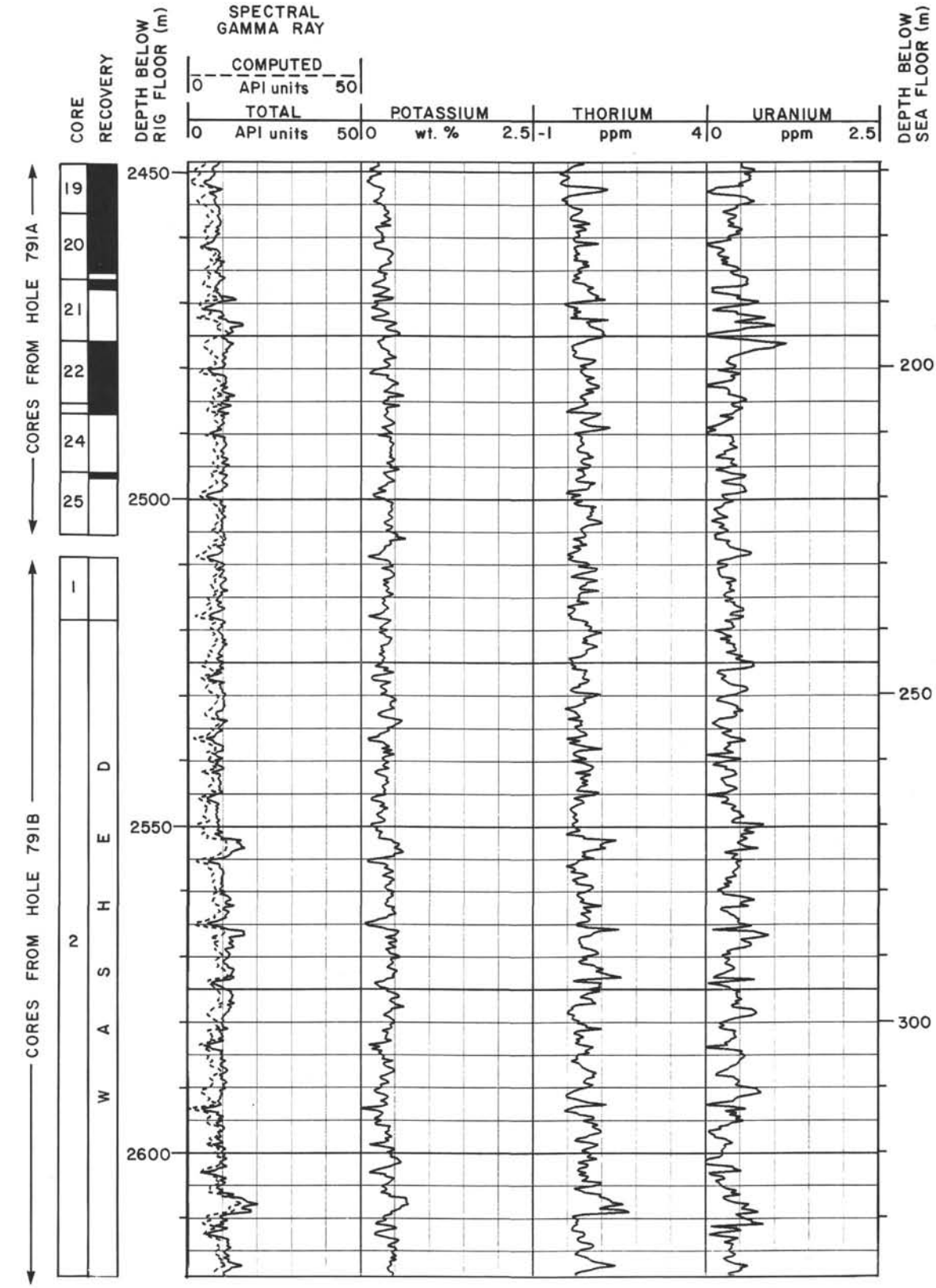

Figure 79 (continued).

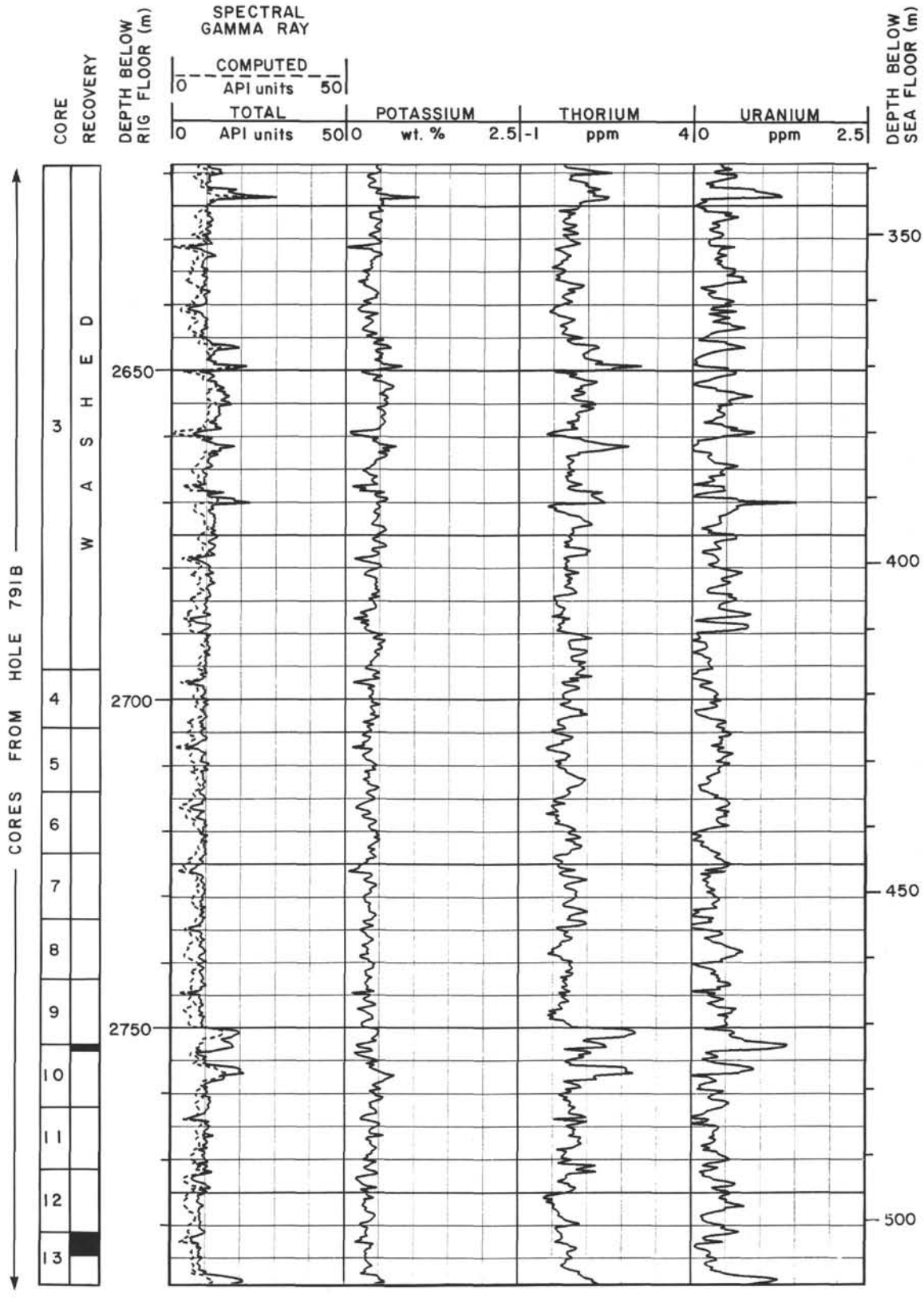

Figure 79 (continued).

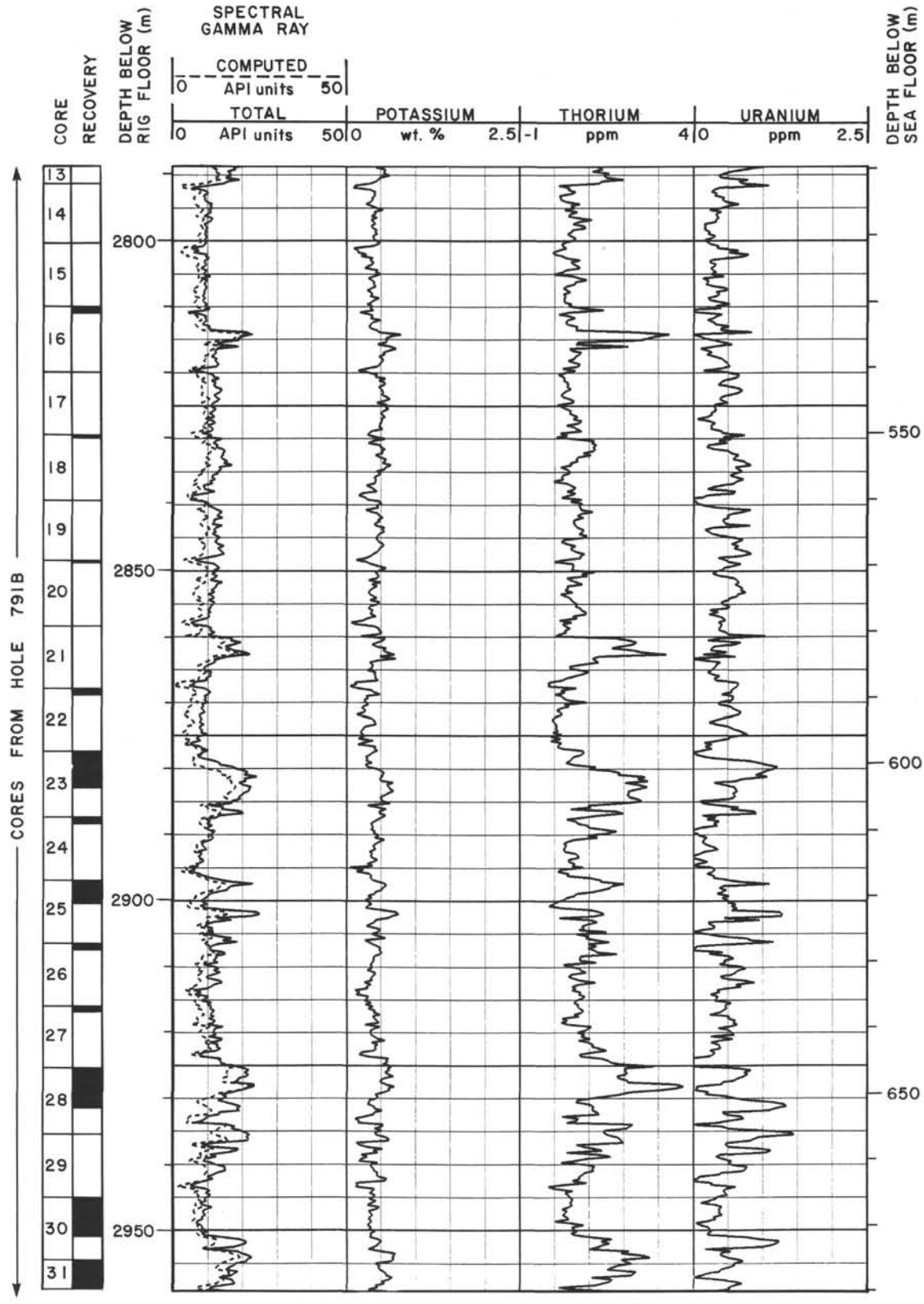

Figure 79 (continued).

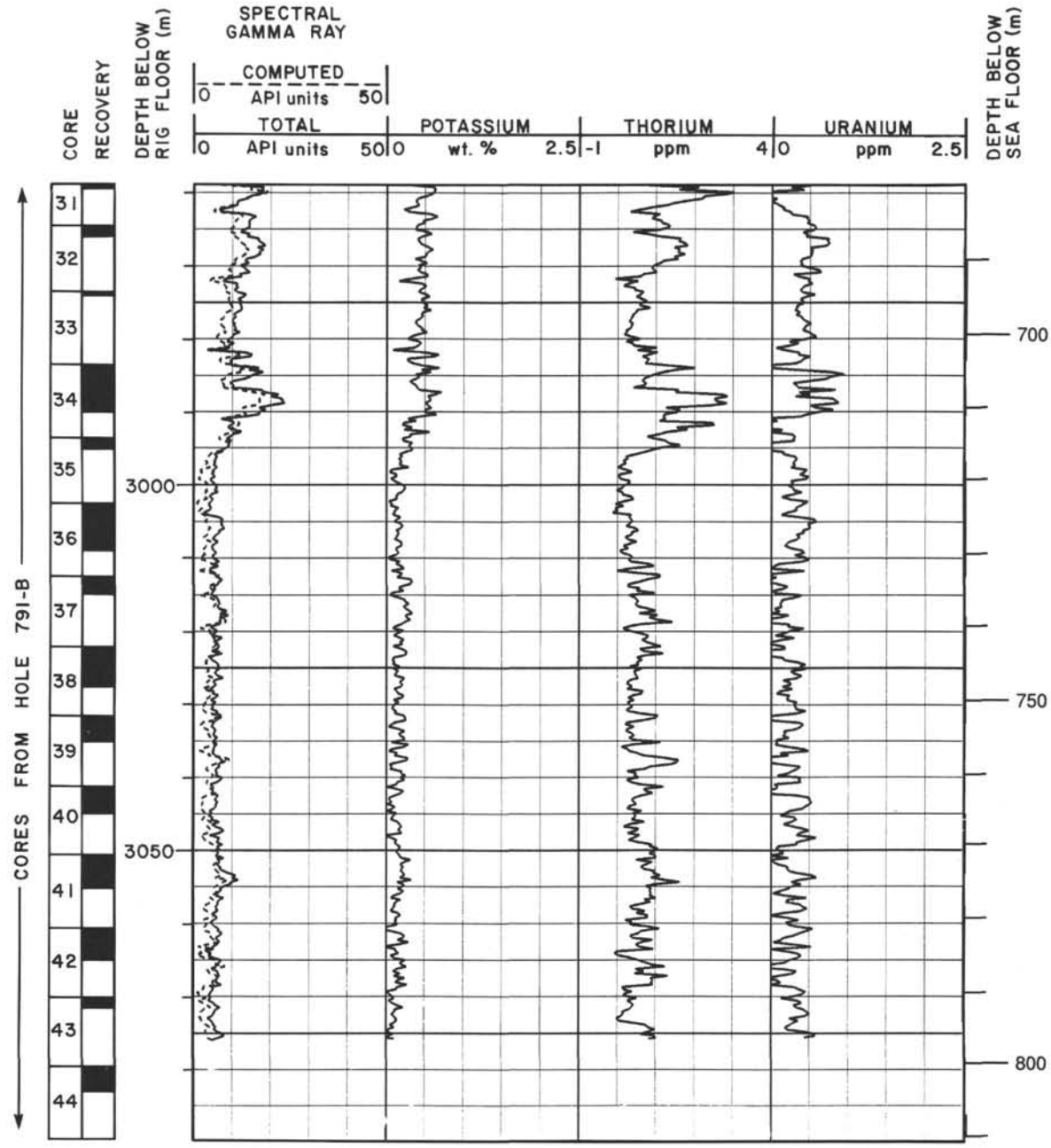

Figure 79 (continued).